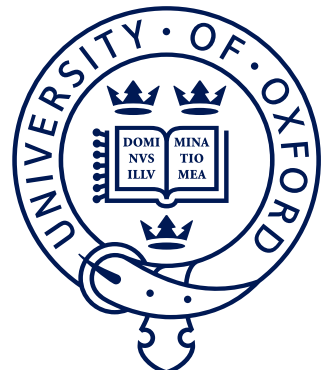


<sup>1</sup> **CP violation in  $B^\pm \rightarrow Dh^\pm$  decays**  
<sup>2</sup> **where  $D \rightarrow K_S^0 h'^+ h'^-$**

<sup>3</sup> *A measurement of the CKM angle  $\gamma$  at LHCb and understanding  
<sup>4</sup> the impact of neutral kaon CP violation*



<sup>6</sup> Mikkel Bjørn  
<sup>7</sup> St. Anne's College  
<sup>8</sup> University of Oxford

<sup>9</sup> A thesis submitted for the degree of  
<sup>10</sup> *Doctor of Philosophy*  
<sup>11</sup> Trinity 2020

# Abstract

This thesis presents a measurement of the Cabibbo-Kobayashi-Maskawa angle  $\gamma$  using  $B^\pm \rightarrow DK^\pm$  and  $B^\pm \rightarrow D\pi^\pm$  decays, where the  $D$  meson decays to one of the final states  $K_S^0\pi^+\pi^-$  and  $K_S^0K^+K^-$ . The measurement relies on the distribution of signal decays over the phase-space of the  $D$  decay, analysed using a model-independent method based on strong-phase measurements by the CLEO and BESIII collaborations. The measurement is performed using proton-proton collision data collected by the LHCb experiment during the full Runs 1 and 2 of the Large Hadron Collider, corresponding to a total integrated luminosity of  $9\text{ fb}^{-1}$  at centre-of-mass energies of  $\sqrt{s} = 7, 8,$  and  $13\text{ TeV}$ . The measurement determines that  $\gamma = (68.7^{+5.2}_{-5.1})^\circ$ , with an alternative solution corresponding to  $\gamma + 180^\circ$ . This is the most precise stand-alone measurement of  $\gamma$  to date, and surpasses the precision of all earlier measurements of  $\gamma$  combined.

The thesis also presents phenomenological study of the impact of neutral kaon  $CP$  violation and material interaction on  $\gamma$  measurements with  $B^\pm \rightarrow (K_S^0h^+h^-)_{DH'}h'^\pm$  decays. Existing literature estimated the potential bias to be  $\mathcal{O}(1^\circ)$  in  $B^\pm \rightarrow DK^\pm$  decays and to scale with  $1/r_B$ . This suggests potentially large biases for a measurement with  $B^\pm \rightarrow D\pi^\pm$  decays, since  $r_B^{D\pi} \simeq 0.005$  is much smaller than  $r_B^{DK} \simeq 0.1$ . However, the thesis argues that the actual impact is an order of magnitude smaller, as long as the  $CP$ -violation observables are determined based on the phase-space distribution of signal decays. This is confirmed in a number of numerical studies that take the detector geometries of the LHCb and Belle II detectors into account.

## Acknowledgements

<sup>36</sup> suitable thank you's

# Contents

37

38	<b>Preface</b>	vii
39	<b>1 Introduction</b>	1
40	<b>2 Theoretical background</b>	4
41	2.1 The C, P and T symmetries and their violation . . . . .	4
42	2.2 CP violation in the Standard Model . . . . .	6
43	2.2.1 The CKM matrix and the Unitarity Triangle . . . . .	7
44	2.2.2 Measuring $\gamma$ in tree level decays . . . . .	11
45	2.3 Measuring $\gamma$ using multi-body D final states . . . . .	14
46	2.3.1 Dalitz plots and the phase space of multi-body decays . . . . .	15
47	2.3.2 The BPGGSZ method to measure $\gamma$ . . . . .	16
48	2.3.3 A model-independent approach . . . . .	19
49	2.3.4 Measuring strong-phase inputs at charm factories . . . . .	21
50	2.3.5 Global CP asymmetry and the relation to GLW and ADS measurements . . . . .	26
51	2.4 Strategy for the LHCb measurement . . . . .	30
53	<b>3 The LHCb experiment</b>	34
54	3.1 The LHCb subdetectors . . . . .	36
55	3.1.1 The VELO . . . . .	37
56	3.1.2 Magnet and tracking stations . . . . .	39
57	3.1.3 The RICH detectors . . . . .	41
58	3.1.4 Calorimeters . . . . .	43
59	3.1.5 Muon detectors . . . . .	45
60	3.2 Reconstruction . . . . .	46
61	3.2.1 Track reconstruction . . . . .	46
62	3.2.2 Particle identification . . . . .	48
63	3.3 The LHCb trigger system . . . . .	50
64	3.3.1 The level-0 hardware trigger . . . . .	51
65	3.3.2 High-level triggers . . . . .	51
66	3.3.3 Offline data filtering: the LHCb stripping . . . . .	53
67	3.4 Simulation . . . . .	53
68	3.5 Data-taking conditions . . . . .	54

69	<b>4 Neutral kaon <math>CP</math> violation and material</b>	
70	<b>interaction in BPGGSZ measurements</b>	<b>55</b>
71	4.1 $CP$ violation and material interaction of neutral kaons . . . . .	56
72	4.1.1 A first look at the impact on $\gamma$ measurements . . . . .	59
73	4.2 Impact on BPGGSZ measurements of $\gamma$ :	
74	principles . . . . .	61
75	4.2.1 Modified symmetry relations . . . . .	61
76	4.2.2 Relationship between the $K_S^0$ and $K_L^0$ amplitudes . . . . .	62
77	4.2.3 Modification of the BPGGSZ yield equations . . . . .	63
78	4.3 Impact on BPGGSZ measurements of $\gamma$ :	
79	LHCb and Belle II measurements . . . . .	66
80	4.3.1 Detector geometries . . . . .	67
81	4.3.2 Kaon momentum distributions . . . . .	68
82	4.3.3 Experimental time acceptance . . . . .	68
83	4.3.4 Detector material budget . . . . .	70
84	4.3.5 Calculation procedure . . . . .	72
85	4.3.6 Results . . . . .	73
86	4.3.7 Coupled $B^\pm \rightarrow DK^\pm$ and $B^\pm \rightarrow D\pi^\pm$ measurements . . . . .	76
87	4.4 Concluding remarks . . . . .	77
88	<b>5 A BPGGSZ measurement of <math>\gamma</math> with <math>B^\pm \rightarrow Dh^\pm</math> decays</b>	<b>78</b>
89	5.1 Candidate reconstruction and selection . . . . .	78
90	5.1.1 Initial requirements . . . . .	79
91	5.1.2 Boosted decision tree . . . . .	81
92	5.1.3 Particle-identification requirements . . . . .	87
93	5.1.4 Final requirements . . . . .	87
94	5.1.5 Selected candidates . . . . .	88
95	5.2 Signal selection efficiencies . . . . .	91
96	5.2.1 Efficiency of the PID requirements . . . . .	92
97	5.2.2 Efficiency profile over the Dalitz plot . . . . .	93
98	5.3 Background studies . . . . .	94
99	5.3.1 Charmless decays . . . . .	98
100	5.3.2 Background from four-body $D$ decays . . . . .	100
101	5.3.3 Semi-leptonic backgrounds . . . . .	102
102	5.3.4 Cross-feed from other $D \rightarrow K_S^0 h^+ h^-$ decays . . . . .	108
103	5.3.5 Swapped-track backgrounds . . . . .	108
104	5.4 Signal and background mass shapes . . . . .	110
105	5.4.1 Signal decays . . . . .	111
106	5.4.2 Cross-feed between $B^\pm \rightarrow Dh^\pm$ channels . . . . .	112

107	5.4.3	Partially reconstructed backgrounds . . . . .	115
108	5.4.4	Combinatorial background . . . . .	120
109	5.4.5	Fit results . . . . .	120
110	5.5	Measurement of the CP-violation observables . . . . .	126
111	5.5.1	Fit setup . . . . .	126
112	5.5.2	Main results . . . . .	133
113	5.5.3	Cross checks . . . . .	136
114	5.6	Systematic uncertainties . . . . .	146
115	5.6.1	Strong phase uncertainties . . . . .	146
116	5.6.2	Efficiency-profile-related systematic uncertainties . . . . .	147
117	5.6.3	Mass shapes . . . . .	151
118	5.6.4	$CP$ violation and material interaction of the $K_S^0$ . . . . .	157
119	5.6.5	Impact of $D$ mixing . . . . .	157
120	5.6.6	PID efficiencies . . . . .	157
121	5.6.7	Dalitz-coordinate resolution . . . . .	158
122	5.6.8	The fixed yield fractions . . . . .	159
123	5.6.9	Systematic uncertainty due to backgrounds that are not modelled in fit . . . . .	159
124	5.6.10	Bias correction . . . . .	161
125	5.6.11	Charmless backgrounds . . . . .	162
126	5.6.12	Summary of systematic uncertainties . . . . .	162
128	5.7	Obtained constraints on $\gamma$ . . . . .	164
129	5.7.1	Statistical approach . . . . .	164
130	5.7.2	Interpretation results . . . . .	167
131	5.7.3	Compatibility with other measurements . . . . .	170
132	<b>6 Summary and outlook</b>		<b>174</b>
133	6.1 A look towards the future . . . . .		176
134	<b>Appendices</b>		
135	<b>A Projections of the main fit to data</b>		<b>179</b>
136	<b>B Contribution for the LHCb collaboration</b>		<b>185</b>
137	<b>Bibliography</b>		<b>186</b>

# Preface

<sup>139</sup> The work presented in this thesis has resulted in two papers, either under review  
<sup>140</sup> or published in the Journal of High Energy Physics. These are

<sup>141</sup> [1] *Measurement of the CKM angle  $\gamma$  using  $B^\pm \rightarrow DK^\pm$  and  $B^\pm \rightarrow D\pi^\pm$*   
<sup>142</sup> *with  $D \rightarrow K_S^0 h^+ h^-$  decays*, submitted to JHEP.

<sup>143</sup> This paper describes a measurement of the CKM angle  $\gamma$  using  $pp$  collision  
<sup>144</sup> data taken with the LHCb experiment during the Run 1 of the LHC, in 2011  
<sup>145</sup> and 2012, and during the full Run 2, in 2015–2018. The measurement uses the  
<sup>146</sup> decay channels  $B^\pm \rightarrow Dh^\pm$  where  $D \rightarrow K_S^0 h'^+ h'^-$ , in which  $h$  and  $h'$  denotes  
<sup>147</sup> pions or kaons. It obtains a value of  $\gamma = (69 \pm 5)^\circ$ , which constitutes the  
<sup>148</sup> world’s best single-measurement determination of  $\gamma$ . The work is the main  
<sup>149</sup> focus of this thesis and described in detail in Chapter 5.

<sup>150</sup> [2] *CP violation and material interaction of neutral kaons in measurements*  
<sup>151</sup> *of the CKM angle  $\gamma$  using  $B^\pm \rightarrow DK^\pm$  decays where  $D \rightarrow K_S^0 \pi^+ \pi^-$* , JHEP  
<sup>152</sup> 19 (2020) 106.

<sup>153</sup> This paper describes a phenomenological study of the impact of neutral-  
<sup>154</sup> kaon *CP* violation and material interaction on measurements of  $\gamma$ . With the  
<sup>155</sup> increased measurement precision to come in the near future, an understanding  
<sup>156</sup> of these effects is crucial, especially in the context of  $B \rightarrow D\pi$  decays; however  
<sup>157</sup> no detailed study had been published at the start of this thesis. The study is  
<sup>158</sup> the subject of Chapter 4. Some text excerpts and figures from the paper have  
<sup>159</sup> been reproduced in the thesis.

<sup>160</sup> All of the work described in the thesis is my own, except where clearly referenced  
<sup>161</sup> to others. Furthermore, I contributed significantly to an analysis of  $B^\pm \rightarrow DK^\pm$   
<sup>162</sup> decays with LHCb data taken in 2015 and 2016, now published in

<sup>163</sup> [3] *Measurement of the CKM angle  $\gamma$  using  $B^\pm \rightarrow DK^\pm$  with  $D \rightarrow K_S^0 \pi^+ \pi^-$ ,*  
<sup>164</sup>  *$K_S^0 K^+ K^-$  decays*, JHEP 08 (2018) 176.

<sup>165</sup> I was responsible for the selection and analysis of the signal channel, studies of  
<sup>166</sup> systematic uncertainties, and the interpretation of the measured observables in  
<sup>167</sup> terms of underlying physics parameters. The measurement is superseded by that  
<sup>168</sup> of Ref. [1] and is not described in detail in the thesis.

169 Beyond my data analysis and phenomenology work, I have made numerous other  
170 contributions to the LHCb experiment. I took part in the preparation for Run 3 by  
171 working as a *migration coordinator* for the *B-decay-to-open-charm* (B2OC) physics  
172 working group, responsible<sup>1</sup> for the migration of the working group's centralised,  
173 offline selections (so called *stripping lines*) to the software trigger framework being  
174 developed for the LHCb Upgrade.<sup>2</sup> With more than 800 lines in the current B2OC  
175 stripping module this is a major task; I took a leading role in the initial design and  
176 testing of the upgraded B2OC module, and in helping the first analysts implement  
177 their selections within it. I have also undertaken shift work as RICH piquet and  
178 Data Manager, and acted as the liaison between the B2OC physics working group  
179 and the *particle-identification* performance working group. This work is described  
180 in more detail in Appendix B.

---

<sup>1</sup>Along with Alessandro Bertolin and Shunan Shang.

<sup>2</sup>The current software trigger and *stripping* framework is presented in Section 3.3.

*Le roi est mort, vive le roi!*

— Traditional French proclamation at the death  
of one monarch and the ascension of a new

# 1

181

182

## Introduction

183    "*The King is dead, long live the King!*". Thus spoke the Duke of Uzès at the death  
184    of every French monarch from 1498 until Louis XVI took the throne (presumably  
185    the current duke had other things on his mind during the winter 1792–93). In the  
186    original setting, the words express the fundamental premise of hereditary monarchy:  
187    at the last breath of the king, the god-given sovereignty of the crown passes to the  
188    oldest, living heir; in an altogether different sense, the words fittingly summarise  
189    the situation in the field of particle physics.

190    In the sub-atomic world, the Standard Model rules supreme in spite of everyone  
191    agreeing that it is in fact quite dead: while the successes of the model are numerous,  
192    it leaves several phenomena that have observed in the world completely unexplained.  
193    Most famously, *gravity* is not included in the model, and no mathematically  
194    consistent unification of general relativity and the Standard Model has been found.  
195    A related short coming is the lack of an explanation of *dark matter* and *dark energy*  
196    within the theory: the Standard Model describes only 5 % of the energy content  
197    of modern cosmological models of the universe. Of special relevance to this thesis  
198    is of course the matter-antimatter asymmetry in our matter-dominated universe,  
199    for which there is no explanation in the Standard Model. Furthermore, there  
200    are a number of theoretical issues, such as the (relatively) low mass of the Higgs'  
201    boson requiring extremely fine tuning of parameter values, and the absence of an  
202    explanation for the hierarchy of masses that the Higgs mechanism gives rise to. When  
203    the Standard Model continues to live long in spite of these shortcomings, it is not  
204    for want of tries at murder: thousands of physicists at dozens of experiments spend  
205    their days looking for physics effects that are *Beyond the Standard Model*, but so far

206 no (statistically significant) experimental results have been obtained that point to a  
207 suitable successor, able to resolve the fundamental issues with the existing theory.<sup>1</sup>

208 These efforts take place at two complimentary frontiers. At the vanguard  
209 of the *energy frontier* is the Large Hadron Collider, where protons are collided  
210 at energies never reached before in any experimental settings. The CMS and  
211 ATLAS experiments look for new, heavy particles produced in these unprecedented  
212 circumstances. However, so far it has only been possible to *rule out* alternative  
213 theories, excluding regions of (infinite) phase space in a multitude of possible  
214 standard model extensions.<sup>2</sup>

215 The other frontier is the *precision frontier*, which seeks to exploit that the  
216 (potential) existence of heavy particles can cause or influence phenomena at energies  
217 that are orders of magnitude smaller than required for their direct production. The  
218 canonical example is that of weak decays that occur in atom nuclei at rest, but  
219 are mediated by the  $W$  boson, which can only be directly produced in powerful  
220 particle accelerators. Thus, by way of precise measurements of processes at a  
221 low energy, characteristics of high energy physics can be derived. The field of  
222 flavour physics, which concerns itself with processes that distinguish the different  
223 generations of quarks and leptons in the Standard Model, plays a significant role  
224 at the precision frontier. Historically, both the existence of the charm and third-  
225 generation quarks were predicted before the particles could be produced, in order  
226 to explain lower energy phenomena (the lack of flavour-changing neutral currents,  
227 and  $CP$  violation, respectively); and the  $c$  and  $t$  masses could be constrained before  
228 their discoveries by mixing measurements of  $\Delta m_K$  and  $\Delta m_B$ , respectively. With  
229 regards to constraints on *new*, as-of-yet unknown physics effects, impressive results  
230 have been achieved in flavour physics experiments, where results of meson mixing  
231 and  $CP$  violation measurements provide bounds on BSM physics at energy scales  
232 of the order  $\Lambda \gtrsim 10^4$  TeV; a much higher energy scale than what can be directly  
233 probed in current and potential particle colliders.<sup>3</sup>

234 This thesis places itself at the forefront of the latter efforts, presenting the  
235 World's most precise measurement of the  $CP$ -violating phase  $\gamma$ ; a fundamental

---

<sup>1</sup>Neutrino masses have been experimentally observed to be different from zero. This can be accounted for by several possible extensions of the Standard Model, which cannot be told apart given current data, but potentially in the near future. However, such extensions are not expected to resolve the issues outlined above.

<sup>2</sup>The, obviously extremely important, observation of the Higg's boson and the determination of its couplings and properties all agree with the Standard Model expectations.

<sup>3</sup>These bounds do not rule out new physics lower energy scales, but they do impose stringent constraints on the possible flavour structure of any new physics model at the  $< 10^4$  TeV scale.

parameter in the Standard Model, in which it describes the sole source of matter-antimatter asymmetry. The measurement is based on samples of  $B^\pm \rightarrow DK^\pm$  and  $B^\pm \rightarrow D\pi^\pm$  decays, where the  $D$  meson is reconstructed in one of the final states  $K_S^0\pi^+\pi^-$  and  $K_S^0K^+K^-$ . The role of  $CP$  violation in the Standard Model and the methodology used to probe it in the thesis are described in detail in Chapter 2.

The measurement is based on data taken with the LHCb experiment during Run 1 and 2 of the LHC. The detector and software used to obtain the data set are described in Chapter 3.

It is the first time that  $B^\pm \rightarrow D\pi^\pm$  decays are used to measure  $\gamma$  with the approach taken in the thesis; therefore, a number of effects had to be considered that were not important in measurements based solely on  $B^\pm \rightarrow DK^\pm$  decays. The most important such effect is due to  $CP$  violation and material interaction of the neutral kaon in the final state, because existing literature at the outset of the work suggested that the impact could potentially be significant. Therefore, these phenomena had to be analysed in detail to establish the feasibility of the main measurement of the thesis. Chapter 4 describes such an analysis, and shows that the existing literature overestimated the potential effect by an order of magnitude; in fact the impact on the measurement is negligible.

The main results of the thesis are presented in Chapter 5, where the measurement of  $\gamma$  is described in detail. The approach differs from earlier measurements in the same decay channel due to the inclusion of  $B^\pm \rightarrow D\pi^\pm$  as a signal channel; therefore, a series of feasibility studies that lead to the specific approach being chosen are also presented.

Naturally, the work presented here is far from the last word to be said on the value of  $\gamma$ . In the very near future, several important results will be updated by the LHCb collaboration, based on the full data set collected during Run 2 of the LHC. In the coming 10–15 years, both the LHCb and Belle II collaborations will record data samples of  $B$  decays that are orders of magnitudes larger than those collected before, pushing the obtainable precision on  $\gamma$  towards, even below, one degree. An outlook towards this ultra-high-precision era of  $CP$ -violation measurements is given in Chapter 6, along with a summary of the contributions made in the thesis.

# 2

267

268

## Theoretical background

269 This chapter lays out the theoretical framework of the thesis. Section 2.1 introduces  
270 charge and parity symmetry violation in general, while Section 2.2 covers the  
271 description in the Standard Model and the general theory behind charge-parity  
272 symmetry violation measurements in charged  $B$  decays. Section 2.3 focuses on  
273 the theory of measurements using  $B^\pm \rightarrow Dh^\pm$  decays with multi-body  $D$  final  
274 states, after which the specific analysis strategy for the measurement described  
275 in the thesis is outlined out in Section 2.4.

276 **2.1 The C, P and T symmetries and their vio-  
277 lation**

278 The concept of symmetry plays a fundamental role in modern physics. By Noether's  
279 theorem [4], the simple assumption of invariance of our physical laws under universal  
280 temporal and spatial translations leads to the very non-trivial prediction of conserved  
281 energy and momentum; within the field of particle physics, the interactions and  
282 dynamics of the Standard Model (SM) follow completely simply from requiring  
283 the fundamental particle fields to satisfy a local  $U(1) \times SU(2) \times SU(3)$  gauge  
284 symmetry [5]; and one of the short-comings of the SM, is that it fails to explain  
285 the apparent *lack* of symmetry in our matter-dominated universe [6]. Indeed, it is  
286 important to experimentally establish the symmetries of our world at a fundamental  
287 level, and the degree to which they are broken.

288 Three discrete symmetries of importance are the symmetries under

- 289     1. The charge operator  $C$ , which conjugates all internal quantum numbers of a  
 290       quantum state and thus converts particles into their anti-particle counter parts.  
 291       For example,  $C$  transforms the electric charge of a particle state  $Q \rightarrow -Q$ .
- 292     2. The parity operator  $P$ , which inverts the spatial dimensions of space time:  
 293        $\vec{x} \rightarrow -\vec{x}$ . As such, it transforms left-handed particle fields into right-handed  
 294       particle fields and vice versa.
- 295     3. The time-inversion operator  $T$ , which inverts the temporal dimension of space  
 296       time:  $t \rightarrow -t$ .

297     These are fundamentally related by the *CPT* theorem [7] , which states that any  
 298       Lorentz-invariant Quantum Field Theory (QFT) must be symmetric under the  
 299       simultaneous application of *all* three operators. However, any one of the symmetries  
 300       can be broken individually, and experiments have shown the physical laws of our  
 301       world to violate each of the  $C$ ,  $P$ , and  $T$  symmetries.

302     Such a symmetry-breaking effect was established for the first time in 1956, when  
 303       Chien-Shiung Wu observed parity violation in weak decays of Co-60 nuclei [8], after  
 304       carrying out an experiment that was proposed by Yang Chen-Ning and Tsung-Dao  
 305       Lee [9]. While this experiment established the breaking of  $P$  symmetry, it left open  
 306       the possibility that the physical laws are invariant under a combination of a charge-  
 307       and parity inversion; that they are *CP* symmetric. However, this was disproved in  
 308       1964 when Kronin and Fitch observed that long-lived kaons, which predominantly  
 309       decay to the *CP*-odd  $3\pi$  state, could also decay to the *CP*-even  $\pi\pi$  states [10].

310     Since then, *CP* violation has been found in the  $B^0$  system by the BaBar and Belle  
 311       collaborations [11, 12] during the early 2000's; the  $B$  factories, along with CDF, also  
 312       saw evidence for *CP* violation in  $B^\pm$  decays [13–18] later confirmed by LHCb [19],  
 313       and *CP* violation was measured in the  $B_s^0$  system by LHCb in 2013 [20]; within the  
 314       last year and a half, the first observation of *CP*-violation in  $D^0$  decays has also been  
 315       made by the LHCb collaboration [21], and most recently evidence for *CP*-violation in  
 316       the neutrino sector has been reported by the T2K collaboration [22]. The observed  
 317       effects can be divided into distinct classes. The conceptually simplest case is

- 318     1. *CP-violation in decay*, where  $|A/\bar{A}| \neq 1$  for some decay amplitude  $A$ , and the  
 319       amplitude  $\bar{A}$  of the *CP*-conjugate decay. The result is different decay rates in  
 320       two *CP*-conjugate decays

$$\Gamma(M \rightarrow f) \neq \Gamma(\bar{M} \rightarrow \bar{f}). \quad (2.1)$$

This type of  $CP$  violation was not seen until the late 1980ies [23, 24], more than 20 years after the first observation of  $CP$  violation, and only finally established around the year 2000 [25, 26]. This discovery was also made in  $K \rightarrow \pi\pi$  decays.

$CP$ -violation in decay is the only type possible for charged initial states, and it is thus the main focus of the thesis. Two additional  $CP$ -violating effects are possible for neutral initial states (a situation that will be the main focus of Chapter 4). These effects are

2.  $CP$ -violation in mixing, which denotes the case where the mixing rates between two  $CP$ -conjugate states,  $M^0$  and  $\bar{M}^0$ , differ

$$\Gamma(M^0 \rightarrow \bar{M}^0) \neq \Gamma(\bar{M}^0 \rightarrow M^0). \quad (2.2)$$

The  $CP$  violation first observed by Kronin and Fitch in the neutral kaon sector [10] is (dominantly) of this type.

3.  $CP$ -violation in interference between mixing and decay, which can be present for a neutral initial states  $M^0$  decaying into a final state  $f$  common to both  $M^0$  and  $\bar{M}^0$ . The decay rate includes an interference term between two amplitudes: the amplitude for a direct  $M^0 \rightarrow f$  decay and the amplitude for a decay after mixing:  $M^0 \rightarrow \bar{M}^0 \rightarrow f$ . Even in the absence of the two aforementioned effects, the rates  $\Gamma(M^0 \rightarrow f)$  and  $\Gamma(\bar{M}^0 \rightarrow \bar{f})$  can differ due to the interference term. Such  $CP$  asymmetries have been measured in eg.  $B^0 \rightarrow J/\psi K$  by LHCb and the  $B$  factories, and in  $B_s^0 \rightarrow J/\psi \phi$  decays by the LHC and Tevatron experiments [27].

$CP$  violation measurements thus have a long, rich, and still-developing history.

## 2.2 CP violation in the Standard Model

All existing measurements of  $CP$  violation in the quark sector are naturally explained in the SM; indeed, the need to explain the observation  $CP$  violation in neutral kaons was a driving force in the development of the model in the first place, when it lead Kobayashi and Maskawa to predict the existence of then-unknown particles in 1973 [28] (now known to be the third generation quarks).

### 2.2.1 The CKM matrix and the Unitarity Triangle

The SM contains three generations of quarks, each consisting of an up-type quark ( $u$ ,  $c$ , and  $t$ ) and a down-type quark ( $d$ ,  $s$ , and  $b$ ). The charged weak interaction of the  $W^\pm$  boson couples up and down-type quarks. The quark states that couple to the  $W$  are not (a priori) identical to the mass eigenstates, and can be denoted  $(u', c', \text{ and } t')$  and  $(d', s', \text{ and } b')$ . A basis for the quark states can be chosen such that the weakly coupling up-quark states are identical to the propagating quark states,  $u = u'$ , but then the down-type quark state are different:  $d' \neq d$ . The two bases of the down-type quarks are related via the Cabibbo-Kobayashi-Maskawa (CKM) matrix [28, 29]<sup>1</sup>

$$\begin{pmatrix} d' \\ s' \\ t' \end{pmatrix} = V \begin{pmatrix} d \\ s \\ t \end{pmatrix} = \begin{pmatrix} V_{ud} & V_{us} & V_{ub} \\ V_{cd} & V_{cs} & V_{cb} \\ V_{td} & V_{ts} & V_{tb} \end{pmatrix} \begin{pmatrix} d \\ s \\ t \end{pmatrix}. \quad (2.3)$$

Thus the Lagrangian terms representing the coupling of a  $W^\pm$  boson with a  $u$ - and a  $d$ -type quark is

$$\mathcal{L}_{W^+} = -\frac{g}{\sqrt{2}} V_{ud} (\bar{u} \gamma^\mu W_\mu^+ d) \quad \mathcal{L}_{W^-} = -\frac{g}{\sqrt{2}} V_{ud}^* (\bar{d} \gamma^\mu W_\mu^- u) \quad (2.4)$$

where  $g$  is the weak coupling constant,  $\gamma_u$  are the Dirac matrices, and  $u$  and  $d$  represent the left-handed components of the physical quark states.

The CKM matrix is a unitary complex  $3 \times 3$  matrix, and hence has  $3^2 = 9$  independent, real parameters. However, 5 of these can be absorbed into non-physical phases of the quark states (both mass and weak eigenstates) and hence the matrix has 4 real, physical parameters: 3 mixing angles and a single phase. Chau and Keung [30] proposed the parameterisation

$$V = \begin{pmatrix} 1 & 0 & 0 \\ 0 & c_{23} & s_{23} \\ 0 & -s_{23} & c_{23} \end{pmatrix} \begin{pmatrix} c_{13} & 0 & s_{13} e^{-i\delta_{CP}} \\ 0 & 1 & 0 \\ -s_{13} e^{-i\delta_{CP}} & 0 & c_{13} \end{pmatrix} \begin{pmatrix} c_{12} & s_{12} & 0 \\ -s_{12} & c_{12} & 1 \\ 0 & 0 & 1 \end{pmatrix} \\ = \begin{pmatrix} c_{12}c_{13} & s_{12}c_{13} & s_{13}e^{-i\delta_{CP}} \\ -s_{12}c_{23} - c_{12}s_{23}s_{13}e^{i\delta_{CP}} & c_{12}c_{23} - s_{12}s_{23}s_{13}e^{i\delta_{CP}} & s_{23}c_{13} \\ s_{12}s_{23} - c_{12}c_{23}s_{13}e^{i\delta_{CP}} & -c_{12}s_{23} - s_{12}s_{23}s_{13}e^{i\delta_{CP}} & c_{23}c_{13} \end{pmatrix} \quad (2.5)$$

which is the preferred standard by the *Particle Data Group* (PDG) [31]. Here,  $s_{ij} \equiv \sin \theta_{ij}$  and  $c_{ij} \equiv \cos \theta_{ij}$  denote the sine and cosine of three rotation angles in quark space;  $\theta_{12} = \theta_C$  being the usual Cabibbo angle [29].

<sup>1</sup> A basis for the quarks can of course be chosen, such that neither the up-quarks or the down-quarks are expressed in their mass eigenstates. In that case the CKM matrix is recovered as  $V = U_u U_d^\dagger$ , where  $U_{u/d}$  is the unitary transformation matrices that transform the  $u/d$  quarks from the weak eigenbasis to their mass eigenstates.

The presence of the complex phase  $\delta_{CP}$  in the Lagrangian term of the  $W$  coupling causes  $CP$  violation because, as evident from Eq. (2.4), if  $\delta_{CP}$  enters the amplitude for some decay mediated by a  $W$  boson,  $A = |A|e^{i(\delta_0 + \delta_{CP})}$ , then it will enter the  $CP$  conjugate decay amplitude with the opposite sign:  $\bar{A} = |A|e^{i(\delta_0 - \delta_{CP})}$ . In these expressions,  $\delta_0$  denotes a  $CP$  conserving phase that is not caused by complex terms in the Lagrangian, but arises due to potential intermediate states in the decay amplitude.<sup>2</sup> Usually the underlying mechanism is due to QCD effects, and these  $CP$  conserving phases are therefore generally dubbed *strong* phases, as opposed to the  $CP$  violating *weak* phase of the  $W$  coupling [31]. This terminology will be applied throughout the thesis.

The absolute values of all nine elements of the CKM matrix have been measured individually, and the PDG average values are [31]<sup>3</sup>

$$\begin{pmatrix} |V_{ud}| & |V_{us}| & |V_{ub}| \\ |V_{cd}| & |V_{cs}| & |V_{cb}| \\ |V_{td}| & |V_{ts}| & |V_{tb}| \end{pmatrix} = \begin{pmatrix} 0.97370 \pm 0.00014 & 0.2245 \pm 0.0008 & 0.00382 \pm 0.00024 \\ 0.221 \pm 0.004 & 0.987 \pm 0.011 & 0.0410 \pm 0.0014 \\ 0.0080 \pm 0.0003 & 0.0388 \pm 0.0011 & 1.013 \pm 0.030 \end{pmatrix}. \quad (2.6)$$

The CKM matrix elements along the diagonal are all approximately equal to unity, with the off-diagonal elements showing a clear hierarchy of sizes, which in terms of the parameterisation of Eq. (2.5) translates to  $s_{13} \ll s_{23} \ll s_{12}$ . This motivates an often used, alternative parameterisation of the matrix, where the elements are expressed as power series in  $\lambda \equiv s_{12} \simeq 0.23$  that naturally incorporates the hierarchy: the Wolfenstein parameterisation [32]. The definitions

$$\begin{aligned} s_{12} &\equiv \lambda \\ s_{23} &\equiv \lambda^2 A \\ s_{13} e^{-i\delta_{CP}} &\equiv \lambda^3 (\rho - i\eta) \end{aligned} \quad (2.7)$$

are made, after which the unitarity conditions (or Eq. 2.5) determine the remaining elements to any order in  $\lambda$ .<sup>4</sup> To  $\mathcal{O}(\lambda^5)$  the Wolfenstein parameterisation of the

<sup>2</sup>It is generally true that all phases of a single term in a given amplitude will be convention dependent, but that the phase differences between terms are not.

<sup>3</sup>References to the individual measurements can be found in the *CKM Quark-Mixing Matrix* review of the 2020 version of the PDG.

<sup>4</sup>Other variants of the Wolfenstein parameterisation do exist [33]. They all agree at the lowest orders of  $\lambda$ .

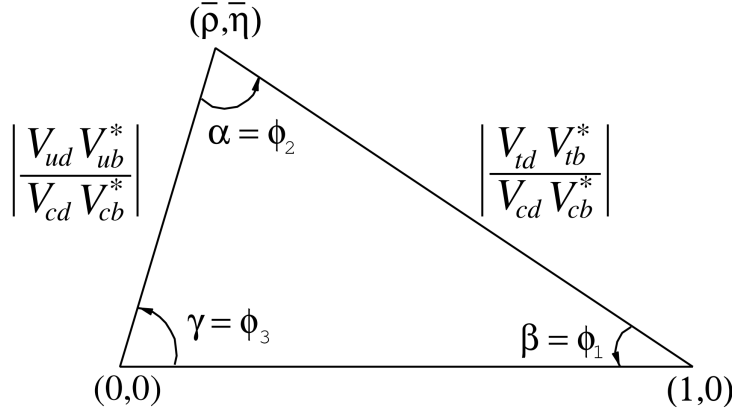


**Figure 2.1:** Definition of the lengths and sides of the Unitarity Triangle. Reproduced from the *CKM Quark-Mixing Matrix* review of the PDG [31].

390 CKM matrix is [34, 35]

$$V = \begin{pmatrix} 1 - \frac{\lambda^2}{2} - \frac{\lambda^4}{8} & \lambda & A\lambda^3(\rho - i\eta) \\ -\lambda + \frac{\lambda^5}{2}A^2(1 - 2(\rho + i\eta)) & 1 - \frac{\lambda^2}{2} - \frac{\lambda^4}{8}(1 + 4A^2) & A\lambda^2 \\ A\lambda^3(1 - (\rho + i\eta)(1 - \frac{\lambda^2}{2})) & -A\lambda^2(1 - \frac{\lambda^2}{2}(1 - 2(\rho + i\eta))) & 1 - \frac{1}{2}A^2\lambda^4 \end{pmatrix}. \quad (2.8)$$

391  
392 The unitarity condition  $V^\dagger V = \mathbb{1}$  of the CKM matrix defines 9 relations between  
393 the CKM elements of the form

$$\sum_j V_{jq}^* V_{jq} = 1 \quad , \quad q \in \{d, s, b\} \quad \text{along the diagonal} \quad (2.9a)$$

$$\sum_j V_{jq}^* V_{jq'} = 0 \quad , \quad q, q' \in \{d, s, b\}, q \neq q' \quad \text{off-diagonal.} \quad (2.9b)$$

394 The off-diagonal conditions constrain three complex numbers to sum to zero, and  
395 can thus be visualised as triangles in the complex plane, the so-called unitarity  
396 triangles. Of these, the triangle corresponding to the  $(d, b)$  elements plays a  
397 special role, because all three sides are of the same order of magnitude,  $\mathcal{O}(\lambda^3)$ .  
398 When expressed in the form

$$\frac{V_{ud}^* V_{ub}}{V_{cd}^* V_{cb}} + \frac{V_{td}^* V_{tb}}{V_{cd}^* V_{cb}} + 1 = 0, \quad (2.10)$$

399 it is often referred to as the singular Unitarity Triangle, illustrated in Fig. 2.1 where  
400 the usual names for the three angles are also given.

401 Over-constraining the unitarity triangle by making separate measurements  
402 of all sides and angles, in as many different decay channels as possible, is an  
403 important, and non-trivial test of the SM. The current experimental constraints

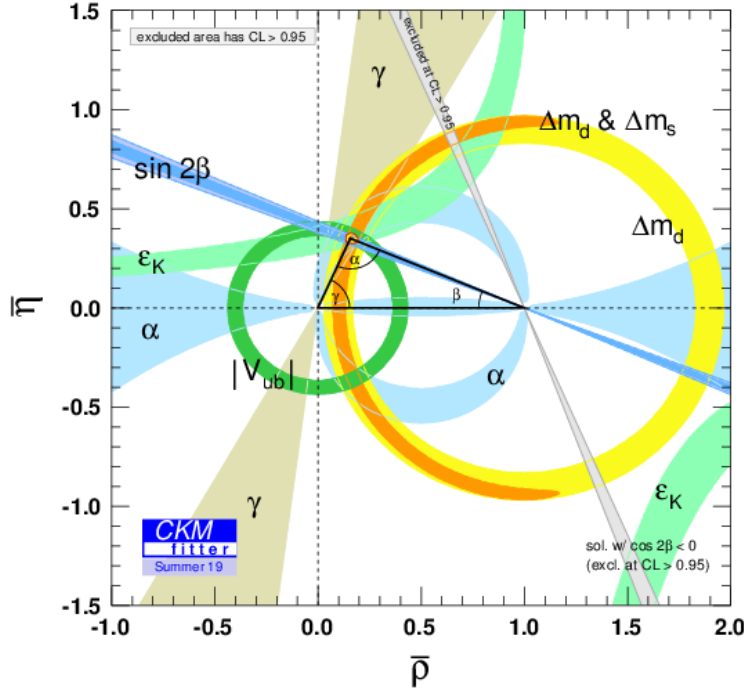


**Figure 2.2:** Current constraints on the Unitarity Triangle parameters as determined by the CKMFitter group for the EPS 2019 conference [36].

are in agreement with the SM predictions, as visualised in Fig. 2.2. The topic of the thesis is a measurement of the CKM angle

$$\gamma \equiv \arg(-V_{ud}V_{ub}^*/V_{cd}V_{cb}^*) = \arg(-V_{cb}V_{cd}^*/V_{ub}V_{ud}^*). \quad (2.11)$$

From the Wolfenstein parameterisation in Eq. (2.8), it is can be seen that  $\gamma$  equals the fundamental  $CP$ -violating phase  $\delta_{CP}$  to  $\mathcal{O}(\lambda^4)$ . The angle  $\gamma$  is unique among the CKM parameters, in that it can be easily measured in tree-level processes, without significant theoretical uncertainty from lattice QCD calculations [37]. Since  $\gamma$  is (essentially) an input parameter in the SM, it is not possible to calculate a theoretical expectation that measurements can be compared to. However, tree-level processes are generally considered unlikely to be affected by Beyond-Standard-Model (BSM) effects. Therefore direct measurements of  $\gamma$  can be considered a SM benchmark, to be compared with constraints based on measurements of other CKM elements that are measured in loop-level processes, and thus are more likely to be affected by BSM effects [38]. These constraints are obtained in global fits, based on measurements of all CKM elements except  $\gamma$ , in which the unitarity of the CKM matrix is assumed to hold true. In practice,  $\gamma$  is constrained by the value of  $\beta$  and the elements defining

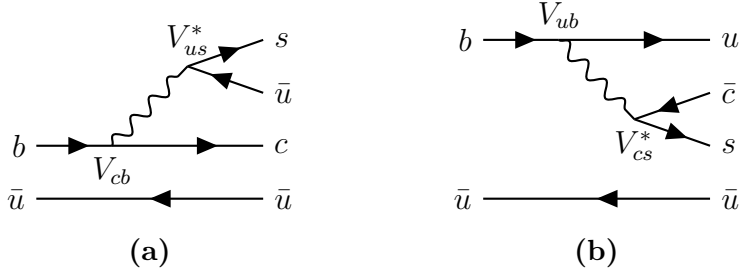


**Figure 2.3:** Tree level Feynman diagrams describing (a)  $B^- \rightarrow D^0 K^-$  and (b)  $B^- \rightarrow \bar{D}^0 K^-$  decays. The electro-weak phase difference between the two decays is  $\Delta\phi = \arg(V_{cb}V_{us}^*/V_{ub}V_{cs}^*) \simeq \gamma$ .

the length of the side of the unitarity triangle opposite  $\gamma$ ; the measurement of both rely on neutral  $B$  mixing processes. If BSM physics enter the mixing loop, but is not accounted for in the global fit, it can result in the value of  $\gamma$  that is determined in the global fit being different to the one obtained in direct measurements. The current, worldwide combination of direct measurements published by the CKMFitter group, is  $\gamma = (72.1^{+5.4}_{-5.7})^\circ$ , to be compared with the estimate from a global fit (without any  $\gamma$  measurements) of  $\gamma = (65.66^{+0.90}_{-2.65})^\circ$  [36]. Other world averages exist [27, 39], but the overall picture is the same: the ability to constrain BSM physics is currently limited by the uncertainty of the direct measurements. Hence further precision measurements of  $\gamma$  are highly motivated. The precision is driven by time-integrated measurements of direct  $CP$ -violation in  $B^\pm \rightarrow DK^\pm$  decays; such a measurement is the topic of this thesis and the theory behind is treated in detail in the following section. It is also possible to measure  $\gamma$  in time-dependent mixing analyses of  $B_s^0 \rightarrow D_s^\mp K^\pm$ ,  $B^0 \rightarrow D^\mp \pi^\pm$  and related decays, by measuring  $CP$  violation in interference between mixing and decay. These modes are expected to provide measurements with a precision of a few degrees in the future [40].

## 2.2.2 Measuring $\gamma$ in tree level decays

The phase  $\gamma$  can be measured in tree-level processes with interference between  $b \rightarrow cs\bar{u}$  and  $b \rightarrow \bar{c}s u$  transitions. The canonical example, also the subject of this thesis, is based on measurements sensitive to interference between the  $B^\pm \rightarrow D^0 K^\pm$  and  $B^\pm \rightarrow \bar{D}^0 K^\pm$  decay amplitudes. As illustrated in Fig. 2.3 for the case of  $B^-$  decays, the electro-weak phase difference between the two decays is  $\Delta\phi = \arg(V_{cb}V_{us}^*/V_{ub}V_{cs}^*)$ . While  $\Delta\phi$  is not identical to the definition of  $\gamma$  in

<sup>442</sup> Eq. (2.11), the ratio of the involved CKM matrix elements is [41]

$$\begin{aligned} -\frac{V_{cd}^*/V_{ud}^*}{V_{us}^*/V_{cs}^*} &= -\frac{-\lambda[1 - \frac{\lambda^4}{2}A^2(1 - 2(\rho - i\eta))](1 - \frac{\lambda^2}{2} - \frac{\lambda^4}{8}(1 + 4A^2))}{\lambda(1 - \frac{\lambda^2}{2} - \frac{\lambda^4}{4})} \\ &= 1 - \lambda^4 A^2(1 - 2(\rho - i\eta)) + \mathcal{O}(\lambda^5). \end{aligned} \quad (2.12)$$

<sup>443</sup> The ratio equals unity to  $\mathcal{O}(\lambda^4) \simeq 2.6 \times 10^{-3}$ , and thus  $\Delta\phi \simeq \gamma$  is a good  
<sup>444</sup> approximation within current experimental uncertainties. For the remainder of this  
<sup>445</sup> thesis the approximation will be used without further comment. The diagrams in  
<sup>446</sup> Fig. 2.3 describe the leading order contributions to the two amplitudes

$$\begin{aligned} A[B^- \rightarrow D^0 K^-] &\equiv A_B \\ A[B^- \rightarrow \bar{D}^0 K^-] &\equiv \bar{A}_B \equiv r_B A_B e^{i(\delta_B - \gamma)}, \end{aligned} \quad (2.13a)$$

<sup>447</sup> where the last equality introduces two new parameters: the amplitude magnitude  
<sup>448</sup> ratio  $r_B \equiv |\bar{A}_B|/|A_B|$ , and  $\delta_B$ , the strong-phase difference between the decay  
<sup>449</sup> amplitudes. Since all  $CP$ -violation is attributed to the electro-weak phase in the  
<sup>450</sup> SM, the  $CP$ -conjugate decay amplitudes are [42]

$$\begin{aligned} A[B^+ \rightarrow \bar{D}^0 K^+] &= A_B \\ A[B^+ \rightarrow D^0 K^+] &= \bar{A}_B = r_B A_B e^{i(\delta_B + \gamma)}. \end{aligned} \quad (2.13b)$$

<sup>451</sup> In an experimental setting, the  $D^0$  and  $\bar{D}^0$  mesons are reconstructed in some final  
<sup>452</sup> state,  $f$ , or its  $CP$ -conjugate state,  $\bar{f}$ . In analogy with the  $B^\pm$  decays, the  $D$   
<sup>453</sup> decay amplitude can be related<sup>5</sup>

$$\begin{aligned} A[D^0 \rightarrow f] &= A[\bar{D}^0 \rightarrow \bar{f}] = A_D \\ A[\bar{D}^0 \rightarrow f] &= A[D^0 \rightarrow \bar{f}] = r_D A_D e^{i\delta_D}. \end{aligned} \quad (2.14)$$

<sup>454</sup> where the assumption has been made that  $CP$  violation in the  $D$  decays is negligible,  
<sup>455</sup> and  $\delta_D$  denotes a  $CP$ -conserving strong-phase difference. While  $CP$ -violation in  
<sup>456</sup>  $D$  decays has recently been measured [21], the size of the effect is small and it is  
<sup>457</sup> considered negligible in this thesis. Based on Eqs. 2.13 and (2.14), the decay rates  
<sup>458</sup> of  $B^+$  and  $B^-$  mesons into the possible final states can be seen to satisfy

$$\Gamma(B^- \rightarrow D(\rightarrow f) K^-) \propto 1 + r_D^2 r_B^2 + 2r_B r_D \cos [\delta_B + \delta_D - \gamma], \quad (2.15a)$$

$$\Gamma(B^+ \rightarrow D(\rightarrow \bar{f}) K^+) \propto 1 + r_D^2 r_B^2 + 2r_B r_D \cos [\delta_B + \delta_D + \gamma], \quad (2.15b)$$

$$\Gamma(B^- \rightarrow D(\rightarrow \bar{f}) K^-) \propto r_D^2 + r_B^2 + 2r_B r_D \cos [\delta_B - \delta_D - \gamma], \quad (2.15c)$$

$$\Gamma(B^+ \rightarrow D(\rightarrow f) K^+) \propto r_D^2 + r_B^2 + 2r_B r_D \cos [\delta_B - \delta_D + \gamma]. \quad (2.15d)$$

---

<sup>5</sup>In this convention  $\delta_D$  is thus phase of the suppressed  $D$ -decay amplitude minus the phase of the favoured  $D$ -decay amplitude. This is the opposite convention to that used in the LHCb measurements with the ADS technique, but aligns with the phase definition used in the literature on  $\gamma$  measurements in  $D \rightarrow K_S^0 \pi^+ \pi^-$  decays.

459 The processes in Eqs. (2.15a) and (2.15b) are  $CP$ -conjugate and it is clear how, in the  
 460 general case where  $\delta_B + \delta_D \neq 0$ , a non-zero value of  $\gamma$  leads to  $CP$  violation in the form  
 461 of differing decay rates. The same is true for the processes in Eqs. (2.15c) and (2.15d).  
 462 Depending on the choice of  $D$  final state, these expressions can be used to relate  
 463  $\gamma$  to various observables that are experimentally accessible. This thesis concerns  
 464 the choice  $f = K_S^0 \pi^+ \pi^-$  or  $f = K_S^0 K^+ K^-$ , where the terms related to the  $D$  decay  
 465 all have a non-trivial variation over the phase space of the decay. However, it is  
 466 useful to first analyse the simpler case where  $f$  is a two-body state.

467 The simplest case is when  $f$  is chosen to be a  $CP$  eigenstate, so that  $f = \pm \bar{f}$   
 468 and the rate equations of (2.15a)–(2.15d) simplify, because  $r_D = 1$  and  $\delta_D \in \{0, \pi\}$ .  
 469 Measurements of  $\gamma$  in such decay modes are denoted GLW measurements, after  
 470 Gronau, London, and Wyler who described the approach in the early 90ies [42, 43].  
 471 Experimentally it is preferable to measure yield ratios rather than absolute rates,  
 472 and the observables of interest are thus the  $CP$  asymmetry

$$\begin{aligned} A_{CP=\pm 1} &= \frac{\Gamma[B^- \rightarrow D_{CP} K^-] - \Gamma[B^+ \rightarrow D_{CP} K^+]}{\Gamma[B^- \rightarrow D_{CP} K^-] + \Gamma[B^+ \rightarrow D_{CP} K^+]} \\ &= \frac{\pm r_B \sin \delta_B \sin \gamma}{1 + r_B^2 \pm 2r_B \cos \delta_B \cos \gamma}, \end{aligned} \quad (2.16a)$$

473 as well as the ratio

$$\begin{aligned} R_{CP=\pm 1} &= 2 \frac{\Gamma[B^- \rightarrow D_{CP} K^-] + \Gamma[B^+ \rightarrow D_{CP} K^+]}{\Gamma[B^- \rightarrow D^0 K^-] + \Gamma[B^+ \rightarrow \bar{D}^0 K^+]} \\ &= 1 + r_B^2 \pm 2r_B \cos \delta_B \cos \gamma. \end{aligned} \quad (2.16b)$$

474 In practice,  $A_{CP}$  and  $R_{CP}$  are obtained from measured yield ratios that are corrected  
 475 with appropriate branching fractions. A measurement of  $A_{CP}$  and  $R_{CP}$  alone is not  
 476 sufficient to determine the underlying physics parameters  $(\gamma, r_B, \delta_B)$ : even if  $r_B$  was  
 477 to be known exactly, the measurements only constrain  $\cos \delta_B \cos \gamma$  and  $\sin \delta_B \sin \gamma$   
 478 and will always allow four solutions for  $(\gamma, \delta_B)$ . One way to break the ambiguity,  
 479 first noted in the original paper [42], is to make further measurements in additional  
 480  $B$  decays, such as the  $B^\pm \rightarrow D^* K^\pm$  or  $B^0 \rightarrow D K^{*0}$  modes. These decays can  
 481 also be described with the formalism derived above, but will not share the same  
 482 ambiguous solutions because the  $r_B$  and  $\delta_B$  values are unique to a given  $B$  decay.  
 483 Another method is to analyse  $D$  decay final states that are not  $CP$  eigenstates.

484 A few years after the GLW method was proposed, Atwood, Dunietz, and  
 485 Soni analysed an alternative choice of  $D$  final states: a simultaneous analysis  
 486 of a Cabibbo-favoured (CF) decay  $D^0 \rightarrow f$  and the doubly-Cabibbo-suppressed  
 487 (DCS) decay  $D^0 \rightarrow \bar{f}$  into the  $CP$  conjugate final state [44, 45]. Their suggested

method is named the ADS method after the authors. The classical example is to take  $f = K^-\pi^+$  and  $\bar{f} = \pi^-K^+$ . The relative suppression means that the  $r_D$  of Eq. (2.15) is small, typically of the same order of magnitude as  $r_B$ , and thus the  $CP$  asymmetry of the suppressed decay is  $\mathcal{O}(1)$ :

$$\begin{aligned} A_{ADS(\bar{f})} &= \frac{\Gamma[B^- \rightarrow D(\rightarrow \bar{f})K^-] - \Gamma[B^+ \rightarrow D(\rightarrow f)K^+]}{\Gamma[B^- \rightarrow D(\rightarrow \bar{f})K^-] + \Gamma[B^+ \rightarrow D(\rightarrow f)K^+]} \\ &= \frac{r_D r_B \sin(\delta_B - \delta_D) \sin \gamma}{r_D^2 + r_B^2 + 2r_D r_B \cos(\delta_B - \delta_D) \cos \gamma}. \end{aligned} \quad (2.17a)$$

The large  $CP$  asymmetry is a prime feature of the ADS method. However, the suppressed-to-favoured yield ratio is also sensitive to the physics parameters of interest:

$$\begin{aligned} R_{ADS(\bar{f})} &= \frac{\Gamma[B^- \rightarrow D(\rightarrow \bar{f})K^-] + \Gamma[B^+ \rightarrow D(\rightarrow f)K^+]}{\Gamma[B^- \rightarrow D(\rightarrow f)K^-] + \Gamma[B^+ \rightarrow D(\rightarrow \bar{f})K^+]} \\ &= \frac{r_B^2 + r_D^2 + 2r_D r_B \cos(\delta_B - \delta_D) \cos \gamma}{1 + r_D^2 r_B^2 + 2r_D r_B \cos(\delta_B + \delta_D) \cos \gamma}. \end{aligned} \quad (2.17b)$$

The interpretation of  $A_{ADS}$  and  $R_{ADS}$  in terms of  $(\gamma, r_B, \delta_B)$  requires knowledge of the  $r_D$  and  $\delta_D$  parameters, but these can be measured independently [27]. In general, the constraints from a single set of ADS observables suffer the same ambiguities as in the GLW case. However, unlike the GLW case, each  $D$  decay mode provides an independent set of constraints, because the parameters related to the  $D$  decay vary.

The discussion of this section has centred on the classical case of  $B^\pm \rightarrow DK^\pm$  decays with a two-body  $D$  final state. With minor modifications the techniques have been used to make measurements sensitive to  $\gamma$  in  $B^0$  decays, with  $B$  decay final states including excited  $D$  mesons or kaons, and in  $B^\pm \rightarrow D\pi^\pm$  decays (summaries of the measurements made by the  $B$  factories and LHCb can be found in Refs. [46–49]). The  $B^\pm \rightarrow D\pi^\pm$  decay is also  $CP$ -violating, although the effect is much smaller than in the  $B^\pm \rightarrow DK^\pm$  decay because  $r_B^{D\pi} \simeq 0.005$  [50], whereas  $r_B^{DK} \simeq 0.1$ . Furthermore, it is possible to use multi-body  $D$  final states. However, in some cases, a better precision can then be obtained by exploiting phase-space dependent decay rates. This is the topic of the next section.

### 2.3 Measuring $\gamma$ using multi-body $D$ final states

In multi-body  $D$  decays, the  $r_D$  and  $\delta_D$  parameters of the fundamental decay rates in Eq. (2.15) vary over the phase space of the  $D$  decay. This section describes a model-independent approach to measure  $\gamma$  in  $B \rightarrow D(\rightarrow K_S^0 \pi^+ \pi^-)h^\pm$  decays

514 by exploiting this variation, where  $h^\pm$  denotes a kaon or a pion. The theory is  
 515 identical for  $D \rightarrow K_S^0 K^+ K^-$  decays, and similar ideas have been proposed for  
 516 the  $D \rightarrow K^+ \pi^- \pi^- \pi^+$  [51],  $D \rightarrow K_S^0 \pi^+ \pi^- \pi^0$  [52], and  $D \rightarrow 2\pi^+ 2\pi^-$  modes [53].  
 517 First, however, the formalism for describing amplitudes of multi-body decays  
 518 is briefly reviewed.

### 519 2.3.1 Dalitz plots and the phase space of multi-body decays

520 In general, the phase space of the  $n$ -body decay  $P \rightarrow p_1 + p_2 + \dots + p_n$  consists of  $n$   
 521 four momenta, with a total of  $4n$  components. The requirement that each of the final  
 522 state particles is on-shell provides  $n$  constraints on these components, and energy-  
 523 momentum conservation removes a further 4 degrees of freedom. If the original  
 524 particle  $P$  is a *scalar*, the decay is isotropic, which removes an additional 3 degrees  
 525 of freedom, leaving the total number of degrees of freedom at  $3n - 7$ . For the specific  
 526 case of three-body decays, the available phase space can thus be parameterised with  
 527 only two parameters. A practical and often used choice is the invariant masses

$$s_{12} = m^2(p_1 p_2) = (p_1^\mu + p_2^\mu)^2, \quad s_{13} = m^2(p_1 p_3) = (p_1^\mu + p_3^\mu)^2. \quad (2.18)$$

528 The choice of particle pairs is arbitrary, and the coordinates easily related

$$m_P^2 + m_{p_1}^2 + m_{p_2}^2 + m_{p_3}^2 = m^2(p_1 p_2) + m^2(p_1 p_3) + m^2(p_2 p_3). \quad (2.19)$$

529 A scatter plot of  $(s_{12}, s_{13})$  values for a sample of particle decays is denoted a Dalitz  
 530 plot [54]. It has the very useful feature that the presence of (narrow) resonances  
 531 in the decay leads to visible bands in the scatter plot. Figure 2.4 illustrates how  
 532 the limits of the Dalitz plot are defined by kinematic constraints, and shows an  
 533 example of a Dalitz plot for  $D \rightarrow K_S^0 \pi^+ \pi^-$  decays in which the  $K^*(892)^\pm$  and  $\rho(770)$   
 534 resonances are clearly visible. The plot shows the sample of  $B^+ \rightarrow D \pi^+$  decays  
 535 used to make the measurement described in Chapter 5 and thus the  $D$  meson is in  
 536 a superposition of  $D^0$  and  $\bar{D}^0$  states (as detailed in the following section).

537 In terms of the coordinates of Eq. (2.18) the differential decay rate is given by

$$d\Gamma = \frac{1}{32(2\pi)^3 m_P^3} |\mathcal{M}|^2 ds_{12} ds_{13}, \quad (2.20)$$

538 where  $\mathcal{M}$  is the QFT matrix element, or total decay amplitude, corresponding to the  
 539 decay. In general, it is not possible to calculate  $\mathcal{M}$  from first principles. Instead, a  
 540 model is defined with an empirically well motivated form, in which a number of free  
 541 parameters must be determined experimentally. The simplest case is that of an *isobar*  
 542 model, where it is assumed that the full decay can be decomposed into consecutive

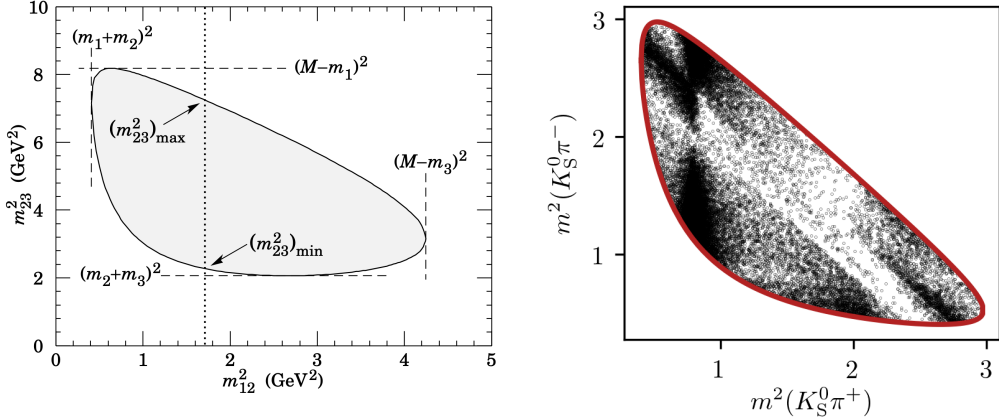


**Figure 2.4:** (Left) Schematic of a Dalitz plot and the limits of the kinematically allowed phase space limits. (Right) Example of a Dalitz plot for  $D \rightarrow K_S^0 \pi^+ \pi^-$  decays where the  $D$  meson originates in a  $B^+ \rightarrow D\pi^+$  decay; the decaying  $D$  meson is in a superposition of the  $D^0$  and  $\bar{D}^0$  states, but predominantly  $\bar{D}^0$ -like.

543 two-body decays of the form  $P \rightarrow R_{ij}(\rightarrow p_i + p_j)p_k$ . Thus,  $\mathcal{M}$  is expressed as a  
 544 non-resonant constant amplitude term,  $k_{NR}$ , plus a sum of resonance terms

$$\mathcal{M}(s_{12}, s_{13}) = k_{NR} + \sum_r k_r \mathcal{M}^r(s_{12}, s_{13}). \quad (2.21)$$

545 The exact form of the  $\mathcal{M}^r$  function depends on the resonance in question. An  
 546 overview is given in the PDG review on resonances and references therein [31].  
 547 The isobar formalism breaks down when resonances in the decay are not well  
 548 separated. In this case, models of the form in Eq. (4.28) can still be employed, if the  
 549 contribution from overlapping resonances are collected in a single term. An example  
 550 of such a model, is the amplitude model for  $D^0 \rightarrow K_S^0 \pi^+ \pi^-$  decays developed by  
 551 the Belle collaboration for a measurement of the CKM angle  $\beta$  in 2018 [55]. In this  
 552 model, individual terms are included for  $D^0 \rightarrow K^*(\rightarrow K_S^0 \pi^\pm)\pi^\mp$  decays, whereas  
 553 the  $\pi\pi$  and  $K\pi$   $S$ -wave contributions are modelled with the so-called  $K$ -matrix-  
 554 and LASS formalisms [56, 57]. The amplitude and phase of  $\mathcal{M}$  as predicted by  
 555 this model are shown in Fig. 2.5.

### 556 2.3.2 The BPGGSZ method to measure $\gamma$

557 The non-trivial phase-space dependence of the  $D \rightarrow K_S^0 \pi^+ \pi^-$  decay amplitude  
 558 can be exploited to measure  $\gamma$  with  $B^\pm \rightarrow DK^\pm$  or  $B^\pm \rightarrow D\pi^\pm$  decays. This  
 559 approach was proposed independently by Bondar and Poluektov [58, 59] within the  
 560 Belle collaboration, and by Giri, Grossman, Soffer, and Zupan [60]. It takes the

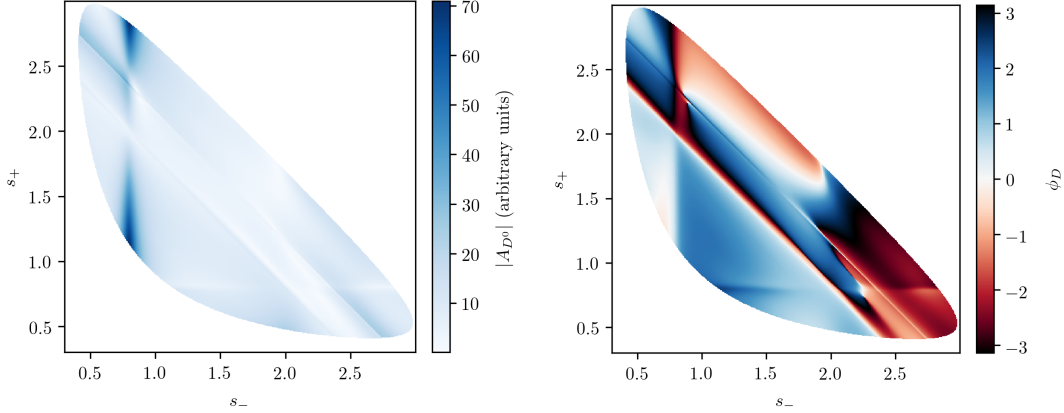


**Figure 2.5:** The (left) magnitude and (right) phase of the  $D \rightarrow K_S^0 \pi^+ \pi^-$  amplitude in the Belle 2018 model [55].

commonly used acronym BPGGSZ after all these authors.<sup>6</sup> For this specific decay  $s_-$  and  $s_+$  are used to described the Dalitz coordinates  $m^2(K_S^0 \pi^-)$  and  $m^2(K_S^0 \pi^+)$ , respectively, and the  $D$  decay amplitude is a function of these coordinates

$$A_S^{\bar{D}}(s_-, s_+) = A(\bar{D}^0 \rightarrow K_S^0 \pi^+ \pi^-). \quad (2.22)$$

To a good approximation the  $K_S^0$  meson is a  $CP$  eigenstate, meaning that the  $K_S^0 \pi^+ \pi^-$  state is self-conjugate. Assuming this approximation to be exact, and that  $CP$  violation in the  $D$  decay is negligible, the  $D$  decay amplitude satisfies the symmetry relation

$$A_S^{\bar{D}}(s_-, s_+) = A_S^D(s_+, s_-). \quad (2.23)$$

The impact of the  $K_S^0$  meson *not* being an exact  $CP$  eigenstate is treated in detail in Chapter 4. In order to simplify equations, the short-hand notation

$$(s_{-+}) = (s_-, s_+), \quad (s_{+-}) = (s_+, s_-) \quad (2.24)$$

will be employed for the remainder of the thesis, so that the relation in Eq. (2.23) can be expressed as  $A_S^{\bar{D}}(s_{-+}) = A_S^D(s_{+-})$ . Thus, the rate equations of Eq. (2.15)

---

<sup>6</sup>The "B" and "P" are a recent addition, in recognition of the role played by Bondar and Poluektov in the development of the method. For a history of the origins of the approach, see Ref. [61].

572 for the  $D \rightarrow K_S^0\pi^+\pi^-$  decay mode are

$$\begin{aligned} d\Gamma^-(s_{-+}) &\propto |\mathcal{A}_S^-|^2 = |A_B|^2 |A_{K_S^0}|^2 \\ &\times [|A_S^D(s_{-+})|^2 + r_B^2 |A_S^D(s_{+-})|^2 + 2r_B |A_S^D(s_{-+})| |A_S^D(s_{+-})| \\ &\times (\cos[\delta_D(s_{-+})] \cos[\delta_B - \gamma] + \sin[\delta_D(s_{-+})] \sin[\delta_B - \gamma])], \end{aligned} \quad (2.25a)$$

$$\begin{aligned} d\Gamma^+(s_{-+}) &\propto |\mathcal{A}_S^+|^2 = |A_B|^2 |A_{K_S^0}|^2 \\ &\times [|A_S^D(s_{-+})|^2 + r_B^2 |A_S^D(s_{+-})|^2 + 2r_B |A_S^D(s_{-+})| |A_S^D(s_{+-})| \\ &\times (\cos[\delta_D(s_{-+})] \cos[\delta_B + \gamma] - \sin[\delta_D(s_{-+})] \sin[\delta_B + \gamma])]. \end{aligned} \quad (2.25b)$$

573 Here,  $A_{K_S^0}$  is the decay amplitude for the  $K_S^0 \rightarrow \pi^+\pi^-$  decay, the strong phase  
574 of the  $D$  decay enters via

$$\delta_D(s_{-+}) = \phi_D(s_{-+}) - \phi_D(s_{+-}) = -\delta_D(s_{+-}), \quad (2.26)$$

575 where  $\phi_D(s_{-+})$  denotes the complex phase of the  $A_S^D(s_{-+})$  amplitude, and a standard  
576 trigonometric relation have been employed to factorise the terms depending on the  
577 complex phases of the  $B$  and  $D$  decays. It can be seen that in the case where  $\gamma = 0$   
578 the  $B^+$  and  $B^-$  decay rates are symmetric if the Dalitz coordinates are exchanged:  
579  $\Gamma^+(s_-, s_+) = \Gamma^-(s_+, s_-)$ . The presence of  $CP$  violation in the  $B$  decay breaks the  
580 symmetry. Therefore it is possible to measure  $\gamma$  (and the nuisance parameters  
581  $r_B$  and  $\delta_B$ ) from the phase-space distribution of  $B^\pm \rightarrow D(\rightarrow K_S^0\pi^+\pi^-)h^\pm$  decays,  
582 given knowledge of  $A_S^D(s_{-+})$ .

583 A series of measurements of  $\gamma$  have been made that use amplitude models of the  $D$   
584 decay [59, 62–68]. However, a model-independent approach was proposed already in  
585 the original GGSZ paper [60], and developed further by Bondar and Poluektov [69, 70].  
586 It relies on binning phase-space, in which case the necessary information on the  
587  $D$  decay amplitude can be summarised in a small set of coefficients that can be  
588 measured in a separate experiment. That is the approach followed in this thesis,  
589 and has been used previously by the Belle [71] and LHCb collaborations [3, 72, 73].  
590 It is described in detail in the following section.

591 Such a model-independent approach is favourable for two reasons. Firstly,  
592 estimating the systematic uncertainty related to the choice of parameterisation in  
593 an amplitude model is non-trivial. The BPGGSZ method relies heavily on knowledge  
594 of  $\delta_D(s_-, s_+)$ , yet the amplitude model parameters are determined in samples of  
595 flavour tagged  $D^0$  and  $\bar{D}^0$  decays, where only the magnitude of the amplitude is  
596 probed directly. Model-related uncertainties are determined by varying the model  
597 parameters within uncertainties, as well as repeating the analysis with alternative  
598 models where, for example, the included set of resonance contributions are changed,

599 or alternative parameterisations are employed for some contributions. This is a  
 600 somewhat subjective procedure, best exemplified by the fact that the BaBar and  
 601 Belle collaborations assigned very different uncertainties on their legacy BPGGSZ  
 602 measurements of  $\gamma$ . The BaBar collaboration assigned a model-related uncertainty  
 603 on  $\gamma$  of  $3^\circ$  [64], much smaller than the  $8.9^\circ$  assigned in the Belle paper [66], where  
 604 it is also observed that the main uncertainty contribution is precisely due the  
 605 imperfect knowledge of the phase of the amplitude, even in the case where a model  
 606 perfectly describes the data. In the model-independent approach described below,  
 607 this uncertainty is avoided in exchange for a statistically dominated measurement  
 608 uncertainty that is trivial to determine. Secondly, in the precision era it is favourable  
 609 that any experiment is easy to reinterpret in extensions of the SM. This is non-trivial  
 610 for an experiment that relies on determining a set parameters in a specific model, in  
 611 which the parameters are only indirectly related to physically observable quantities.  
 612 On the contrary, it is non-problematic for an experiment that measures a small  
 613 set of well-defined, model-independent physical observables. The model-independent  
 614 approach described below does sacrifice some statistical performance due to the  
 615 necessity of binning phase space: the statistical uncertainties on  $\gamma$  are 10–20 %  
 616 larger than in unbinned, model-dependent measurements [74]. However, slightly  
 617 reduced statistical performance is preferable to systematic uncertainties that are less  
 618 interpretable when  $\gamma$  is to serve as a high-precision SM benchmark; this motivates  
 619 the approach followed in the thesis.

620 An alternative model-independent approach has recently been proposed by  
 621 Poluektov [75] where the externally measured input on the  $D$ -decay phase are  
 622 Fourier expansion coefficients, and which therefore avoids binning phase space; this  
 623 approach may have the potential to improve the obtainable precision in the future.

### 624 2.3.3 A model-independent approach

625 The phase-space distribution can be analysed in a model-independent way, if the  
 626  $D$ -decay phase space is split into regions, or bins, and the  $B$  decay yield in each bin  
 627 determined experimentally. A measurement of  $\gamma$  using this approach is the main  
 628 topic of the thesis. This section describes the fundamental principle, whereas the  
 629 details pertaining to the exact experimental approach are delegated to Section 2.4.

630 The amplitude symmetry of Eq. (2.23) is exploited by defining  $2N$  bins to be  
 631 symmetric around the  $s_- = s_+$  diagonal of the Dalitz plot, numbered  
 632  $i = -\mathcal{N}$  to  $\mathcal{N}$  (omitting zero) such that if the point  $(s_-, s_+)$  is in bin  $i$ , then  
 633  $(s_+, s_-)$  is in bin  $-i$ , and by convention  $i > 0$  for bins where  $s_- > s_+$ . The principle  
 634 is illustrated in Fig. 2.6, but the binning schemes used in actual measurements

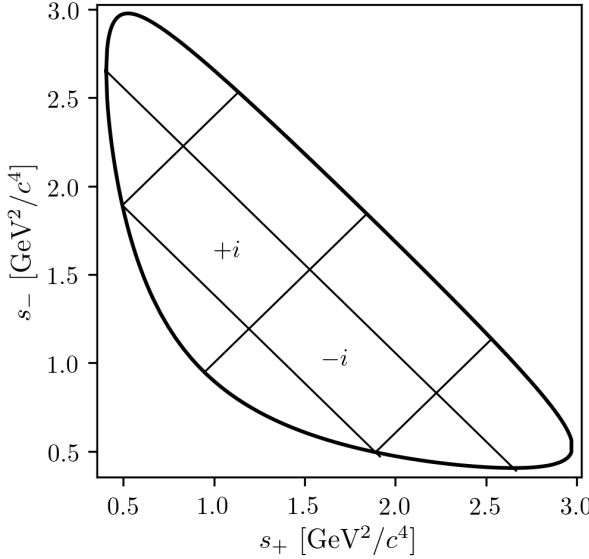


**Figure 2.6:** Illustration of the binning scheme used in BPGBGSZ measurements: the bins are symmetric around the  $m^2(K_S^0 \pi^+) = m^2(K_S^0 \pi^-)$  diagonal, and numbered so that opposite bins have the same number, except with opposite sign.

are more complicated. The decay rates in Eq. (2.25) can be integrated over such bins, and give the bin yields

$$\begin{aligned} N_i^- &\propto h^- \left[ K_i + r_B^2 K_{-i} + 2\sqrt{K_i K_{-i}} (c_i x_- + s_i y_-) \right], \\ N_i^+ &\propto h^+ \left[ K_{-i} + r_B^2 K_i + 2\sqrt{K_i K_{-i}} (c_i x_+ - s_i y_+) \right], \end{aligned} \quad (2.27)$$

where the parameters describing the  $B$  decay have been expressed in terms of the observables

$$x_\pm = r_B \cos(\delta_B \pm \gamma), \quad y_\pm = r_B \sin(\delta_B \pm \gamma), \quad (2.28)$$

and a number of phase-space integrated quantities related to the  $D$ -decay have been introduced. The  $K_i$  parameters denote fractional yield of a flavour-tagged  $D^0$  decaying into bin  $i$ , defined as

$$K_i = \frac{1}{N_K} \int_i ds^2 |A_S^D(s_{-+})|^2, \quad N_K = \int ds^2 |A_S^D(s_{-+})|^2, \quad (2.29)$$

where  $\int_i ds^2$  denotes integration over bin  $i$  of the Dalitz plot. The  $c_i$  and  $s_i$  denote the amplitude-weighted average of  $\cos \delta_D(s_{-+})$  and  $\sin \delta_D(s_{-+})$  over bin  $i$

$$\begin{aligned} c_i &= \frac{\int_i ds^2 |A_S^D(s_{-+})| |A_S^D(s_{-+})| \cos[\delta_D(s_{-+})]}{\sqrt{\int_i ds^2 |A_S^D(s_{-+})|^2} \sqrt{\int_i ds^2 |A_S^D(s_{-+})|^2}}, \\ s_i &= \frac{\int_i ds^2 |A_S^D(s_{-+})| |A_S^D(s_{-+})| \sin[\delta_D(s_{-+})]}{\sqrt{\int_i ds^2 |A_S^D(s_{-+})|^2} \sqrt{\int_i ds^2 |A_S^D(s_{-+})|^2}}. \end{aligned} \quad (2.30)$$

644 By the symmetry properties of  $\delta_D(s_{-+})$  these parameters satisfy  $c_i = c_{-i}$  and  
 645  $s_i = -s_{-i}$ . The normalisation constants  $h^+$  and  $h^-$  are identical in the ideal case,  
 646 but it is convenient to define them separately for practical reasons: depending on  
 647 the experimental setup, there may be overall production and detection asymmetries  
 648 that affect the total signal yields. If an experimental analysis measures the  $CP$   
 649 observables  $(x_{\pm}, y_{\pm})$  and the normalisations  $h^{\pm}$  separately, based on the expressions  
 650 in Eq. (2.27), the analysis is insensitive to these effects, because they are absorbed  
 651 into the normalisation constants (as long as they are constant over the  $D$ -decay phase  
 652 space). This comes at the cost that the information on  $x_{\pm}$  and  $y_{\pm}$  from the overall  
 653  $CP$  asymmetry is lost, but Section 2.3.5 will show the loss in precision to be minimal.

654 Thus, for a set of  $2\mathcal{N}$  bins, the bin yields of Eqs. (2.27) provide  $4\mathcal{N}$  constraints  
 655 on a total of  $4\mathcal{N} + 5$  parameters:  $(h^{\pm}, K_i, c_i, s_i, x_{\pm}, y_{\pm})$ <sup>7</sup>. However, the  $K_i$ ,  $c_i$ , and  
 656  $s_i$  parameters relate only to the  $D$  decay, and can thus, in principle, be measured  
 657 in independent experiments. With such external inputs, a measurement of the  
 658  $B^{\pm} \rightarrow D(\rightarrow K_S^0 \pi^+ \pi^-) h^{\pm}$  yields in a set of bins can be used to constrain  $x_{\pm}$  and  $y_{\pm}$ ,  
 659 and thereby  $(\gamma, r_B, \delta_B)$ . The measurement presented in this thesis determines the  
 660  $K_i$  parameters directly, but uses externally measured values of  $c_i$  and  $s_i$  as input,  
 661 as measured in quantum correlated  $D$  decays by the CLEO [74] and BESIII [76, 77]  
 662 collaborations. Because these measurements are the foundation of the approach,  
 663 they are described in some detail in the following section. In the future, it is possible  
 664 that the  $c_i$  and  $s_i$  parameters may be measured in quantum-correlated  $D$  decays  
 665 in LHCb [78], and in charm-mixing measurements [79].

#### 666 2.3.4 Measuring strong-phase inputs at charm factories

667 The strong-phase parameters  $c_i$  and  $s_i$  have been measured by the CLEO and  
 668 BESIII collaborations, using quantum correlated  $D^0 \bar{D}^0$  pairs from decays of the  
 669  $\psi(3770)$  resonance state, itself produced in  $e^+ e^-$  collisions at the resonance energy.  
 670 The  $\psi(3770)$  has quantum-number  $C = -1$ , which is conserved in the strong decay  
 671 into two  $D$  mesons, and thus the two  $D$  mesons are produced in an anti-symmetric  
 672 wave function. By observing the decay of one  $D$  meson into a specific final state,  
 673 say a  $CP$  eigenstate, the quantum state of the other  $D$  meson can be determined.  
 674 The measurement is based on decays where both  $D$  decays are reconstructed, one  
 675 in the  $K_S^0 \pi^+ \pi^-$  final state, the other in one of several different tag categories.  
 676 The main principles are outlined below, but most experimental considerations and  
 677 implementation details are left out for the sake of brevity.

---

<sup>7</sup>There are  $2\mathcal{N}$  different  $K_i$  parameters but only  $2\mathcal{N} - 1$  of them are free, as they are constrained to sum to unity by definition.

678 The simplest case is when one  $D$  meson decays into a final state that uniquely  
 679 tags the flavour, such as  $\bar{D}^0 \rightarrow K^+ e^- \bar{\nu}_e$ . In that case, the  $D$  meson decaying to  
 680  $K_S^0 \pi^+ \pi^-$  is known to be in the  $D^0$  state and the decay rate is simply determined by  
 681  $A_S^D : \Gamma(s_{-+}) \propto |A_S^D(s_{-+})|^2$ . This allows for a measurement of the  $K_i$  parameters.

682 If one  $D$  meson is reconstructed in a  $CP$ -even state, eg.  $K^+ K^-$ , or a  $CP$ -odd  
 683 state, eg.  $K_S^0 \pi^0$ , the  $D$  meson decaying to  $K_S^0 \pi^+ \pi^-$  is known to be in a state of  
 684 opposite  $CP$ . Thus, for a tag-decay of  $CP = \pm 1$  the decay rate has the form

$$\Gamma_{CP=\pm 1} \propto |A_S^D(s_{-+}) \mp A_S^D(s_{+-})|^2 \quad (2.31a)$$

685 and the bin yields will be given by

$$M_i^\pm \propto K_i + K_{-i} \mp 2\sqrt{K_i K_{-i}} c_i. \quad (2.31b)$$

686 Thus a simultaneous analysis of flavour and  $CP$  tagged decays allow for a deter-  
 687 mination of the  $K_i$  and  $c_i$  parameter sets.

688 Finally, the case where both  $D$  mesons, for now denoted  $D$  and  $D'$ , decay into  
 689 the  $K_S^0 \pi \pi$  final state can be considered. The total amplitudes have contributions  
 690 from the case where  $D$  is in the  $D^0$  state and  $D'$  is in the  $\bar{D}^0$  state, as well as the  
 691 opposite flavour assignment. Thus the decay rate satisfies

$$\Gamma_{CP=\pm 1} \propto |A_S^D(s_{-+}) A_S^D(s'_{+-}) + A_S^D(s_{+-}) A_S^D(s'_{-+})|^2 \quad (2.32a)$$

692 where  $s_{-+}$  denotes the Dalitz-plot coordinates of the  $D$  meson, and  $s'_{-+}$  those of  
 693 the  $D'$  meson. Defining  $M_{ij}$  to be the yield of decays where the  $D$  decay is in  
 694 bin  $i$  and the  $D'$  in bin  $j$ , the bin yields satisfy

$$M_{ij} \propto K_i K_{-j} + K_j K_{-i} - 2\sqrt{K_i K_{-i} K_j K_{-j}} (c_i c_j + s_i s_j). \quad (2.32b)$$

695 Thus, analysing these decays in addition to the  $CP$  and flavour tagged decays provide  
 696 information on all of  $K_i$ ,  $c_i$ , and  $s_i$ . Note, however, that Eqs. (2.31) and (2.32) are  
 697 invariant under the transformation  $\delta_D \rightarrow -\delta_D$ . In practice, the analysis is extended  
 698 in a number of ways to enhance the statistics: using "flavour-tag" states that are not  
 699 exact flavour tags, such as  $K^- \pi^+$ , using self-conjugate multi-body  $D$ -decay final  
 700 states that are not exact  $CP$  eigenstates, such as  $\pi^+ \pi^- \pi^0$ , and using the  $K_L^0 \pi^+ \pi^-$   
 701 final state as well. However, the main principles are the same as described above.

702 The measurements of  $c_i$  and  $s_i$  are made for a range of different binning schemes.  
 703 It was noted already in Ref. [70] that a rectangular binning scheme, such as the  
 704 example in Fig. 2.6, does not provide the optimal sensitivity to  $\gamma$ . It will always be  
 705 the case that some statistical sensitivity is lost in a binned analysed, as compared

to an unbinned, model-dependent analysis; however, the degree to which this is the case depends on the choice of binning. A better sensitivity can be obtained if the bins are defined such that  $\delta_D$  is approximately constant over a given bin, by defining bin  $i$  out of  $\mathcal{N}$  via the condition

$$\text{bin}_i = \{(s_-, s_+) \mid 2\pi(i - 3/2)/\mathcal{N} < \delta_D(s_-, s_+) < 2\pi \times (i - 1/2)/\mathcal{N}\}. \quad (2.33)$$

In practice, the binning scheme is defined by splitting the  $D$ -decay phase-space into quadratic *micro bins* with a width of  $0.0054$  ( $\text{GeV}/c^2$ ) $^2$  and assigning a bin number to each micro bin via the condition in (2.33) as evaluated in an amplitude model of choice. The obtained binning scheme when using an amplitude model developed by the BaBar collaboration in 2008 [63] is shown in Fig. 2.7a. In Ref [70] it was also shown that the binning can be even further optimised for sensitivity.

The suggested figure of merit is

$$Q^2 = \frac{\sum_i \left( \frac{1}{\sqrt{N_i^B}} \frac{dN_i^B}{dx} \right)^2 + \left( \frac{1}{\sqrt{N_i^B}} \frac{dN_i^B}{dy} \right)^2}{\int ds^2 \left[ \left( \frac{1}{|\Gamma^B(s_{-+})|} \frac{d|\Gamma^B(s_{-+})|^2}{dx} \right)^2 + \left( \frac{1}{|\Gamma^B(s_{-+})|} \frac{d|\Gamma^B(s_{-+})|^2}{dy} \right)^2 \right]} \quad (2.34)$$

which quantifies the statistical sensitivity for a given binning, relative to the one achievable in an unbinned analysis. The CLEO collaboration defined an *optimal* binning scheme by an iterative procedure where, starting from the equal binning scheme, a micro-bin is randomly reassigned new bin numbers in each step, and a step accepted if  $Q^2$  increases. The optimisation is done for the case where  $x = y = 0$  and thus  $Q^2$  simplifies to  $Q_{x=y=0}^2 = \sum_i N_i^{x=y=0} (c_i^2 + s_i^2) / N_{total}^{x=y=0}$ . The resulting binning scheme is shown in Fig. 2.7b. An additional binning scheme is defined, denoted the *modified optimal* scheme and shown in Fig. 2.7c, where the  $Q^2$  figure of merit is modified to take into account the presence of backgrounds [74]. The modified optimal binning scheme has proven beneficial to use in measurements with small signal yields [80], but is not employed in the present thesis.

Both the CLEO [74] and BESIII [76] collaborations have measured the values of  $c_i$  and  $s_i$  for the equal, optimal, and modified optimal binning schemes. The results are also shown in Fig. 2.7, where they are compared to the expectation from the latest amplitude model [55]. The measurements presented in this thesis are based on a combination of the BESIII and CLEO results for the optimal binning scheme, made by the BESIII collaboration [76] and tabulated in Table 2.1.

While the *definition* and *optimisation* of these binning schemes depend on knowledge of  $A_S^D(s_-, s_+)$  via an amplitude model, it is important to note that no model information is needed when the binning schemes are used in the subsequent

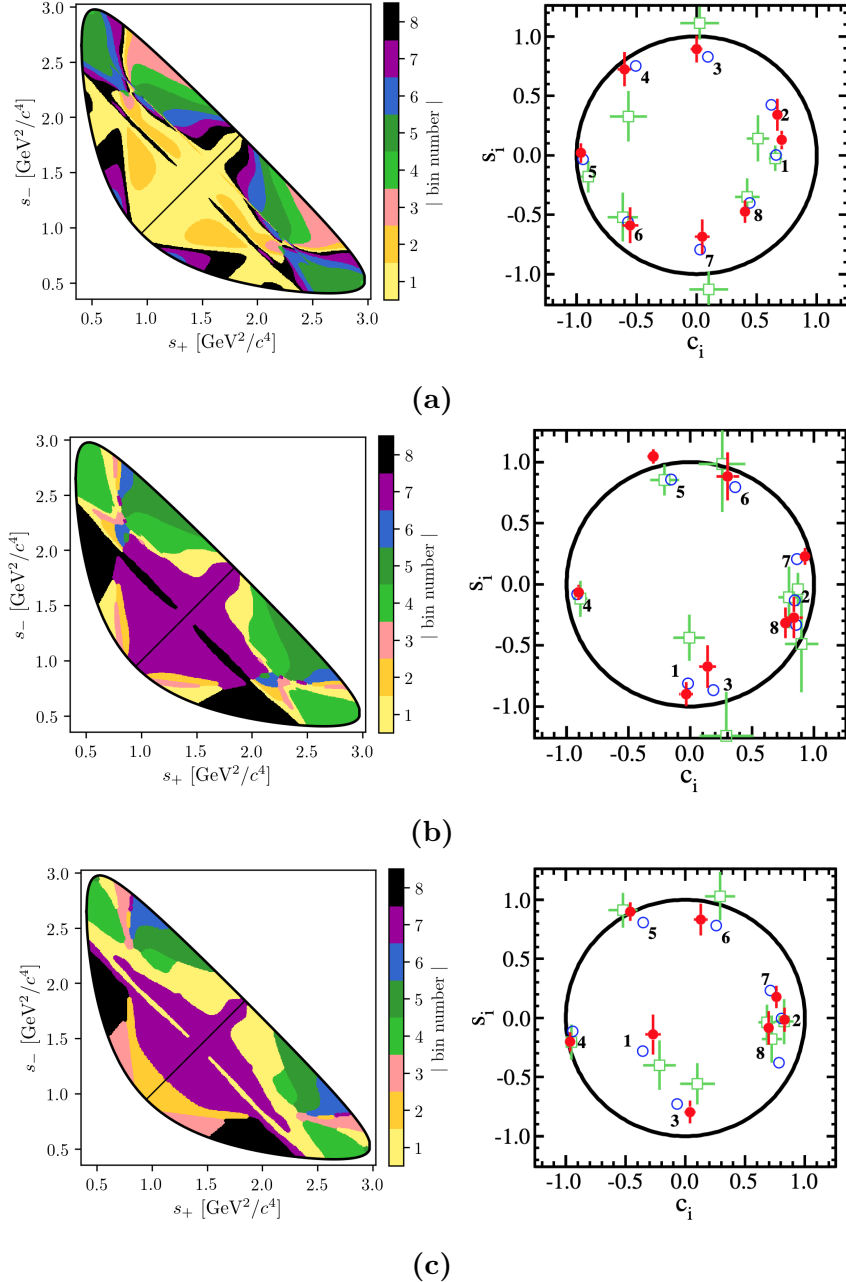


**Figure 2.7:** The (left) binning schemes and (right) measured values of  $(c_i, s_i)$  for (a) equal, (b) optimal, and (c) modified optimal binning schemes for  $D \rightarrow K_S^0 \pi^+ \pi^-$  decays. The plots of the measured values are taken from Ref. [76] and show the results obtained by (red) BESIII, (green) CLEO, and (blue) the model expectation using the model from Ref. [55]. The measurement featured in this thesis used the optimal binning scheme. Due to a different sign convention for the bin numbers, the  $s_i$  values shown in the BESIII figures have the opposite sign to those defined in the text.

**Table 2.1:** The experimentally measured  $c_i$  and  $s_i$  values used in the thesis. For both the  $D \rightarrow K_S^0\pi^+\pi^-$  and  $D \rightarrow K_S^0K^+K^-$  channels, the values are the combined values from the BESIII [76, 77] and CLEO [74] measurements published by BESIII in Refs. [76] and [77], respectively. Due to a different sign convention for the bin numbers, the  $s_i$  values are quoted with the opposite sign to those in the BESIII publications.

Optimal binning scheme: $D \rightarrow K_S^0\pi^+\pi^-$		
Bin $i$	$c_i$	$s_i$
1	$-0.037 \pm 0.049$	$0.829 \pm 0.097$
2	$0.837 \pm 0.067$	$0.286 \pm 0.152$
3	$0.147 \pm 0.066$	$0.786 \pm 0.154$
4	$-0.905 \pm 0.021$	$0.079 \pm 0.059$
5	$-0.291 \pm 0.041$	$-1.022 \pm 0.062$
6	$0.272 \pm 0.082$	$-0.977 \pm 0.176$
7	$0.918 \pm 0.017$	$-0.184 \pm 0.065$
8	$0.773 \pm 0.033$	$0.277 \pm 0.118$

2-bins binning scheme: $D \rightarrow K_S^0K^+K^-$		
Bin $i$	$c_i$	$s_i$
1	$0.713 \pm 0.032$	$-0.107 \pm 0.132$
2	$-0.758 \pm 0.037$	$-0.394 \pm 0.173$

measurements of strong-phases<sup>8</sup> or  $CP$ -observables. Therefore the measurements will not be biased by any modelling imperfections, although the obtained precision might be lower than expected.

The preceding discussion has been focusing on the  $D \rightarrow K_S^0\pi^+\pi^-$  channel, however the  $D \rightarrow K_S^0K^+K^-$  channel can be analysed completely analogously. The BESIII and CLEO collaborations have measured  $c_i$  and  $s_i$  values for this mode as well, in three binning schemes [74, 77]. These are all equal-phase binning schemes, with 2, 3, and 4 bins, respectively, shown in Fig. 2.8. The  $D \rightarrow K_S^0K^+K^-$  decay amplitude is almost completely dominated by two  $K^+K^-$  resonances, the  $CP$ -odd  $\phi(1020)$  and the  $CP$ -even  $a_0(980)$ , and this means that very little gain in sensitivity can be made by altering the equal-phase binning schemes [74]. The measured  $c_i$  and  $s_i$  values are shown in Fig. 2.8, and tabulated in Table 2.1, for the 2-bins scheme, which is used in this thesis.

The strong-phase measurements are dominated by statistical uncertainties for both the  $D \rightarrow K_S^0\pi^+\pi^-$  and  $D \rightarrow K_S^0K^+K^-$  decay channels. The current BESIII

<sup>8</sup>With the exception of minimal model-dependence introduced when the  $K_L^0\pi^+\pi^-$  final state is employed to constrain the  $s_i$  parameters by the  $D$ -factories [74, 76, 77], the impact of which is well under control.

measurements are based on a data set corresponding to an integrated luminosity of  $2.9 \text{ fb}^{-1}$ ; the BESIII collaboration is planning to continue collect data at the  $\psi(3770)$  resonance energy corresponding to an additional  $17 \text{ fb}^{-1}$  during 2021 and 2022 [?], and therefore significantly improved measurements can be made in the near future.

### 2.3.5 Global CP asymmetry and the relation to GLW and ADS measurements

The introduction of separate normalisation factors  $h^+$  and  $h^-$  in Eq. (2.27) hides the fact that information on  $\gamma$  (in principle) can be obtained from the asymmetry in phase-space-integrated  $B^+$  and  $B^-$  yields. In the ideal case where  $h^- = h^+$  the total yield asymmetry is

$$\begin{aligned} A_{GGSZ} &= \frac{\sum_{i=-\mathcal{N}}^{\mathcal{N}} N_i^- - N_i^+}{\sum_{i=-\mathcal{N}}^{\mathcal{N}} N_i^- + N_i^+} = \frac{\sum_{i=-\mathcal{N}}^{\mathcal{N}} \sqrt{K_i K_{-i}} c_i (x_- - x_+)}{1 + r_B^2 + 2 \sum_{i=-\mathcal{N}}^{\mathcal{N}} \sqrt{K_i K_{-i}} c_i (x_- + x_+)} \\ &= \frac{2 \sum_{i=1}^{\mathcal{N}} \sqrt{K_i K_{-i}} c_i (x_- - x_+)}{1 + r_B^2 + 4 \sum_{i=1}^{\mathcal{N}} \sqrt{K_i K_{-i}} c_i (x_- + x_+)}, \end{aligned} \quad (2.35)$$

using that  $\sum_{i=-\mathcal{N}}^{\mathcal{N}} \sqrt{K_i K_{-i}} s_i = 0$  by definition. The size of the asymmetry is governed by the factor  $\sum_{i=1}^{\mathcal{N}} \sqrt{K_i K_{-i}} c_i$ , which is small for  $D \rightarrow K_S^0 \pi^+ \pi^-$  and  $D \rightarrow K_S^0 K^+ K^-$  decays. The underlying reason is that  $\delta_D(s_-, s_+)$  varies significantly across phase-space for these decays, as evident by the spread in the values of  $c_i$  in Table 2.1, which reduces the *average* of the asymmetry-generating  $D^0 - \bar{D}^0$  interference term to being close to zero. The value of  $\sum_{i=1}^{\mathcal{N}} \sqrt{K_i K_{-i}} c_i$  is closely related to the *CP* content of the final state in question: for a self-conjugate *CP* even (odd) final state the  $D^0$  and  $\bar{D}^0$  decay amplitudes satisfy

$$A_{D^0}(s_-, s_+) = {}^{(\pm)} A_{\bar{D}^0}(s_-, s_+) = {}^{(\pm)} A_{D^0}(s_+, s_-), \quad (2.36)$$

meaning that  $K_i = K_{-i}$  and  $c_i = \pm 1$ ; thus  $\sum_{i=-\mathcal{N}}^{\mathcal{N}} \sqrt{K_i K_{-i}} c_i = {}^{(\pm)} 1$ . This motivates the definition of the *CP*-even fraction of the decay

$$\mathcal{F}_+ \equiv \frac{1}{2} \left( 1 + \sum_{i=-\mathcal{N}}^{\mathcal{N}} \sqrt{K_i K_{-i}} c_i \right), \quad (2.37)$$

equivalent to the definition in Ref. [81] for the case  $\mathcal{N} = 1$ . With  $\mathcal{F}_+$  in hand, the asymmetry in Eq. (2.35) can be rewritten

$$A_{BPGGSZ} = \frac{(2\mathcal{F}_+ - 1)r_B \sin \delta_B \sin \gamma}{1 + r_B^2(2\mathcal{F}_+ - 1)2r_B \cos \delta_B \cos \gamma}, \quad (2.38)$$

which is the usual form used in quasi-GLW measurements [81, 82]. The value of  $\mathcal{F}_+$  is independent of the number and shape of bins in a given binning scheme, as

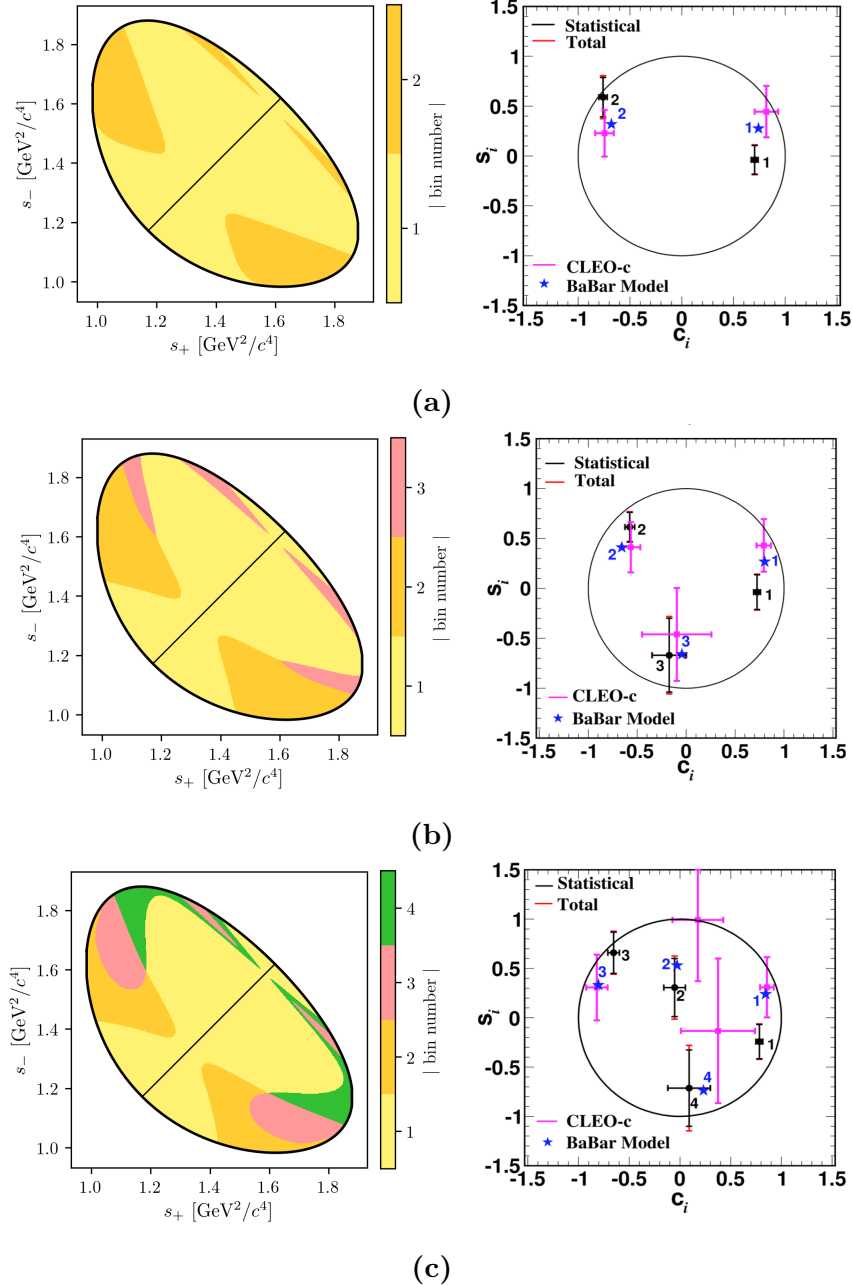


**Figure 2.8:** The (left) binning schemes and (right) measured values of  $(c_i, s_i)$  for the (a) 2-, (b) 3-, and (c) 4-bins binning schemes for  $D \rightarrow K_S^0 K^+ K^-$  decays. The plots of the measured values are taken from Ref. [77] and show the (error bars) results obtained by (black) BESIII, (pink) CLEO, and (blue) the model expectation using the model from Ref. [64]. The measurement featured in this thesis uses the 2-bins scheme. Due to a different sign convention for the bin numbers, the  $s_i$  values shown in the BESIII figures have the opposite sign to those defined in the text.

<sup>776</sup> long as the bin definitions follow the symmetry principles outlined in Section 2.3.3.  
<sup>777</sup> For  $D \rightarrow K_S^0\pi^+\pi^-$  and  $D \rightarrow K_S^0K^+K^-$  decays the values of  $\mathcal{F}_+$  are

$$\begin{aligned}\mathcal{F}_+(K_S^0\pi^+\pi^-) &= 57\% \\ \mathcal{F}_+(K_S^0K^+K^-) &= 51\%\end{aligned}\tag{2.39}$$

<sup>778</sup> as evaluated with the Belle 2018 model for  $D \rightarrow K_S^0\pi^+\pi^-$  decays and the BaBar  
<sup>779</sup> 2010 model for  $D \rightarrow K_S^0K^+K^-$  decays. Since  $r_B^{DK^\pm} \sim 0.1$  the predicted global  
<sup>780</sup> asymmetries are thus approximately 1–2 %, which is not resolvable with the current  
<sup>781</sup> experimental yields. As shown in Chapter 4,  $CP$  violation in the  $K_S^0$  sector leads to  
<sup>782</sup> asymmetries of a similar size, further complicating the use of global asymmetries to  
<sup>783</sup> constrain  $x_\pm$  and  $y_\pm$ . Thus these modes are ill-suited for quasi-GLW measurements,  
<sup>784</sup> and ignoring global asymmetries leads to a negligible loss of information on  $\gamma$  in  
<sup>785</sup> a BPGGSZ measurement. The reverse is true for a well-suited quasi-GLW mode,  
<sup>786</sup> such as  $D \rightarrow \pi^+\pi^-\pi^0$ : if  $\mathcal{F}_+$  is close to either zero or unity, it means that  $(c_i, s_i)$   
<sup>787</sup> will be close to  $(\pm 1, 0)$  in all bins for *any* given binning scheme, and the set of bins  
<sup>788</sup> will provide almost identical constraints on  $x_\pm$  and  $y_\pm$ . Thus, the binning of phase  
<sup>789</sup> space leads to no significant gain in precision compared to a global analysis.

<sup>790</sup> Indeed, a crucial quality of the BPGGSZ method, is that exactly because each  
<sup>791</sup> bin-pair provides independent constraints on  $x_\pm$  and  $y_\pm$ , the method provides a  
<sup>792</sup> single solution for  $(\gamma, r_B, \delta_B)$  that does not suffer the ambiguities of the ADS and  
<sup>793</sup> GLW approaches. In order to illustrate this further, it is useful to make one more  
<sup>794</sup> comparison of the model-independent BPGGSZ formalism to the ADS and GLW  
<sup>795</sup> formalisms. In a  $CP$  symmetric world, the  $B^+$  yield in bin  $+i$  would equal the  $B^-$   
<sup>796</sup> yield in bin  $-i$ . Therefore the relevant  $CP$  asymmetry for a given Dalitz bin is

$$\begin{aligned}A_{BPGGSZ}^i &\equiv \frac{N_i^- - N_{-i}^+}{N_i^- + N_{-i}^+} \\ &= \frac{\sqrt{K_i K_{-i}}(c_i(x_- - x_+) + s_i(y_- - y_+))}{K_i + r_B^2 K_{-i} + 2\sqrt{K_i K_{-i}}(c_i(x_- + x_+) + s_i(y_- + y_+))}.\end{aligned}\tag{2.40}$$

<sup>797</sup> This expression is identical to the ADS asymmetry in Eq. (2.17a) if the effective  
<sup>798</sup>  $D$ -decay parameters  $r_D^i$  and  $\delta_D^i$  are defined via

$$\kappa_i \cos \delta_D^i \equiv c_i \quad , \quad \kappa_i \sin \delta_D^i \equiv s_i \quad , \quad r_D^i \equiv \sqrt{K_i / K_{-i}},\tag{2.41}$$

<sup>799</sup> and a coherence factor,  $\kappa$ , is included in the interference terms of the ADS expression,  
<sup>800</sup> as is standard for multi-body  $D$  decays [83]. These parameters allow us to classify  
<sup>801</sup> a given pair of bins with number  $\pm i$  as either *GLW-like*, if  $\delta_D^i$  is close to 0 or

**Table 2.2:** Classification of the bins used in model-independent GGSZ measurements, in terms of whether the interplay between the  $D^0$  and  $\bar{D}^0$  amplitudes in the bin resemble typical GLW or ADS behaviour. The parameters are calculated using the 2018 Belle model [55] for  $D \rightarrow K_S^0\pi^+\pi^-$  decays and the 2010 BaBar model [64] for  $D \rightarrow K_S^0K^+K^-$  decays.

Optimal binning scheme: $D \rightarrow K_S^0\pi^+\pi^-$					
Bin $i$	$\hat{r}_D$	$\hat{\delta}_D$	$\mathcal{F}_+$	$\kappa$	Bin type
1	0.473	91.9°	48.97 %	0.81	Odd-even
2	0.164	11.1°	63.38 %	0.85	ADS-like
3	0.157	79.4°	52.50 %	0.89	ADS-like
4	0.768	175.3°	5.85 %	0.92	GLW-odd-like
5	0.759	-99.9°	42.84 %	0.87	Odd-even
6	0.223	-64.5°	57.92 %	0.87	ADS-like
7	0.651	-13.3°	89.44 %	0.89	GLW-even-like
8	1.745	21.0°	87.08 %	0.92	GLW-even-like

2-bins binning scheme: $D \rightarrow K_S^0K^+K^-$					
Bin $i$	$\hat{r}_D$	$\hat{\delta}_D$	$\mathcal{F}_+$	$\kappa$	Bin type
1	0.816	19.8°	86.14 %	0.78	GLW-even-like
2	0.775	154.5°	16.23 %	0.77	GLW-odd-like

802  $\pi$  and  $r_D^i$  is close to unity, or *ADS-like* if  $r_D^i \ll 1$ . The *CP*-even fraction of the  
 803  $D$ -decay can also be defined for a given bin-pair:

$$\mathcal{F}_+^i = \mathcal{F}_+^{-i} \equiv \frac{1}{2} \left( 1 + 2c_i \frac{\sqrt{K_i K_{-i}}}{K_i + K_{-i}} \right) = \frac{1}{2} \left( 1 + 2c_i \frac{r_D^i}{1 + r_D^i} \right). \quad (2.42)$$

804 A GLW-even-like bin pair will have  $\mathcal{F}_+^i \simeq 1$  and a GLW-odd-like bin pair will  
 805 have  $\mathcal{F}_+^i \simeq 0$ .

806 Table 2.2 summarises a classification of the bins for the optimal  $D \rightarrow K_S^0\pi^+\pi^-$   
 807 binning scheme and the 2-bins  $D \rightarrow K_S^0K^+K^-$  binning scheme following these  
 808 principles. Two bins are classified as *Odd-even*; in these bins,  $r_D^i$  is not particularly  
 809 small but  $\mathcal{F}_+^i$  is close to 0.5. The name refers to the fact that for these bins  
 810  $A_{BPGBS}^i$ , as defined in Eq (2.40), will be positive and  $A_{BPGBS}^{-i}$  negative (or vice  
 811 versa). The fact that multiple bin types appear for both the  $D \rightarrow K_S^0\pi^+\pi^-$  and  
 812  $D \rightarrow K_S^0K^+K^-$  modes underline that each mode benefits from being analysed  
 813 in the BPGBS formalism, and that the bins provide independent constraints,  
 814 allowing for a non-ambiguous solution for  $(\gamma, r_B, \delta_B)$ .

## 2.4 Strategy for the LHCb measurement

The main topic of the thesis is a model-independent BPGGSZ measurement using  $B^\pm \rightarrow DK^\pm$  and  $B^\pm \rightarrow D\pi^\pm$  decays, and the two  $D$  final states  $K_S^0\pi^+\pi^-$  and  $K_S^0K^+K^-$ . The measurement uses the optimal binning scheme for the  $D \rightarrow K_S^0\pi^+\pi^-$  mode, with the combined strong-phase inputs from the BESIII [76] and CLEO [74] collaborations published in Ref. [76]. For the  $D \rightarrow K_S^0K^+K^-$  channel, the 2-bins scheme is used, again using a combination [77] of measurements from the CLEO [74] and BESIII [77] collaborations. The details of the analysis are presented in Chapter 5, but the overall strategy and a few extensions of the formalism from the previous sections are given here.

It is the first time that  $\gamma$  is measured in  $B^\pm \rightarrow D\pi^\pm$  decays with the BPGGSZ method (although it has been used as a control channel in previous measurements with  $B^\pm \rightarrow DK^\pm$  decays). The promotion of  $B^\pm \rightarrow D\pi^\pm$  to a signal channel has two benefits. First of all, there is a small degree of  $CP$  violation in  $B^\pm \rightarrow D\pi^\pm$  decays, and therefore a measurement of  $CP$  observables in  $B^\pm \rightarrow D\pi^\pm$  decays does provide some further information on  $\gamma$ . However, the latest LHCb combinations have generally *not* included this information, because the currently measured  $B^\pm \rightarrow D\pi^\pm$  observables allow for two solutions for  $(r_B^{D\pi}, \delta_B^{D\pi})$  [48]. One of these is bound to be non-physical, and the presence of both makes the statistical interpretation of the results on  $\gamma$  highly non-trivial. This situation is resolved by the measurement presented in the thesis, and therefore  $B^\pm \rightarrow D\pi^\pm$  measurements can be included without incurring such problems in the future. However, the  $B^\pm \rightarrow D\pi^\pm$  channel constrains  $\gamma$  much less than the  $B^\pm \rightarrow DK^\pm$  channel, and therefore the impact on the overall precision is small. The second, more significant, benefit from the promotion of  $B^\pm \rightarrow D\pi^\pm$  to a signal channel, is that the analysis avoids a significant systematic uncertainty due LHCb acceptance effects that was present in earlier analyses. This is described further below.

Due to the geometry of the LHCb detector, the signal reconstruction efficiency for  $B^\pm \rightarrow D(\rightarrow K_S^0h^+h^-)h'^\pm$  decays varies significantly across the  $D$ -decay phase space. This is clearly visible in Fig. 2.9, where examples of the acceptance profile for  $B^\pm \rightarrow D(\rightarrow K_S^0h^+h^-)K^\pm$  decays in LHCb simulation are shown. The main feature, especially visible for  $D \rightarrow K_S^0\pi^+\pi^-$  decays, is a falling acceptance along the diagonal of the Dalitz plot, which is caused by the fact that a non-significant fraction of  $K_S^0$  mesons escape the LHCb tracking region before decaying, and that there is a correlation between  $m^2(h^+h^-)$  and the  $K_S^0$  momentum in the LHCb frame. The non-uniform acceptance results in yield equations that differ slightly

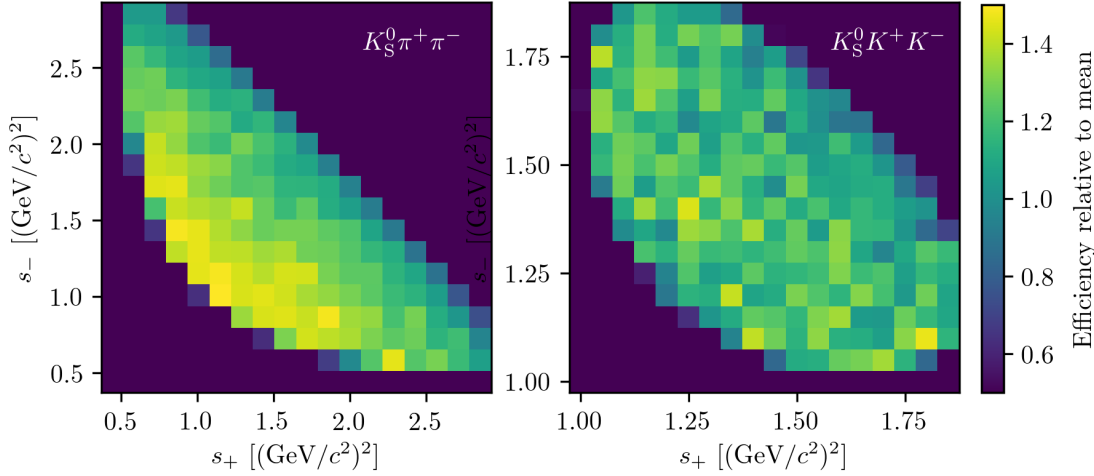


**Figure 2.9:** The LHCb acceptance in simulated  $B^\pm \rightarrow DK^\pm$  decays where (left)  $D \rightarrow K_S^0 \pi^+ \pi^-$  and (right)  $D \rightarrow K_S^0 K^+ K^-$ .

from those derived in the preceding sections. Denoting the efficiency profile as  $\eta(s_-, s_+)$ , the expressions in Eq. (2.27) are modified to

$$\begin{aligned} N_i^- &= h^{B^-} \left[ F_i + r_B^2 F_{-i} + 2\sqrt{F_i F_{-i}} (c'_i x_- + s'_i y_-) \right], \\ N_i^+ &= h^{B^+} \left[ F_{-i} + r_B^2 F_i + 2\sqrt{F_i F_{-i}} (c'_i x_+ - s'_i y_+) \right], \end{aligned} \quad (2.43)$$

where the phase-space integrated quantities now include the efficiency profile

$$F_i = \frac{1}{N_F} \int ds^2 \eta(s_{-+}) |A_S^D(s_{-+})|^2, \quad N_F = \int ds^2 \eta(s_{-+}) |A_S^D(s_{-+})|^2, \quad (2.44)$$

854

$$c'_i = \frac{\int_i ds^2 \eta(s_{-+}) |A_S^D(s_{-+})| |A_S^D(s_{-+})| \cos[\delta_D(s_{-+})]}{\sqrt{\int_i ds^2 \eta(s_{-+}) |A_S^D(s_{-+})|^2} \sqrt{\int_i ds^2 \eta(s_{-+}) |A_S^D(s_{-+})|^2}}, \quad (2.45)$$

855 with an analogous definition of  $s'_i$ . At leading order, the strong-phase parameters  
 856 are unaffected by the non-uniform efficiency, and, in addition, the bin definitions  
 857 favour bins for which  $\cos[\delta_D(s_{-+})]$  and  $\sin[\delta_D(s_{-+})]$  take on similar values across  
 858 each bin. Therefore, the  $c_i$  and  $s_i$  values reported by the charm factories are used  
 859 directly in the measurement. The impact on the obtained central values is negligible,  
 860 as described in detail in Section 5.6 where a systematic uncertainty is assigned.

861 The  $F_i$  and  $K_i$  parameters are significantly different, because the experimental  
 862 acceptance profile in LHCb is significantly non-uniform. Given external inputs for  
 863 the strong-phase parameters, it is possible to fit the  $F_i$  parameters and  $x_\pm$  and  
 864  $y_\pm$  simultaneously in a fit to the LHCb  $B^\pm \rightarrow DK^\pm$  data set, in which case the  
 865 obtained  $F_i$  parameters incorporate the correct acceptance profile correction by

866 construction. However, the obtainable precision for the  $CP$  observables measured by  
 867 this procedure is suboptimal. As an alternative, the first LHCb measurement [72]  
 868 determined the  $F_i$  parameters based on model predictions of  $K_i$ , adjusted using the  
 869 relative acceptance between bins determined in  $B^\pm \rightarrow D\pi^\pm$  decays (assuming  $CP$   
 870 symmetry and that the  $K_i$  were correctly predicted by the model). Since the  $F_i$   
 871 parameters relate to the  $D$  decay, they can effectively be obtained in the  $D\pi^\pm$  sample  
 872 and shared between the two  $B^\pm \rightarrow Dh^\pm$  channels. However, there is  $CP$  violation  
 873 present in the  $B^\pm \rightarrow D\pi^\pm$  decays, which led to a dominant systematic uncertainty.  
 874 Later LHCb measurements [3, 73] instead relied on flavour tagged  $D$  mesons from  
 875  $\bar{B}^0 \rightarrow D^{*+}(\rightarrow D^0\pi^+)\mu^-\bar{\nu}_\mu X$  decays to obtain  $F_i$ , where no  $CP$  violation is possible.  
 876 However, due to necessarily different triggering paths and selections, the acceptance  
 877 profile is not exactly identical between semi-leptonic decays and the  $B^\pm \rightarrow Dh^\pm$   
 878 decays of interest. An efficiency correction based on simulation was therefore applied  
 879 to obtain the correct  $F_i$ , and in this case, the uncertainty related to the correction  
 880 constituted the largest systematic uncertainty on the measurement.

881 Both sources of systematic uncertainty can be avoided by making a simultaneous  
 882 analysis of  $B^\pm \rightarrow DK^\pm$  and  $B^\pm \rightarrow D\pi^\pm$  decays, where  $CP$ -violating observables  
 883 are measured in *both* channels and the  $F_i$  parameters are shared. It is a reasonable  
 884 assumption that  $F_i^{DK} = F_i^{D\pi}$  to a very good approximation, given the similar  
 885 kinematics of the decays. The assumption is confirmed using simulated decays in  
 886 Section 5.2.2, for the candidate selection used in the measurement of the thesis.  
 887 Effectively, the  $F_i$  are determined in the high statistics  $B^\pm \rightarrow D\pi^\pm$  channel, but  
 888 with no systematic effect from  $CP$ -violation in that channel, since the  $CP$ -violation  
 889 is incorporated in the yield description.

890 At the start of the work that lead to this thesis, it was not clear to what degree  
 891 the measured  $CP$ -violating observables in  $B^\pm \rightarrow D\pi^\pm$  decays were affected by  $CP$   
 892 violation in the neutral kaon sector. The potential bias had been shown to be  
 893  $\sim 1^\circ$  in the  $B^\pm \rightarrow DK^\pm$  channel, which is negligible, but to scale with  $1/r_B$  [41]  
 894 suggesting potentially large biases in the  $B^\pm \rightarrow D\pi^\pm$  channel where  $r_B$  is  $\sim 20$   
 895 times smaller. However, the dedicated analysis presented in Chapter 4 has proved  
 896 the effect to be an order of magnitude smaller in BPGBSZ measurements than  
 897 suggested in Ref [41], and the simultaneous measurement is indeed viable.

898 The measurement is performed by making extended maximum-likelihood fits to  
 899 the  $m_B$  spectra of  $B \rightarrow D(\rightarrow K_S^0 h^+ h^-)h'^\pm$  candidates split by charge and Dalitz bin.  
 900 The  $B^\pm \rightarrow DK^\pm$  signal yields are parameterised using the expressions in Eq. (2.43)  
 901 directly, thus obtaining values for  $x_\pm^{DK}$  and  $y_\pm^{DK}$  directly. The Cartesian  $CP$ -  
 902 violating observables  $x_\pm$  and  $y_\pm$  are employed because they lead to better statistical

behaviour than fits to data where the underlying parameters  $(\gamma, r_B^{DK^\pm}, \delta_B^{DK^\pm})$  are determined directly, at the cost of introducing a fourth degree of freedom. With the addition of the  $B^\pm \rightarrow D\pi^\pm$  mode as a true signal channel, two new underlying parameters are introduced,  $r_B^{D\pi^\pm}$  and  $\delta_B^{D\pi^\pm}$ . There is a choice to be made, in terms of how to define the observables that are measured. One is to introduce an additional set of four observables,  $(x_-^{D\pi}, y_-^{D\pi}, x_+^{D\pi}, y_+^{D\pi})$ , that are analogous to the  $B^\pm \rightarrow DK^\pm$  parameters. As an alternative, it is possible to introduce only two Cartesian parameters [84, 85], by defining

$$\xi_{D\pi^\pm} = \left( \frac{r_B^{D\pi^\pm}}{r_B^{DK^\pm}} \right) \exp[i(\delta_B^{D\pi^\pm} - \delta_B^{DK^\pm})] \quad (2.46a)$$

and letting

$$x_\xi^{D\pi} = \text{Re}[\xi_{D\pi^\pm}] \quad y_\xi^{D\pi} = \text{Im}[\xi_{D\pi^\pm}]. \quad (2.46b)$$

In terms of these parameters, the usual Cartesian  $x_\pm$  and  $y_\pm$  are given by

$$x_\pm^{D\pi} = x_\xi^{D\pi} x_\pm^{DK} - y_\xi^{D\pi} y_\pm^{DK}, \quad y_\pm^{D\pi} = x_\xi^{D\pi} y_\pm^{DK} + y_\xi^{D\pi} x_\pm^{DK}. \quad (2.47)$$

Using this expression, the  $B^\pm \rightarrow D\pi^\pm$  yields can also be defined via Eq. (2.43) in the maximum-likelihood fit. Note that  $\xi$  does not depend on  $\gamma$ : all information on  $CP$  asymmetries in both the  $B^\pm \rightarrow DK^\pm$  and  $B^\pm \rightarrow D\pi^\pm$  channels is encoded in  $x_\pm^{DK}$  and  $y_\pm^{DK}$ . In the thesis, the latter parameterisation is chosen, because it allows for a stable fit for all six  $x$  and  $y$  parameters and the shared  $F_i$ ; the choice is described in much greater detail in Section 5.5.1.

The combined analysis of  $B^\pm \rightarrow DK^\pm$  and  $B^\pm \rightarrow D\pi^\pm$  decays presents a significant step forward, because it solves the problem of obtaining  $F_i$  parameters for the appropriate acceptance profile in a manner that avoids leading systematic uncertainties, and almost all reliance on simulation. This is of great importance, if the large data samples that will be collected by LHCb in the future are to be exploited to their full potential.

# 3

925

926

## The LHCb experiment

927 The LHCb experiment is one of the four large experiments at the Large Hadron  
928 Collider (LHC), the World's most powerful accelerator, able to accelerate protons  
929 to record centre-of-mass energies of  $\sqrt{s} = 13$  TeV in a 27 km long tunnel underneath  
930 Geneva. The LHCb experiment is specifically designed to study the large number  
931 of particles containing  $b$  or  $c$  quarks produced in such collisions, which has led  
932 to a number of design decisions that make the LHCb unique among the LHC  
933 experiments. The LHCb detector is not a full-solid-angle detector like the other  
934 three LHC experiments, CMS, ATLAS, and ALICE, but a single-arm spectrometer,  
935 instrumented in the forward region where a large fraction of  $b\bar{b}$  pairs are produced.  
936 During data-taking the experiment is operated at a lower instantaneous luminosity  
937 than the other experiments, leading to far fewer  $pp$  interactions. This, in combination  
938 with a vertex detector located extremely close to the interaction point, allows for  
939 excellent resolution in the reconstruction of primary and secondary vertex locations,  
940 crucial to many of the central measurements of the experiment. Finally, dedicated  
941 particle-identification detectors allow for very efficient separation of hadron species,  
942 absolutely crucial to isolate a number important signal decays (including the  
943  $B^\pm \rightarrow DK^\pm$  decay studied in the thesis). Each of these features is described in  
944 much greater detail in the sections below.

945 During operation of the LHC, bunches of about  $\mathcal{O}(10^{11})$  protons are accelerated  
946 to the desired centre-of-mass energy in a series of linear and circular accelerators,  
947 the final one being the LHC itself. This is illustrated in Fig. 3.1. The bunches  
948 remain in the LHC for the duration of a *fill*, typically about 12 hours, where they are  
949 made to collide at four distinct locations, the collision points, each home to one of

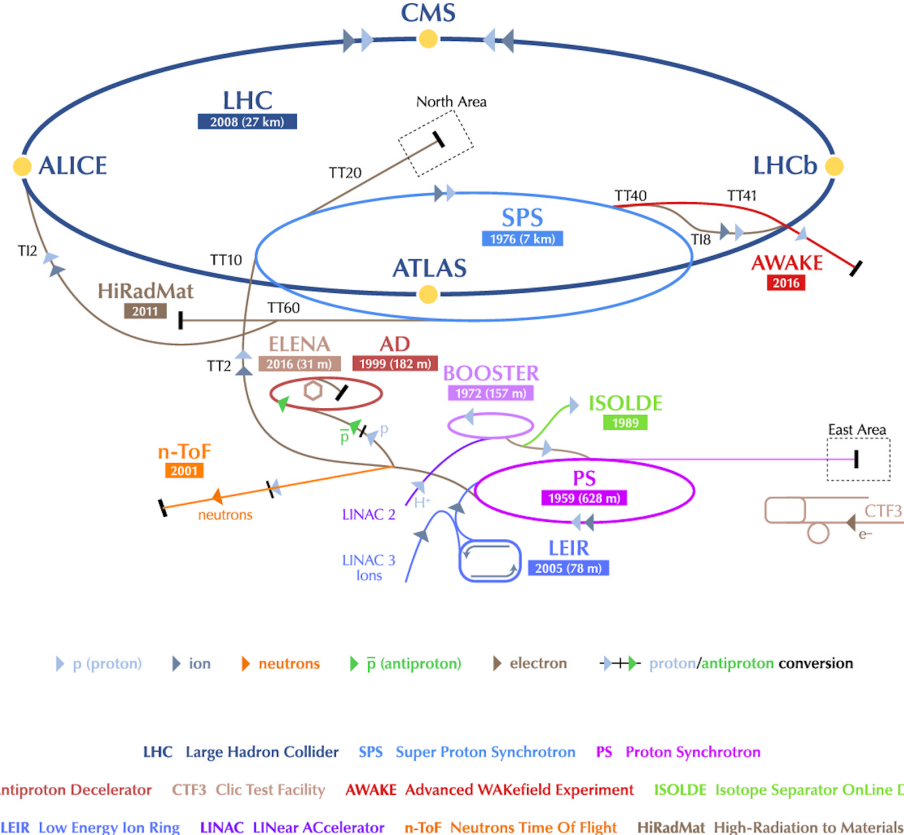


**Figure 3.1:** The CERN accelerator complex, including the length and construction year for a number of accelerators, not all of which are used in  $pp$  operations. During  $pp$  operation, the proton acceleration chain is: LINAC 2 → BOOSTER → PS → SPS → LHC. The figure is reproduced from Ref. [86].

the large experiments. The collisions occur with a frequency of up to 40 MHz. A fill ends when the beams are dumped, typically because the average number of protons in the bunches has become too low, after which the whole process begins again.

The LHC has been providing  $pp$  collisions during two periods so far: Run 1 during 2011 and 2012, where the centre-of mass energies were  $\sqrt{s} = 7 \text{ TeV}$  and  $8 \text{ TeV}$  respectively, and Run 2 from 2015 to 2018, where  $\sqrt{s} = 13 \text{ TeV}$ . The instantaneous luminosity at the LHCb collision point has been  $4 \times 10^{32} \text{ cm}^{-2} \text{ s}^{-1}$ , and has allowed for the collection of a data set corresponding to an integrated luminosity of approximately  $3 \text{ fb}^{-1}$  during Run 1 and  $6 \text{ fb}^{-1}$  during Run 2. The full data set forms the basis of the thesis. This instantaneous luminosity is significantly lower than at other collision points, for example the peak instantaneous luminosity in the ATLAS detector was about  $20 \times 10^{33} \text{ cm}^{-2} \text{ s}^{-1}$  in 2018 [87], 50 times higher than in LHCb. The lower luminosity is necessary to limit the number of  $pp$  interactions per bunch crossing to an average of about 1.1–1.4 (depending on the data taking period), necessary for a vertex reconstruction with the required precision.

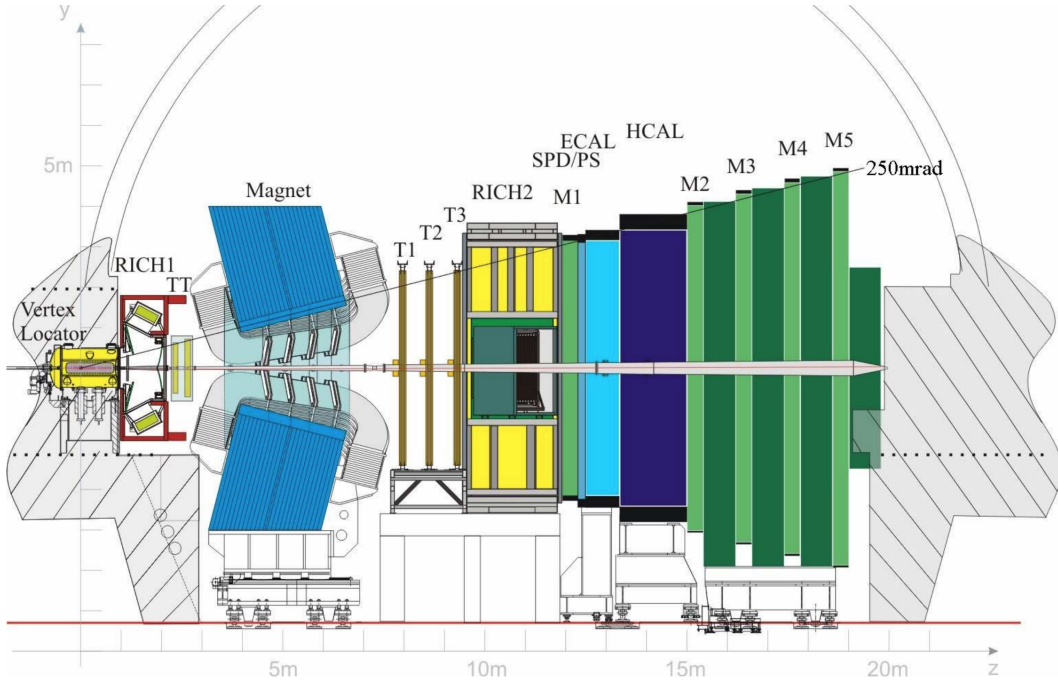


**Figure 3.2:** Overview of the LHCb detector reproduced from Ref. [88,89]. The individual subdetectors are described in detail in the text.

965 The lower luminosity is achieved by colliding the proton beams with an off-set  
 966 at the LHCb collision point. This has the added benefit that the offset can be  
 967 continuously adjusted during a fill of the LHC, and thus all data can be taken  
 968 at the same instantaneous luminosity, allowing for simpler trigger configuration,  
 969 and simpler subsequent analysis because the detector occupancy is constant. The  
 970 lower luminosity, of course, comes with the downside that the collected data  
 971 sample is smaller.

### 972 3.1 The LHCb subdetectors

973 The LHCb detector, shown in Fig. 3.2, is able to detect particles in the forward  
 974 region  $\eta \in [2, 5]$ , corresponding to an angle  $\theta$  with respect to the beam line between  
 975 15 and 300/250 mrad in the horizontal/vertical direction. As illustrated in Fig. 3.3,  
 976 the  $b\bar{b}$  production cross section is very large within the LHCb acceptance: even  
 977 though the acceptance covers less than 2 % of the solid angle, 24 % of all  $b\bar{b}$  pairs  
 978 created at  $\sqrt{s} = 14$  TeV are within the acceptance [90] (for  $\sqrt{s} = 8$  TeV the number  
 979 is 25 %). The detector is described with a coordinate system, where the  $z$ -axis is  
 980 along the beam line and the  $x$  ( $y$ ) axis is in the horizontal (vertical) directions normal  
 981 to the beam line. The origin is at the collision point. The experiment consists of a

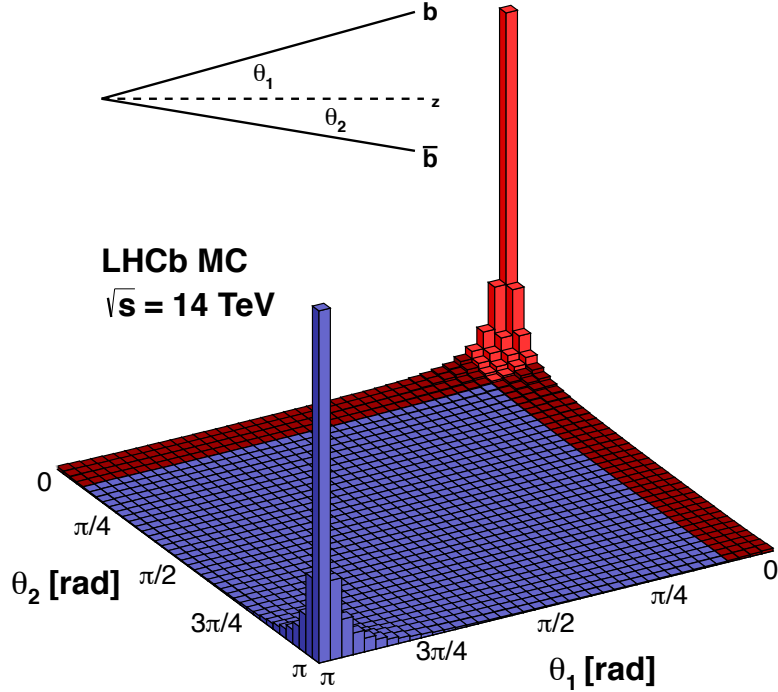


**Figure 3.3:** Production cross section of  $b\bar{b}$  pairs at a centre-of-mass energy of  $\sqrt{s} = 14 \text{ TeV}$ , as a function of  $\theta_1$  and  $\theta_2$ , the angle of the  $b$  and  $\bar{b}$  quark, respectively, with respect to the beam axis  $z$ . The LHCb acceptance is marked in red. The cross-section looks very similar for  $\sqrt{s} = 7, 8 \text{ TeV}$ . The figure is taken from Ref. [90].

number of sub detectors, located in the region from around the interaction point, and up to a distance of  $z = 20 \text{ m}$  along the beam line (in the following, the direction from the interaction point towards the sub detectors is denoted *downstream*, and the opposite direction *upstream*). This section describes each of them in detail.

### 3.1.1 The VELO

The VErtex LOcator (VELO) [91] is a silicon detector located immediately around the collision point, used to provide precise measurements of the particle track coordinates in the interaction region. These are used to reconstruct the production and decay vertices of beauty and charm hadrons with a very high accuracy, allowing for an accurate reconstruction of their life times, and play an important role in the full track reconstruction. The ability to distinguish tracks originating in secondary vertices also plays a crucial role in efficient triggering, as described further below.

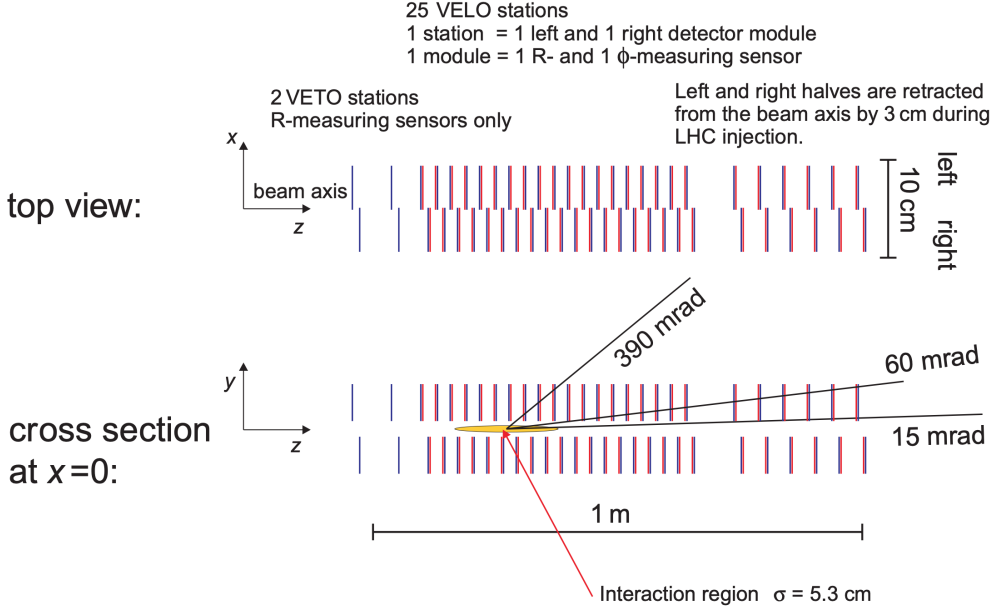


**Figure 3.4:** Overview of the arrangement of VELO stations from the VELO Technical Design Report (TDR) [91]. The actual detector includes 21 stations instead of 25, but the overall design is identical [92].

The detector consists of 21 VELO stations positioned along the beam line as illustrated in Fig. 3.4. Each station consists of two *modules*, mounted on each side of the beam line; each module, in turn, consists of two silicon strip detectors, where the strips are oriented to provide a measurement of  $r$ , the radial distance from the beam line, and  $\phi$ , the azimuthal angle, respectively. This is illustrated in Fig. 3.5. The strip pitch varies between 40 and 100  $\mu\text{m}$  depending on the distance from the beam line. The stations are positioned such that all tracks that are within the acceptance region of the downstream detectors and originate at the interaction point are guaranteed to intersect 3 detector stations. During operation, the segments are located only 8 mm from the beam; this is achieved by mounting them on a moving frame that can be retracted during beam commissioning to avoid radiation damage. The detectors are kept in a vacuum, shielded from the beam vacuum by a 0.3 mm thick *RF foil* made of aluminium that also serves to screen the detector from electric fields induced by the proton beam. The silicon sensors were kept at an operating temperature of about -7  $^{\circ}\text{C}$ , achieved with a liquid- $\text{CO}_2$  cooling system.

The primary vertex (PV) resolution of the VELO is typically  $\sim 10 \mu\text{m}$  in the  $x$  and  $y$  directions and  $\sim 50 \mu\text{m}$  in the  $z$  direction, improving with the number of tracks originating at the PV, and deteriorating with the overall number of PVs [92]. The typical uncertainty on the decay length of a  $B$  meson is about 230  $\mu\text{m}$ , compared to a typical decay length  $O(10)$  mm. The resolution of the *impact parameter*, IP, of

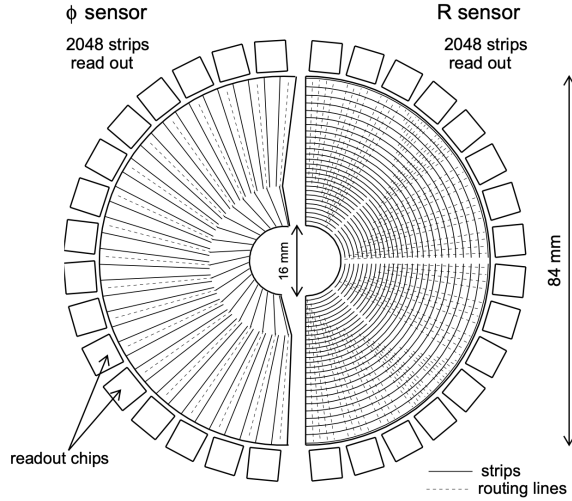


**Figure 3.5:** Illustration of the silicon strip layout in the VELO modules designed to measure (left) the azimuthal angle,  $\phi$ , of a track, and (right) the radial distance from the beam,  $r$ . Reproduced from Ref. [91].

1014 a track is well-described by the formula  $\sigma_{\text{IP}} = (15 + 29/[p_T/( \text{GeV}/c)]) \mu\text{m}$ . This  
 1015 parameter excellently distinguished particles produced in secondary decays, from  
 1016 those produced in the primary interaction (for which the IP would be zero, were  
 1017 it not for the experimental resolution).

### 1018 3.1.2 Magnet and tracking stations

1019 The LHCb experiments uses a warm (non-superconducting) dipole magnet to  
 1020 measure the momentum of charged particles, by providing a maximum magnetic  
 1021 field strength of approximate  $1T$  and a total bending power of about  $4 \text{ T m}$  over  
 1022 the region where  $z \in [2.5, 8] \text{ m}$ . The magnetic field has been measured to a relative  
 1023 precision of about  $4 \times 10^{-4}$  and is uniform within a percent within the tracking  
 1024 volume. The profile of the magnetic field along the  $z$ -axis is shown in Fig. 3.14 on  
 1025 page 46, where the track types within LHCb are defined. The magnet can provide  
 1026 a magnetic field in either vertical direction; over the span of a year of running the  
 1027 experiment approximately equal amounts of data are collected with the magnet in  
 1028 the "Up" and "Down" configurations; this leads to the cancellation of a number of  
 1029 charge-asymmetry effects, significantly reducing potential systematic uncertainties.

1030 The tracking system consists of the VELO, and four other tracking stations:  
 1031 the Tracker Turicensis (TT) upstream of the magnet, and the tracking stations  
 1032 1–3 (T1, T2, T3) downstream of the magnet. The downstream tracking stations  
 1033 each consist of an Inner Tracker (IT) based on silicon strips, and an Outer Tracker  
 1034 (OT) that employs drift tubes.

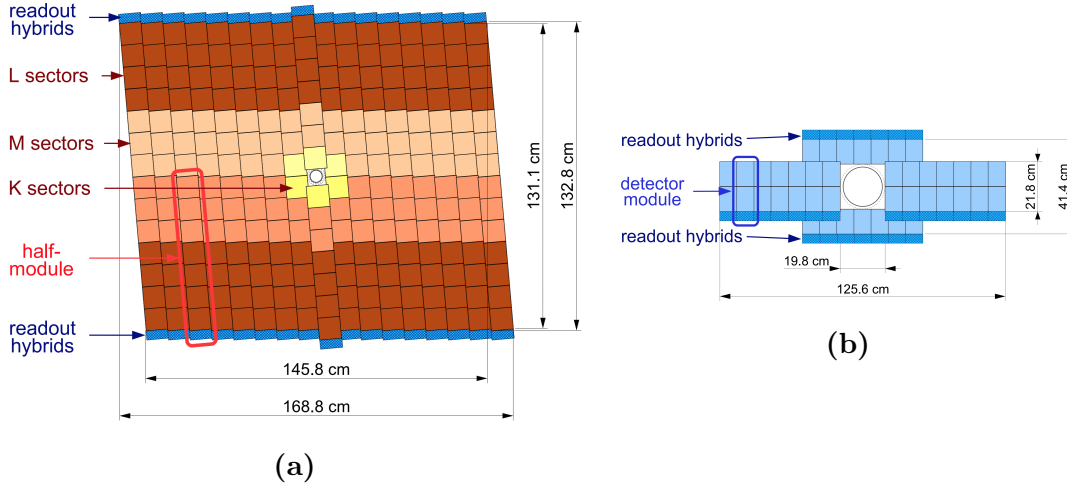


**Figure 3.6:** Overview of (a) a  $v$ -layer module of the IT and (b) an  $x$ -layer module of the IT. Reproduced from Ref. [88]

Both the TT and IT are based on silicon strip detectors with a pitch of about 200  $\mu\text{m}$ ; they were developed as a single project and are collectively known as the Silicon Tracker (ST). The TT is a 140 cm wide and 130 cm tall planar tracking station, covering the whole LHCb acceptance. It is shown in Fig. 3.6a. At each of the T1–T3 stations, the IT consist of four modules, arranged around the beam pipe as illustrated in Fig. 3.6b. They do not cover the full LHCb acceptance, only the very-forward region where the number of tracks is largest. Each TT or IT module comprises of four layers of silicon strips, where the central two layers are rotated  $\pm 5^\circ$  with respect to the first and last layer (an  $x$ - $u$ - $v$ - $x$  geometry). The ST has a spatial resolution for a given track of approximately 50  $\mu\text{m}$ , chosen because the overall momentum resolution is then dominated by multiple-scattering effects for almost all reconstructed tracks.

At the T1–T3 stations, the OT covers the part of the overall acceptance of 300 (250) mrad in the horizontal bending (vertical non-bending) plane that is not covered by the IT. The OT consists of arrays of gas-tight drift tubes with inner diameters of 4.9 mm. The OT is shown illustrated in Fig. 3.7. An Ar/CO<sub>2</sub>/O<sub>2</sub> (70/28.5/1.5) gas mixture is used to fill the tubes that ensures a drift time below 50 ns and a drift coordinate resolution of 200  $\mu\text{m}$ . The use of a drift-chamber detector is necessary, because it was not economically feasible to instrument the whole LHCb acceptance with silicon strip detectors in T1–T3. The condition that the OT occupancy should not be above 10 % in typical run conditions determined the boundary between the IT and the OT.

The overall relative momentum resolution achieved for most charged tracks in LHCb is less than a percent, as illustrated in Fig. 3.8, where it has been determined from a fit to the mass peak in  $J/\psi \rightarrow \mu^+\mu^-$  decays in Run 1 data.

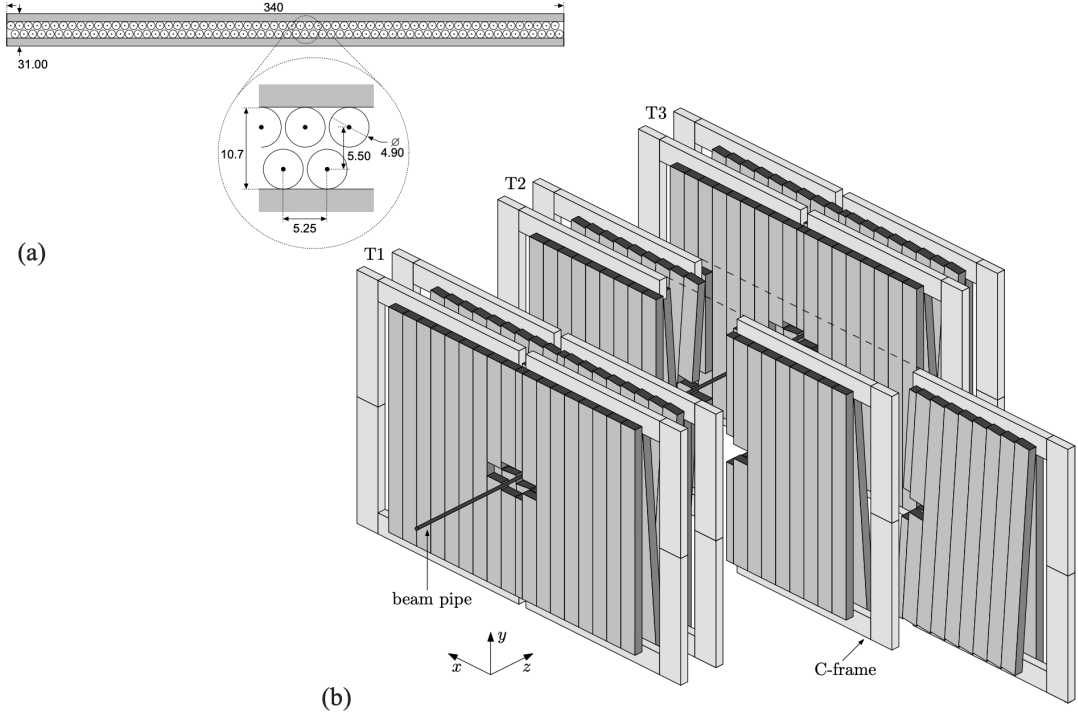


**Figure 3.7:** (a) Cross section of an OT module. (b) Arrangement of the OT modules in tracking stations. Reproduced from Ref. [93].

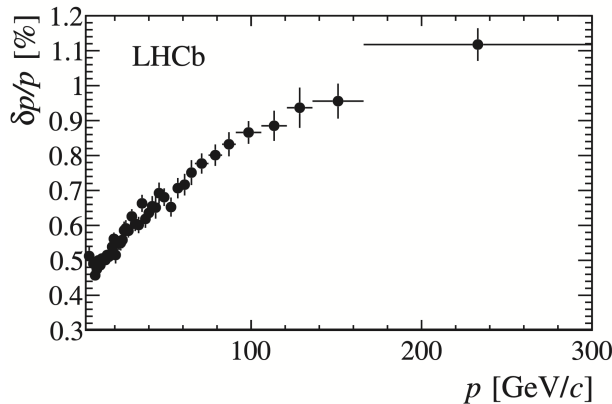


**Figure 3.8:** Relative uncertainty on the momentum of charged tracks (specifically long tracks, cf. the definitions in Section 3.2) in the LHCb detector, determined via the mass resolution obtained in  $J/\psi \rightarrow \mu^+\mu^-$  decays in Run 1 data. Reproduced from Ref. [94]

### 1060 3.1.3 The RICH detectors

1061 Two Ring Imaging Cherenkov detectors (RICH) provide crucial information for  
 1062 particle identification (PID) in LHCb, in particular the ability to separate pions  
 1063 and kaons that is absolutely essential for the measurement presented in the thesis.  
 1064 The RICH 1 detector is located upstream of the magnet, in between the VELO  
 1065 and the TT tracking station. It is designed to provide PID capability for tracks

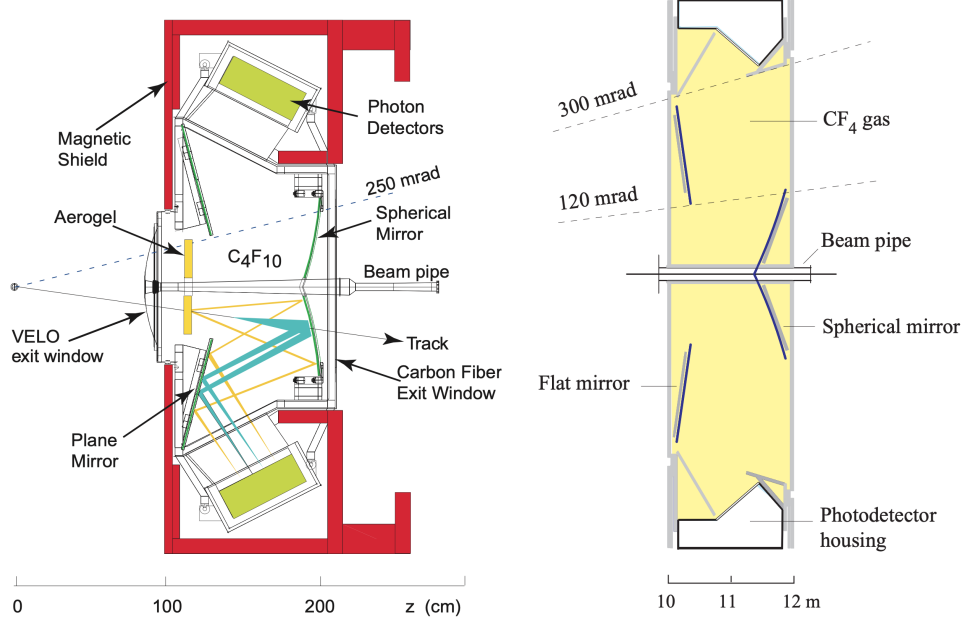


**Figure 3.9:** Overview of (left) the Rich 1 and (right) the RICH 2 detectors. Reproduced from Ref. [88, 95].

in the momentum range  $p \in [1, 60] \text{ GeV}/c$  using a  $\text{C}_4\text{F}_{10}$  radiator, and covers the full LHCb acceptance. During Run 1 the RICH 1 detector also included an Aerogel radiator designed to provide PID for very low momentum particles; however, it was removed before Run 2 because it did not meet the performance requirements during Run 1 [96, 97]. The RICH 2 detector is located downstream of the T1–T3 tracking stations. It is designed to provide PID capabilities for higher momentum tracks in the range  $p \in [15, 100] \text{ GeV}/c$  using a  $\text{CF}_4$  radiator. It only covers the very forward region where  $|\theta| < 120 \text{ mrad}(100 \text{ mrad})$  in the horizontal (vertical) directions, as high momentum particles are produced in that region. In both RICH detectors, mirrors are used to reflect the Cherenkov photons to arrays of Hybrid Photon Detectors (HPDs) located outside the LHCb acceptance. The optics are designed such that photons originating from a given track form rings in the HPD arrays, where the radius is determined by the Cherenkov angle  $\theta_c$ . The detectors are illustrated in Fig. 3.9.

The resolution on  $\theta_c$  can be measured by fitting the obtained  $\theta_c$  distribution in high momentum tracks, where the Cherenkov angle is saturated. It is found to be  $1.618 \pm 0.002 \text{ mrad}$  for RICH 1 and  $0.68 \pm 0.02 \text{ mrad}$  for RICH 2 in Run 1 data [96], and was essentially unchanged in Run 2 [97]. Figure 3.10 shows the relation between track momentum and  $\theta_c$  in RICH 1 for *isolated tracks* in Run 1 data; these are tracks where the Cherenkov ring does not overlap with any other

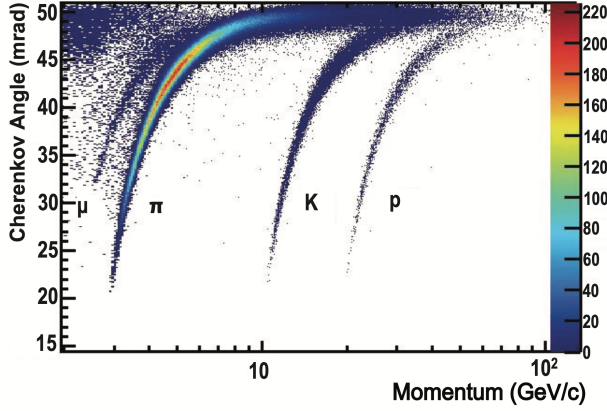


**Figure 3.10:** Cherenkov angle for isolated tracks in the RICH 1 radiator as a function of track momentum. Reproduced from Ref. [96].

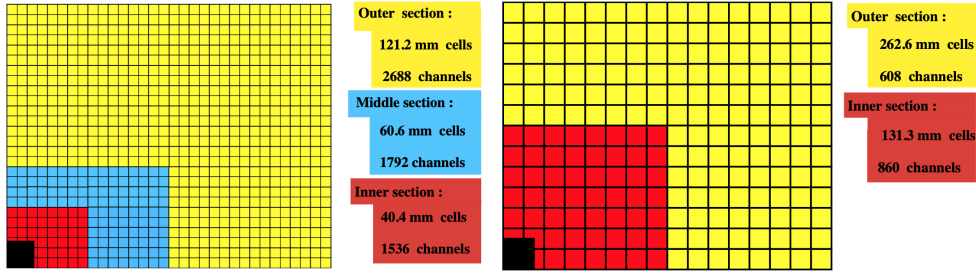


**Figure 3.11:** Illustration of the calorimeter cell size of (left) the ECAL and (right) the HCAL. Reproduced from Ref. [98].

Cherenkov rings. The bands for each hadron species are clearly visible, and it can be seen that the RICH detector also provide some ability to distinguish muons. The definition of the PID variables used in analysis is discussed in Section 3.2.2, along with the achieved PID performance.

### 3.1.4 Calorimeters

The calorimeter system of the LHCb detector has four components. Ordered from the interaction point, these are the Scintillating Pad Detector (SPD), the Pre-Shower (PS) detector, an Electromagnetic Calorimeter (ECAL), and a Hadron Calorimeter (HCAL). Information from the calorimeters also provide identification of electrons, photons, and hadrons, and measurements of their energies and positions, and also plays a crucial role in the triggering, as described below. In all four cases, light is produced in organic scintillators and transmitted to Photo Multiplier Tubes (PMTs) via optical fibres [88].

The SPD and PS detectors consist of almost identical planes of rectangular scintillator pads, with a 15 mm thick lead absorber located in between. The presence

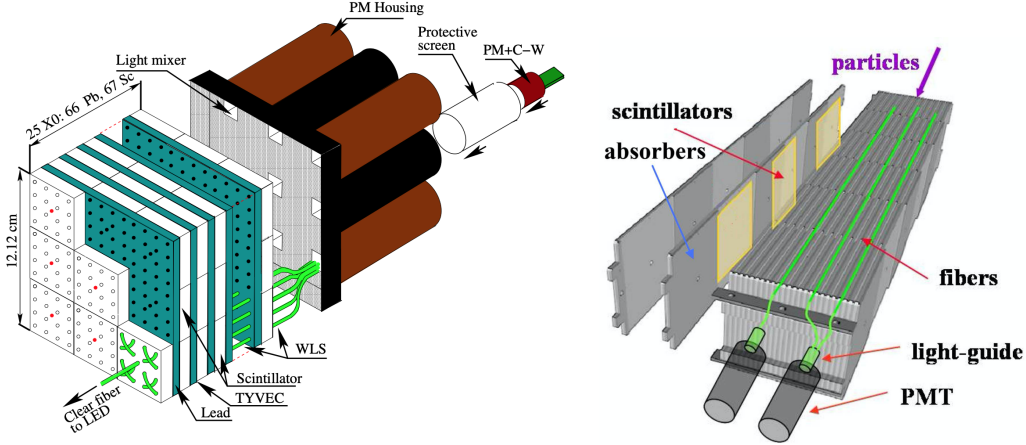


**Figure 3.12:** Illustration of (left) an ECAL and (right) a HCAL module. Reproduced from Ref. [94, 99].

of the SPD before the first absorption layer allows for the separation of photons and electrons in the trigger, because only electrons cause a signal in the SPD. The PS allows for the separation of pion and electron tracks, as only the latter interact significantly with the thin layer of lead. The cell divisions of the detectors closely follow that of the ECAL, shown in Fig. 3.11, to allow for the matching of energy deposits.

The ECAL has a Shashlik structure, with 66 layers consisting of 2 mm of lead absorber and 4 mm of scintillator; an example of a calorimeter module is shown in Fig. 3.12. Accurate energy measurements require that the full electronic shower is contained in the ECAL, which is achieved since the structure extends for 25 radiation lengths. The scintillators are divided into cells that allow for the determination of the location and shape of energy deposits; the cell dimensions vary as a function of radial distance from the beam pipe as shown in Fig. 3.11, to take into account the varying occupancy. The resolution of the ECAL has been measured to be  $\Delta E/E \simeq (9/\sqrt{E} \oplus 0.8)\%$  ( $E$  in  $\text{GeV}/c^2$ ) [88].

The HCAL is located downstream of the ECAL, designed to measure the energy of charged hadrons (which leave relatively little energy in the ECAL). It is constructed with layers of 1 cm iron absorbers inter-spaced with scintillators, oriented *along* the beam direction, such that a typical track will traverse 16 mm of iron per 4 mm of scintillator [98]. As for the ECAL, the cell size varies as a function of distance to the beam line, as shown in Fig. 3.11. An example of a module is shown in Fig. 3.12. The energy resolution required for efficient triggering is moderate; therefore, the HCAL only has a length of 5.6 interaction lengths and can measure the hadron energies at a resolution of  $\Delta E/E \simeq (69/\sqrt{E} \oplus 9)\%$  ( $E$  in  $\text{GeV}/c^2$ ) [88].

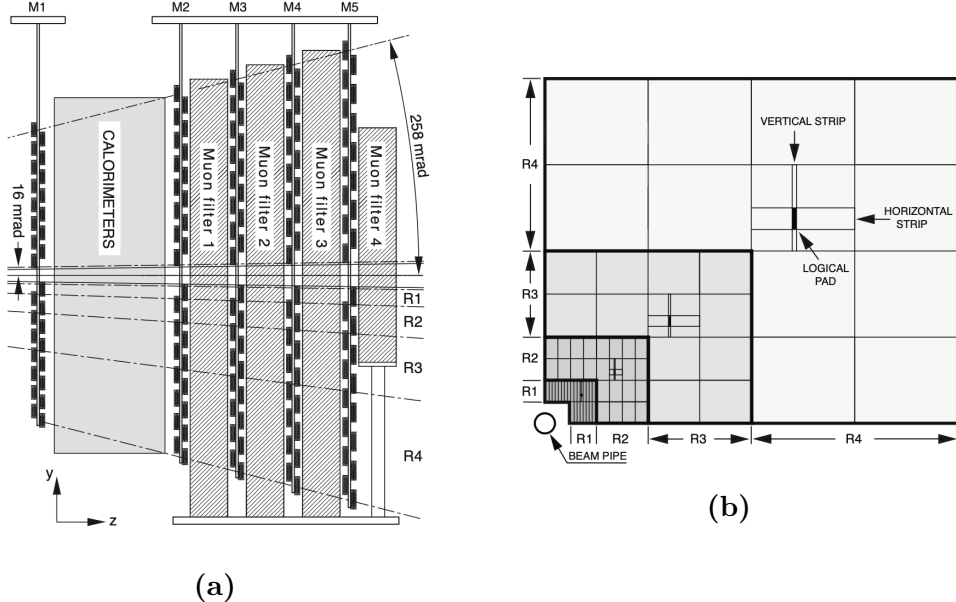


**Figure 3.13:** Illustration of (a) the location of the muon stations along the  $z$ -axis of the experiment, and (b) the geometry of the logical pads of the M3 muon station. Reproduced from Ref. [94].

### 3.1.5 Muon detectors

Muon identification and triggering is crucial for a range of high-profile LHCb measurements, such as lepton-universality tests [100, 101] or measurements of  $B_{(s)}^0 \rightarrow \mu^+ \mu^-$  decays [102]. In the thesis, muon identification plays a role in suppressing a number of backgrounds. The LHCb muon system consists of 5 tracking stations, M1–M5, covering the full LHCb acceptance. M1 is located upstream of the ECAL, whereas M2–M5 are located downstream of the HCAL and inter-spaced with 80 cm thick ion absorbers in order to select penetrating muons. This is illustrated in Fig. 3.13a. The detectors are predominantly multiwire proportional chambers (MWPC), organised into logical pads, the dimensions of which define the  $(x, y)$  resolution of the measured spatial points. The exception is the central region of the M1 station, which is a triple gas-electron-multiplier detector, due to the higher track density in that region [103]. As for the calorimeters, the size of the pads vary as a function of the radial distance from the beam pipe, as illustrated in Fig. 3.13b. The resolution is significantly better in the bending plane ( $x$ ) than in the non-bending plane ( $y$ ). The resolution is also significantly better in the M1–3 stations than in M4 and M5, which are mostly used to identify penetrating tracks. The muon system can independently measure the  $p_T$  of a muon to within 20 %, which allows for efficient triggering.

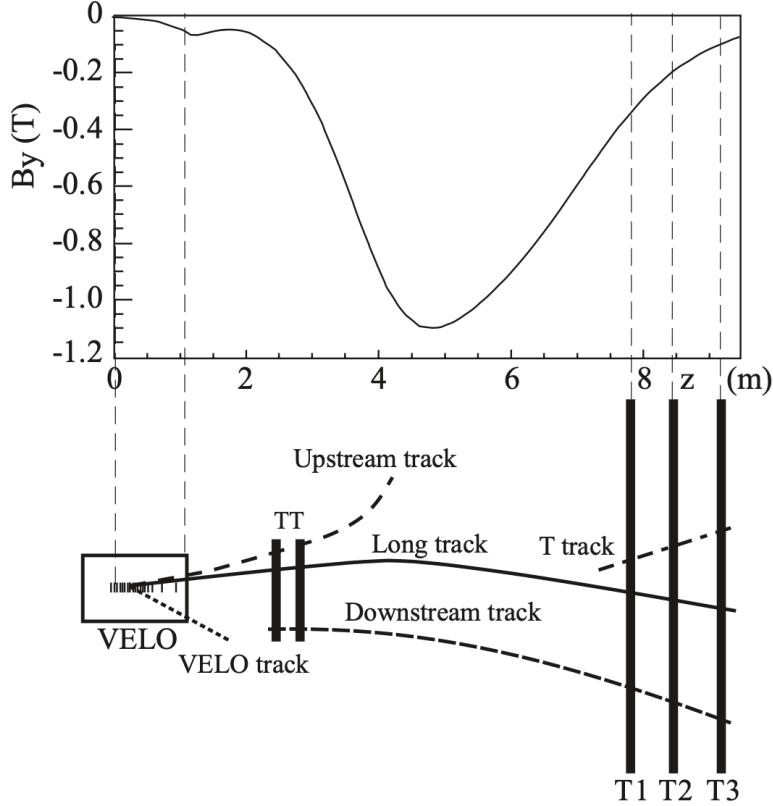


**Figure 3.14:** Definition of track types within the LHCb detector, depending on which set of tracking detectors the track intersects. The profile of the magnetic field is also shown. Reproduced from Ref. [94].

## 1144 3.2 Reconstruction

1145 This section describes the reconstruction algorithms that fit the detector hits in  
 1146 the tracking stations to form track candidates, as well as the algorithms used to  
 1147 identify the types of the particles that formed these tracks.

### 1148 3.2.1 Track reconstruction

1149 The LHCb experiments operates with a number of different particle track types,  
 1150 depending on which sub detectors a track intersects; these are summarised in  
 1151 Fig. 3.14. The two track types that are important for this thesis are *long* tracks,  
 1152 which have hits in the VELO and the TT and T1–T3 tracking stations, and  
 1153 *downstream* tracks that only have hits in the TT and T1–3 tracking stations. The  
 1154 analysis depends on both track types because a number of  $K_S^0$  mesons produced in  
 1155 the signal decay leave the VELO before they decay into the  $\pi^+\pi^-$  final state that  
 1156 is reconstructed; hence these pions necessarily form downstream tracks.

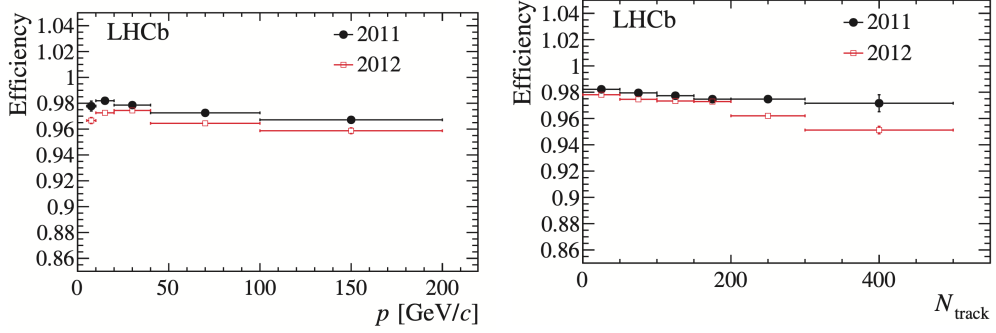


**Figure 3.15:** The long track reconstruction efficiency as a function of (left) track momentum and (right) the number of charged tracks in the event. The lower efficiency in 2012 than 2011 is partially due to the higher event multiplicity, given the higher centre-of-mass energy. The figure is reproduced from Ref. [94].

1157     The first step is to form track candidates from hits in the VELO (VELO tracks)  
 1158     and T1–3 stations (T tracks) separately; because the magnetic field is low in the  
 1159     tracking detectors, these tracks are fairly straight. Long tracks are formed using  
 1160     two separate search strategies: in one, *forward tracking* [104], VELO tracks are  
 1161     used as seeds and matched with hits in the TT and T1–3 tracking stations by  
 1162     extrapolation. These are combined to form long tracks that are required to pass  
 1163     a set of quality conditions. An alternative approach, *track matching* [105, 106],  
 1164     matches VELO and T tracks by extrapolating both through the bending region,  
 1165     and deciding if they below together; finally TT hits are added. The union of tracks  
 1166     found via both approaches is saved, where only the track candidate with the best  
 1167     fit quality is kept in the case where a track appears twice. Downstream tracks  
 1168     are formed based on T tracks as seeds, matched with hits in the TT detector in  
 1169     a search region obtained by extrapolation of the seed [107]. Finally, each track  
 1170     is reprocessed using a Kalman filter that takes into account multiple scattering  
 1171     and corrects for energy loss due to ionisation [108, 109].

1172     Many of the interesting signal decay channels of LHCb have 4–6 charged final  
 1173     state tracks, and therefore it is crucial to have a single-track reconstruction efficiency  
 1174     close to 100 %. The single-track reconstruction efficiency is shown in Fig. 3.15 as  
 1175     a function of track momentum and the number of tracks in an *event* (an *event*  
 1176     denotes a  $pp$  collision and all the particles produced therein and in subsequent  
 1177     decays). The efficiencies have been obtained in data, using a tag-and-probe method  
 1178     in  $J/\psi \rightarrow \mu^+\mu^-$  decays [110]. One muon, the *tag*, is fully reconstructed, while the  
 1179     other, the *probe* is only partially reconstructed, allowing for the  $J/\psi$  invariant mass  
 1180     to be reconstructed with reasonable resolution. If the partially reconstructed probe  
 1181     track is matched to a full long track, the track is classified as efficient. Similar  
 1182     efficiencies have been achieved in Run 2.

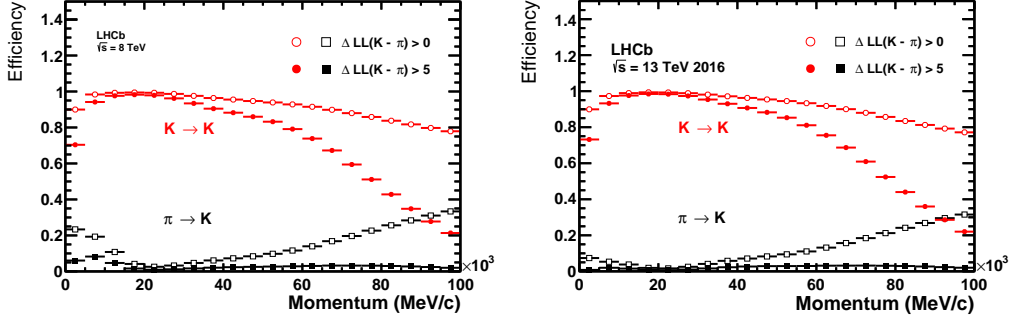


**Figure 3.16:** The probability to correctly identify a kaon/misidentify a pion as a kaon given two different requirements on  $\Delta LL(K)$ , as a function of track momentum in (left) Run 1 data from 2012 and (right) Run 2 data from 2016. Reproduced from Ref. [111].

### 3.2.2 Particle identification

The information from the RICH detectors, the calorimeters, and the muon system is combined for optimal identification of charged tracks as electrons, muons, pions, kaons, or protons. Photons and neutral pions are identified using the ECAL, but play no role in the thesis, and will not be discussed further.

The ability to separate  $B^\pm \rightarrow DK^\pm$  and  $B^\pm \rightarrow D\pi^\pm$  decays is essential to the measurement presented in this thesis. In LHCb, hadron separation is achieved via information from the RICH detectors, using a likelihood method where the observed pattern of hit pixels in the photo detectors is compared to the expected pattern, given all reconstructed tracks in an event under a given set of particle hypothesis. The likelihood is maximised by varying the particle hypotheses for each track being an electron, muon, pion, kaon, or proton [112]. It is necessary to consider all tracks of an event simultaneously because the Cherenkov rings of different tracks overlap. For each track, the maximum log likelihood of a particle hypothesis, say that the track is a kaon, relative to the hypothesis that it is a pion

$$\Delta LL_{\text{track}_i}(K) = \ln \mathcal{L}_{\max}^{\text{RICH}}(\text{pattern} | \text{track}_i = K) - \ln \mathcal{L}_{\max}^{\text{RICH}}(\text{pattern} | \text{track}_i = \pi), \quad (3.1)$$

is saved to inform PID decisions. In the case of pion-kaon separation, this variable alone is enough to achieve good separation power; in the remainder of the thesis it is denoted PIDK. The PID performance for pion-kaon separation has been measured in calibration data, following a procedure described in Section 5.2.1, and is illustrated in Fig. 3.16.

Muons are identified by extrapolating tracks to the muon stations to define fields-of-interest (FOI). A track is considered as a muon candidate when a minimum number of stations (2–4 depending on the track momentum) have hits in the

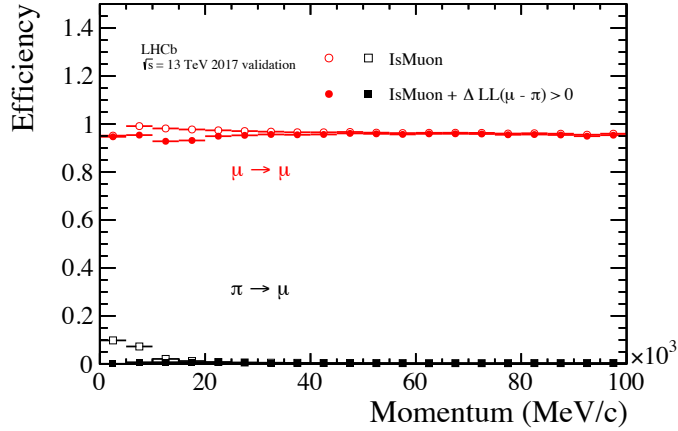


**Figure 3.17:** The probability to correctly identify a muon/misidentify a pion as a muon given requirements on either `isMuon` or  $\Delta LL(\mu)$ , as a function of track momentum in Run 2 data from 2017. Reproduced from Ref. [111].

corresponding FOI [113, 114]. This information is encoded in a variable denoted `isMuon` throughout the thesis. Additional information, such as a comparison of the slopes of the track in the main tracker and the muon stations, and the average track-hit distance in the FOI is used to form a  $\Delta LL^{\text{muon}}(\mu)$  variable analogous to the one defined in Eq. (3.1) for the RICH detectors; again defining as the relative likelihood with respect to the pion hypothesis. This variable can be combined with  $\Delta LL^{\text{RICH}}(\mu)$  to form a PID variable that takes information from both detectors into account, denoted `PIDmu`. The performance of the muon PID variables is shown in Fig. 3.17 as obtained in data. It can be seen that requiring `isMuon=0` rejects muon tracks efficiently at all momenta; this is used in the analysis to veto a number of semi-leptonic backgrounds.

In similar manner, a potential semi-leptonic background with electrons is also vetoed in the analysis presented in the thesis. In LHCb, electron PID is mainly based on the balance between deposited energy and track momentum in the ECAL [115]. This information is combined with information on photon energy deposits from brehmstrahlung, and energy deposits in the PS and HCAL, as well as information from the RICH and muon detectors, to form yet another  $\Delta LL$  variable as the likelihood difference between the electron and pion hypotheses, denoted `PIDe`. As an example of the obtainable performance, an average electron selection efficiency of  $(91.9 \pm 1.3\%)$  was achieved in displaced  $J/\psi \rightarrow e^+e^-$  decays in Run 1, with a hadron misidentification rate of  $(5.54 \pm 0.02)\%$  [94].

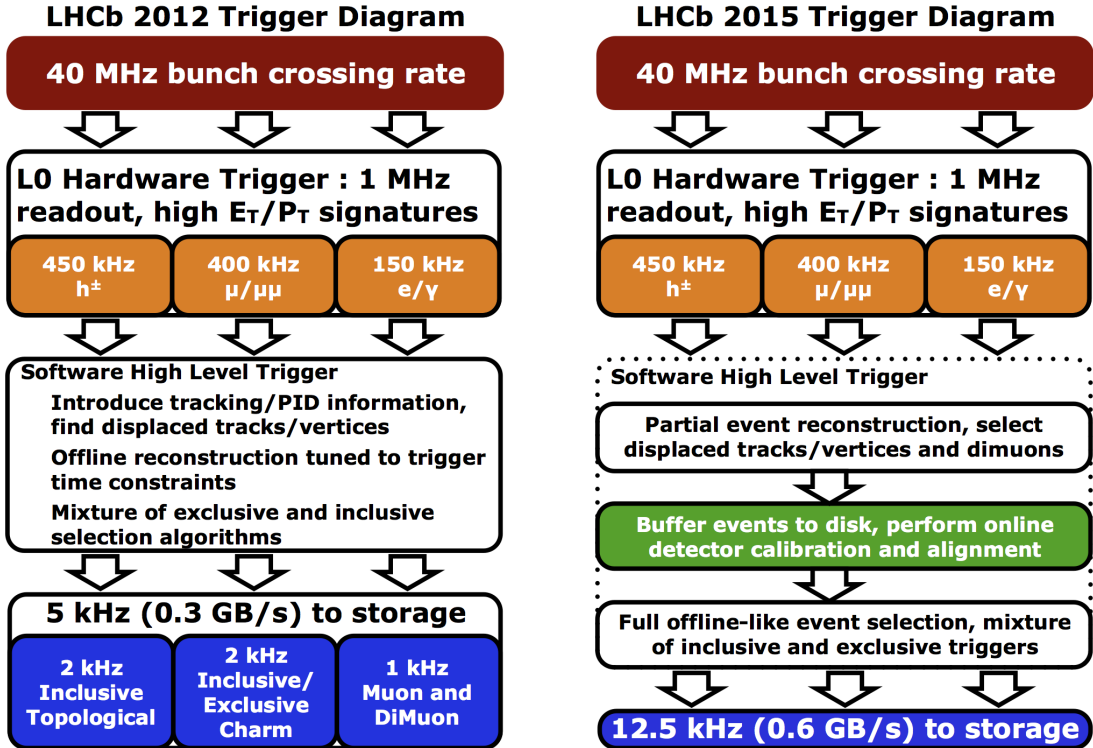


**Figure 3.18:** Illustration of stages and event processing rates in the LHCb trigger during (left) Run 1 and (right) Run 2.

### 3.3 The LHCb trigger system

The collision rate in the LHC is up to 40 MHz, with a visible inelastic collision rate in LHCb of up to 30 MHz. The LHCb uses a multi-stage trigger to reduce rate with which events are stored to a manageable level (of eg. 12.5 kHz during Run 2). The first stage consists of a hardware trigger that selects events with high transverse energy in the calorimeters, or hits in the muon detectors. This is followed by two software stages that rely on a reconstruction of tracks in the detector to select events that are likely to include interesting physics. The overall trigger stages were identical in Run 1 and Run 2, however the throughput rate was upgraded significantly between the two data taking periods, as was the quality of the reconstruction in the software trigger stages; in Run 2, the final software trigger decisions are in fact based on an event reconstruction that is fully equivalent to the one performed offline [116]. The stages are illustrated in Fig. 3.18, and described in detail in the following.

A further, offline processing and reconstruction step is applied to all events before they are made available to most LHCb analyses, commonly denoted as the *stripping* step. Although the stripping does not form part of the LHCb trigger, it does constitute an additional, centralised filter on the data, and a description is included in Section 3.3.3.

### 3.3.1 The level-0 hardware trigger

The level-0 (L0) triggers that select physics events are based on the calorimeters and the muon system. The ECAL and HCAL are divided into clusters of  $2 \times 2$  cells, for which the transverse energy is defined as

$$E_T = \sum_j E_j \sin \theta_j, \quad (3.2)$$

where  $\theta_j$  is the angle of cell  $j$  with respect to the beam axis and the average collision point. The trigger forms a L0Hadron candidate with the highest  $E_T$  found in the HCAL, combined with the ECAL cluster in front of it if such a cluster is present. Photon and electron candidates are formed based on clusters in the ECAL, identified by the presence (lack) of hits in the SPD for an electron (photon). The transverse energies of the candidates are compared to a fixed set of thresholds, and events where at least one candidate is above threshold are retained.

The muon trigger searches for straight line tracks in the muon stations, estimating the associated muon  $p_T$  based on the track direction. An event is retained if either the largest muon  $p_T$  is above a given threshold, or the product of the two highest muon  $p_T$  values is above a different threshold.

High-multiplicity events take a long time to process in the subsequent software stage; therefore it is favourable for the overall retention rate of interesting physics decays to put a maximum limit on the event multiplicity at the L0 stage. This is achieved by requiring the number of hits in the SPD detector to be below a threshold value in most L0 lines.

### 3.3.2 High-level triggers

The events that pass the L0 trigger are passed to a farm of multiprocessor computing node, the Event Filter Farm (EFF), tasked with bringing the rate down from approximately 1 MHz to the  $\mathcal{O}(1 - 10)$  kHz rate that can be saved to disk. The EFF consisted of 900 (1700) nodes during Run 1 (Run 2). The software-based filtering proceeds in two stages: a first filter (HLT1) brings the rate down to approximately 40 (110) kHz based on a limited reconstruction of the event, after which a second stage (HLT2) filters the events further based on a more complete reconstruction. Each step executes a number of different algorithms, each of which can allow an event to be accepted; these are denoted *trigger lines*.

During both runs, the HLT1 performed a partial event reconstruction by building long tracks that satisfy a  $p_T$  requirement using the forward tracking approach described in Section 3.2.1, and determining the location of PVs using Velo tracks.

1278 In both runs, the HLT1 included an inclusive trigger that selected a high  $p_T$   
1279 track with significant displacement of all PVs (typical of a  $b$  or  $c$  decay). This  
1280 line is denoted `HLT1TrackAllL0` in Run 1 [117]; for Run 2 the track requirements  
1281 were reoptimised and it is denoted `Hlt1TrackMVA`. Further, an additional inclusive  
1282 trigger was added that forms a two-prong vertex out of high  $p_T$  tracks inconsistent  
1283 with originating in a PV, and applies a multivariate classifier to determine if  
1284 it is signal-like based on a number of track and vertex properties. This line is  
1285 denoted `Hlt1TwoTrackMVA` [116]. These lines triggered all events included in the  
1286 analysis of the thesis; other lines exist for selecting events that include muons,  
1287 calibration data, low-multiplicity events, and a number of exclusive lines, for a  
1288 total of approximately 20 lines during Run 2 [116].

1289 Because the rate of events is reduced significantly by HLT1, the HLT2 decisions  
1290 can be based in a more complete reconstruction of the event. Indeed, during Run 2  
1291 it was based on a complete, fully aligned reconstruction equivalent to the offline  
1292 reconstruction. During Run 1 the HLT2 reconstruction only included long tracks  
1293 and did exclude some low momentum tracks; this was a main motivation for the  
1294 upgrade of the EFF during the shutdown period. The need for full alignment in  
1295 HLT2 means that it could not be run fully online in Run 2; instead the output events  
1296 from HLT1 were saved to disk in the EFF, and processed with some delay [116].  
1297 The analysis presented in the thesis is based on a number of inclusive "topological"  
1298 trigger lines, based on combinations of 2, 3, or 4 tracks that satisfy fit quality  
1299 requirements, have high  $p_T$ , are separated from the PVs, and have a distance-of-  
1300 closest-approach below 0.2 mm. A multivariate classifier [118] is applied to each  
1301 formed  $n$ -body object, to determine if the event should be accepted based on  
1302 the track momenta, invariant mass, a corrected invariant mass that takes into  
1303 account missing transverse momentum, distance of closest approach, and the impact  
1304 parameter and separation with the associated PV. The resulting trigger lines were  
1305 denoted `Hlt2Topo{2, 3, 4}BodyBBDT` during Run 1 and `Hlt2Topo{2, 3, 4}Body`  
1306 during Run 2. A large number of other HLT2 lines exist (more than 500 in Run 2),  
1307 including a significant number of exclusive lines that aim to select specific decays  
1308 and only save information on the signal decay, not the whole event. This was made  
1309 possible by the full reconstruction within HLT2 [116], and have allowed for larger  
1310 signal yields to be collected within the data storage limits.

### 3.3.3 Offline data filtering: the LHCb stripping

Events that are written to disk are processed with the full detector alignment and calibration. In a further, offline processing step denoted the *stripping*, hundreds of different, dedicated reconstructions are performed; decay candidates for various signal decays are built and a number of requirements are made to reject backgrounds from random track combinations. For example, the  $B^\pm \rightarrow D(\rightarrow K_S^0 h'^+ h'^-) h^\pm$  candidates that are analysed in this thesis are built during the stripping stage, as described further in Section 5.1. The stripping is a centralised computing task, executed on the Worldwide LHC Computing Grid [119], and allows the analysts to process much smaller data sets during their individual analysis. Because the stripping is based on data saved to offline storage it can be repeated; however, the processing of data collected during a year of data taking takes many weeks, so this does not happen often.

## 3.4 Simulation

A centralised LHCb simulation is able to simulate  $pp$  collisions with the proper conditions within LHCb, model subsequent secondary decays and the full detector response, and process the output in the full LHCb reconstruction. In this thesis, simulated decays are used to determine the reconstructed invariant-mass distribution of a number of decay modes, as well as a number of relative selection efficiencies. The  $pp$  collisions are generated using PYTHIA [120] with a specific configuration specific to LHCb [121]. The time-dependent evolution and decays of unstable particles are described by the EVTGEN [122] package, designed specifically for  $B$  physics. Final-state radiation is generated using PHOTOS [123]. The interaction of the generated particles with the detector, and its response, are implemented using the GEANT4 toolkit [124] as described in Ref. [125].

The most significant computational cost of the simulation is due to the detector simulation. A single  $pp$  collision produces  $\mathcal{O}(100)$  tracks in the detector, out of which only a handful belong to the signal decay under study. Therefore, significant computational resources can be saved by reusing the detector simulation of non-signal tracks a number of times, while redescaying the signal particle, say a  $B^+$ , each time. This approach is called ReDecay [126], and has been relatively widely adopted within LHCb. ReDecay has been used to produce simulation samples corresponding to the conditions in 2017 and 2018 for this thesis. In some cases, the use of ReDecay necessitates special statistical treatment due the correlated detector occupancies between signal candidates, but for the analysis in this thesis the impact is negligible.

**Table 3.1:** Overview of the running condition and collected data samples by the LHCb experiment during Run 1 and 2 of the LHC [128]. A brief overview of data taking periods planned for the future is also shown.

LHC phase	Year	$\sqrt{s}$ / TeV	$\int \mathcal{L} dt$ / $\text{fb}^{-1}$
Run 1	2011	7	1.0
	2012	8	2.0
Run 2	2015	13	0.3
	2016		1.6
	2017		1.7
	2018		2.1

1346       A number of sub-dominant backgrounds are investigated using the fast-simulation  
 1347 package `RapidSim` [127]. This package can decay heavy  $b$  and  $c$  hadrons with  
 1348 kinematic distributions similar to those in LHCb  $pp$  collisions, or with user defined  
 1349 input distributions. The decays are typically evenly distributed over phase space,  
 1350 but can also be handled with `EVTGEN` [122] to take involved spins and resonant  
 1351 structure into account. Furthermore, a smearing of the obtained momenta can  
 1352 be applied that is based on the LHCb resolution.

### 1353       3.5 Data-taking conditions

1354       The LHCb experiment has collected a data set corresponding to  $8.7 \text{ fb}^{-1}$  during  
 1355 Run 1 and 2 of the LHC. The running conditions for each year are summarised  
 1356 in Table 3.1. The measurement that is the main topic of the thesis is based  
 1357 on the full data set.

1358       The  $B^\pm$  production cross section increased significantly with the higher centre-  
 1359 of-mass energy during Run 2. In the LHCb acceptance, the cross section has been  
 1360 measured to be approximately  $43 \mu\text{b}$  at  $\sqrt{s} = 7 \text{ TeV}$ , increasing to about  $87 \mu\text{b}$   
 1361 at  $\sqrt{s} = 13 \text{ TeV}$  [129]. In combination with an increased selection efficiency due  
 1362 to improvements to the trigger, this resulted in signal yields per  $\text{fb}^{-1}$  that were  
 1363 about 2.5 times higher in Run 2 than in Run 1, in the measurement described in  
 1364 Chapter 5. Before delving into the details of that analysis, Chapter 4 is dedicated  
 1365 to a phenomenological study of how it is impacted neutral kaon  $CP$  violation and  
 1366 interaction with the LHCb detector.

# 4

1367

## 1368 Neutral kaon $CP$ violation and material 1369 interaction in BPGGSZ measurements

1370 The presence of a  $K_S^0$  meson in the  $D \rightarrow K_S^0 h^+ h^-$  final states introduces a small  
1371 bias in BPGGSZ measurements due to  $CP$ -violation in the neutral kaon sector  
1372 and asymmetries caused by the interaction between the neutral kaons and detector  
1373 material. These fundamental physics effects are reviewed in Section 4.1, after which  
1374 the chapter presents a detailed analysis of the impact on the LHCb measurement  
1375 that is the subject of the thesis, as well as future  $\gamma$  measurements with the Belle II  
1376 experiment. Prior to this analysis, the only existing work on the effect on  $\gamma$   
1377 measurements suggested a small effect in  $B^\pm \rightarrow D K^\pm$  measurements but potentially  
1378 very significant effects in measurements based on  $B^\pm \rightarrow D \pi^\pm$  decays [41]. However,  
1379 as described in Section 4.1.1, the analysis in Ref. [41] does not take into account  
1380 the fundamental aspect of the BPGGSZ method: that it relies on the phase-space  
1381 distribution of signal decays, not phase-space integrated asymmetries. Furthermore,  
1382 the earlier study only considers the  $CP$ -violation effect, not material interaction.  
1383 Therefore, a more detailed study was necessary before the  $B^\pm \rightarrow D \pi^\pm$  decay mode  
1384 could reliably be promoted to a signal channel. The full analysis shows the impact  
1385 on the  $\gamma$  measurement in Chapter 5 to be small, and allows for the assignment  
1386 of an appropriate systematic uncertainty.

## 1387 4.1 CP violation and material interaction of neu- 1388 tral kaons

1389 A brief review of the general phenomenology of mixing and  $CP$  violation in the  
1390 neutral kaon system is useful, before analysing the impact on  $\gamma$  measurements.  
1391 The presentation in this section follows the PDG review of *CP violation in the*  
1392 *quark section* [31]. The general theory considers any pair of neutral mesons  $|M^0\rangle$   
1393 and  $|\bar{M}^0\rangle$  related by  $CP$  conjugation

$$CP|M^0\rangle = e^{i\phi_M}|\bar{M}^0\rangle \quad CP|\bar{M}^0\rangle = e^{-i\phi_M}|M^0\rangle, \quad (4.1a)$$

1394 where  $\phi_M$  is an arbitrary phase. In this thesis, the convention  $\phi_M = 0$  is chosen  
1395 to equal zero, so that

$$CP|M^0\rangle = |\bar{M}^0\rangle \quad CP|\bar{M}^0\rangle = |M^0\rangle. \quad (4.1b)$$

1396 A meson state that starts as a general superposition of  $|M^0\rangle$  and  $|\bar{M}^0\rangle$  states

$$\begin{aligned} \psi_M^0 &\equiv \psi_M(0) = a(0)|M^0\rangle + b(0)|\bar{M}^0\rangle \\ &\equiv \psi_{M^0}^0 + \psi_{\bar{M}^0}^0 \end{aligned} \quad (4.2)$$

1397 will, over time, evolve into a state that consists of a different superposition of  
1398  $|M^0\rangle$  and  $|\bar{M}^0\rangle$ , as well as components for all possible states the meson system  
1399 can decay into

$$\begin{aligned} \psi_M(t) &= a(t)|M^0\rangle + b(t)|\bar{M}^0\rangle + \sum c_i(t)f_i \\ &\equiv \psi_{M^0}(t) + \psi_{\bar{M}^0}(t) + \sum c_i(t)f_i. \end{aligned} \quad (4.3)$$

1400 For time scales that are longer than the typical strong-interaction, the time evolution  
1401 of the  $M^0-\bar{M}^0$  superposition can be described by a  $2 \times 2$  Hamiltonian

$$\frac{d}{dt} \begin{pmatrix} \psi_{M^0}(t) \\ \psi_{\bar{M}^0}(t) \end{pmatrix} = -i\mathcal{H}_0 \begin{pmatrix} \psi_{M^0}(t) \\ \psi_{\bar{M}^0}(t) \end{pmatrix} \quad (4.4)$$

1402 that is *non-Hermitian* (to allow for decay) but can be parameterised in terms  
1403 of two Hermitian matrices  $\mathcal{M}$  and  $\Gamma_0$

$$\mathcal{H}_0 = \mathcal{M} - \frac{i}{2}\Gamma_0. \quad (4.5)$$

1404 The quantum states with well-defined (real) masses,  $m_j$ , and (real) decay widths,  
1405  $\Gamma_j$ , are the two eigenstates of  $\mathcal{H}_0$  with eigenvalues  $\lambda_j = m_j - \frac{i}{2}\Gamma_j$ . The eigenstates  
1406 (of course) evolve independently in time, so that

$$\psi_j(t) = e^{-i\lambda_j t}\psi_j^0 = e^{-im_j t - \frac{\Gamma_j}{2}t}\psi_j^0. \quad (4.6)$$

1407 The eigenstates are denoted  $H$  and  $L$  according to the size of  $m_j$ , the real part  
1408 of the eigenvalues, such that  $m_H > m_L$ . Assuming that  $\mathcal{H}_0$  conserves  $CPT$  the  
1409 eigenstates have the general form

$$\begin{aligned} |M_H\rangle &\equiv p|M^0\rangle - q|\bar{M}^0\rangle \\ |M_L\rangle &\equiv p|M^0\rangle + q|\bar{M}^0\rangle \end{aligned} \quad (4.7)$$

1410 where  $p$  and  $q$  are complex numbers that satisfy  $|q|^2 + |p|^2 = 1$ . With the convention  
1411 in Eq. (4.1b) it follows that if  $\mathcal{H}_0$  also conserves  $CP$ , so that  $|M_H\rangle$  and  $|M_L\rangle$  are  
1412  $CP$  eigenstates, then  $p = \pm q$ , where the sign depends on which of the heavy and  
1413 the light meson states is  $CP$  even, and which is  $CP$  odd.

1414 The eigenstates of the Hamiltonian governing the neutral kaon system are  
1415 almost, but not exactly, equal to the  $CP$  eigenstates

$$|K_1\rangle = \frac{|K^0\rangle + |\bar{K}^0\rangle}{\sqrt{2}} \quad |K_2\rangle = \frac{|K^0\rangle - |\bar{K}^0\rangle}{\sqrt{2}}, \quad (4.8)$$

1416 which are  $CP$  even and odd, respectively. This approximate equality leads to the  
1417 most prominent feature of the neutral kaon system: the two eigenstates of  $\mathcal{H}_0$  have  
1418 lifetimes that differ by orders of magnitude. This is best understood by assuming,  
1419 for a moment, that the states in Eq. (4.8) *do* equal the eigenstates with definite  
1420 life times. The  $K_1$  state can decay in the  $CP$  even  $\pi^+\pi^-$  and  $\pi^0\pi^0$  modes, and  
1421 does so almost 100% of the time; these decay modes are not available to the  $K_2$   
1422 (in the absence of direct  $CP$  violation) which results in a much lower decay rate  
1423 and a much longer life time. Therefore, the eigenstates in the kaon system are  
1424 labelled the *short-lived* kaon,  $K_S^0$ , which is almost  $CP$  even, and the *long-lived* kaon,  
1425  $K_L^0$ , which is almost  $CP$  odd. The life times are [31]

$$\tau_{K_S^0} = (8.954 \pm 0.004) \times 10^{-11} \text{s} \quad \tau_{K_L^0} = (5.116 \pm 0.021) \times 10^{-8} \text{s}. \quad (4.9)$$

1426 Experimentally, it is found that the  $K_S^0$  corresponds to the light eigenstate, but  
1427 that the mass splitting [31]

$$\begin{aligned} \Delta m = m_{K_L^0} - m_{K_S^0} &= (0.5289 \pm 0.0009) \times 10^{10} \hbar s^{-1} \\ &\simeq 3.5 \times 10^{-6} \text{ eV} \end{aligned} \quad (4.10)$$

1428 is tiny compared to the neutral kaon masses of  $m_{K_S^0} = 497.6 \text{ MeV}/c^2$  [31].

1429 However, the discovery of  $K_L^0 \rightarrow \pi\pi$  decays by Kronin and Fitch in 1964  
1430 established that the  $K_S^0$  and  $K_L^0$  are *not* exactly equal to the  $CP$  eigenstates in  
1431 Eq. (4.8), because the  $\mathcal{H}_0$  relevant to the kaon system is  $CP$ -violating. The  $CP$

<sup>1432</sup> violation in the kaon sector is conventionally parameterised in terms of the complex  
<sup>1433</sup> parameters  $\epsilon$  and  $\epsilon'$ , in terms of which

$$\frac{A(K_L^0 \rightarrow \pi^+ \pi^-)}{A(K_S^0 \rightarrow \pi^+ \pi^-)} = \epsilon + \epsilon' \quad \frac{A(K_L^0 \rightarrow \pi^0 \pi^0)}{A(K_S^0 \rightarrow \pi^0 \pi^0)} = \epsilon - 2\epsilon'. \quad (4.11)$$

<sup>1434</sup> In these expressions  $\epsilon$  denotes the contribution from  $CP$  violation in mixing and  
<sup>1435</sup>  $\epsilon'$  the contribution due to direct  $CP$  violation in the decays. The  $\epsilon$  parameter  
<sup>1436</sup> has been measured to be [31]

$$|\epsilon| = (2.228 \pm 0.011) \times 10^{-3}, \quad \arg \epsilon = (43.52 \pm 0.05)^\circ, \quad (4.12)$$

<sup>1437</sup> while the  $\epsilon'$  parameter satisfies [31]

$$\text{Re}(\epsilon'/\epsilon) \simeq \epsilon'/\epsilon \simeq (1.66 \pm 0.23) \times 10^{-3} \quad (4.13)$$

<sup>1438</sup> Direct  $CP$  violation is ignored for the remainder of the thesis, because  $\epsilon'$  is measured  
<sup>1439</sup> to be three orders of magnitude smaller than  $\epsilon$ . In terms of the  $CP$  eigenstates  
<sup>1440</sup> of Eq. (4.8), the mass eigenstates  $K_S^0$  and  $K_L^0$  are given by

$$\begin{aligned} |K_S^0\rangle &= \frac{|K_1\rangle + \epsilon|K_2\rangle}{\sqrt{1 + |\epsilon|^2}} &= \frac{(1 + \epsilon)|K^0\rangle + (1 - \epsilon)|\bar{K}^0\rangle}{\sqrt{2(1 + |\epsilon|^2)}} \\ |K_L^0\rangle &= \frac{|K_2\rangle + \epsilon|K_1\rangle}{\sqrt{1 + |\epsilon|^2}} &= \frac{(1 + \epsilon)|K^0\rangle - (1 - \epsilon)|\bar{K}^0\rangle}{\sqrt{2(1 + |\epsilon|^2)}}, \end{aligned} \quad (4.14)$$

<sup>1441</sup> corresponding to the definition  $p = (1 + \epsilon)/\sqrt{2(1 + |\epsilon|^2)}$  and  $q = (1 - \epsilon)/\sqrt{2(1 + |\epsilon|^2)}$   
<sup>1442</sup> in Eq. (4.7).

<sup>1443</sup> In an experimental setting, the time evolution of a neutral kaon state is affected  
<sup>1444</sup> by nuclear interactions with the detector. The interaction is governed by the strong  
<sup>1445</sup> force, and therefore sensitive to the *flavour* of the kaon state; the interaction  
<sup>1446</sup> strength is thus different for  $K^0$  and  $\bar{K}^0$  mesons. This difference introduces a  
<sup>1447</sup> non-zero  $K_S^0 \leftrightarrow K_L^0$  transition amplitude for neutral kaons traversing a detector  
<sup>1448</sup> segment. This effect was predicted early in the history of kaon physics [130] and is  
<sup>1449</sup> commonly denoted *kaon regeneration*. The effect can be described by including a  
<sup>1450</sup> material-interaction term in the Hamiltonian that is diagonal in the  $(|K^0\rangle, |\bar{K}^0\rangle)$   
<sup>1451</sup> basis, so that the equation governing the time evolution is [131, 132]

$$\frac{d}{dt} \begin{pmatrix} \psi_{K^0}(t) \\ \psi_{\bar{K}^0}(t) \end{pmatrix} = -i \left[ \mathcal{H}_0 + \begin{pmatrix} \chi & 0 \\ 0 & \bar{\chi} \end{pmatrix} \right] \begin{pmatrix} \psi_{K^0}(t) \\ \psi_{\bar{K}^0}(t) \end{pmatrix}. \quad (4.15)$$

<sup>1452</sup> The complex parameters  $\chi$  and  $\bar{\chi}$  describe the material interaction of the  $K^0$   
<sup>1453</sup> and  $\bar{K}^0$  flavour eigenstates and are related to their scattering cross section, as

<sup>1454</sup> described further in Section 4.3.4. The solution of Eq. (4.15) for the time evolution  
<sup>1455</sup> in the  $K_S^0$  and  $K_L^0$  states is [132]

$$\begin{aligned}\psi_S(t) &= e^{-i\Sigma t} \left( \psi_S^0 \cos \Omega t + \frac{i}{2\Omega} (\Delta\lambda\psi_S^0 - \Delta\chi\psi_L^0) \sin \Omega t \right), \\ \psi_L(t) &= e^{-i\Sigma t} \left( \psi_L^0 \cos \Omega t - \frac{i}{2\Omega} (\Delta\lambda\psi_L^0 + \Delta\chi\psi_S^0) \sin \Omega t \right),\end{aligned}\quad (4.16)$$

<sup>1456</sup> in terms of the parameters

$$\begin{aligned}\Delta\chi &= \chi - \bar{\chi}, \\ \Delta\lambda &= \lambda_L - \lambda_S = (m_L - m_S) - \frac{i}{2}(\Gamma_L - \Gamma_S), \\ \Sigma &= \frac{1}{2}(\lambda_S + \lambda_L + \chi + \bar{\chi}), \\ \Omega &= \frac{1}{2}\sqrt{\Delta\lambda^2 + \Delta\chi^2}.\end{aligned}\quad (4.17)$$

<sup>1457</sup> In the vacuum limit where  $\chi = \bar{\chi} = 0$ , the expressions in Eq. (4.6) and Eq. (4.16) are  
<sup>1458</sup> equal.

### <sup>1459</sup> 4.1.1 A first look at the impact on $\gamma$ measurements

<sup>1460</sup> The effects described above have an impact on measurements of  $CP$  asymmetries  
<sup>1461</sup> in modes with a neutral kaon in the final state. This was analysed for the first  
<sup>1462</sup> time in relation to  $\gamma$  measurements by Grossman and Savastio in 2014 [41]. The  
<sup>1463</sup> authors point out two sources of corrections to be included:

- <sup>1464</sup> • the fact that  $K_S^0$  is not an exact  $CP$  eigenstate can break potential symmetry  
<sup>1465</sup> relations employed in an analysis, and
- <sup>1466</sup> • that when the neutral kaon is reconstructed in a  $\pi\pi$  final state there will be  
<sup>1467</sup> contributions from both  $K_S^0$  and  $K_L^0$  decays.

<sup>1468</sup> The analysis in this chapter considers yet another effect, not treated by Grossman  
<sup>1469</sup> and Savastio, namely that

- <sup>1470</sup> • material interaction can emulate the effect of neutral kaon  $CP$  violation,  
<sup>1471</sup> because it couples the almost- $CP$ -even  $K_S^0$  and the almost- $CP$ -odd  $K_L^0$  states.

<sup>1472</sup> Due to the presence of  $K_L^0 \rightarrow \pi\pi$  decays, Grossman and Savastio point out that the  
<sup>1473</sup> relevant decay rates to consider in an experimental setting are of the form

$$d\Gamma(t) \propto |\psi_S(t) + \epsilon\psi_L(t)|^2. \quad (4.18)$$

<sup>1474</sup> The time dependence of the decay rates considered in Chapter 2 was left out because  
<sup>1475</sup> all terms shared a common time dependence. That is not the case in Eq. (4.18),  
<sup>1476</sup> due to the very different decay rates of the  $K_S^0$  and  $K_L^0$  components of the kaon  
<sup>1477</sup> state. As a consequence, the time-integrated yields have the form

$$N \propto \int dt \eta(t) |\psi_S(t) + \epsilon\psi_L(t)|^2, \quad (4.19)$$

<sup>1478</sup> where  $\eta(t)$  is the time acceptance in a given experimental setting. Thus, the  
<sup>1479</sup> acceptance is crucial to model in order to correctly estimate the impact of kaon  
<sup>1480</sup>  $CP$ -violation effects on a given measurement.

<sup>1481</sup> Considering BPGBSZ measurements, the main effect of neutral kaon  $CP$   
<sup>1482</sup> violation is a breakdown of the fundamental Dalitz-plot symmetry that is exploited  
<sup>1483</sup> in the derivation of the bin yield equations. Extending the amplitude definition  
<sup>1484</sup> of Eq. (2.22) to include  $K_L^0$  decays

$$A_{S(L)}^{(\bar{D})}(s_-, s_+) = A(\bar{D}^0 \rightarrow K_{S(L)}^0 \pi^+ \pi^-), \quad (4.20)$$

<sup>1485</sup> the authors point out that  $CP$ -violation in the  $K_S^0$  system means that the relation  
<sup>1486</sup>  $A_S^{(\bar{D})}(s_{+-}) = A_S^{(D)}(s_{+-})$  is not exactly true; and in addition, there is now a  
<sup>1487</sup> dependence on  $A_L^{(D)}(s_{+-})$  which satisfies a different approximate symmetry, namely  
<sup>1488</sup>  $A_L^{(\bar{D})}(s_{+-}) \simeq -A_L^{(D)}(s_{+-})$ . Grossman and Savastio describe these symmetry breaking  
<sup>1489</sup> effects in detail, but do not explicitly derive the corrections to the yield equations  
<sup>1490</sup> of Chapter 2, nor try to quantify the potential bias on  $\gamma$  in a measurement based on  
<sup>1491</sup> the binned yields. Instead, they derive expressions for the bias in a measurement  
<sup>1492</sup> obtained from phase-space integrated  $CP$  asymmetries. This is done for both  
<sup>1493</sup> GLW measurements that use  $D \rightarrow K_S^0 X$  final states and for the  $D \rightarrow K_S^0 h^+ h^-$   
<sup>1494</sup> final states; however, for their quantitative estimate of  $\Delta\gamma$  the authors make an  
<sup>1495</sup> approximation that corresponds to assuming that the  $D \rightarrow K_S^0 h^+ h^-$  final state  
<sup>1496</sup> is a  $CP$  eigenstate, making the two results identical. The authors find that in  
<sup>1497</sup> this case, assuming a uniform experimental acceptance for all kaon decay times,  
<sup>1498</sup> the asymmetry has the form<sup>1</sup>

$$A = \frac{2r_B \sin \gamma \sin \delta_B + 2\text{Re}[\epsilon]}{1 + r_B^2 - 2r_B \cos \gamma \cos \delta_B}, \quad (4.21)$$

<sup>1499</sup> If a measured value of  $A$  is interpreted to obtain  $\gamma$  without taking the  $\epsilon$  term  
<sup>1500</sup> into account, it leads to a bias of

$$\Delta\gamma = -\frac{\text{Re}[\epsilon]}{r_B \cos \gamma \sin \delta_B} + O(|\epsilon|). \quad (4.22)$$

---

<sup>1</sup>In fact the expression in Eq. (4.21) is missing a term, as will be clear when an analogous expression is derived in detail in Section 4.2.3.

1501 The scaling  $\Delta\gamma \sim \mathcal{O}(r_B/|\epsilon|)$  is the main result of the analysis by Grossman and  
1502 Savastio. For  $B^\pm \rightarrow DK^\pm$  decays, where  $r_B^{DK^\pm} \simeq 0.1$  this suggests a bias at the  
1503 percent level, which is negligible compared to current experimental uncertainties.  
1504 However, in the  $B^\pm \rightarrow D\pi^\pm$  case, where  $r_B^{D\pi^\pm} \simeq 0.005$  [50], their result suggests  
1505 relative biases that are potentially of  $\mathcal{O}(1)$ .

1506 The conclusions are lacking on two accounts, however. Firstly, as made clear in  
1507 Section 2.3.5, the  $K_S^0\pi^+\pi^-$  and  $K_S^0K^+K^-$  states are *far from*  $CP$  eigenstates. From  
1508 the asymmetry expression in that section, it is clear that the bias in a determination  
1509 of  $\gamma$  based on phase-space asymmetries will in fact scale as

$$\Delta\gamma \sim \mathcal{O}\left(\frac{|\epsilon|}{(2\mathcal{F}_+ - 1)r_B}\right), \quad (4.23)$$

1510 which suggests that Grossman and Savastio severely *underestimated* the potential  
1511 impact. This is described in detail in Section 4.2.3. More importantly, the analysis of  
1512 the phase-space integrated asymmetry is in fact *irrelevant* to BPGGSZ measurements  
1513 as they are currently performed: as described in Section 2.3.5 the information from  
1514 the global asymmetry is completely discarded. Therefore it is necessary to analyse  
1515 the effects of kaon  $CP$ -violation on a full, binned analysis of  $D \rightarrow K_S^0h^+h^-$  decays,  
1516 which is done in detail in the following sections. While the aim is to extend  
1517 the analysis if Grossman and Savastio, the treatment in the following sections is  
1518 completely independent of that in Ref. [41]; instead taking inspiration from the  
1519 discussion of  $D^0 \rightarrow K_S^0\pi^+\pi^-$  and  $D^0 \rightarrow K_S^0\pi^+\pi^-$  decay amplitudes in Ref. [74].

## 1520 4.2 Impact on BPGGSZ measurements of $\gamma$ : 1521 principles

1522 The analysis of the impact on BPGGSZ measurements is carried out in two stages.  
1523 This section treats the leading order effects analytically, and derives the overall  
1524 order of magnitude of the expected bias in a general setting. Then Section 4.3  
1525 presents a detailed numerical study of the expected effect in measurements with  
1526 the LHCb and Belle II experiments specifically, because these will be crucial to  
1527 constrain  $\gamma$  during the coming decade [40, 133].

### 1528 4.2.1 Modified symmetry relations

1529 In order to derive the corrections to the asymmetry relation  $A_S^D(s_{-+}) \simeq A_S^{\bar{D}}(s_{+-})$ ,  
1530 it is beneficial to express  $A_{S(L)}^D$  in terms of the amplitudes

$$A_{1/2}^{(\bar{D})} = A(\bar{D}^0 \rightarrow K_{1/2}^0\pi^+\pi^-), \quad (4.24)$$

because these amplitudes satisfy the exact symmetries  $A_1^D(s_{+-}) = A_1^{\bar{D}}(s_{+-})$  and  $A_2^D(s_{+-}) = -A_2^{\bar{D}}(s_{+-})$ . This approach is different to that of Grossman and Savastio, but the final results are equivalent. After the decay of a  $D^0$  meson to a neutral kaon, the kaon state is

$$\begin{aligned}\psi^0 &= A_1^D|K_1\rangle + A_2^D|K_2\rangle \\ &= N \left[ (A_1^D - \epsilon A_2^D)|K_S^0\rangle + (A_2^D - \epsilon A_1^D)|K_L^0\rangle \right],\end{aligned}\quad (4.25)$$

with the normalisation constant  $N = \sqrt{1 + |\epsilon|^2}/(1 - \epsilon^2)$ . Thus it can be seen that

$$\begin{aligned}A_S^D(s_{+-}) &= N \left[ (A_1^D(s_{+-}) - \epsilon A_2^D(s_{+-})) \right], \\ A_L^D(s_{+-}) &= N \left[ (A_2^D(s_{+-}) - \epsilon A_1^D(s_{+-})) \right],\end{aligned}\quad (4.26)$$

with an analogous expression for the  $\bar{D}^0$  decay amplitudes. Therefore, the generalised relations between the  $D^0$  and  $\bar{D}^0$  amplitudes are

$$\begin{aligned}A_S^{\bar{D}}(s_{+-}) &= N[A_1^{\bar{D}}(s_{+-}) - \epsilon A_2^{\bar{D}}(s_{+-})] \\ &= N[A_1^D(s_{+-}) + \epsilon A_2^D(s_{+-})] = A_S^D(s_{+-}) + 2N\epsilon A_2^D(s_{+-}), \\ A_L^{\bar{D}}(s_{+-}) &= N[A_2^{\bar{D}}(s_{+-}) - \epsilon A_1^{\bar{D}}(s_{+-})] \\ &= -N[A_2^D(s_{+-}) + \epsilon A_1^D(s_{+-})] = -A_L^D(s_{+-}) - 2N\epsilon A_1^D(s_{+-}).\end{aligned}\quad (4.27)$$

### 4.2.2 Relationship between the $K_S^0$ and $K_L^0$ amplitudes

The decay amplitude  $A(D^0 \rightarrow K_S^0 \pi^+ \pi^-)$  has been carefully studied, and a number of amplitude models have been published [55, 62–64, 66]. No models have been published for  $D^0 \rightarrow K_L^0 \pi^+ \pi^-$  decays. However, following an approach laid out by the CLEO collaboration [74], the two amplitudes can be related. Again, this is most easily done by relating the  $A_1^D(s_{+-})$  and  $A_2^D(s_{+-})$  amplitudes. In the isobar formalism, the decay amplitude  $A(D^0 \rightarrow K_1 \pi^+ \pi^-)$  is expressed as a non-resonant constant amplitude plus a sum of resonances

$$A(D^0 \rightarrow K_1 \pi^+ \pi^-) = k_{NR} + \sum_{CF} k_i R^i(s_{K\pi^-}) + \sum_{DCS} k_j R^j(s_{K\pi^+}) + \sum_{R_{\pi\pi}} k_k R^k(s_{\pi^+\pi^-}).\quad (4.28)$$

The resonances are split into Cabibbo-favoured (CF)  $K^{*-}$  resonances, doubly Cabibbo-suppressed (DCS)  $K^{*+}$  resonances and  $\pi\pi$  resonances.<sup>2</sup> The CF resonances

---

<sup>2</sup>In modern models, the  $\pi\pi$  and  $K\pi$   $S$ -wave components are modelled via the  $K$ -matrix formalism and LASS parametrisations, respectively, instead of sums of individual resonances [55]. This does not alter the arguments below, as the  $R$  functions of Eq. (4.28) can equally well represent such terms.

couple to the  $\bar{K}^0$  component of  $K_1 (\propto K^0 + \bar{K}^0)$ , and therefore the corresponding  $k_i$  in the  $K_2 (\propto K^0 - \bar{K}^0)$  amplitude will have a relative minus sign. The DCS resonances couple to the  $K^0$  component of  $K_1$ , and so the corresponding  $k_j$  in the  $K_2$  amplitude will have a relative plus sign. For the  $h^+h^-$  resonances, there will be a coupling to both the  $K^0$  and  $\bar{K}^0$  components, however the coupling to the  $K^0$  component is expected to be suppressed with a Cabibbo suppression factor  $r_k e^{i\delta_k}$ , where  $r_k \simeq \tan^2 \theta_C \simeq 0.05$  is determined by the Cabibbo angle  $\theta_C$  and  $\delta_k$  can take any value. Therefore, the  $k_k$  for these resonances have a relative  $-(1 - 2r_k e^{i\delta_k})$  factor in the  $K_2$  amplitude. The same effect leads to the differences in decay rates between  $D^0 \rightarrow K_S^0 \pi^0$  and  $D^0 \rightarrow K_L^0 \pi^0$  decays [134, 135]. Thus, given a model of the form in Eq. (4.28), a model for the  $A(D^0 \rightarrow K_2 \pi^+ \pi^-)$  amplitude will have the form

$$A(D^0 \rightarrow K_2 \pi^+ \pi^-) = k_{NR} + \sum_{CF} (-k_i) R^i(s_{K\pi^-}) + \sum_{DCS} (+k_j) R^j(s_{K\pi^+}) + \sum_{R_{\pi\pi}} (-(1 - 2r_k e^{i\delta_k}) k_k) R^k(s_{\pi^+\pi^-}). \quad (4.29)$$

An important consequence of these substitution rules is that

$$A_2^D(s_{+-}) = -A_1^D(s_{+-}) + r_A \Delta A(s_{+-}), \quad (4.30)$$

where  $r_A \simeq \tan^2 \theta_C$  and  $\Delta A(s_{+-}) \sim A_1^D(s_{+-})$  are of the same order of magnitude (at least when averaged over the bins used in  $\gamma$  measurements). This relation is sufficient to make the qualitative arguments of this section, while the full set of substitution rules above are used in the quantitative studies of Section 4.3.

### 4.2.3 Modification of the BPGBSZ yield equations

With suitable models to calculate  $A_{S(L)}^{\bar{D}}$  (or  $A_{1/2}^{\bar{D}}$ ) and knowledge of  $\Delta\chi$  for the materials relevant to an experimental setting, the relations derived in the preceding sections can be employed to calculate the expected phase-space bin yields,  $N_i^\pm$ , including the effects of kaon  $CP$  violation and material interaction. The decay rates have additional terms compared to those in Eq. (2.25), because the  $K_L^0$  contribution must be taken into account

$$d\Gamma(t, s_{+-}) \propto |\psi_S(t, s_{+-}) + \epsilon\psi_L(t, s_{+-})|^2, \quad (4.31)$$

where the time-dependence of  $\psi_{S/L}(t, s_{+-})$  is governed by Eq. (4.16), and the phase-space dependence is included in the state component, by defining  $\psi_{S/L}^0$  in terms of  $A_{S(L)}^{\bar{D}}(s_{+-})$ . For example, for the case of a  $B^- \rightarrow DK^-$  decay, the definition is

$$\begin{aligned} \psi_{S/L}^{0,B^-}(s_{+-}) &= A_S^D(s_{+-}) + r_B e^{i(\delta_B - \gamma)} A_S^{\bar{D}}(s_{+-}) \\ &= A_1^D(s_{+-}) - \epsilon A_2^D(s_{+-}) + r_B e^{i(\delta_B - \gamma)} (A_1^{\bar{D}}(s_{+-}) - \epsilon A_2^{\bar{D}}(s_{+-})) \\ &= A_1^D(s_{+-}) - \epsilon A_2^D(s_{+-}) + r_B e^{i(\delta_B - \gamma)} (A_1^D(s_{+-}) + \epsilon A_2^D(s_{+-})). \end{aligned} \quad (4.32)$$

1574 It is useful to look at the corrections to the BPGBSZ yield expressions in Eq. (2.27)  
 1575 to lowest order in  $\epsilon$  and  $r_\chi = \frac{1}{2} \frac{\Delta\chi}{\Delta\lambda}$ , the dimensionless parameter governing material  
 1576 interactions. For LHCb and Belle II the average  $|r_\chi| \simeq 10^{-3}$ , as detailed in the  
 1577 Section 4.3. To first order in  $r_\chi$ , the time-dependent kaon states within a material,  
 1578 given in Eq. (4.16), simplify to [132]

$$\begin{aligned}\psi_S(t, s_{+-}) &= e^{-\frac{i}{2}(x+\bar{x})t} e^{-i\lambda_{ST}} (\psi_S^0(s_{+-}) - r_\chi (1 - e^{-i\Delta\lambda t}) \psi_L^0(s_{+-})) , \\ \psi_L(t, s_{+-}) &= e^{-\frac{i}{2}(x+\bar{x})t} e^{-i\lambda_{LT}} (\psi_L^0(s_{+-}) + r_\chi (1 - e^{+i\Delta\lambda t}) \psi_S^0(s_{+-})) .\end{aligned}\quad (4.33)$$

1579 By inserting these expressions into Eq. (4.31) and employing the definition in  
 1580 Eq. (4.32) (and a similar definition for  $B^+$  decays), the binned yields can be  
 1581 calculated by an integration over time and phase space. In the remainder of this  
 1582 section, it is assumed that the experimental time acceptance is  $\eta(t) = 1$  for all times  
 1583 and that  $r_\chi$  is constant at all times; more realistic assumptions are introduced in  
 1584 Section 4.3. In this case, the binned yields are given by the expression

$$\begin{aligned}N_i^- &= h_B^{-'} \left( \hat{K}_{+i} + r_B^2 \hat{K}_{-i} + 2\sqrt{\hat{K}_{+i} \hat{K}_{-i}} (x_- \hat{c}_i + y_- \hat{s}_i) + O(r\epsilon) \right) , \\ N_i^+ &= h_B^{+'} \left( \hat{K}_{-i} + r_B^2 \hat{K}_{+i} + 2\sqrt{\hat{K}_{+i} \hat{K}_{-i}} (x_+ \hat{c}_i - y_+ \hat{s}_i) + O(r\epsilon) \right) ,\end{aligned}\quad (4.34)$$

1585 where a number of new parameters have been defined, and where  $O(r\epsilon)$  denotes terms  
 1586 of  $O(r_A\epsilon)$ ,  $O(r_B\epsilon)$ ,  $O(r_A r_\chi)$ , and  $O(r_B r_\chi)$ . Since  $r_B \sim r_A \sim 10^{-1}$  (in  $B^\pm \rightarrow DK^\pm$   
 1587 decays) and  $r_\chi \sim \epsilon \sim 10^{-3}$ , these terms are all of the same order of magnitude.

1588 The new normalisation constants  $h_B^{\pm'} = h_B^\pm (1 + |\epsilon + r_\chi|^2 \frac{\Gamma_S}{\Gamma_L} \mp \Delta h)$  are de-  
 1589 fined in terms of

$$\Delta h = 2\text{Re}[\epsilon + r_\chi] - 4 \frac{\Gamma_S}{\Gamma_L + \Gamma_S} \frac{\text{Re}[\epsilon + r_\chi] + \mu \text{Im}[\epsilon + r_\chi]}{1 + \mu^2}, \quad \mu = 2 \frac{m_L - m_S}{\Gamma_L + \Gamma_S}. \quad (4.35)$$

1590 The  $\hat{K}_i$  parameters are defined to be

$$\hat{K}_i = \frac{1}{1 + |\epsilon + r_\chi|^2 \frac{\Gamma_S}{\Gamma_L}} \left( K_i^{(1)} + |\epsilon + r_\chi|^2 \frac{\Gamma_S}{\Gamma_L} K_i^{(2)} \right), \quad (4.36)$$

1591 in which the  $K_i^{(1/2)}$  parameters are phase-space integrals, defined as in Eq. (2.29)  
 1592 but for  $A_{1/2}^D$ . To lowest order, the  $\hat{K}_i$  correspond to the fractional  $D^0$  decay yield  
 1593 in each bin, as obtained in a measurement that averages  $D^0$  and  $\bar{D}^0$  decays, and  
 1594 assumes the  $A_S^{\bar{D}}(s_{-+}) = A_S^D(s_{+-})$  symmetry to be exact:

$$K_i^{\text{meas}} \equiv \frac{N_i^D + N_{-i}^{\bar{D}}}{\sum_j N_j^D + N_j^{\bar{D}}} = \hat{K}_i + \mathcal{O}(r\epsilon). \quad (4.37)$$

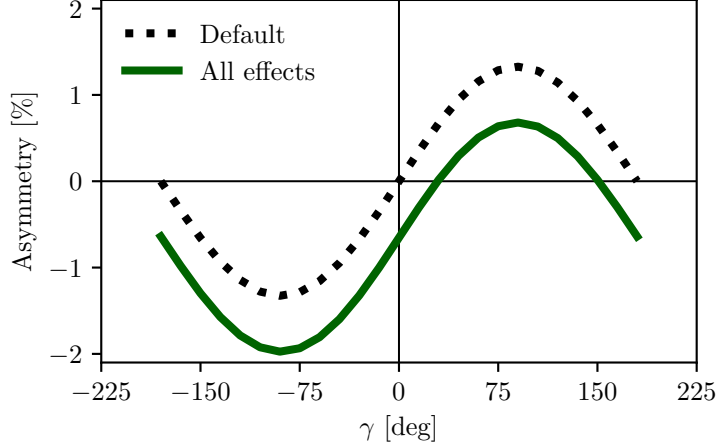


**Figure 4.1:** The asymmetry  $A_{\text{total}}$  as a function of  $\gamma$  calculated to  $O(\epsilon)$  using Eq. (4.38). The calculation is made using for (black dotted line) the default case where  $\Delta h = 0$  and (green) including neutral kaon  $CP$ -violation and material interaction with  $r_\chi = \epsilon$ .

1595 Here,  $N_i^D$  ( $N_i^{\bar{D}}$ ) is the expected yield of flavour tagged  $D^0$  ( $\bar{D}^0$ ) mesons into bin  
1596  $i$  of the  $D$  decay phase-space.

1597 In similar fashion, the parameters  $(\hat{c}_i, \hat{s}_i)$  have been introduced to denote the  
1598 *measured* average strong-phases, which are expected to differ from  $(c_i, s_i)$  at  $O(\epsilon)$ ,  
1599 since neutral kaon  $CP$  violation is not taken into account in the measurements  
1600 by CLEO. Thus, any corrections arising if  $(\hat{c}_i, \hat{s}_i)$  and  $(c_i, s_i)$  are substituted in  
1601 Eq. (4.34) will appear in the  $O(r_B \epsilon)$  terms.

1602 Two observations can be made from the expression in (4.34). The first is that  
1603 the phase-space *distribution* is only changed at  $O(r \epsilon)$  compared to the expression in  
1604 Eq. (2.27), if the measured  $\hat{K}_i$  are used in the experimental analysis. This equally  
1605 true whether the  $K_i$  are fitted in the signal channel along with  $x_\pm$  and  $y_\pm$ , as is the  
1606 case in the measurement presented in the thesis, or if they are obtained in a control  
1607 channel with flavour tagged  $D$  decays, according to Eq. (4.37). As the  $D^0 - \bar{D}^0$   
1608 interference term that provides sensitivity to  $\gamma$  enters at order  $O(r_B)$ , the impact on  
1609  $\gamma$  measurements can be expected to be  $\Delta\gamma/\gamma \sim O(r \epsilon / r_B)$ . For  $B \rightarrow DK$  analyses,  
1610 where  $r_B \simeq 0.1$ , this is at the permille level, so the induced  $\Delta\gamma$  bias can be expected  
1611 to be smaller than  $1^\circ$ . Even in the case of  $B^\pm \rightarrow D\pi^\pm$  decays, this suggests biases  
1612 that are maximally a few percent. This is the main result of the chapter, because it  
1613 means that the effect of neutral kaon  $CP$  violation and material interaction is small  
1614 compared to the precision of the measurement that is the main subject of the thesis.

1615 The second observation relates to potential future measurements of  $\gamma$ , which  
1616 may also include sensitivity from the total, phase-space-integrated yield asymmetry

$$A_{\text{total}} = \frac{N^- - N^+}{N^- + N^+} = \frac{2(2\mathcal{F}_+ - 1)r_B \sin \delta_B \sin \gamma + \Delta h}{1 + r_B^2 + 2(2\mathcal{F}_+ - 1)r_B \cos \delta_B \cos \gamma} + O(r \epsilon), \quad (4.38)$$

where the definition of  $\mathcal{F}_+$  from Section 2.3.5 has been employed. In the limit  $r_B \rightarrow 0$  the expression agrees with the result for the analogous asymmetry in  $D^\pm \rightarrow \pi^\pm K_S^0$  decays in Ref. [136], evaluated to  $O(\epsilon)$  for an infinite and uniform time-acceptance. As hinted at above, the fact that  $\mathcal{F}_+ \simeq 0.5$  means that the asymmetry due to  $\gamma$  being non-zero is not  $\mathcal{O}(r_B)$ , but of approximately the same order of magnitude as the asymmetry due to  $CP$  violation in the neutral kaon sector, governed by  $\Delta h$ . This is illustrated in Fig. 4.1, where the expression in Eq. (4.38) is plotted in the default case where  $\Delta h = 0$ , using the model in Ref. [55] to calculate  $K_i$  and  $c_i$ , as well as including neutral kaon  $CP$  violation and material interaction effects, calculated using  $r_\chi = \epsilon$ , with  $\epsilon$  taking the value in Eq. (4.12). The asymmetry changes significantly when including the latter effects. Therefore, measurements based only on the global asymmetry will suffer relative biases of tens of degrees, not a few degrees, if neutral kaon  $CP$  violation and material interaction is not taken into account.

### 4.3 Impact on BPGBSZ measurements of $\gamma$ : LHCb and Belle II measurements

The previous section has established that the bias due to neutral kaon  $CP$  violation and material interaction is at the sub-percent level for measurements based on  $B^\pm \rightarrow DK^\pm$  decays, and just a few percent in  $B^\pm \rightarrow D\pi^\pm$  decays. Thus, the effects only contribute a manageable systematic uncertainty in the measurement that is the subject of the thesis. However, the expected precision on  $\gamma$  measurements will increase significantly in the coming decade, as both the LHCb [40] and Belle II [133] collaborations expect to make BPGBSZ measurements that measure  $\gamma$  with a precision of 1–3°. Therefore a deeper understanding of the expected bias for these specific experiments is important.

This section details a study, where the equations of the previous section are evaluated numerically to all orders, and care is taken to realistically model the experiment specific conditions. The scope of the original analysis, published in Ref. [2], was a stand-alone paper that covers both LHCb and Belle II, and which therefore does not rely on full detector simulation. Instead the following approaches are taken to model the necessary input

- the experimental time-acceptance is modelled based on the detector geometry and typical neutral kaon momentum spectrum
- the material interaction is included, using the material budget information available in the technical design reports on each experiment

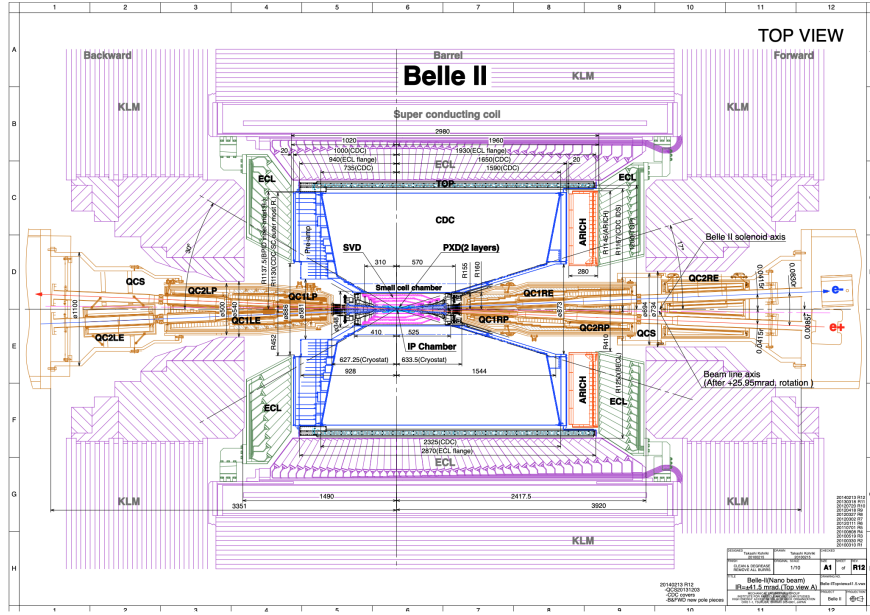


**Figure 4.2:** Schematic of the Belle II detector, reproduced from Ref. [133].

- both the time-acceptance and material interaction depends on the neutral kaon momentum, for which realistic distributions are estimated using the RapidSim simulation package [127].

Each input is described in detail in the following sections. The study has been repeated to assign a systematic uncertainty to the LHCb measurement in Chapter 5, with slight adjustments to match the exact fit setup and with the inputs above extracted from full LHCb simulation. This is described further in Section 4.3.7.

### 4.3.1 Detector geometries

The LHCb geometry and sub detectors are described in details in Chapter 3. In the LHCb measurement discussed in Chapter 5, the  $K_S^0$  mesons are reconstructed in the  $\pi^+\pi^-$  final state and two distinct categories of decay are considered, depending on where in the detector the  $K_S^0$  decay occurs. The categories have very different decay-time acceptance, and therefore two scenarios are considered for LHCb: one in which the decay products of the  $K_S^0$  leave reconstructed tracks in both the silicon vertex detector and downstream tracking detectors (denoted *long-long* or LL), and one in which the decay products of the  $K_S^0$  only leave tracks in the downstream tracking detectors (denoted *down-down* or DD).

The Belle II detector is a general purpose spectrometer, built to collect data from asymmetric  $e^+e^-$  collisions provided by the SuperKEKB accelerator in Japan [137]. A schematic of the detector is shown in Fig. 4.2. The relevant sub

detectors for the present study are the tracking detectors: a central silicon vertex detector, comprised of a total of six layers within 140 mm of the beam, and a large volume drift chamber with 56 wire layers, extending to a radius of 1130 mm [133]. A single scenario is considered for Belle II, because essentially all the  $K_S^0$  mesons produced in signal decays in Belle II decay within the tracking volume, with more than 90 % decaying in the vertex detector according to the studies described below. Thus, three scenarios are considered in total: LL LHCb, DD LHCb, and Belle II.

### 4.3.2 Kaon momentum distributions

The neutral kaon momentum distributions are obtained using **RapidSim** [127], a simple tool to generate MC samples. **RapidSim** has an inbuilt capability to generate decays of  $B$  mesons with the kinematic distribution found in LHCb collisions and falling in the LHCb acceptance. However, the distributions need to be reweighted to take the kaon-decay-time acceptance into account. After being reweighted, the **RapidSim** momentum spectra are reasonably close to those found in full LHCb simulation samples of  $B^\pm \rightarrow D(\rightarrow K_S^0\pi^+\pi^-)K^\pm$  decays, as seen in Fig. 4.3

At Belle II, the signal  $B$  mesons stem from decays of  $\Upsilon(4S)$  mesons produced in asymmetric electron-positron collisions. This leads to substantially different decay kinematics in comparison to those found at LHCb. The momentum distribution in Belle II is estimated by letting **RapidSim** decay  $B$  mesons with a momentum of 1.50 GeV/ $c$  along the  $z$ -axis using **RapidSim**, corresponding to the  $\gamma\beta = 0.28$  boost of the centre-of-mass system in Belle II when operated at the  $\Upsilon(4S)$  resonance [133]. A perfect  $4\pi$  angular acceptance is assumed. It is not necessary to reweigh the Belle II momentum spectrum to account for the kaon-decay-time acceptance because all produced  $K_S^0$  mesons decay in the tracking volume.

The resulting momentum distributions for the three types of sample are shown in Fig. 4.4.

### 4.3.3 Experimental time acceptance

In order to model the experimental time acceptance, the time-dependent decay rates are only integrated over a finite time interval  $(\tau_1, \tau_2)$ . The intervals are defined for each of the three experimental categories, by requiring that a neutral kaon, if produced at  $x = y = z = 0$  with momentum  $p = (p_T, p_z)$ , decays within the relevant part of the corresponding detector. For the LL LHCb category, it is required that the kaon decays before reaching  $z_{max} = 280$  mm, corresponding to a decay where the decay products traverse at least 3 VELO segments (ignoring

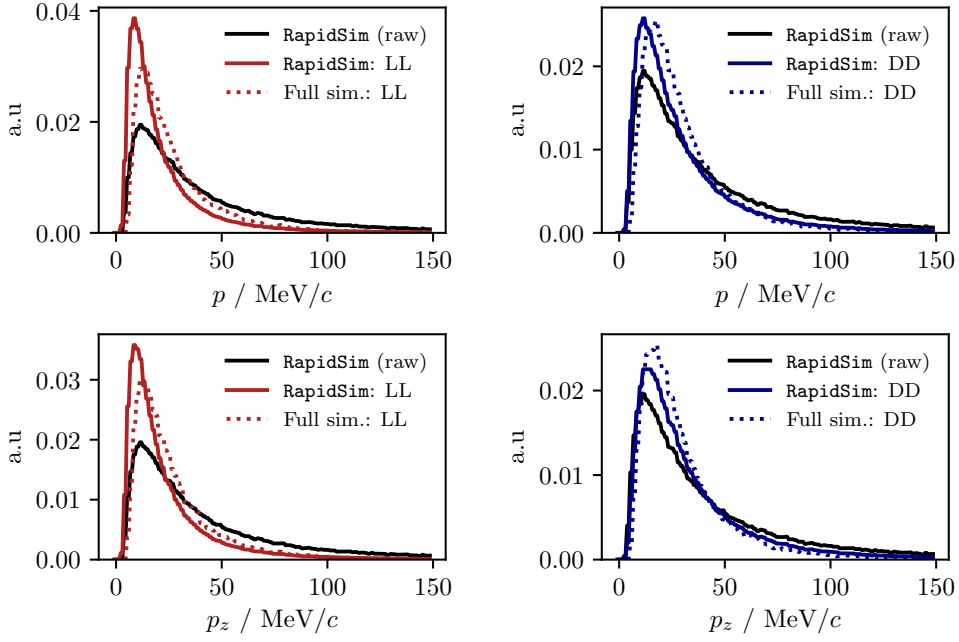


**Figure 4.3:** Momentum spectra for the  $K_S^0$  meson in LHCb, as generated using **RapidSim** (black lines) directly, as well as reweighed to match decay time acceptance in the (red) LL and (blue) DD data categories of LHCb. The LHCb spectra are compared with the spectra in fully simulated signal decays, for both the (dotted red lines) LL and (dotted blue lines) DD data categories.

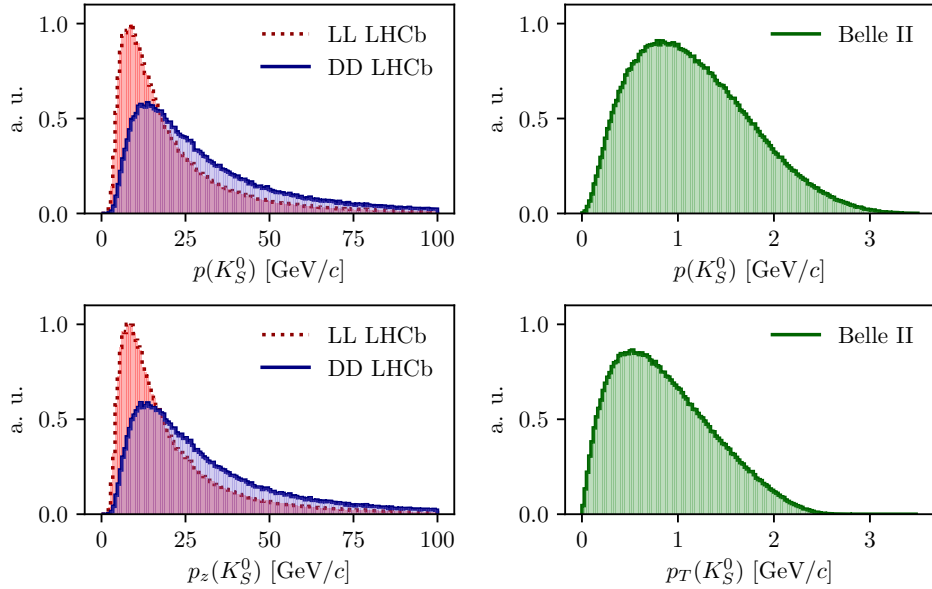


**Figure 4.4:** Momentum distributions for the LHCb (red dotted line) LL and (blue) DD categories, as well as (green) Belle II, obtained using **RapidSim**.

1705 a number of widely spaced VELO segments placed at a distance of up to  $z =$   
 1706 750 mm from the interaction point) [89]. For the DD LHCb category a decay at  
 1707  $z \in [280, 2350]$  mm is required, corresponding to decay between the LL cut-off and  
 1708 the first downstream tracking station [138]. The time acceptance has a significant  
 1709 impact for the LHCb categories, where some 20 % of the kaons escape the tracking  
 1710 stations completely before decaying.

1711 For Belle II, it is assumed that the  $K_S^0$  reconstruction is similar to the Belle  $K_S^0$   
 1712 reconstruction, which is based on a neural network and reconstructs  $K_S^0$  decays  
 1713 for which the decay product leave tracks in both the drift chamber and silicon  
 1714 vertex detectors, as well as decays that leave tracks in the drift chamber only [139,  
 1715 140]. Therefore, the  $K_S^0$  decay is required to be within  $r_{max} = 1130$  mm of the  
 1716 beam axis, corresponding to a decay within the outer radius of the drift-chamber.  
 1717 In practice, most of the kaons already decay inside the silicon vertex detector,  
 1718 and requiring a decay before the outer radius of the drift chamber is essentially  
 1719 equivalent to having no time cut-off.

#### 1720 4.3.4 Detector material budget

1721 The effect of the material interaction is governed by parameter  $\Delta\chi$  of Eq. (4.17). The  
 1722 parameter varies along a given kaon path, as the kaon intersects detector components  
 1723 made of different materials. In these studies, the calculations are simplified by  
 1724 using a single average material parameter for each experimental scenario. The  
 1725 average material parameters can be estimated for a given experimental scenario by  
 1726 considering the type and length of material traversed by a kaon in the relevant sub-  
 1727 detector(s). The average value is estimated, by exploiting that  $\Delta\chi$  is related to the  
 1728 forward scattering amplitude  $f$  ( $\bar{f}$ ) of  $K^0$  ( $\bar{K}^0$ ) mesons in a given material [131, 132]

$$\Delta\chi = -\frac{2\pi\mathcal{N}}{m_K}(f - \bar{f}) = -\frac{2\pi(N_A\rho/A)}{m_K}(f - \bar{f}), \quad (4.39)$$

1729 where  $\mathcal{N} = N_A\rho/A$  is the scattering centre density of the material,  $m_K$  is the mass  
 1730 of the kaon state,  $A$  and  $\rho$  are the nucleon number and density of the material,  
 1731 and  $N_A$  is Avogadro's number. Measurements made for a range of nuclei [141]  
 1732 show that in the momentum range  $p_K \in [20, 140]$  GeV/ $c$

$$\left| \frac{f - \bar{f}}{p_K} \right| = 2.23 \frac{A^{0.758}}{p_K^{0.614}(\text{GeV}/c)} \text{ mb}, \quad \arg[f - \bar{f}] = -\frac{\pi}{2} (2 - 0.614), \quad (4.40)$$

1733 where the phase of  $\Delta f$  is determined via a phase-power relation [142]. In the  
 1734 numerical studies presented here, Eq. (4.40) is also used for the low momentum

neutral kaons in the Belle II calculations, as a more detailed modelling of the low momentum  $\Delta\chi$  based on Ref. [143] is found to yield very similar results. The scattering centre density  $\mathcal{N}$  is approximated as being constant, equal to the average density along a neutral kaon path due to its intersection with different detector segments. This average is estimated using the simplifying assumption that the total detector material budget is due to silicon. In practice,  $\mathcal{N} = N_A \rho / A$  is calculated using  $A = 28$  and  $\rho = f^{\text{Si}} \rho^{\text{Si}}$ , where  $f^{\text{Si}} < 1$  is the average fraction of a neutral kaon path length that is inside detector material, estimated via the known dimensions of the detector, the average nuclear interaction length seen by a track traversing it cf. the technical design reports [89, 95], and the nuclear interaction length of silicon  $\lambda_I^{\text{Si}} = 465.2 \text{ mm}$  [31]. The average value of  $r_\chi = \frac{1}{2} \frac{\Delta\chi}{\Delta\lambda}$ , which governs the size of the matter regeneration effect, can be calculated for the three considered experimental scenarios and satisfy  $|r_\chi^{\text{LL}}| = 2.7 \times 10^{-3}$ ,  $|r_\chi^{\text{DD}}| = 2.2 \times 10^{-3}$ , and  $|r_\chi^{\text{Belle II}}| = 1.0 \times 10^{-3}$ .

The neutral kaon tracks in LHCb generally pass through somewhere between zero (for a significant amount of the LL tracks) and a hundred (for some DD tracks) distinct detector segments. Therefore it is worth examining the degree to which using a single average  $\Delta\chi$  value, obtained following the procedure outlined above, provides a reasonable description of the average material interaction. This can be done using full LHCb simulation, where the kaon state for a simulated track can be evaluated at all times, by applying Eq. (4.16) iteratively for each detector segment the track traverses, using a  $\Delta\chi$  value appropriate for that segment. This is done in Fig. 4.5 for a simple observable: the yield asymmetry

$$A_{K^0} = \frac{|\psi_K^0(t)|^2 - |\psi_{\bar{K}^0}(t)|^2}{|\psi_K^0(t)|^2 + |\psi_{\bar{K}^0}(t)|^2}, \quad (4.41)$$

where  $\psi_K^0(t)$  ( $\psi_{\bar{K}^0}(t)$ ) is the amplitude for an initial  $K^0$  ( $\bar{K}^0$ ) to decay to two pions at time  $t$ . In this calculation, it is assumed that  $\epsilon = 0$  to isolate the material effect with no asymmetry contribution from the inherent  $CP$ -violation in the neutral kaon sector. While the track-by-track asymmetries are found to differ significantly depending on the exact detector segments a track intersects, the average asymmetry is seen to evolve smoothly as a function of decay time, and in reasonable agreement with the asymmetry value that is calculated using the average  $\Delta\chi$  values estimated above.

The LHCb detector is undergoing a significant upgrade prior to the start of the LHC Run 3. However, the material budget and geometry of the relevant sub-detectors will be similar to the sub-detectors used during Run 1 and 2 [144, 145]. Hence the results of this study will be valid for measurements during the upgrade phases of LHCb, even though the detector parameters presented in this section relate to the original LHCb detector.

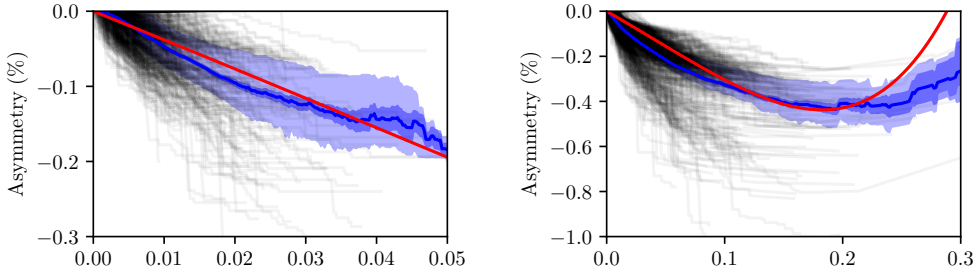


**Figure 4.5:** The asymmetry in Eq. (4.41) as a function of time for  $K_S^0$  tracks in samples of simulated (left) LL and (right) DD decays, using the full LHCb simulation. The light blue area is the central 50 % quantile of all tracks, the dark blue area is the  $1\sigma$  uncertainty band on the mean. The black lines show the result for a subset of individual, randomly sampled tracks. The red lines are calculated using the average  $\Delta\chi$  values that are also used in the calculation of biases in BPGBS measurements.

### 4.3.5 Calculation procedure

The main idea in the bias study is to calculate the BPGBS bin yields including the full effect of neutral kaon  $CP$  violation and material, fit them using the default equations of Chapter 2, and thereby obtain the bias  $\Delta\gamma = \gamma - \gamma^0$  due to the kaon effects not being considered in the parameter extraction. For the purpose of Ref. [2], a simple fit setup of a single  $B^\pm \rightarrow Dh^\pm$  mode is investigated, where the  $K_i$  parameters are determined in a control channel with the relevant experimental acceptance. This setup is modified in the study used to assign a systematic uncertainty on the LHCb measurement of Chapter 5, as described in Section 4.3.7 below.

In practice, the amplitude model for  $D^0 \rightarrow K_S^0 \pi^+ \pi^-$  decays in Ref. [55] is taken to represent the  $A_1(s_{+-})$  amplitude. Then  $A_2(s_{+-})$  is obtained as described in Section 4.2.2. In terms of  $A_1$  and  $A_2$ , the amplitudes  $A_{S(L)}^{(\bar{D})}(s_{+-})$  can be expressed and related via Eqs. (4.26) and (4.27), and the full signal decay amplitudes as a function of phase-space coordinates, time, and the material interaction parameter  $\Delta\chi$  can be calculated for a given set of input parameters  $(\gamma^0, r_B^0, \delta_B^0)$ . The squared decay amplitudes are then integrated over phase space and the kaon decay times to obtain the binned signal yield.

The signal yields depend on the momentum via the time-acceptance parameters  $\tau_1$  and  $\tau_2$ , and because the material interaction parameter  $\Delta\chi$  is momentum dependent. Therefore, the yields are averaged over the  $K_S^0$  momentum distributions of LHCb and Belle II.

The parameters  $x_\pm$  and  $y_\pm$  are determined by a maximum likelihood fit to the calculated yields, after which the fit result and covariance matrix are interpreted in terms of the physics parameters  $(\gamma, r_B, \delta_B)$  using another maximum likelihood

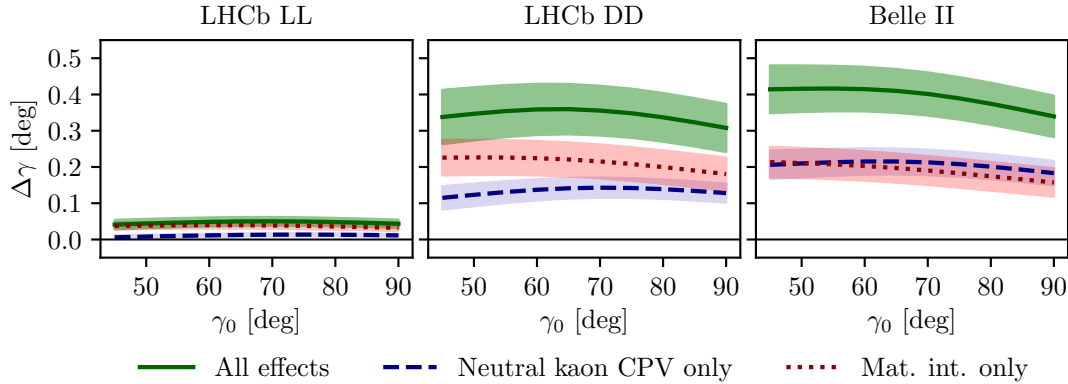


**Figure 4.6:** The bias  $\Delta\gamma$  as a function of input  $\gamma_0$  for (left) the LL LHCb category, (centre) the DD LHCb category, and (right) Belle II. The bias is calculated due to (blue, dashed line) neutral kaon  $CP$  violation alone, (red, dotted line) material interaction alone, and (green line) both effects. The shaded region shows the estimated  $1\sigma$  uncertainty band.

1795 fit [48]. In the fits, the  $K_i$  are obtained using the definition  $K_i = K_i^{\text{meas}} =$   
1796  $(N_i^D + N_{-i}^{\bar{D}})/(\sum_j N_j^D + N_{-j}^{\bar{D}})$ , in terms of the expected yields  $N_i^D$  ( $N_i^{\bar{D}}$ ) of a flavour-  
1797 tagged  $D^0$  ( $\bar{D}^0$ ) decays in bin  $i$  of the  $D$  decay phase space, calculated as described  
1798 above for  $r_B^0 = 0$ . This corresponds to experimentally measuring the  $K_i$  in a control  
1799 channel, and takes the effect of neutral kaon  $CP$  violation and material interaction  
1800 on  $K_i$  measurements into account, as well the experimental time acceptance. The  
1801  $(c_i, s_i)$  are calculated using  $A_1(s_{+-})$  and the experimental time acceptance is taken  
1802 into account in this calculation as well.

### 1803 4.3.6 Results

1804 The obtained bias  $\Delta\gamma$  is shown as a function of input  $\gamma^0$  for the various experimental  
1805 conditions in Fig. 4.6. The calculations are made using  $(r_B^0, \delta_B^0) = (0.1, 130^\circ)$ ,  
1806 approximately equal to the physics parameters relevant for  $B^\pm \rightarrow DK^\pm$  decays [27,  
1807 39]. The bias does not vary significantly with  $\gamma^0$  in the plotted range, which includes  
1808 the world average value of direct  $\gamma$  measurements as well as the values obtained in  
1809 full unitarity-triangle fits [27, 36, 39], and for all cases, the bias is found to be below  
1810  $0.5^\circ$ , corresponding to relative biases of about half a percent. Thus the biases are  
1811 of  $O(r\epsilon/r_B)$  as expected, given the arguments of Section 4.2.3. The contributions  
1812 from the individual  $K_S^0$  CPV and material interaction effects are also shown. It  
1813 is seen that the neutral kaon  $CP$  violation and material interaction effects leads  
1814 to approximately equal biases in all three cases.

1815 Given the decay-time acceptance and momentum distribution for each experimen-  
1816 tal category, the mean life time,  $\langle\tau\rangle$ , of the reconstructed kaons can be calculated.

In terms of the  $K_S^0$  lifetime  $\tau_{K_S^0} = (0.895 \pm 0.004) \times 10^{-11}$  s [31],  $\langle \tau_{LL} \rangle \simeq 0.1\tau_{K_S^0}$  for the LHCb LL category,  $\langle \tau_{DD} \rangle \simeq 0.8\tau_{K_S^0}$  for the LHCb DD category, and at Belle II  $\langle \tau_{Belle\,II} \rangle \simeq \tau_{K_S^0}$ . The difference in average kaon lifetime is reflected in the observed biases, which are found to be larger in the samples with longer lived kaons. The very small effect in the LL category is to be expected because the  $CP$ -violation effect due to  $K_S^0$  not being  $CP$ -even is approximately cancelled by the  $CP$ -violation effect arising from  $K_S^0 - K_L^0$  interference for kaons with decay times much smaller than  $\tau_{K_S^0}$  [136].

The uncertainty bands in Fig. 4.6 are calculated by repeating the study while varying some of the inputs. The model dependence of the predicted biases is probed by repeating the study using two other amplitude models as input for  $A_1(s_{+-})$  and  $A_2(s_{+-})$ : the model published in Ref. [66] and the model included in EVTGEN [122]. Then defining  $A_2(s_{+-})$  in terms of  $A_1(s_{+-})$ , there is an uncertainty due to the unknown  $(r_k, \delta_k)$  parameters used to describe the  $\pi\pi$  resonance terms. This uncertainty is assessed by making the study with several different random realisations of the parameter set. The studies are repeated while varying the time acceptances and material densities with  $\pm 10\%$ . There is an additional uncertainty due to the use of simulation samples generated with `RapidSim` to describe the kaon momentum distribution, in lieu of full detector simulations.

There is also an uncertainty from the use of  $(c_i, s_i)$  as calculated using  $A_1(s_{+-})$ . It is to be expected that the measured values  $(\hat{c}_i, \hat{s}_i)$  from the CLEO collaboration differ by those calculated using  $A_1^D(s_-, s_+)$  by terms of  $O(\epsilon)$  due to neutral kaon  $CP$  violation, which is not taken into account in the measurement [74]. These corrections can be calculated via a procedure analogous to the one used to estimate the corrections on measurements of  $\gamma$  in this paper. However, as these corrections are much smaller than the experimental uncertainties in the measurement, they have not been studied further.

For the purpose of this thesis, it is important to consider the bias in measurements that use  $B^\pm \rightarrow D\pi^\pm$  decays as well, and other  $B$  decay modes can also be used in BPFGSZ measurements, such as  $B^\pm \rightarrow D^*K^\pm$ ,  $B^\pm \rightarrow DK^{*\pm}$ , and  $B^0 \rightarrow DK^{*0}$ . For the purpose of the study presented here, the main difference between the decay channels is that they have different values of  $r_B$  and  $\delta_B$ . Figure 4.7 shows  $\Delta\gamma$  as a function of input  $\delta_B^0$ , for  $\gamma^0 = 75^\circ$  and three different values of  $r_B^0$ . Aside from  $r_B^0 = 0.1$ , the results are shown for  $r_B^0 = 0.005$ , which corresponds to the expectation in  $B^\pm \rightarrow D\pi^\pm$  decays [50] and  $r_B^0 = 0.25$ , which corresponds to  $B^0 \rightarrow DK^{*0}$  decays [49]. The most notable feature is that the biases are significantly larger in the  $B^\pm \rightarrow D\pi^\pm$  case. This is expected: the  $r_B^0$  dependent behaviour is governed

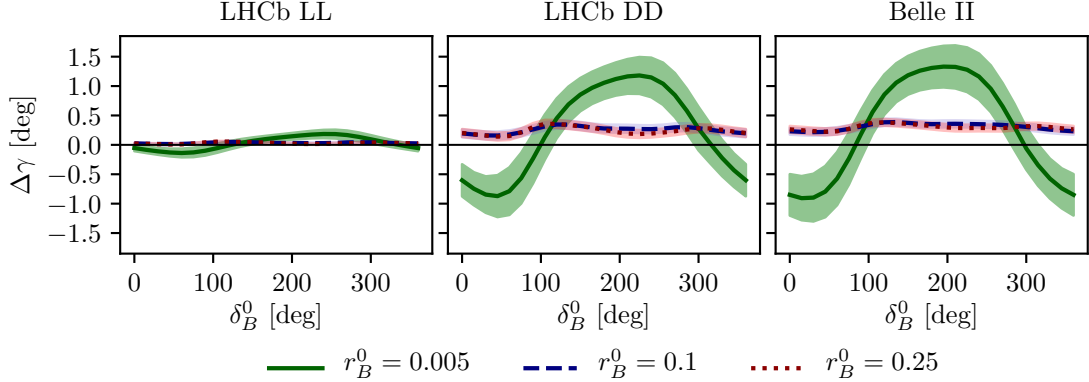


**Figure 4.7:** The bias  $\Delta\gamma$  as a function of input  $\delta_B$  for (left) the LL LHCb category, (centre) the DD LHCb category, and (right) Belle II. The bias is calculated for  $\gamma = 75^\circ$  and (green line)  $r_B = 0.005$ , (blue, dashed line)  $r_B = 0.1$ , and (red, dotted line)  $r_B = 0.25$ . The shaded region shows the estimated  $1\sigma$  uncertainty band.

1854 by the relative importance of different  $O(r\epsilon)$  correction terms to the phase-space  
1855 distribution. There are terms of both  $O(r_A\epsilon)$  and  $O(r_B\epsilon)^3$ , which lead to expected  
1856 biases of size  $O(r_A\epsilon/r_B)$  and  $O(r_B\epsilon/r_B) = O(\epsilon)$ , respectively, cf. the discussion  
1857 of Section 4.2.3. In the  $B^\pm \rightarrow D\pi^\pm$  case, the  $O(r_A\epsilon)$  correction terms dominate  
1858 because  $r_A/r_B \simeq (0.05/0.005) = 10$ . This explains the relatively large bias, as  
1859  $|r_A\epsilon/r_B^{D\pi}| \simeq 4\%$ . The bias is seen to be up to  $\pm 1.5^\circ$ , but only about  $+0.2^\circ$  with  
1860 the expected value of  $\delta_B^{D\pi} \simeq 300^\circ$  [48, 50]. These biases are *much smaller* than the  
1861 precision on  $\gamma$  that is obtainable in a  $B^\pm \rightarrow D\pi^\pm$  analysis with current experimental  
1862 yields, and do thus not pose a problem. In the  $r_B^0 = 0.1$  and  $r_B^0 = 0.25$  cases the  
1863  $O(r_B\epsilon)$  correction terms dominate, and the biases are of  $O(\epsilon)$ , independent of the  
1864  $r_B^0$  value. Therefore both cases have biases of similar size.

1865 Further, it is clear that the biases depend on  $\delta_B^0$  and that the oscillation period of  
1866 the  $\delta_B$  dependence is different between the  $r_B^0 = 0.005$  case and the  $r_B^0 \in \{0.1, 0.25\}$   
1867 cases. It is to be expected that  $\Delta\gamma$  oscillates as a function of  $\delta_B^0$ , because  $\delta_B^0$  enters  
1868 the yield equations via  $\cos(\delta_B^0 \pm \gamma)$  and  $\sin(\delta_B^0 \pm \gamma)$  terms. As explained above,  
1869 the  $O(r_A\epsilon)$  terms dominate the  $B^\pm \rightarrow D\pi^\pm$  bias, and these are independent of  
1870  $\delta_B^0$ . The  $O(r_B\epsilon)$  terms, however, are important for the bias corrections for larger  
1871  $r_B$  values, and the terms include factors of  $\cos(\delta_B^0 \pm \gamma)$  and  $\sin(\delta_B^0 \pm \gamma)$ . This  
1872 explains the different bias dependence on  $\delta_B^0$ .

1873 While the input value of  $\gamma^0 = 75^\circ$  was chosen for these studies, there is minimal  
1874 variation in the results if another value of  $\gamma^0$  in the range  $[60^\circ, 85^\circ]$  is used.

<sup>3</sup>There are similar terms of  $O(r_A r_\chi)$  and  $O(r_B r_\chi)$ , but as  $\epsilon$  and  $r_\chi$  are of the same order of magnitude, these terms can be treated completely analogously to the  $O(r_A\epsilon)$  and  $O(r_B\epsilon)$  terms, and have been left out of the discussion for brevity.

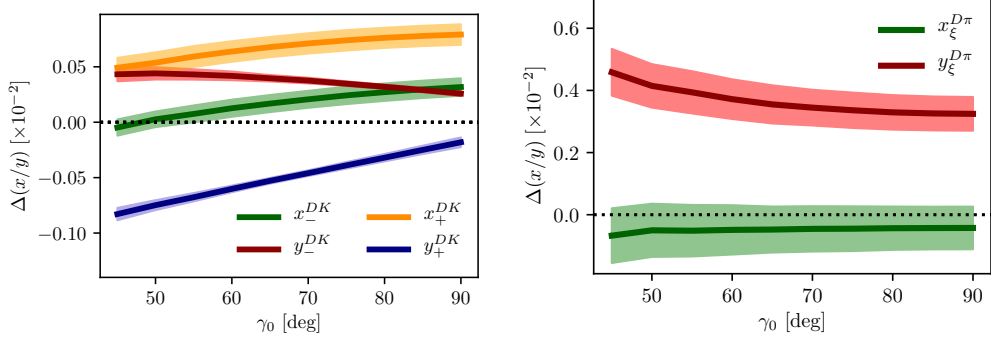


**Figure 4.8:** The bias on (left) the  $B^\pm \rightarrow DK^\pm$  and (right)  $B^\pm \rightarrow D\pi^\pm$   $CP$ -violation observables in the LHCb DD category, evaluated in bias studies with inputs based on full LHCb simulation, calculated as a function of input  $\gamma_0$ .

### 4.3.7 Coupled $B^\pm \rightarrow DK^\pm$ and $B^\pm \rightarrow D\pi^\pm$ measurements

The studies presented above have been extended on two accounts in order to assign a systematic uncertainty to the LHCb measurement presented in Chapter 5. Firstly, full LHCb simulation has been used to obtain the momentum distributions, as well as to fit a better description of the time acceptance and the reconstruction efficiency profile over the  $D$ -decay phase space. Secondly, the fit setup is modified to correspond to the experimental approach described in Section 2.4 and Chapter 5: the signal yields are calculated for both the  $B^\pm \rightarrow DK^\pm$  and  $B^\pm \rightarrow D\pi^\pm$  channels, and fitted in a combined fit to obtain  $(x_\pm^{DK}, y_\pm^{DK}, x_\xi^{D\pi}, y_\xi^{D\pi})$ , where the  $F_i$  parameters are allowed to float in the fit. The biases obtained for each observable are shown in Fig. 4.8, evaluated using the time-acceptance, momentum distribution, and material budget relevant for the DD category (since the effect in the LL category is much smaller). As will be clear in Chapter 5, these biases are all significantly smaller than the corresponding statistical uncertainties. Thus, the effects of neutral kaon  $CP$  violation and material interactions contribute a manageable systematic uncertainty in current BPGBS measurements, even if the  $B^\pm \rightarrow D\pi^\pm$  channel is promoted to a signal channel.

As the statistical uncertainty becomes comparable with the bias effects described in this chapter, the systematic uncertainty should be assigned by a more accurate study, incorporating the traversed material on a track-by-track basis in full detector simulation. Such a detailed calculations can also be used to apply a bias correction if desired.

## 1897 4.4 Concluding remarks

1898 The analysis presented in this chapter has shown the expected impact of neutral  
1899 kaon  $CP$  violation and material interaction on current BPGBSZ measurements  
1900 to be small compared to the statistical uncertainties; first by simple order-of-  
1901 magnitude estimates and then by a detailed calculation of the expected effect  
1902 in LHCb and Belle II.

1903 While the calculations were made for the case of  $D \rightarrow K_S^0\pi^+\pi^-$  decays, the  
1904 BPGBSZ approach can of course also be applied in other  $D$ -decay final states,  
1905 such as  $D \rightarrow K_S^0K^+K^-$  and  $D \rightarrow K_S^0\pi^+\pi^-\pi^0$ . The biases on measurements of  $\gamma$   
1906 based the  $D$  decay phase-space distributions should be of similar size in these decay  
1907 channels. The impact on  $\gamma$  measurements based on the phase-space-integrated  
1908 yield asymmetry can be expected to be tens of degrees for the  $D \rightarrow K_S^0K^+K^-$   
1909 channel, where the yield asymmetry is expected to be around 2 %, for the reasons  
1910 explained in Section 4.2.3. The  $D \rightarrow K_S^0\pi^+\pi^-\pi^0$  decay, however, is dominantly  
1911  $CP$ -odd [146], and the bias in measurements based on the total asymmetry is  
1912 therefore expected to be  $O(\epsilon/r_B)$ , ie. a few degrees [41]. More precise calculations  
1913 of the biases would require a repeat of the study included here, with relevant  
1914 amplitude models and binning schemes in place.

1915 The chapter focuses on the model-independent, binned approach that is the  
1916 subject of the thesis. However, the underlying mechanism that determines the scale  
1917 of the bias, namely that the phase-space *distribution* of signal decays is unaffected  
1918 at  $\mathcal{O}(\epsilon)$  and  $\mathcal{O}(r_\chi)$ , is independent on the exact measurement approach. Therefore  
1919 it is expected that amplitude-model-based measurements and measurements made  
1920 with new unbinned methods such as those in Ref [75] will be similarly biased if  
1921 kaon  $CP$  violation and regeneration are not accounted for.

# 5

1922

1923

1924

## A BPGBGSZ measurement of $\gamma$ with $B^\pm \rightarrow Dh^\pm$ decays

1925 This chapter describes a model-independent BPGBGSZ measurement of  $\gamma$  with  
1926  $B^\pm \rightarrow DK^\pm$  and  $B^\pm \rightarrow D\pi^\pm$  decays where  $D \rightarrow K_S^0\pi^+\pi^-$  and  $D \rightarrow K_S^0K^+K^-$ ,  
1927 commonly denoted  $B^\pm \rightarrow D(\rightarrow K_S^0h^+h^-)h'^\pm$  decays. The measurement is made  
1928 with the full LHCb data set collected during Run 1 and 2 of the LHC, corresponding  
1929 to an integrated luminosity of about  $9\text{ fb}^{-1}$ . The analysis is under review for  
1930 publication in the Journal of High Energy Physics at the time of writing [1]  
1931 (one can hope).

### 1932 5.1 Candidate reconstruction and selection

1933 The  $B^\pm \rightarrow D(\rightarrow K_S^0h^+h^-)h'^\pm$  candidates are constructed during the offline *stripping*  
1934 stage described in Section 3.3.3. The candidates are defined by first combining  
1935 tracks to form a  $K_S^0 \rightarrow \pi^+\pi^-$  vertex, then a  $D \rightarrow K_S^0h^+h^-$  vertex, and finally  
1936 the  $B^\pm \rightarrow Dh'^\pm$  candidate. Each final state track is required to satisfy certain  
1937 momentum thresholds and track-quality requirements, and to be separated from all  
1938 primary interaction vertices. Each decay vertex is required to satisfy a fit-quality  
1939 threshold and to be separated from the primary vertex. Momentum thresholds  
1940 are applied to the composite particles and they are required to have reconstructed  
1941 invariant masses close to their known masses<sup>1</sup> except that the  $B$  candidate is  
1942 required to have a reconstructed invariant mass in the interval  $4750\text{--}7000\text{ MeV}/c^2$ .

---

<sup>1</sup>The exact mass window depends on the particle type and reconstruction category; narrower mass windows are applied at a later stage, as described below.

1943 The  $B$  candidate is required to satisfy  $\chi^2_{\text{IP}} < 25$ , where  $\chi^2_{\text{IP}}$  is the difference in  $\chi^2$   
1944 value of the primary vertex fit, when the vertex is formed with- and without the  $B$   
1945 candidate. As the final *stripping* stage, a multivariate classifier [118] is applied to the  
1946 formed  $B$  candidate to reduce the amount of random track combinations, denoted  
1947 combinatorial background, even further than the aforementioned requirements.

1948 Two data categories are defined, depending the tracks used to form the  $K_S^0$   
1949 candidate: the LL category where both pions are long tracks, and DD category where  
1950 both pions are downstream tracks, using the track classifications of Section 3.2.1.

1951 Each candidate is re-analysed with the `DecayTreeFitter` (DTF) frame work [147],  
1952 where a simultaneous fit of the full decay chain is made with a number of constraints  
1953 applied: the momenta of the composite  $D$  and  $K_S^0$  particles are required to form  
1954 invariant masses exactly equal to the known particle masses [31], and the momentum  
1955 of the  $B$  candidate is required to point in the direction defined by the  $B$  decay vertex  
1956 and the primary vertex. This refit results in improved resolution of the invariant  
1957 mass of the  $B$  candidate and, very importantly, of the Dalitz coordinates in the  
1958  $D$ -decay phase space. It also ensures that all candidates fall in the kinematically  
1959 allowed region of the  $D$ -decay phase space. Unless otherwise specified, all results  
1960 in this chapter are based on the refitted track momenta; for reasons explained  
1961 below, some studies have to be based on parameters that are obtained without the  
1962 constraints described above, or with only a subset of them applied.

1963 Following the stripping stage, the further selection of signal candidates is  
1964 performed in three steps: an initial set of requirements to remove candidates  
1965 that are very likely to be background and vetoes a number of specific backgrounds,  
1966 the application of a multivariate analysis algorithm designed to reject combinatorial  
1967 background decays, and finally a set of particle-identification requirements. The  
1968 requirements are summarised in Table 5.1, and each step is described in detail  
1969 in the following sections.

### 1970 5.1.1 Initial requirements

1971 At the hardware trigger level, it is required that a particle associated with the  
1972 signal decay triggered the hadronic L0 trigger (classifying the event as *Trigger*  
1973 *on Signal*, or TOS), or that the L0 decision was caused by a particle that is not  
1974 associated with the signal decay (*Trigger Independent of Signal*, or TIS). The  
1975 inclusion of the latter category increases the data sample about 50 %. At the  
1976 software trigger level, a particle belonging to the signal decay is required to have  
1977 caused one of each of the inclusive HLT1 and HLT2 lines to accept the events.  
1978 Specifically, the Run 1 events are required to be TOS on the `HLT1TrackAllL0` and

**Table 5.1:** Summary of requirements applied to data. The base requirements are applied to all data samples before training or applying the BDT.

Base requirements		
Variable	Cut	Comment
Companion momentum, $p$	$< 100 \text{ GeV}/c$	
Companion has RICH	<i>true</i>	
$K^\pm$ in $D$ decay: momentum, $p$	$< 100 \text{ GeV}/c$	In $D \rightarrow K_S^0 K^+ K^-$
$K^\pm$ in $D$ decay: have RICH	<i>true</i>	In $D \rightarrow K_S^0 K^+ K^-$
DecayTreeFit converged	<i>true</i>	
$D$ mass	$m_{D^0} \in m_{D^0}^{PDG} \pm 25 \text{ MeV}/c^2$	From DTF with constrained $K_S^0$ mass
$K_S^0$ mass	$m_{K_S^0} \in m_{K_S^0}^{PDG} \pm 15 \text{ MeV}/c^2$	From DTF with constrained $D^0$ mass
Background suppressing requirements		
Variable	Cut	Comment
$K_S^0$ flight distance $\chi^2$	$> 49$	for LL only
$\Delta z_{\text{significance}}^{DB}$	$> 0.5$	for all candidates
PID requirements		
Channel	Cut	Comment
$B^\pm \rightarrow DK^\pm$	$\text{PIDK} > 4$	for companion
$B^\pm \rightarrow D\pi^\pm$	$\text{PIDK} < 4$	for companion
$B^\pm \rightarrow Dh^\pm$	$\text{IsMuon} = 0$	for companion
$B^\pm \rightarrow D(\rightarrow K_S^0 \pi^+ \pi^-)h^\pm$	$\text{IsMuon} = 0$	for both charged $D$ decay products
$B^\pm \rightarrow D(\rightarrow K_S^0 \pi^+ \pi^-)h^\pm$	$\text{PIDe} < 0$	for charged $D$ decay product with opposite charge to companion particle
$B^\pm \rightarrow D(\rightarrow K_S^0 K^+ K^-)h^\pm$	$\text{PIDK} > -5 \& \text{ IsMuon} = 0$	for charged $D$ decay products
BDT requirements		
Channel	Cut	Comment
Run 1, DD	$> 0.6$	
Others	$> 0.8$	

<sup>1979</sup> Hlt2Topo{2, 3, 4}BodyBBDT lines and the Run 2 events are required to be TOS on  
<sup>1980</sup> the Hlt1{Track, TwoTrack}MVA and Hlt2Topo{2, 3, 4}Body lines. These trigger  
<sup>1981</sup> lines were described in Section 3.3.

<sup>1982</sup> Before any processing of the data, a loose preselection is applied to remove  
<sup>1983</sup> obvious background candidates. The reconstructed  $D$  ( $K_S^0$ ) mass is required to  
<sup>1984</sup> be within  $25$  ( $15$ )  $\text{MeV}/c^2$  of the known values [31]. The *companion* particle, the  
<sup>1985</sup> pion or kaon produced in the  $B^\pm \rightarrow Dh^\pm$  decay, is required to have associated  
<sup>1986</sup> RICH information and a momentum less than  $100 \text{ GeV}/c$ ; this ensures good particle-  
<sup>1987</sup> identification performance. Finally, all of the DTF fits of the full decay chain  
<sup>1988</sup> are required to have converged properly.

<sup>1989</sup> Two additional requirements are made at this stage in order to suppress specific  
<sup>1990</sup> backgrounds. In order to suppress decays of the type  $B^\pm \rightarrow K_S^0 h^+ h^- h'^\pm$  with  
<sup>1991</sup> no intermediate  $D$  meson, so called *charmless* decays, it is required that the  
<sup>1992</sup> significance of the  $z$ -separation of the  $D^0$  decay vertex and the  $B^\pm$  decay vertex

1993 is above 0.5. The significance of the  $z$ -separation of the  $D^0$  decay vertex and  
1994 the  $B^\pm$  decay vertex is defined as

$$\Delta z_{\text{significance}}^{D-B} = \frac{z_{vtx}^D - z_{vtx}^B}{\sqrt{\sigma^2(z_{vtx}^D) + \sigma^2(z_{vtx}^B)}}. \quad (5.1)$$

1995 This source of background described further in section 5.3.1. In order to suppress  
1996 a background from  $D \rightarrow 4\pi$  and  $D \rightarrow \pi\pi KK$  decays, it is required that the  $K_S^0$   
1997 flight distance  $\chi_{\text{FD}}^2$  is greater than 49, where

$$\chi_{\text{FD}}^2 = \left( \frac{\Delta r}{\sigma(\Delta r)} \right)^2, \quad (5.2)$$

1998 and  $\Delta r$  is the measured flight distance of the  $K_S^0$  meson. This background is  
1999 described in further detail in section 5.3.2.

### 2000 5.1.2 Boosted decision tree

2001 A Gradient Boosted Decision Tree [148] (abbreviated BDT in the following) is  
2002 applied to classify each candidate on a scale from  $-1$  to  $+1$  as signal-like ( $+1$ )  
2003 or combinatorial-background-like ( $-1$ ), based on the values of a number of input  
2004 parameters for a candidate in question. The BDT is implemented in the TMVA  
2005 frame work [149].

2006 A boosted decision tree classifier consists of a number of sequentially trained  
2007 decision trees, each of which classify events as either signal or background. Each tree  
2008 bases the decision on an individual subset of variables, out of an overall set of input  
2009 variables. At each training step, the input events are weighted when training a new  
2010 tree, so that events that the already-trained trees classify incorrectly are given a  
2011 higher weight; this is denoted boosting. The term *gradient boosting* denotes a specific  
2012 weight calculation scheme [148]. The final score is the average over all decision trees.

2013 The full set of input variables are given in Table 5.2. It includes the momenta  
2014 of particles in the decay; a number of geometric parameters such a absolute and  
2015 relative vertex positions, and distances of closest approach between tracks;  $\chi_{\text{IP}}^2$   
2016 values for a number of particles in the decay chain; the  $\chi^2$  per degree of freedom  
2017 of the DTF refit; DIRA values, which denote the angle between the fitted particle  
2018 momenta and the vector spanned by it's production ad decay vertices; and finally  
2019 an isolation variable, defined as

$$A_{pT} = \frac{p_T(B) - \sum p_T(\text{other})}{p_T(B) + \sum p_T(\text{other})} \quad (5.3)$$

**Table 5.2:** Input parameter set used in BDT trained to separate signal and combinatorial background, sorted according to importance in the LL classifier.

Variable name	Importance LL/DD (Rank in DD)	Description
<code>log10(1-Ks_DIRA_BPV)</code>	7.2 % / 3.5 % (16)	$\log \cos \theta_{\text{DIRA}}$ for $K_S^0$
<code>log(Bu_RHO_BPV)</code>	5.7 % / 5.5 % (5)	Radial distance of $B$ vertex to beam line
<code>log(Bach_PT)</code>	5.2 % / 6.9 % (1)	$p_T$ of the companion particle
<code>log10(1-DO_DIRA_BPV)</code>	4.9 % / 5.8 % (4)	$\log \cos \theta_{\text{DIRA}}$ for $D$
<code>log10(1-Bu_DIRA_BPV)</code>	4.9 % / 6.4 % (3)	$\log \cos \theta_{\text{DIRA}}$ for $B^\pm$
<code>log(DO_RHO_BPV)</code>	4.8 % / 5.3 % (6)	Radial distance of $D$ vertex to beam line
<code>Bu_FTASY_1_5</code>	4.7 % / 4.9 % (7)	Asymmetry parameters of $B^\pm$
<code>log(DO_PT)</code>	4.7 % / 6.6 % (2)	$p_T$ of the $D$ meson
<code>log(Bu_constDDOKSPV_CHI2NDDF)</code>	4.2 % / 4.5 % (9)	$\chi^2$ /d.o.f of kinematical refit with DecayTreeFitter
<code>log(Bu_FDGHI2_QWNPV)</code>	3.9 % / 4.1 % (11)	Flight distance $\chi^2$ of the $B^\pm$
<code>log(max_Ksh1h2_IPCHI2_0WNPV)</code>	3.9 % / 3.0 % (20)	Largest $\chi^2_{\text{IP}}$ of the $K_S^0$ decay products
<code>log(DO_IPCHI2_QWNPV)</code>	3.8 % / 3.3 % (17)	$\chi^2_{\text{IP}}$ of the $D$
<code>log(min_Ksh1h2_IPCHI2_0WNPV)</code>	3.7 % / 0.9 % (26)	Smallest $\chi^2_{\text{IP}}$ of the $K_S^0$ decay products
<code>log(Bu_P)</code>	3.7 % / 3.9 % (12)	$p$ of the $B_\pm^0$ meson
<code>log(Bu_IPCHI2_QWNPV)</code>	3.6 % / 4.6 % (8)	$\chi^2_{\text{IP}}$ of the $B_\pm^0$
<code>Bu_MAXDOCA</code>	3.6 % / 3.3 % (18)	"Distance of closest approach" for $B^\pm$ vertex
<code>log(Bach_IPCHI2_0WNPV)</code>	3.3 % / 4.3 % (10)	$\chi^2_{\text{IP}}$ of the companion particle
<code>log(Bu_PT)</code>	3.3 % / 3.7 % (14)	$p_T$ of the $B^\pm$ meson
<code>log(max_h1h2_IPCHI2_0WNPV)</code>	3.1 % / 3.8 % (13)	Largest $\chi^2_{\text{IP}}$ of the $D$ decay products
<code>log(min_h1h2_IPCHI2_0WNPV)</code>	3.0 % / 3.4 % (19)	Smallest $\chi^2_{\text{IP}}$ of the $D$ decay products
<code>log(Ks_VTXCHI2D0F)</code>	2.9 % / 2.3 % (21)	$\chi^2$ of vertex fit for $K_S^0$
<code>DO_MAXDOCA</code>	2.9 % / 1.0 % (25)	"Distance of closest approach" for $D$ vertex
<code>log(DO_VTXCHI2D0F)</code>	2.7 % / 1.6 % (24)	$\chi^2$ of vertex fit for $D$
<code>log(DO_P)</code>	2.7 % / 1.8 % (22)	$p$ of the $D$ meson
<code>log(Bach_P)</code>	2.2 % / 3.6 % (15)	$p$ of the companion particle
<code>log(Bu_VTXCHI2D0F)</code>	1.8 % / 1.7 % (23)	$\chi^2$ of vertex fit for $B^\pm$

where the sum is over all other tracks in a cone around the  $B$ -candidate. The cone is defined as being within a circle with a radius of 1.5 units around the  $B$  candidate in the  $(\eta, \phi_{azim})$ -plane. This variable is highly efficient in rejecting combinatorial background. Two algorithms are trained, one for the LL category of  $K_S^0$  mesons and one for the DD category, because some input parameters relate to the  $K_S^0$  meson and have very different distributions between the two categories.

The BDTs are trained and tested with input samples representing typical signal and background decay candidates: a signal sample that consists of simulated  $B^\pm \rightarrow D(\rightarrow K_S^0\pi^+\pi^-)\pi^\pm$  decays corresponding to the LHCb running conditions for the years 2012–2018, and a sample of combinatorial background candidates from real data, where the reconstructed invariant mass of the  $B$  meson is larger than 5800 MeV/ $c^2$ . The candidates in both samples were required to have passed the initial requirements described in the preceding section. The input-parameter distributions in the signal and background training samples are shown in Figs. 5.1 and 5.2. The signal and background samples are each split into two before the training stage: one sub sample, the training sample, is used to train the BDT, after which the trained algorithm is applied to the other sub sample, the test sample. The classifier is found to perform well on the test sample, not just the training sample, which ensures that it does not suffer significant overtraining. The BDT output distribution are shown for both test and training samples in Fig. 5.3, where it is clear that the classifier very effectively separates signal and background candidates.

Each candidate in data is classified using the BDT, and candidates that are assigned a score below some threshold value are discarded. The threshold values are chosen in a set of pseudo experiments, such that the expected sensitivity to  $\gamma$  is maximised. This is done by performing preliminary fits to the data set for a range of different BDT threshold values, then generating many pseudo data sets with the obtained yields, and applying the full fit and interpretation procedure described in Sections 5.4–5.7 to each data set. Thus, the expected uncertainty on  $\gamma$  is obtained for a range of threshold values. The procedure is applied independently for the LL and DD categories, as well as for the Run 1 and Run 2 data sets, because some parameter distributions differ slightly between the two runs. The optimal threshold values are found to be 0.8 in all situations, except for DD candidates in Run 1 where it is 0.6. This is illustrated in Fig. 5.4 where the results of the threshold scans are shown. The same classifier is applied to both  $B^\pm \rightarrow D\pi^\pm$  and  $B^\pm \rightarrow DK^\pm$  candidates, and both  $D$  final state categories. While the classifiers were trained using samples of  $B^\pm \rightarrow D(\rightarrow K_S^0\pi^+\pi^-)\pi^\pm$  simulation and data, the decays are similar enough that no significant improvement in performance was obtained

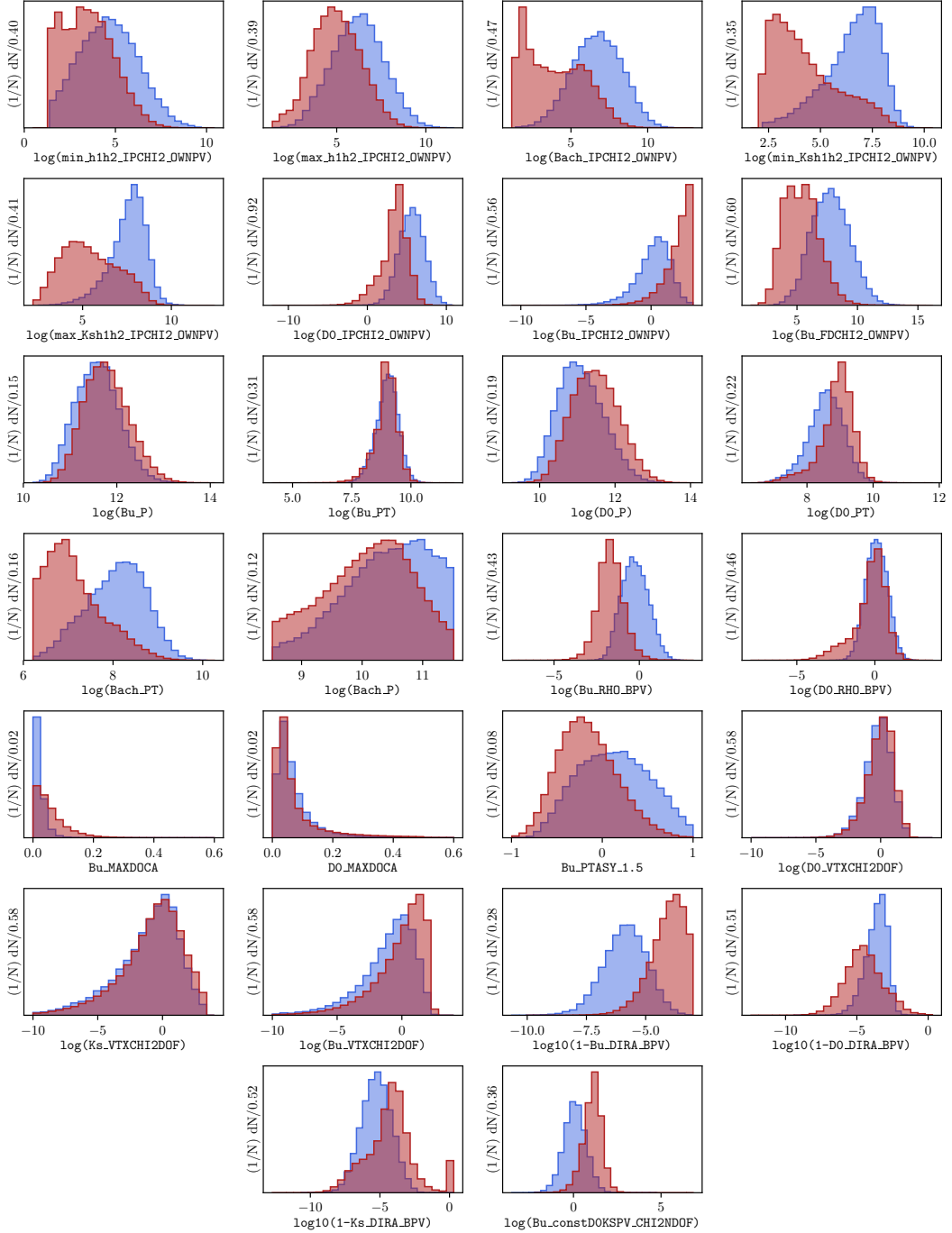


**Figure 5.1:** Distribution of input parameters in the LL training samples of (blue) signal decays from simulation and (red) background decays from the upper  $B$  sideband. The variable names are defined in Table 5.2.

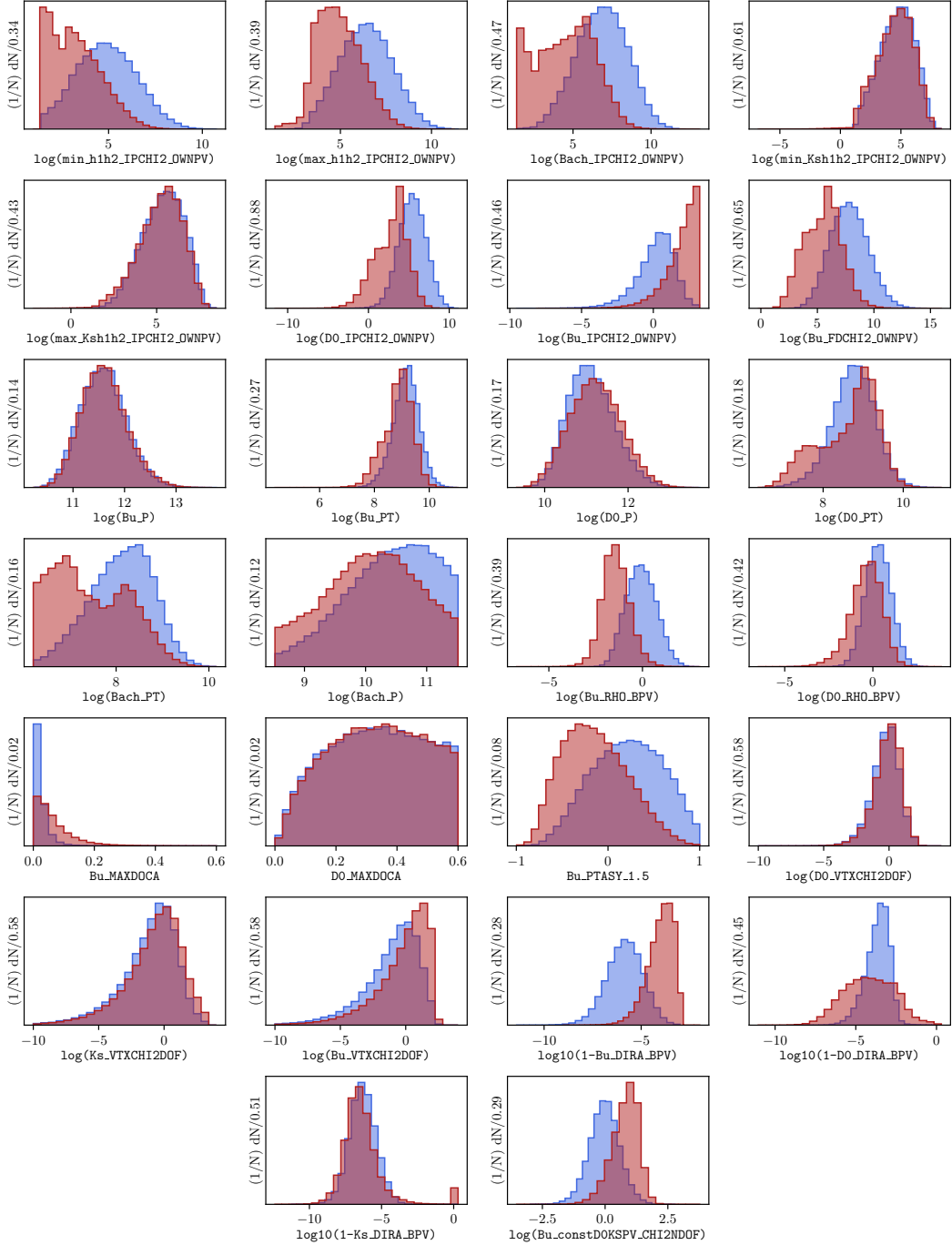


**Figure 5.2:** Distribution of input parameters in the DD training samples of (blue) signal decays from simulation and (red) background decays from the upper  $B$  sideband. The variable names are defined in Table 5.2.

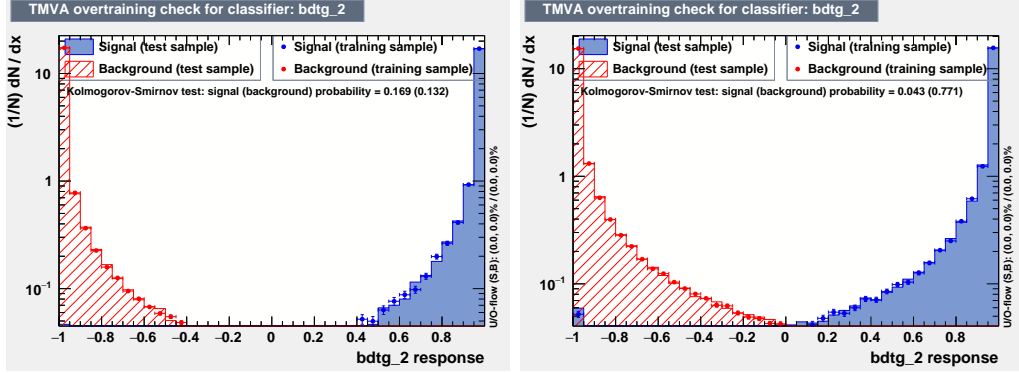


**Figure 5.3:** Distribution of BDT variable on test and training samples for (left) the LL and (right) the DD category, with logarithmic  $y$ -scale.

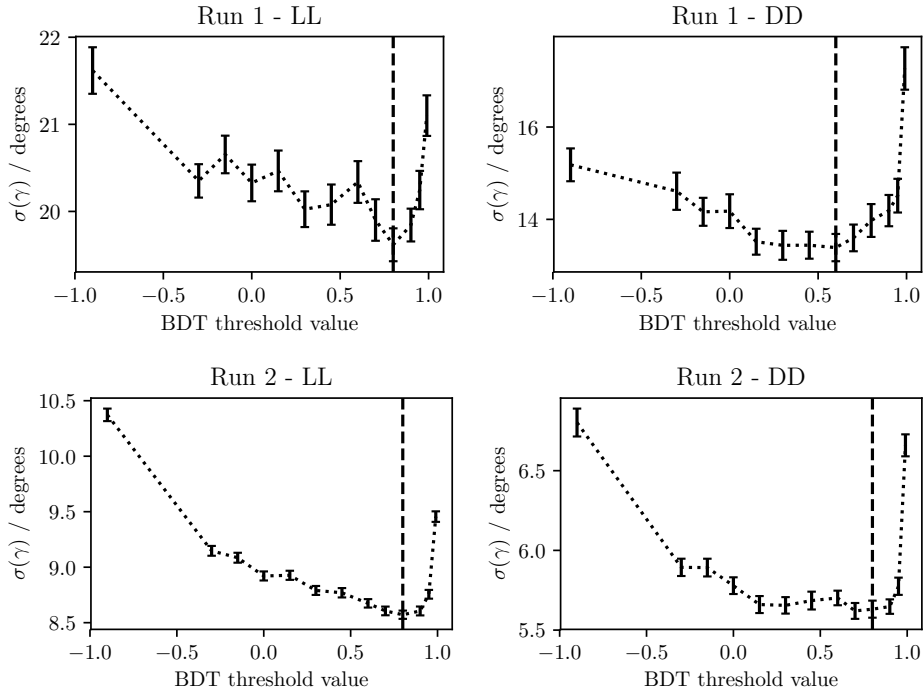


**Figure 5.4:** The mean uncertainty on  $\gamma$  in toy studies, performed with the signal and background yields corresponding to a given BDT requirement, using (top) the Run 1 and (bottom) Run 2 datasets, using only candidates in (left) the LL category and (right) the DD category. The dashed line shows the threshold value employed to discard background-like candidates in the selection.

when considering a more elaborate setup. Across all categories, the requirement on the BDT output is found to remove approximately 98 % of the combinatorial background, while being approximately 93 % efficient on signal.

2060 **5.1.3 Particle-identification requirements**

2061 A PID requirement is made to separate  $B^\pm \rightarrow DK^\pm$  and  $B^\pm \rightarrow D\pi^\pm$  candidates  
 2062 in the data sample, by requiring that the PIDK of the companion particle satisfies  
 2063  $\text{PIDK} < 4$  for  $B^\pm \rightarrow D\pi^\pm$  candidates and  $\text{PIDK} > 4$  for  $B^\pm \rightarrow DK^\pm$  candidates. The  
 2064 PIDK variable was defined in Section 3.1.3. This ensures that any given candidate  
 2065 is selected into only one of these samples.

2066 Further to the requirement on the companion, PID requirements are made to  
 2067 suppress semi-leptonic backgrounds as well as decays where a final state particle  
 2068 decays in flight, and a loose PID requirement is made in the  $D \rightarrow K_S^0 K^+ K^-$   
 2069 channels where it leads to a higher signal purity:

- 2070 • the companion particle is required to satisfy `IsMuon` = 0.
- 2071 • For the  $B \rightarrow D(\rightarrow K_S^0 \pi^+ \pi^-) h^\pm$  samples it is required that the charged pion  
 2072 track from the  $D$  decay with opposite charge to the companion satisfies  
 2073  $\text{PIDe} < 0 \& \text{IsMuon} = 0$ , and for the other charged pion that `IsMuon` = 0. A  
 2074 very loose requirement of  $\text{PIDK} < 20$  is applied to both pions from the  $D$ -decay  
 2075 in the stripping stage.
- 2076 • For the  $B \rightarrow D(\rightarrow K_S^0 K^+ K^-) h^\pm$  samples it is required that the charged kaon  
 2077 tracks from the  $D$  decay have RICH information, a momentum less than 100  
 2078 GeV/c and  $\text{PIDK} > -5 \& \text{IsMuon} = 0$ .

2079 These backgrounds are described in Section 5.3.3.

2080 **5.1.4 Final requirements**

2081 For a small fraction of candidates in the final sample, it is the case that two  
 2082 or more candidates originate in the same  $pp$  collision. In order to make sure  
 2083 that all candidates are completely independent, a single, arbitrary candidate from  
 2084 each  $pp$  collision is kept for these collisions, and the other candidates discarded.  
 2085 This requirement results in the removal of less than 0.7% of candidates in  
 2086 each data category.

2087 Furthermore, the  $D$  mass used to define the binning schemes described in  
 2088 Ref. [74] differs slightly from the mass used in the DTF refit. Therefore a  
 2089 few of the decays are reconstructed with Dalitz coordinates outside the allowed  
 2090 kinematic region. This problem concerns less than 0.5% (1%) of candidates in  
 2091 the  $D \rightarrow K_S^0 \pi^+ \pi^-$  ( $D \rightarrow K_S^0 K^+ K^-$ ) channel and they are simply discarded. The  
 2092  $B^\pm \rightarrow DK^\pm$  and  $B^\pm \rightarrow D\pi^\pm$  channels are equally affected, and therefore the effect  
 2093 is inherently taken into account in the analysis, similarly to other phase-space-  
 2094 dependent acceptance effects.

**Table 5.3:** Final candidate yield in each data category after the full selection has been applied, including removing candidates outside the region  $m_B \in [5080, 5800] \text{ MeV}/c^2$ .

$B$ Decay	$D$ final state	$K_S^0$ type	Run 1	Run 2	Total
$B^\pm \rightarrow DK^\pm$	$K_S^0\pi^+\pi^-$	LL	2275	10525	12800
		DD	5097	23508	28605
	$K_S^0K^+K^-$	LL	383	1610	1993
		DD	772	3397	4169
$B^\pm \rightarrow D\pi^\pm$	$K_S^0\pi^+\pi^-$	LL	18209	90509	108718
		DD	40167	205807	245974
	$K_S^0K^+K^-$	LL	2879	13757	16636
		DD	6033	29790	35823

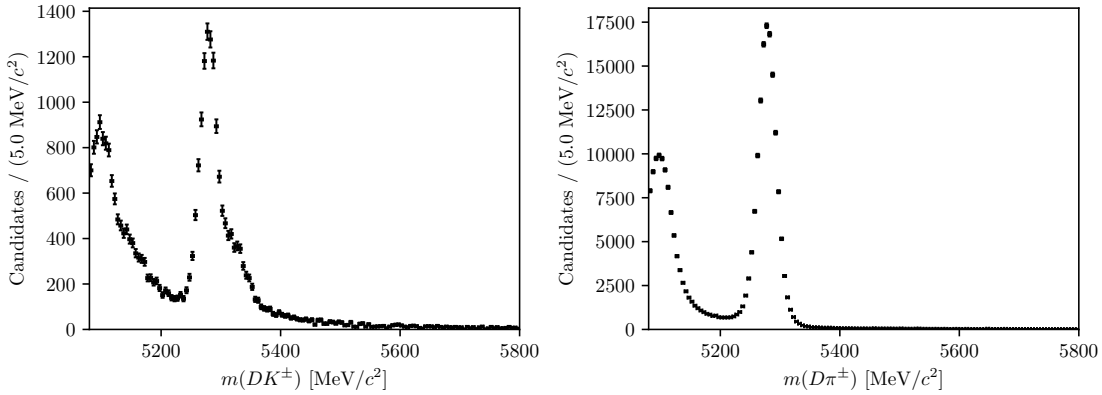


**Figure 5.5:** The spectrum of  $m_B$  in the (left)  $B^\pm \rightarrow DK^\pm$  and (right)  $B^\pm \rightarrow D\pi^\pm$  samples where  $D \rightarrow K_S^0\pi^+\pi^-$  and the  $K_S^0$  meson is reconstructed in the DD category, after the full selection has been applied.

### 2095 5.1.5 Selected candidates

2096 In total, about 47,000  $B^\pm \rightarrow DK^\pm$  candidates and 400,000  $B^\pm \rightarrow D\pi^\pm$  candidates  
 2097 are selected, as summarised in Table 5.3. An example of the  $B$  mass distribution in  
 2098 one of the data categories is shown in Fig. 5.5; it is clear that a significant number  
 2099 of these candidates are background decays. The Dalitz plots for candidates in the  
 2100 signal region where  $m_B \in [5249, 5309] \text{ MeV}/c^2$  are shown in Fig. 5.6 and 5.7. Due to  
 2101 the large yields in the full Run 1 and 2 LHCb data set, the asymmetries between  
 2102 the  $B^+$  and  $B^-$  distributions are visible to the eye in the  $B^\pm \rightarrow DK^\pm$  plots.

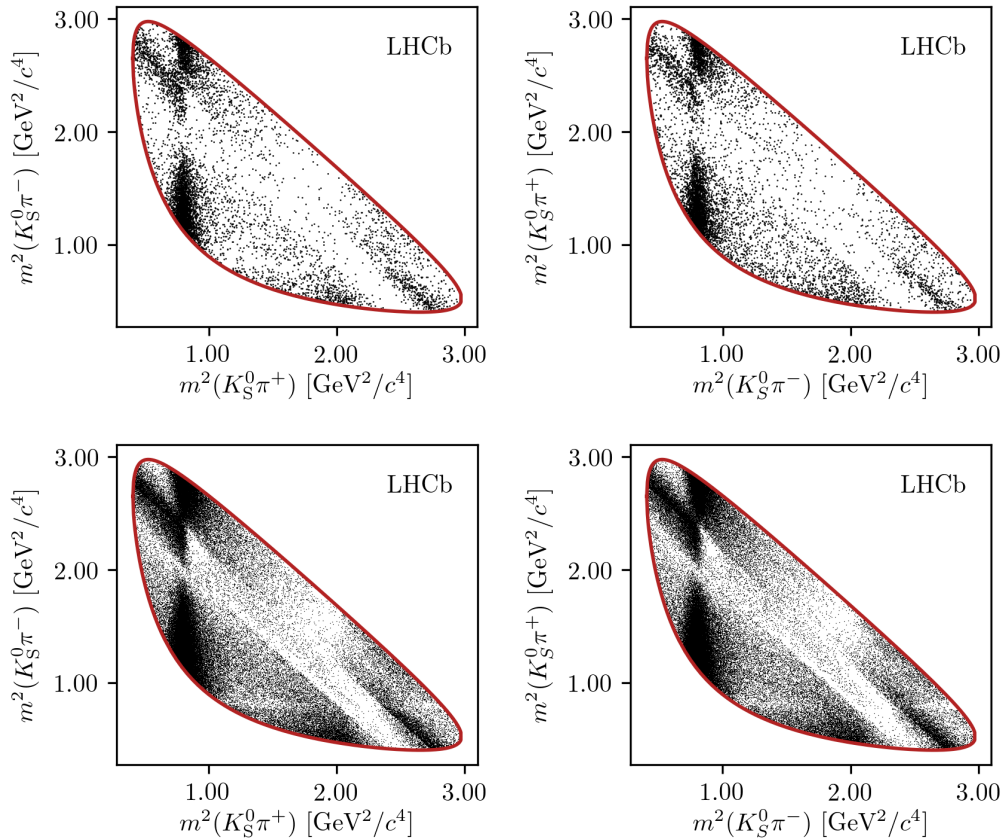


**Figure 5.6:** Dalitz plots of (left)  $B^+ \rightarrow Dh^+$  and (right)  $B^- \rightarrow Dh^-$  candidates in the signal region, in the (top)  $B^\pm \rightarrow DK^\pm$  and (bottom)  $B^\pm \rightarrow D\pi^\pm$  channels where  $D \rightarrow K_S^0 \pi^+ \pi^-$ . The LL and DD categories have been combined.

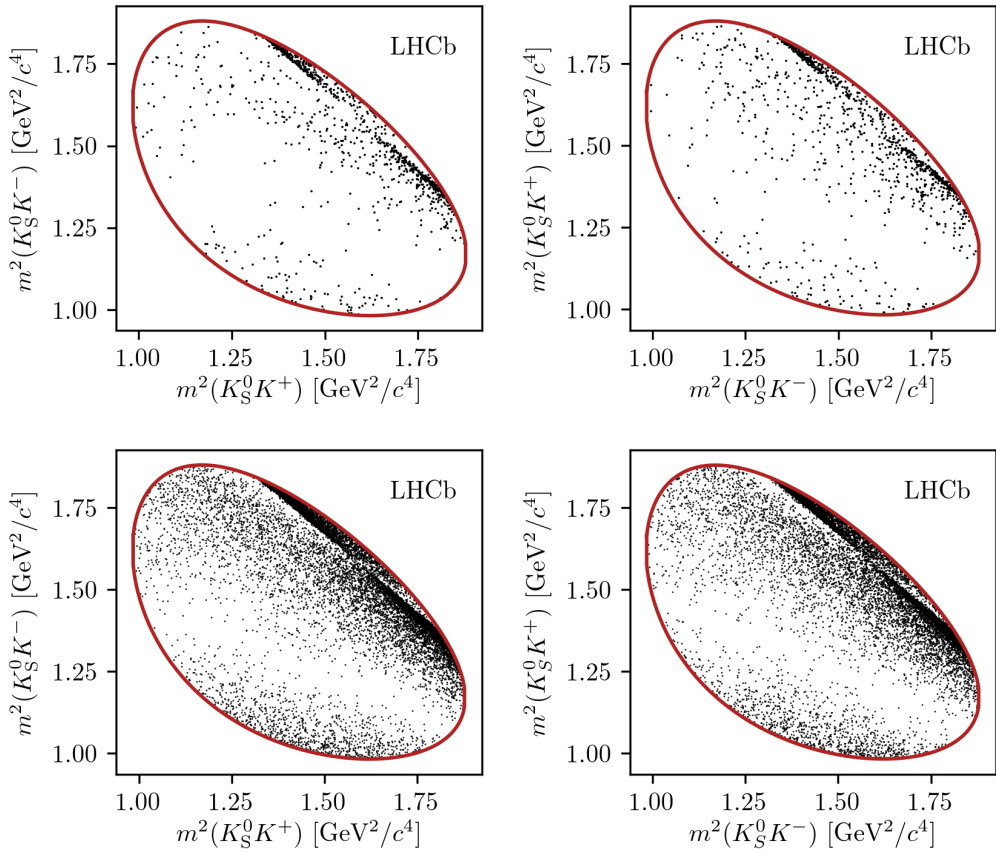


**Figure 5.7:** Dalitz plots of (left)  $B^+ \rightarrow Dh^+$  and (right)  $B^- \rightarrow Dh^-$  candidates in the signal region, in the (top)  $B^\pm \rightarrow DK^\pm$  and (bottom)  $B^\pm \rightarrow D\pi^\pm$  channels where  $D \rightarrow K_S^0 K^+ K^-$ . The LL and DD categories have been combined.

## 2103 5.2 Signal selection efficiencies

2104 The efficiency of each step of the selection on signal decays can be investigated  
 2105 using simulated decays. In the  $B^\pm \rightarrow D\pi^\pm$  channel, only decays that were placed  
 2106 in the "test" sample when training the BDT are used, in order to avoid over-  
 2107 estimating the efficiency.

2108 In general, the total selection efficiency up until the PID requirements, including  
 2109 the offline stage and the effect of the geometrical LHCb acceptance, is about 1  
 2110 permille, slightly higher for  $B^\pm \rightarrow DK^\pm$  than  $B^\pm \rightarrow D\pi^\pm$  decays, slightly higher  
 2111 for  $D \rightarrow K_S^0 K^+ K^-$  than  $D \rightarrow K_S^0 \pi^+ \pi^-$  decays, and somewhat higher in the Run 2  
 2112 than in Run 1 due to improvements in the trigger. The PID requirements are  
 2113 investigated separately in Section 5.2.1 below, using samples of calibration data.  
 2114 The overall selection efficiency does not impact the measurement at all, because  
 2115 the observables of interest are sensitive *only* to the distribution of decays over the  
 2116 Dalitz plot (except, of course, in the sense that a higher signal efficiency is desirable  
 2117 because it leads to larger signal yields). Likewise, it makes no difference that the  
 2118 overall selection efficiencies differ slightly between  $B^\pm \rightarrow DK^\pm$  and  $B^\pm \rightarrow D\pi^\pm$   
 2119 decays, as long as the efficiency profile over the Dalitz plot is identical between the  
 2120 two decay channels. This is confirmed separately in Section 5.2.2 below.

2121 The efficiencies of each individual selection step are shown in Fig. 5.8, obtained  
 2122 using simulated  $B^\pm \rightarrow D\pi^\pm$  decays. The main reason that some signal decays  
 2123 do not survive the base requirement is the  $p_{\text{companion}} < 100 \text{ GeV}/c$  requirement,  
 2124 which is in place to ensure that the PID performance for the companion is good.  
 2125 For decays with  $p_{\text{companion}} > 100 \text{ GeV}/c$ , only about 60 % of  $B^\pm \rightarrow DK^\pm$  decays  
 2126 survive the subsequent  $\text{PID}_K > 4$  requirement and the cross-feed from misidentified  
 2127  $B^\pm \rightarrow D\pi^\pm$  decays is 50 % larger than in the current selection. Thus, loosening  
 2128 this requirement leads to little statistical gain, while leading to larger systematic  
 2129 effects from the crossfeed background.

2130 An equivalent plot for the combinatorial background is shown in Fig. 5.9, using  
 2131  $B^\pm \rightarrow D(\rightarrow K_S^0 \pi^+ \pi^-) \pi^\pm$  candidates in data with a reconstructed  $B$  mass above  
 2132  $5600 \text{ MeV}/c^2$ ; it can be seen that the BDT is very efficient at rejecting combinatorial  
 2133 background, but that the base requirements and the requirement on the  $K_S^0$  flight  
 2134 distance also remove a decent amount of background.

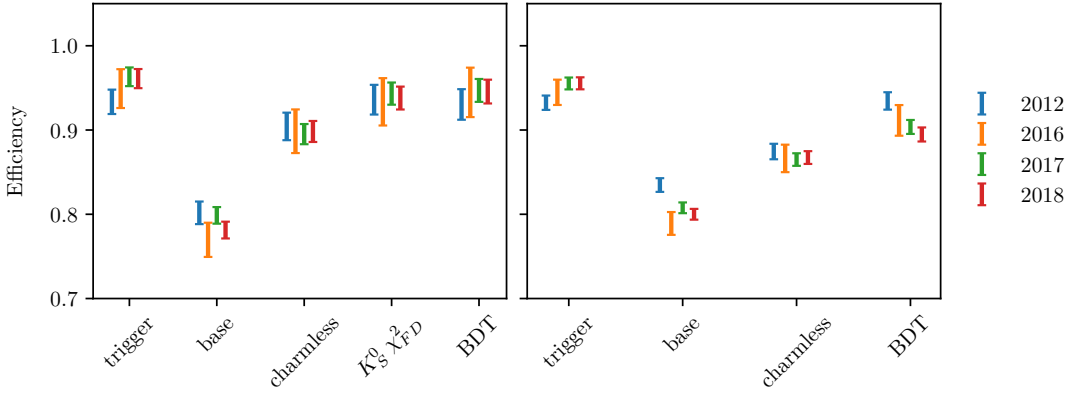


**Figure 5.8:** The efficiency of each selection step in samples of simulated  $B^\pm \rightarrow D(\rightarrow K_0^0\pi^+\pi^-)\pi^\pm$  signal decays in the (left) LL and (right) DD categories. The selection steps are applied on top of each other, from left to right on the horizontal axis. The samples are split by year.

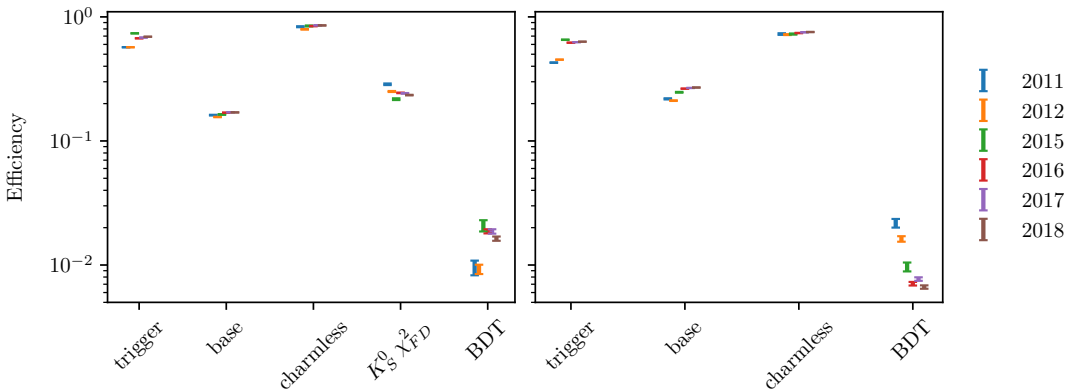


**Figure 5.9:** The efficiency of each selection step in samples of  $B^\pm \rightarrow D(\rightarrow K_0^0\pi^+\pi^-)\pi^\pm$  candidates in data where the reconstructed  $B$  mass is above  $5600 \text{ MeV}/c^2$ , meaning the candidates stem from combinatorial background. The efficiency is shown for candidates in the (left) LL and (right) DD categories. The selection steps are applied on top of each other, from left to right on the horizontal axis. The samples are split by year. Notice the logarithmic scale on the vertical axis.

### 2135 5.2.1 Efficiency of the PID requirements

2136 The efficiencies of the PID requirements on the companion enter the yield parame-  
 2137 terisations of the mass fits in Section 5.4 and 5.5 and must therefore be known.  
 2138 They are determined using samples of calibration data selected without relying on  
 2139 PID variables, as implemented in the `PIDCalib` frame work [150]. Reasonably pure  
 2140 samples of pion and kaon tracks are obtained from  $D^0 \rightarrow K^-\pi^+$  decays, where the  
 2141  $D$  meson originates in a  $D^{*+} \rightarrow D^0\pi^+$  decay and can therefore be flavour tagged.  
 2142 The remaining background is subtracted via the `sPlot` [151] procedure, based on

**Table 5.4:** PID efficiencies obtained with the `PIDCalib` tool. The uncertainty incorporates statistical uncertainty due to the size of the reference sample, the systematic uncertainty due to the choice of binning scheme in `PIDCalib`, and a systematic uncertainty due to the `sWeight` calculation in `PIDCalib` of 0.1 %.

Efficiency	Particle	$D$ final state	$\varepsilon_{\text{PID}} (\%)$	
			LL	DD
Run I and II				
Correct ID	Kaon	$D \rightarrow K_S^0 \pi^+ \pi^-$	$86.74 \pm 0.13$	$86.90 \pm 0.22$
		$D \rightarrow K_S^0 K^+ K^-$	$86.22 \pm 0.26$	$86.56 \pm 0.30$
	Pion	$D \rightarrow K_S^0 \pi^+ \pi^-$	$97.11 \pm 0.11$	$97.17 \pm 0.13$
		$D \rightarrow K_S^0 K^+ K^-$	$97.07 \pm 0.11$	$97.16 \pm 0.14$

a two-dimensional fit of the  $m(K^- \pi^+)$  and  $m(D^0 \pi^+) - m(D^0)$  distributions. The obtained weights are employed to calculate the average efficiency of the requirement on `PIDK` for a number of bins in the momentum and pseudorapidity of the calibration tracks, and the number of charged tracks in the detector, thus constructing a three-dimensional efficiency lookup table. The procedure is carried out for each PID requirement, companion species, data-taking year, track charge, and magnet polarity. Based on these tables, expected PID efficiencies for the  $B^\pm \rightarrow D\pi^\pm$  and  $B^\pm \rightarrow DK^\pm$  signal decays are calculated that take the kinematical distribution and detector occupancy in the *BPGGSZ* data samples into account, by using the high-purity sample of  $B^\pm \rightarrow D\pi^\pm$  candidates in the signal region as a reference. The dominating uncertainty on the efficiencies is statistical in nature, due to the finite size of the reference sample. In addition, systematic uncertainties are included due to the `sPlot` procedure, estimated at 0.1 % [150], and due to the choice of binning scheme, estimated by repeating the procedure using a number of alternative binning schemes. The final estimates of the correct-ID efficiencies,  $\varepsilon_{\text{PID}}$ , are shown in Table 5.4, including all sources of uncertainty. Note that the probability to misidentify a decay satisfies  $\varepsilon_{\text{mis-ID}} = 1 - \varepsilon_{\text{PID}}$  by construction, due to the the definition of the `PIDK` variable (given in Section 3.2.2) and the chosen PID requirement.

### 5.2.2 Efficiency profile over the Dalitz plot

The analysis strategy depends on sharing the  $F_i$  parameters between the  $B \rightarrow D\pi$  and  $B \rightarrow DK$  channels. This is reasonable, since the phase-space dependence of the reconstruction efficiency is expected to be very similar between the two decays, given the similar kinematics; an assumption that is verified using samples of simulated decays. The full selection is applied to the samples. The  $B \rightarrow D\pi$  sample of LL (DD) candidates includes about 63,000 (146,000) simulated decays, and the  $B \rightarrow DK$

2168 samples include 60,000 (142,000) simulated decays. For the  $B \rightarrow D\pi$  mode, this is  
2169 approximately equal to the number of decays in the full Run 1+2 data sample, and  
2170 for  $B \rightarrow DK$  this is a factor of about 12 larger than the data sample. The decays  
2171 were simulated with an equal decay probability across the  $D$ -decay phase space, so  
2172 that any non-uniform distribution of reconstructed decays is completely determined  
2173 by a phase-space dependent reconstruction and selection efficiency. Therefore the  
2174 assumption that the phase-space dependence is identical between the  $B \rightarrow D\pi$  and  
2175  $B \rightarrow DK$  channels is verified by seeing if the Dalitz coordinates are distributed  
2176 differently between the samples of simulated  $B \rightarrow D\pi$  and  $B \rightarrow DK$  decays.

2177 This is investigated with two statistical tests. The first is a  $\chi^2$  comparison  
2178 of two-dimensional histograms of the distribution of  $m^2(K_S^0 h^+)$  and  $m^2(K_S^0 h^-)$  in  
2179 the different  $B \rightarrow D\pi$  and  $B \rightarrow DK$  channels. These histograms, and the ratio  
2180 between them, are shown in Figs. 5.10 and 5.11, along with the  $p$ -values from  
2181 the  $\chi^2$  tests. It can be seen that, in all cases, the probability of obtaining the  
2182 two histograms assuming that they share the same underlying distribution has a  
2183 reasonable value, and that there is no clear trend in the ratio plots. The second  
2184 test is a Kolmogorov-Smirnov test [152] of the compatibility of the one-dimensional  
2185 distributions of  $m^2(K_S^0 h^+)$ ,  $m^2(K_S^0 h^-)$ , and  $m^2(h^+ h^-)$ . These distributions, and  
2186 the corresponding  $p$ -values, are shown in Fig. 5.12 and 5.13. Again, all the  $p$  values  
2187 are reasonable. Therefore, it is concluded that there are no statistically significant  
2188 differences between the phase-space dependence of the reconstruction and selection  
2189 efficiency between the  $B \rightarrow D\pi$  and  $B \rightarrow DK$  channels, given the present sample  
2190 sizes. Because the simulation samples have approximately the same amount of  
2191 decays as data (or significantly more, in the  $B \rightarrow DK$  case), any potential differences  
2192 will be negligible with data yields. Thus, sharing the  $F_i$  parameters between the  
2193  $B \rightarrow D\pi$  and  $B \rightarrow DK$  channels is viable, and no efficiency correction is necessary.

### 2194 5.3 Background studies

2195 A wide range of backgrounds can potentially pollute the sample of signal candidates.  
2196 The backgrounds group into three categories depending on how they are treated  
2197 in the analysis:

- 2198 • Backgrounds that can be effectively removed in the selection
- 2199 • Backgrounds that are only present at a level where the impact on the  
2200 measurement result is small, and which do therefore not have to be modelled

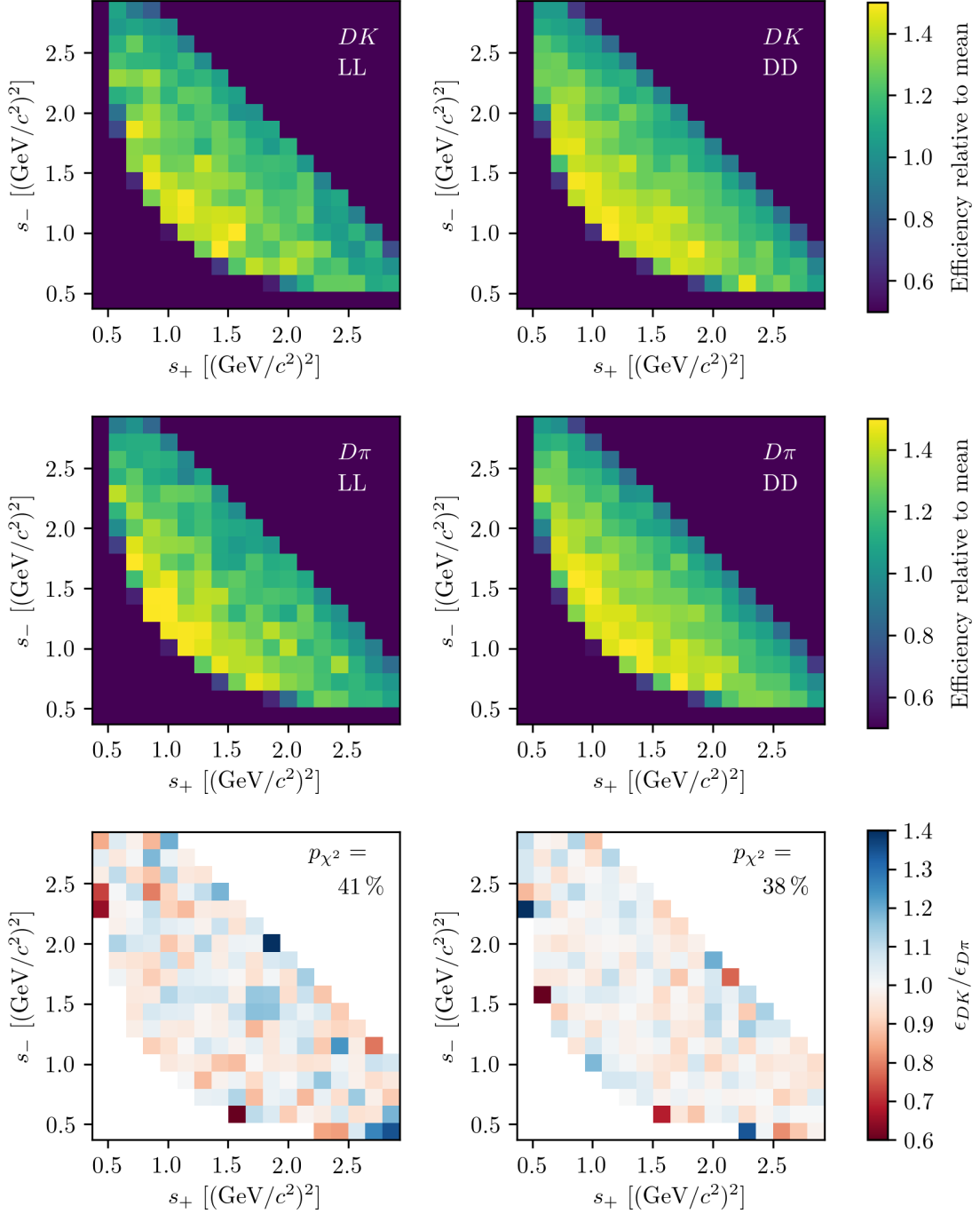


**Figure 5.10:** The acceptance profile in simulated samples of (top row)  $B \rightarrow DK$  decays and (centre row)  $B \rightarrow D\pi$  decays where  $D \rightarrow K_S^0 \pi^+ \pi^-$ , as well as (bottom row) the ratio between the two histograms. The plots are shown for candidates in the (left) LL and (right) DD categories. The  $p$  values are the results of  $\chi^2$  compatibility tests between the two histograms.

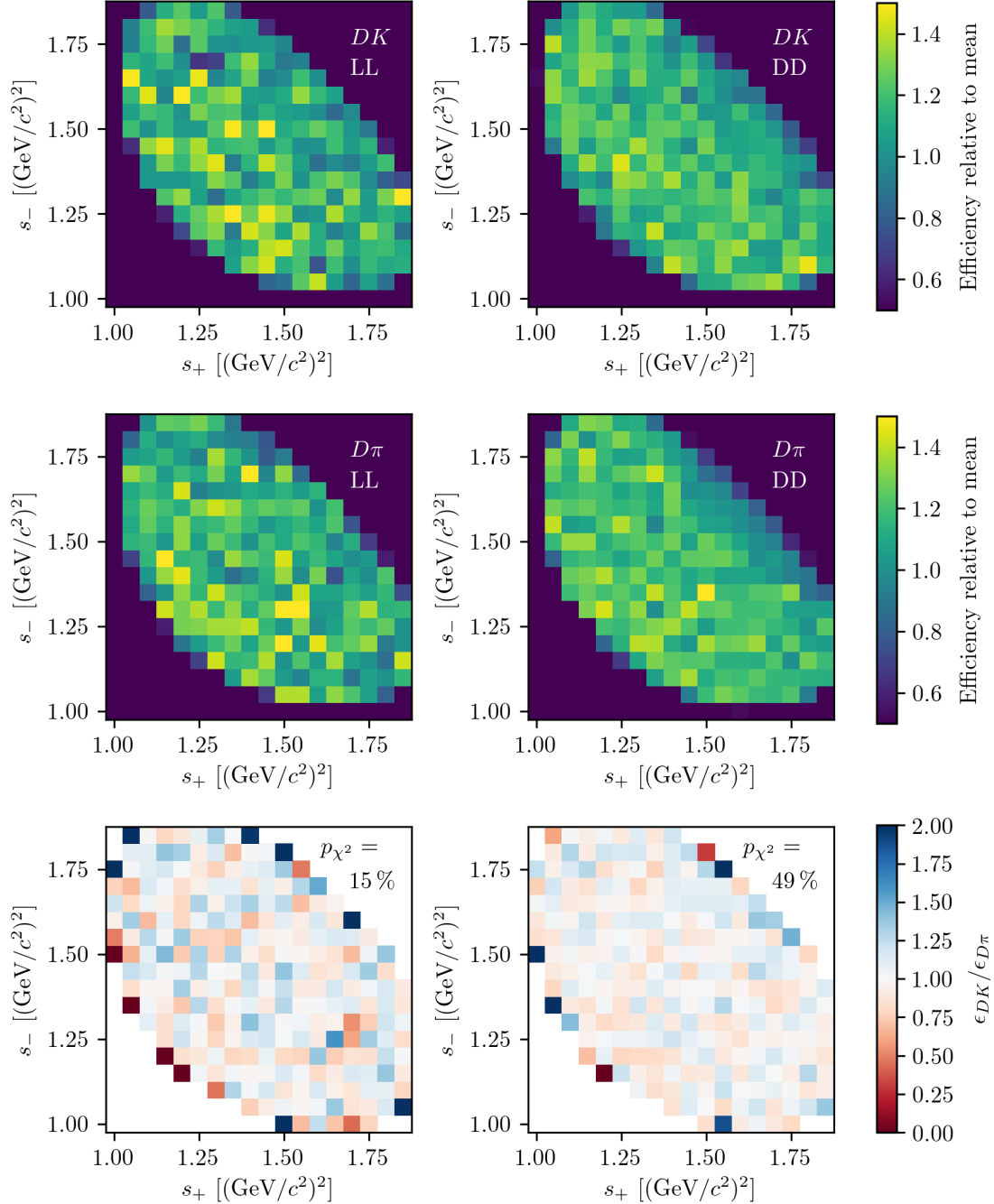


**Figure 5.11:** The acceptance profile in simulated samples of (top row)  $B \rightarrow DK$  decays and (centre row)  $B \rightarrow D\pi$  decays where  $D \rightarrow K_S^0 K^+ K^-$ , as well as (bottom row) the ratio between the two histograms. The plots are shown for candidates in the (left) LL and (right) DD categories. The  $p$  values are the results of  $\chi^2$  compatibility tests between the two histograms.

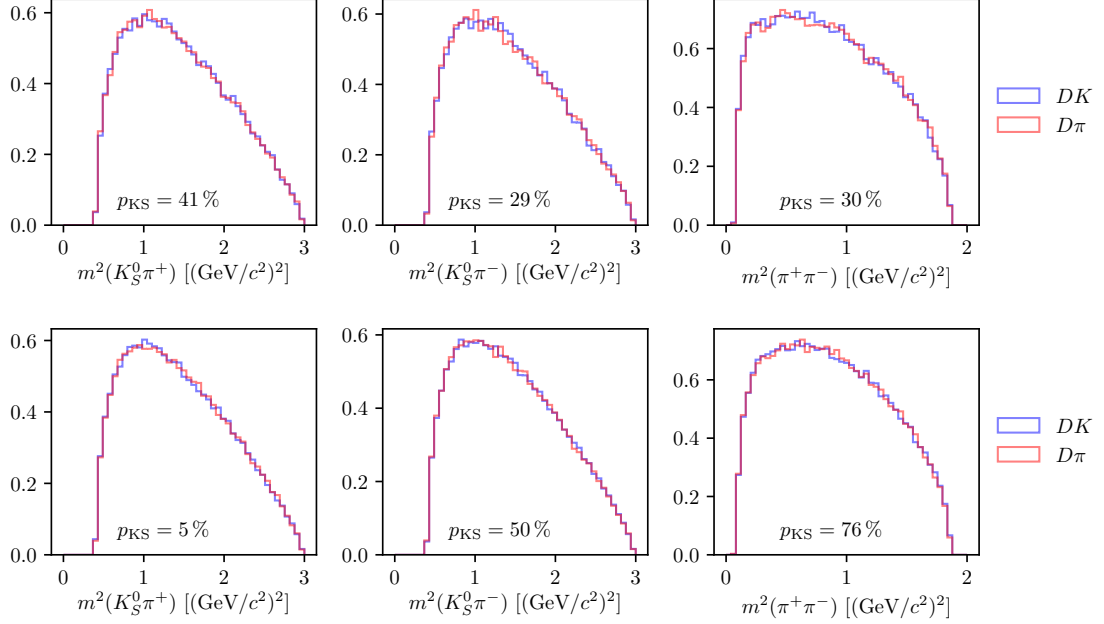


**Figure 5.12:** One-dimensional distributions of  $m^2(K_S^0\pi^+)$ ,  $m^2(K_S^0\pi^-)$ , and  $m^2(\pi^+\pi^-)$  in simulated (blue)  $B^\pm \rightarrow DK^\pm$  and (red)  $B^\pm \rightarrow D\pi^\pm$  decays where  $D \rightarrow K_S^0\pi^+\pi^-$  in the (top) LL and (bottom) DD categories. The  $p$  values are the results of Kolmogorov-Smirnov compatibility tests between the distributions.

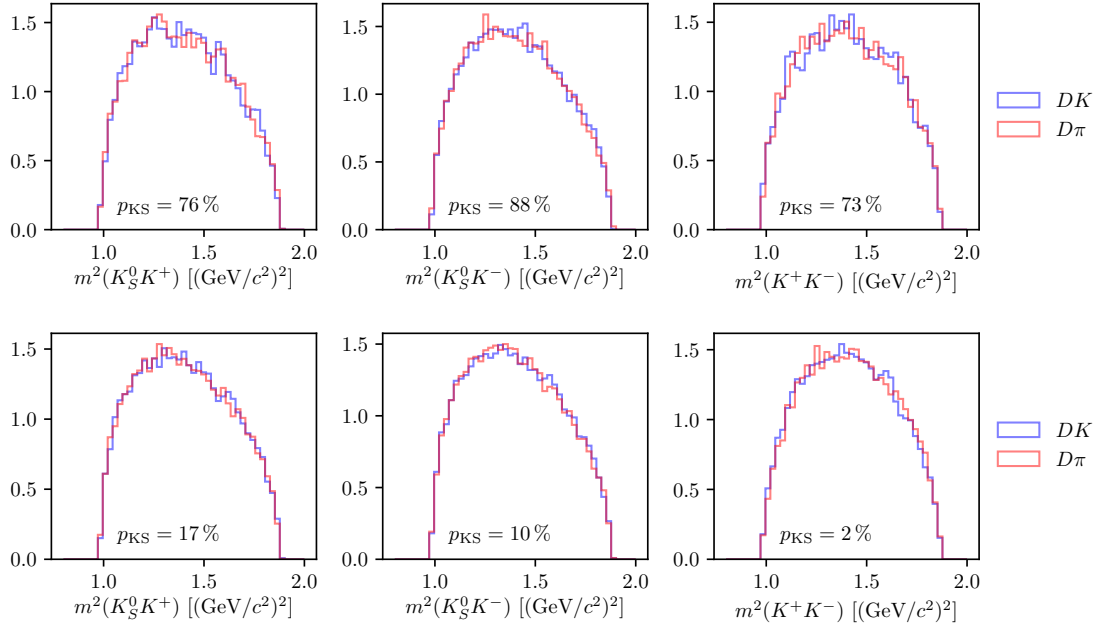


**Figure 5.13:** One-dimensional distributions of  $m^2(K_S^0K^+)$ ,  $m^2(K_S^0K^-)$ , and  $m^2(\pi^+\pi^-)$  in simulated (blue)  $B^\pm \rightarrow DK^\pm$  and (red)  $B^\pm \rightarrow D\pi^\pm$  decays where  $D \rightarrow K_S^0K^+K^-$  in the (top) LL and (bottom) DD categories. The  $p$  values are the results of Kolmogorov-Smirnov compatibility tests between the distributions.

2201     • Backgrounds that are present at a level where they have to be modelled in  
 2202       the fit to data, and cannot effectively be rejected further in the selection

2203     The latter category comprises of combinatorial background, which remains present  
 2204     at a non-negligible level after the application of the BDT described in Section 5.1.2;  
 2205     contributions from a number of partly reconstructed  $B \rightarrow Dh^\pm X$  decays, where  
 2206      $X$  denotes a pion or photon that is not included in the reconstructed decay, and  
 2207     which can only be separated from signal decays by their  $m(Dh)$  distribution; and  
 2208     finally  $B^\pm \rightarrow D\pi^\pm$  decays that are categorised as  $B^\pm \rightarrow DK^\pm$  decays in the particle-  
 2209     identification step and vice-versa. These background sources are described in detail  
 2210     in Section 5.4. This section focuses on backgrounds that led to specific requirements  
 2211     in the selection or proved to be small enough to not merit special treatment.

### 2212     5.3.1 Charmless decays

2213     There is potentially a so-called *charmless* background present in data, consisting  
 2214     of  $B^\pm \rightarrow K_S^0 h^+ h^- h^\pm$  decays. These have the same final state as the signal decay,  
 2215     but no intermediate  $D$  meson. Because all final state particles are reconstructed,  
 2216     this background peaks in the  $B$  mass spectrum. This background is suppressed  
 2217     by requiring the reconstructed  $B$  and  $D$  decay vertices to be separated in the  
 2218      $z$  direction; specifically by requiring that  $\Delta z_{\text{significance}}^{D-B} > 0.5$ , where  $\Delta z_{\text{significance}}^{D-B}$   
 2219     was defined in Eq. (5.1). The remaining background level can be investigated  
 2220     by investigating the  $D$  mass sidebands.

2221     However, the use of the `DecayTreeFitter`  $\chi^2_{\text{DTF}}$  as an input variable in the BDT  
 2222     removes essentially all of the  $D$  (and  $K_S^0$ ) sideband, due to the mass constraints in  
 2223     the decay chain fit. Therefore separate BDT's are trained for LL and DD candidates  
 2224     without the  $\chi^2_{\text{DTF}}$  as an input variable, and used when selecting candidates for  
 2225     the background studies presented in this section, and the following. In a similar  
 2226     manner, all mass window requirements are made on the *default* reconstructed  
 2227     masses, obtained with no use of `DecayTreeFitter`. The overlap of the two sets  
 2228     of selected candidates in the signal  $B$ -mass window is above 95 %.

2229     The reconstructed  $B$  mass spectrum is shown for  $B^\pm \rightarrow D\pi^\pm$  candidates in the  
 2230      $D$  sidebands in Fig. 5.14, both before and after making a requirement on  $\Delta z_{\text{significance}}^{D-B}$ .  
 2231     The check is based on the upper  $D$  sideband for  $D \rightarrow K_S^0 \pi^+ \pi^-$  decays and the  
 2232     lower  $D$  sideband for  $D \rightarrow K_S^0 K^+ K^-$  decays to avoid contamination from real  
 2233      $B^\pm \rightarrow Dh^\pm$  decays with subsequent  $D \rightarrow K_S^0 K^\pm \pi^\mp$  decays, or crossfeed between the  
 2234     two signal  $D$ -decay modes. A peak is clearly visible, the size of which is reduced by  
 2235     the requirement. This peak is partly due to a contribution from  $B^\pm \rightarrow K_S^0 \pi^+ \pi^- \pi^\pm$

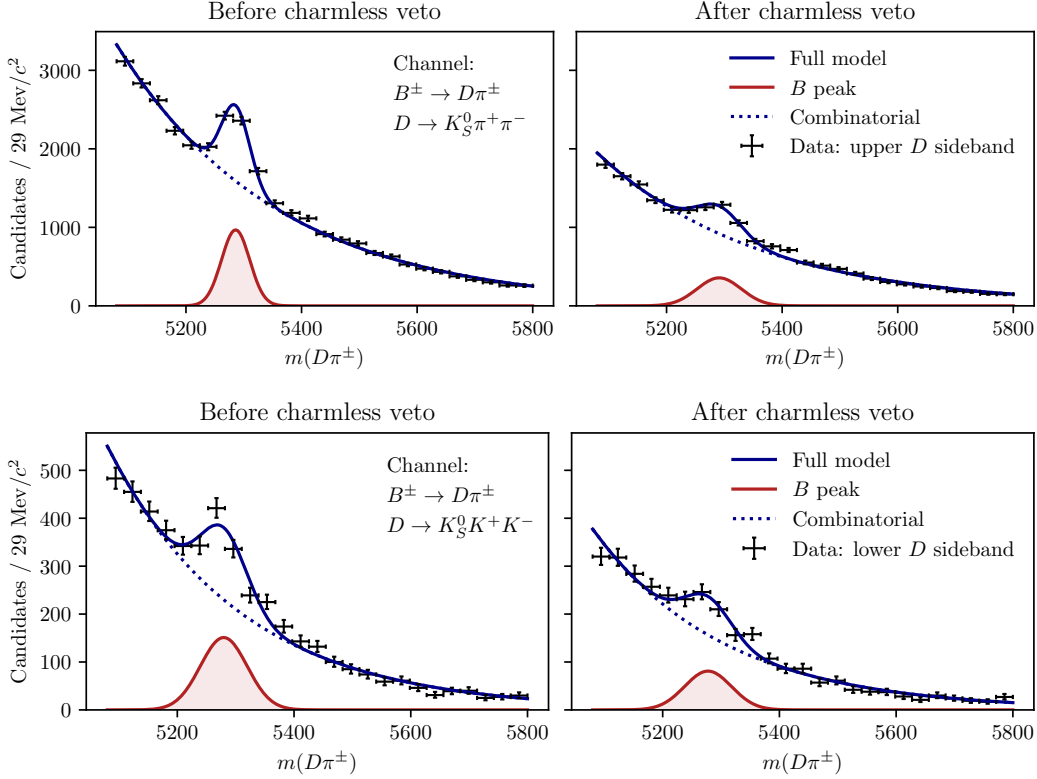


**Figure 5.14:** The  $B$  mass distribution of (top)  $B^\pm \rightarrow D(\rightarrow K_S^0 \pi^+ \pi^-)\pi^\pm$  and (bottom)  $B^\pm \rightarrow D(\rightarrow K_S^0 K^+ K^-)\pi^\pm$  candidates reconstructed in both the LL and DD categories, residing in the upper  $D$  mass sideband  $m_D \in [1910, 1960] \text{ MeV}/c^2$  for  $D \rightarrow K_S^0 \pi^+ \pi^-$  and in the lower sideband  $m_D \in [1910, 1960] \text{ MeV}/c^2$  for  $D \rightarrow K_S^0 K^+ K^-$ , with (left) no requirement on  $\Delta z_{\text{significance}}^{BD}$  and (right) after a requirement of  $\Delta z_{\text{significance}}^{BD} > 0.5$ .

decays ( $B^\pm \rightarrow K_S^0 K^+ K^- \pi^\pm$  decays) in the  $D \rightarrow K_S^0 \pi^+ \pi^-$  ( $D \rightarrow K_S^0 K^+ K^-$ ) channel, and partly due to real signal decays that leak into the  $D$  sidebands. The number of real signal decays can be calculated from the yield obtained in the fit of Section 5.4, and the reconstructed  $m_D$  distribution in simulated signal decays. Subtracting this contribution, it is estimated that approximately 450 (200) charmless decays are present in the  $K_S^0 \pi^+ \pi^-$  ( $K_S^0 K^+ K^-$ ) data samples. In similar fashion, Fig. 5.15 shows the  $m_B$  spectra for  $B^\pm \rightarrow DK^\pm$  candidates in the  $D$  sidebands. In these plots, the peaks are at  $m_B$  values that are lower (higher) than the  $B$  mass in the  $K_S^0 \pi^+ \pi^-$  ( $K_S^0 K^+ K^-$ ) categories, because they stem from real  $B^\pm \rightarrow K_S^0 K^+ K^- \pi^\pm$  decays where a kaon is mis-reconstructed as a pion or a pion is misreconstructed as a kaon, respectively. The total contribution of charmless decays in the  $B^\pm \rightarrow DK^\pm$  data samples is estimated to be about 200 decays. As described further in Section 5.6.11, the presence of a charmless background at these levels has a negligible impact on the measurement results. It is not favourable to tighten the requirement further due to the associated loss in the selection efficiency of signal decays.

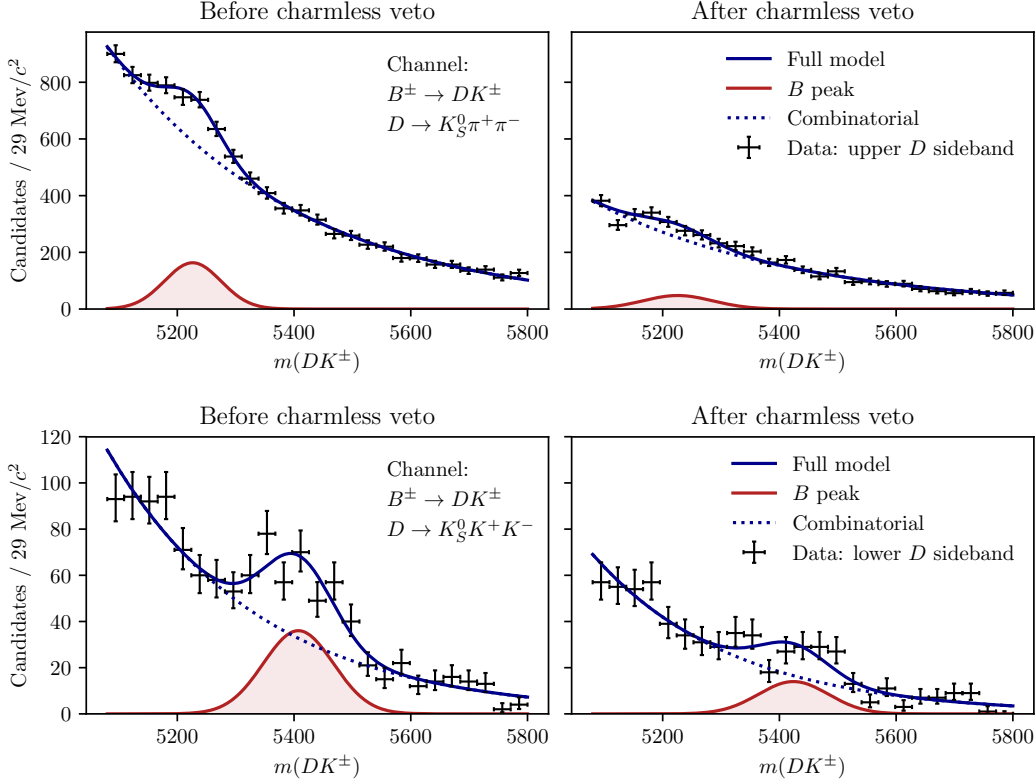


**Figure 5.15:** The  $B$  mass distribution of (top)  $B^\pm \rightarrow D(\rightarrow K_S^0 \pi^+ \pi^-)K^\pm$  and (bottom)  $B^\pm \rightarrow D(\rightarrow K_S^0 K^+ K^-)K^\pm$  candidates reconstructed in both the LL and DD categories, residing in the upper  $D$  mass sideband  $m_D \in [1910, 1960] \text{ MeV}/c^2$  for  $D \rightarrow K_S^0 \pi^+ \pi^-$  and in the lower sideband  $m_D \in [1910, 1960] \text{ MeV}/c^2$  for  $D \rightarrow K_S^0 K^+ K^-$ , with (left) no requirement on  $\Delta z_{\text{significance}}^{BD}$  and (right) after a requirement of  $\Delta z_{\text{significance}}^{BD} > 0.5$ .

### 2251 5.3.2 Background from four-body $D$ decays

2252 A similar potential background is from real  $B^\pm \rightarrow Dh^\pm$  decays where the  $D$  meson  
 2253 decays directly to the  $\pi^+ \pi^- h^+ h^-$  final state, without an intermediate  $K_S^0$  meson.  
 2254 This background can be investigated by looking for a peak in the  $B$  mass spectrum  
 2255 for candidates in the  $K_S^0$  sideband, as illustrated in Fig. 5.16. The figure shows  
 2256 the spectrum in the final data sample, illustrating the significant effect of making  
 2257 the requirement on the  $K_S^0$  flight distance that was discussed in Section 5.1.1. The  
 2258 BDT that does *not* rely on the DTF  $\chi^2$  has been used to suppress combinatorial  
 2259 background. The remaining peak after requiring  $\chi_{\text{FD}}^2 > 49$  is completely accounted  
 2260 for by real signal decays that leak into the  $K_S^0$  sideband. The requirement is  
 2261 made for candidates in the LL category only; if the pions stemming from a  $K_S^0$   
 2262 candidate are reconstructed as downstream tracks it implies that the  $K_S^0$  has  
 2263 travelled from the interaction region.

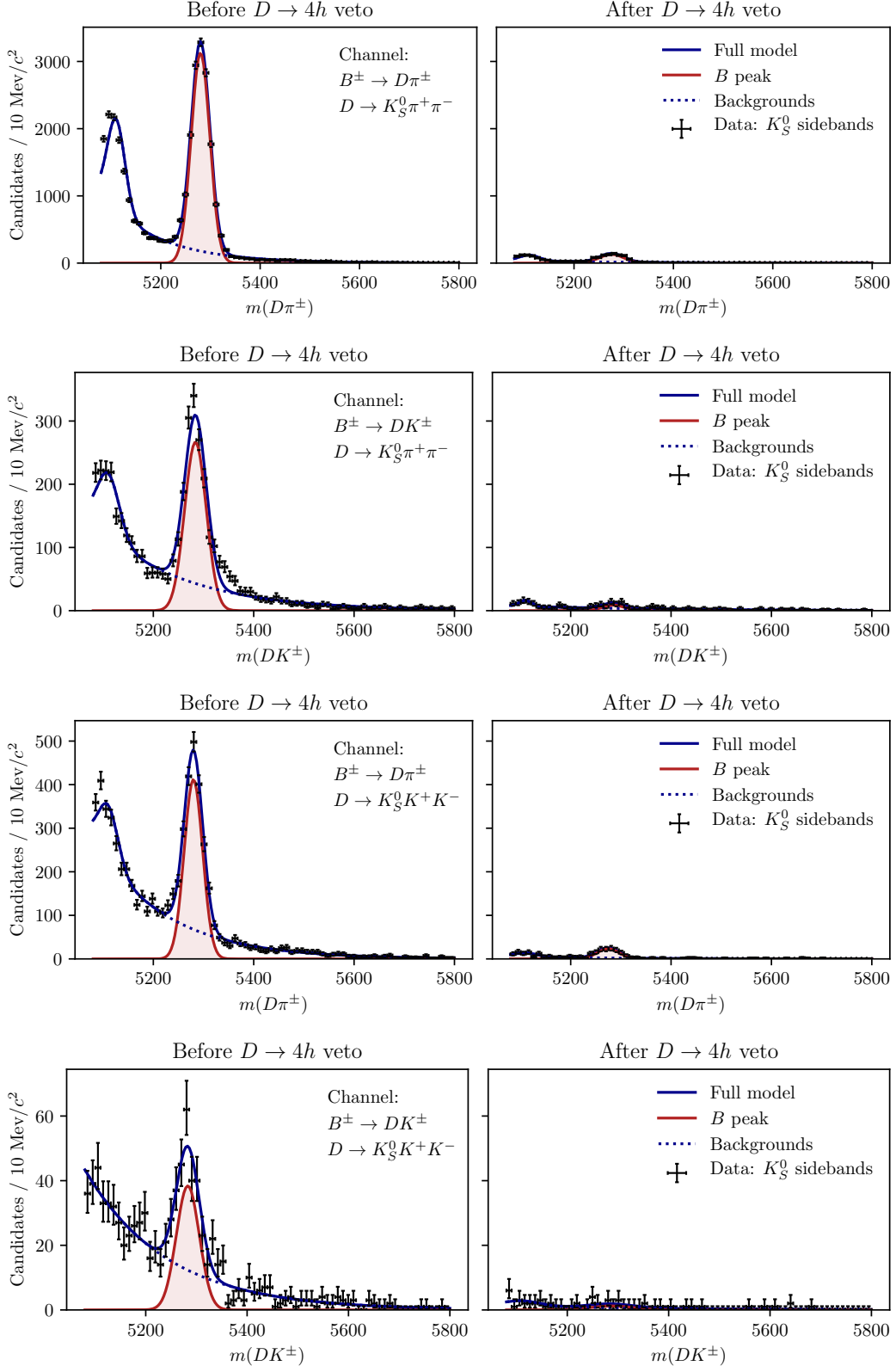


**Figure 5.16:** The  $B$  mass spectrum in the  $K_S^0$  sideband where  $m_{K_S^0} \in [467, 482] \text{ MeV}/c^2$  or  $m_{K_S^0} \in [512, 527] \text{ MeV}/c^2$  (left) without a requirement on the  $K_S^0$  flight distance significance, and (right) after the requirement implemented in the analysis.

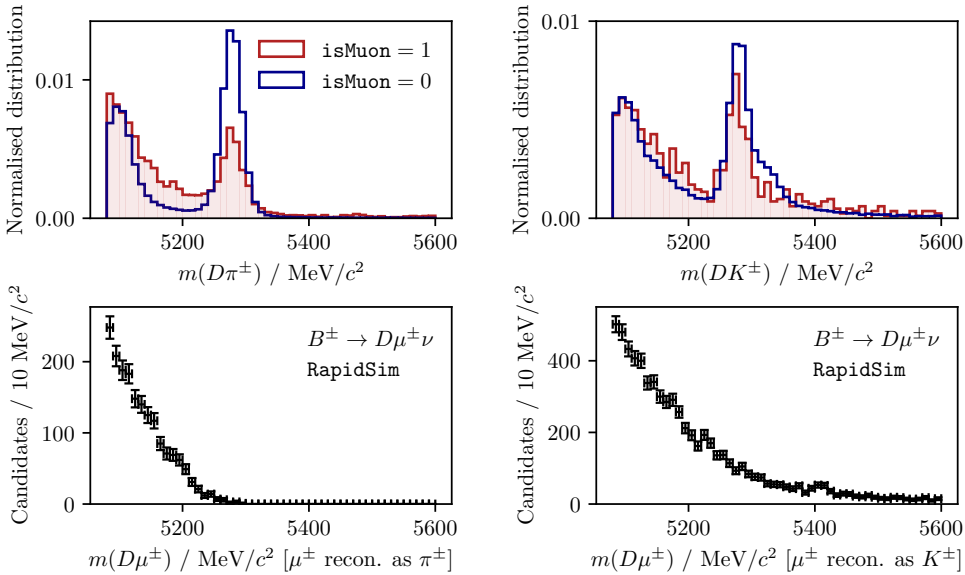


**Figure 5.17:** (Top) The  $m_B$  spectra in data split by the value of `isMuon` for the companion particle, in (left) the  $D\pi^\pm$  and (right) the  $DK^\pm$  samples where  $D \rightarrow K_S^0 \pi^+ \pi^-$ . The two histograms are normalised independently, so that the distributions can be compared. The fractions of candidates in data (with  $m_B \in [5080, 5800] \text{ MeV}/c^2$ ) where the companion satisfies `isMuon=1` are 1.6 % and 1.8 % for the  $D\pi^\pm$  and  $DK^\pm$  channels respectively. (Bottom) the `RapidSim` mass spectra for  $B^\pm \rightarrow D^0 \mu^\pm \nu_\mu$  decays reconstructed in the (left)  $D\pi^\pm$  and (right)  $DK^\pm$  categories.

### 2264 5.3.3 Semi-leptonic backgrounds

2265 The data sample has a minor background from  $B \rightarrow D\mu\nu_\mu X$  decays, visible  
 2266 in the  $B$  mass spectrum when the companion is required to satisfy `isMuon=1`.  
 2267 This is shown in Fig. 5.17 for both the  $B^\pm \rightarrow DK^\pm$  and  $B^\pm \rightarrow D\pi^\pm$  channels  
 2268 where  $D \rightarrow K_S^0 \pi^+ \pi^-$ . The  $B$  mass spectra for simulated  $B^\pm \rightarrow D\mu^\pm \nu_\mu$  decays  
 2269 reconstructed in each category are also shown, from simulation samples produced via  
 2270 `RapidSim`. The background is very efficiently vetoed by requiring `IsMuon=0` on the  
 2271 companion. This requirement removes approximately 85 % of the background decays,  
 2272 as estimated using the `PIDCalib` calibration samples and the  $(p, p_T)$  distribution  
 2273 for the muon in the `RapidSim` samples. The fraction of signal candidates for which  
 2274 the companion satisfies `IsMuon=1` in simulated signal samples is  $\leq 0.9$  % so the  
 2275 impact on signal yield is small.

2276 The analogous  $B \rightarrow D e \nu_e X$  background is investigated by inspecting the  $B$   
 2277 mass spectra after making requirements on `PIDe` for the companion candidate, but  
 2278 a presence of the semi-leptonic background in data is not visible and no electron  
 2279 veto is applied to the companion.

2280 **Background from semi-leptonic D decays**

2281 There is a potential background from real  $B^\pm \rightarrow Dh^\pm$  decays where the  $D$   
2282 meson decays semi-leptonically:  $D^0 \rightarrow K_S^0\pi^-\ell^+\nu_\ell$ . This background is particularly  
2283 dangerous because it peaks at the  $B$  mass, when the  $D$ -mass requirement is applied  
2284 and it is reconstructed in the  $D \rightarrow K_S^0\pi^+\pi^-$  category. This is illustrated in  
2285 Fig. 5.18 using **RapidSim** samples of  $B^\pm \rightarrow D(\rightarrow K^{*-}(\rightarrow K_S^0\pi^-)\ell^+\nu_\ell)h^\pm$  decays  
2286 for  $K^* \in \{K^*(892), K_0^*(1430), K_2^*(1430), K^*(1680)\}$ . The respective spin of each  
2287 resonance is taken into account in generation, by handling the decay via **EVTGEN**.  
2288 The expected background yields relative to signal can be estimated by applying the  $B$   
2289 and  $D$  mass cuts to decays in the **RapidSim** samples, and using the relative branching  
2290 ratios. Only the  $D^0 \rightarrow K^{*-}(892)\ell\nu_\ell$  branching fractions have been measured [31],  
2291 but there is no reason to expect that higher  $K^*$  resonances should not contribute.  
2292 To estimate their potential contribution, the branching ratios are approximated by

$$\text{BR}[D^0 \rightarrow K^{*-}(X)(\rightarrow K_S^0\pi^-)\ell\nu_\ell] \simeq \frac{\text{BR}[D^0 \rightarrow K^{*-}(X)(\rightarrow K_S^0\pi^-)\pi^+]}{\text{BR}[D^0 \rightarrow K^{*-}(892)(\rightarrow K_S^0\pi^-)\pi^+]} \text{BR}[D^0 \rightarrow K^{*-}(892)(\rightarrow K_S^0\pi^-)\ell\nu_\ell]$$

2293 because all the relevant  $D^0 \rightarrow K^{*-}(\rightarrow K_S^0\pi^-)\pi^+$  branching fractions are known [31].  
2294 The efficiencies and branching ratios relative to the signal channel are given in  
2295 Table 5.5. It is clear that the higher  $K^*$  resonances are important: the smaller  
2296 branching ratios are compensated for by a higher selection efficiency, due to the  
2297 smaller phase-space of the missed neutrino. The total background yield is 1.1 %  
2298 of the signal yield in both the  $B^\pm \rightarrow D\pi^\pm$  and  $B^\pm \rightarrow DK^\pm$  channels. However,  
2299 there will be an additional contribution in the  $B^\pm \rightarrow DK^\pm$  channel from real  
2300  $B^\pm \rightarrow D\pi^\pm$  decays with semi-leptonic  $D$  decays and a mis-identification of the  
2301 companion. This background also peaks, and the yield is approximately 0.4 %  
2302 of the  $B^\pm \rightarrow DK^\pm$  signal yield.

2303 The potential impact from the presence of the background is estimated by

- 2304 1. calculating the expected  $B^\pm \rightarrow D\pi^\pm$  and  $B^\pm \rightarrow DK^\pm$  signal yields in each  
2305 bin for physics parameters similar to the world average values
- 2306 2. then calculating the background bin yields in each bin, using the relative  
2307 branching fractions and efficiencies described above and taking the bin-  
2308 distribution from the **RapidSim** samples. The **RapidSim** samples are produced  
2309 using the **ISGW2** model in **EVTGEN** [122], yielding the Dalitz distributions in  
2310 Fig. 5.19.

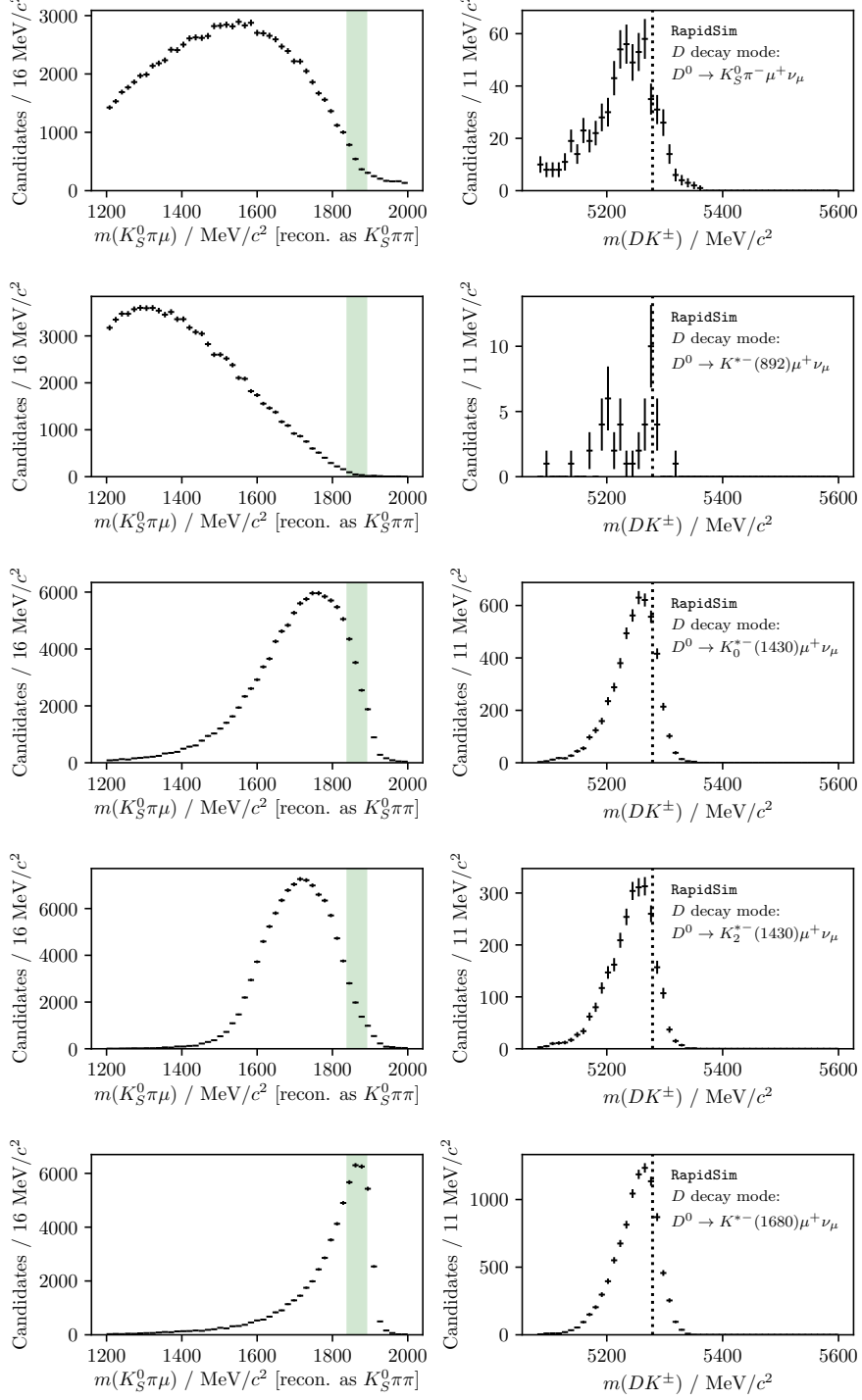


**Figure 5.18:** The reconstructed (left)  $m(K_S^0\pi^+\pi^-)$  and (right)  $m(Dh)$  distributions in **RapidSim** samples of  $B^\pm \rightarrow DK^\pm$  decays where  $D^0 \rightarrow K_S^0\pi^-\mu^+\nu_\mu$ . The top plot is for decays that were uniformly distributed over phase space, and the following plots show the distribution where the  $K_S^0\pi^-$  originate in the resonances  $K^{*-}(892)$ ,  $K_0^{*-}(1430)$ ,  $K_2^{*-}(1430)$ , and  $K^{*-}(1680)$ . The shapes for the  $D^0 \rightarrow K_S^0\pi^-e^+\nu_e$  case are almost identical.

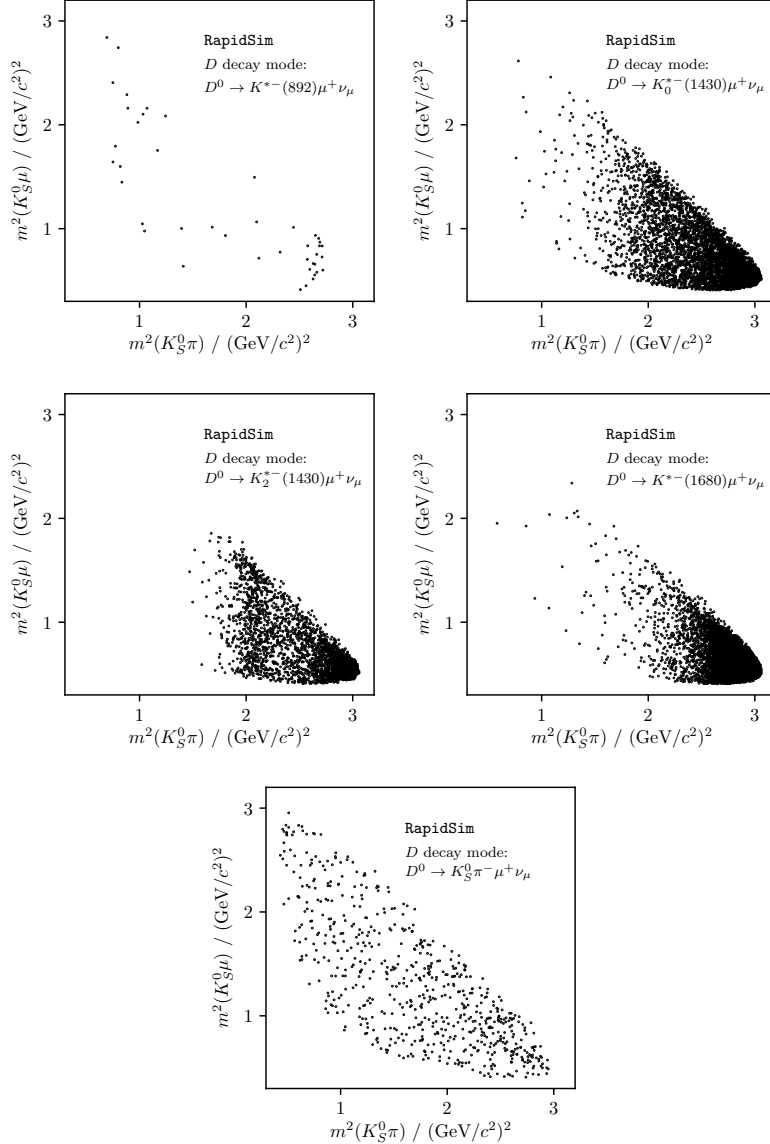


**Figure 5.19:** Dalitz distribution for  $D \rightarrow K_S^0 \pi \mu \nu_\mu$  decays in **RapidSim**, where the  $K_S^0 \pi^-$  originate in the resonances  $K^{*-}(892)$ ,  $K_0^{*-}(1430)$ ,  $K_2^{*-}(1430)$ , and  $K^{*-}(1680)$ , as well as for a uniform distribution over phase space.

2311     3. adding the signal and background yields, and fitting the new  $B^\pm \rightarrow D\pi^\pm$  and  
 2312      $B^\pm \rightarrow DK^\pm$  yields back with the default signal-yield expressions (including a  
 2313     fit of the  $F_i$  parameters)

2314     The obtained biases are shown in Fig. 5.20, where they are calculated a number  
 2315     of times, each time varying the efficiencies within statistical uncertainties and the  
 2316     relevant branching fractions within the measurement uncertainties. The systematic  
 2317     uncertainty due to the unknown branching fractions and the use of **RapidSim** in  
 2318     lieu of full simulation is not included, but is of course significant. Nevertheless

**Table 5.5:** The selection efficiencies of  $B^\pm \rightarrow DK^\pm$  decays where  $D^0 \rightarrow K_S^0\pi^-\ell^+\nu_\ell$  when reconstructed in the  $D \rightarrow K_S^0\pi^+\pi^-$  mode in **RapidSim** relative to the signal selection efficiencies, for a number of decay modes: PHSP as well as resonant production where the  $K_S^0\pi^-$  pair originates in one of several  $K^*$  resonances. The relative branching ratios are also shown, calculated as explained in the main text, as well as the predicted relative yields.

Mode	$\epsilon_{bkg}/\epsilon_{signal}$ (%)	$\Gamma_{bkg}/\Gamma_{signal}$ (%)	$N_{bkg}/N_{signal}$ (%)
$D \rightarrow K_S^0\pi^-\mu^+\nu_\mu$ (PHSP)	$0.92 \pm 0.05$	$18.3 \pm 14.8$	$0.17 \pm 0.14$
$D \rightarrow (K_S^0\pi^-)_{K^{*-}(892)}\mu^+\nu_\mu$	$0.06 \pm 0.01$	$22.3 \pm 3.2$	$0.013 \pm 0.003$
$D \rightarrow (K_S^0\pi^-)_{K_0^{*-}(1430)}\mu^+\nu_\mu$	$7.3 \pm 0.1$	$3.7 \pm 0.8$	$0.27 \pm 0.06$
$D \rightarrow (K_S^0\pi^-)_{K_2^{*-}(1430)}\mu^+\nu_\mu$	$3.7 \pm 0.1$	$0.5 \pm 0.3$	$0.02 \pm 0.01$
$D \rightarrow (K_S^0\pi^-)_{K^{*-}(1680)}\mu^+\nu_\mu$	$24.4 \pm 0.3$	$0.6 \pm 0.5$	$0.15 \pm 0.12$
$D \rightarrow K_S^0\pi^-e^+\nu_e$ (PHSP)	$0.53 \pm 0.02$	$20.8 \pm 16.3$	$0.11 \pm 0.09$
$D \rightarrow (K_S^0\pi^-)_{K^{*-}(892)}e^+\nu_e$	$0.15 \pm 0.02$	$25.6 \pm 2.5$	$0.04 \pm 0.01$
$D \rightarrow (K_S^0\pi^-)_{K_0^{*-}(1430)}e^+\nu_e$	$6.3 \pm 0.1$	$4.2 \pm 0.8$	$0.26 \pm 0.05$
$D \rightarrow (K_S^0\pi^-)_{K_2^{*-}(1430)}e^+\nu_e$	$4.12 \pm 0.08$	$0.5 \pm 0.3$	$0.02 \pm 0.01$
$D \rightarrow (K_S^0\pi^-)_{K^{*-}(1680)}e^+\nu_e$	$10.0 \pm 0.2$	$0.7 \pm 0.5$	$0.07 \pm 0.05$
Total	-	-	$1.1 \pm 0.4$

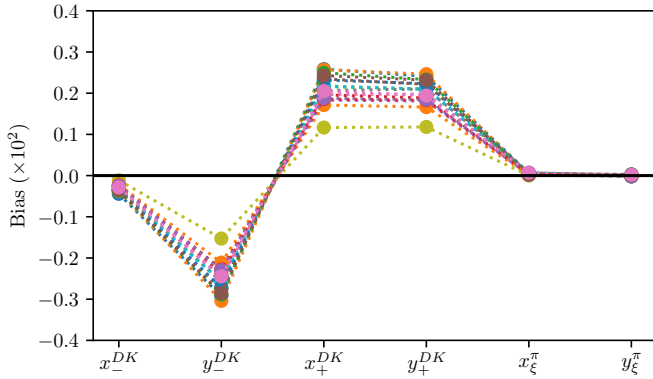


**Figure 5.20:** Estimated biases on the measured observables due to the presence of  $D \rightarrow K_S^0\pi\ell\nu_\ell$  backgrounds, calculated while varying efficiencies and branching ratios within uncertainties.

it is clear that the potential biases are significant compared to the size of the systematic uncertainties of the analysis presented in Section 5.6. Therefore the backgrounds are vetoed by requiring `IsMuon=0` and `PIDe < 0` on the pions from the  $D$ -decay with opposite charge to the companion in the  $D \rightarrow K_S^0\pi^+\pi^-$  channel. This requirement removes 88 % of the muonic background and 99 % of the electron background, according to PID efficiencies obtained via the `PIDCalib` package, using the  $(p, p_T)$  distribution for the muon/electron in the **RapidSim** samples. The

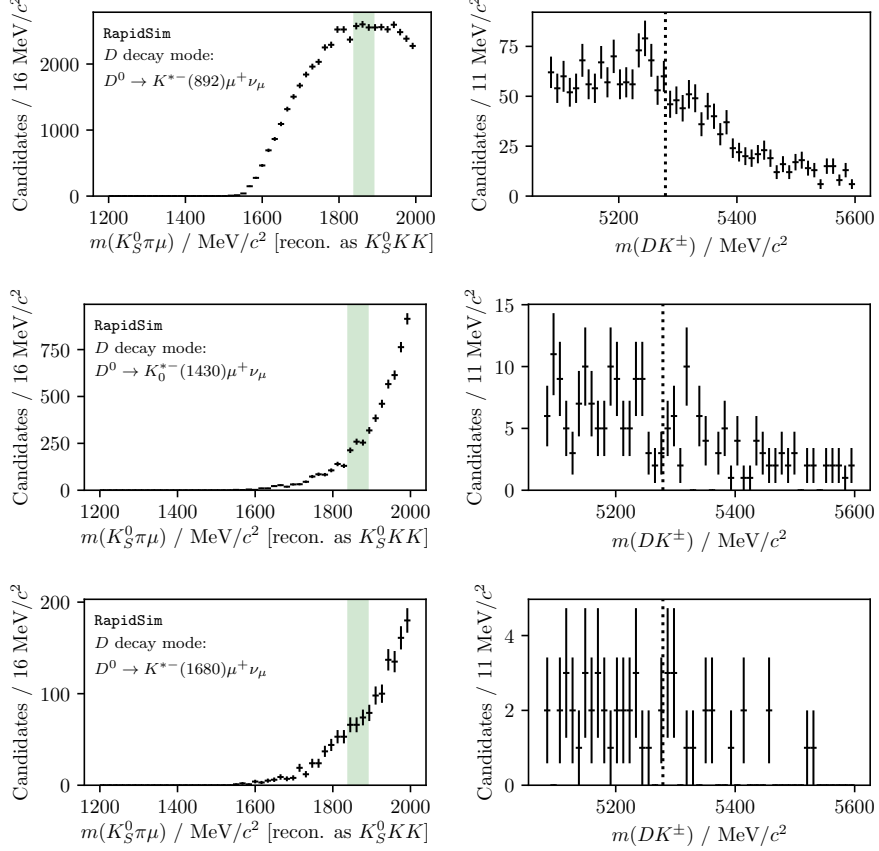


**Figure 5.21:** The reconstructed (left)  $m(K_S^0 K^+ K^-)$  and (right)  $m(Dh)$  distributions in **RapidSim** samples of  $B^\pm \rightarrow DK^\pm$  decays where  $D^0 \rightarrow K_S^0\pi^-\mu^+\nu_\mu$ , where the  $K_S^0\pi^-$  originate in (top to bottom) the resonances  $K^{*-}(892)$ ,  $K_0^{*-}(1430)$ , and  $K^{*-}(1680)$ . The shapes for the  $D^0 \rightarrow K_S^0\pi^-e^+\nu_e$  case are almost identical.

survival rate for signal decays in full simulation is 94 %, so the impact on the obtainable precision is only about 3 %. A systematic uncertainty is assigned to account for the potential remaining background.

In the  $D \rightarrow K_S^0 K^+ K^-$  channel an analogous study shows the relative yields to be similar. The selection efficiencies are higher, as are the relative branching ratios due to the lower  $D \rightarrow K_S^0 K^+ K^-$  branching fraction, but in this mode the PIDK > -5 requirement placed on the pion and lepton removes approximately 90 % of the background, leaving the relative rate similar to in  $D \rightarrow K_S^0\pi^+\pi^-$ . However, importantly, *the background is not peaking*, as shown in Fig. 5.21. The presence of a percent-level, *non-peaking* background in the  $D \rightarrow K_S^0 K^+ K^-$  channel is safe to ignore and thus no veto is applied to remove semileptonic  $D$  decays in the  $D \rightarrow K_S^0 K^+ K^-$  channel.

The muon-veto for the semi-leptonic background does remove some signal decays, where an original pion or kaon results in hits in the muon detectors. A

2340 significant contribution is from particles that decay in flight. The track quality  
 2341 of these decays is worse than for nominal decays, which affects the resolution on  
 2342 the reconstructed Dalitz coordinates. In simulated signal decays the standard  
 2343 deviation of  $\Delta m_\pm^2 = m_{reco}^2(K_S^0\pi^\pm) - m_{TRUE}^2(K_S^0\pi^\pm)$  is 50 % larger for decays where  
 2344 one of the  $D$ -decay products has `IsMuon=1` than in decays where this is not the  
 2345 case. This can lead to systematic biases on the observables, as described further in  
 2346 Section 5.6.7. The overall effect is small, as evidenced by the systematic uncertainty  
 2347 described in that section; nevertheless this fact motivates removing decay-in-flight  
 2348 decays of the  $D$ -decay products. Therefore it is also required that `IsMuon=0` for  
 2349 the  $D$ -decay pion with the same charge as the companion in the  $D \rightarrow K_S^0\pi^+\pi^-$   
 2350 channels, and on the  $D$ -decay kaons in the  $D \rightarrow K_S^0K^+K^-$  channels. This veto  
 2351 removes about 2 % of signal candidates in simulation that survive the lepton vetoes  
 2352 described in the previous sections.

### 2353 5.3.4 Cross-feed from other $D \rightarrow K_S^0h^+h^-$ decays

2354 Misidentification of a  $D$  decay product can lead to background from cross-feed be-  
 2355 tween the  $B^\pm \rightarrow D(\rightarrow K_S^0\pi^+\pi^-)h^\pm$  and  $B^\pm \rightarrow D(\rightarrow K_S^0K^+K^-)h^\pm$  signal channels,  
 2356 or cross-feed from  $B^\pm \rightarrow D(\rightarrow K_S^0K\pi)h^\pm$  decays into either of the signal channels.  
 2357 However, this background is very highly suppressed by the employed requirement  
 2358 on the  $D$  mass. This is illustrated in Fig. 5.22, where the  $D$  mass distribution in  
 2359 samples of simulated  $B^\pm \rightarrow D(\rightarrow K_S^0K\pi)K^\pm$  decays are shown, when reconstructed  
 2360 as  $D \rightarrow K_S^0\pi^+\pi^-$  and  $D \rightarrow K_S^0K^+K^-$  decays. Essentially no decays that fall in  
 2361 the selected  $D$  mass window survive the full selection. Therefore this background  
 2362 is not considered further. Neither is the background due to cross-feed between  
 2363  $B^\pm \rightarrow D(\rightarrow K_S^0\pi^+\pi^-)h^\pm$  and  $B^\pm \rightarrow D(\rightarrow K_S^0K^+K^-)h^\pm$ , since it involves two  
 2364 misidentified particles, and therefore will result in reconstructed  $D$  masses even  
 2365 further away from the selected mass window. A very loose PID requirement on the  
 2366 charged  $D$  decay products is nonetheless included in the  $D \rightarrow K_S^0K^+K^-$  channel,  
 2367 because it helps reduce the level of combinatorial background.

### 2368 5.3.5 Swapped-track backgrounds

2369 A possible peaking background stems from real  $B \rightarrow DhX$  decays with the  
 2370 same final state tracks as in the signal case, but where some tracks are mis-  
 2371 assigned in the reconstruction. Examples are  $B^+ \rightarrow (K_S^0h^+h^-)_D h^+$  decays where  
 2372 the companion and the  $D$ -decay product with the same charge are swapped, or  
 2373  $B^\pm \rightarrow (K^-\pi^+)_D K_S^0 h^\pm$  decays, where the  $K_S^0$  is assigned to the  $D$  decay and the

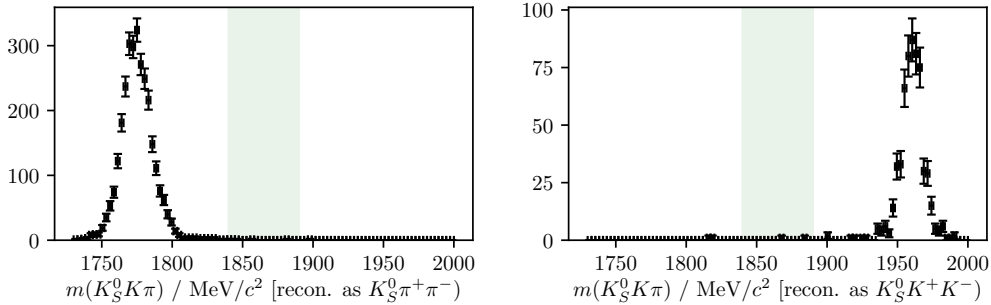


**Figure 5.22:** Simulated samples of  $B^\pm \rightarrow D(\rightarrow K_S^0 K\pi)\pi^\pm$  decays reconstructed in the (left)  $D \rightarrow K_S^0 \pi^+ \pi^-$  and (right)  $D \rightarrow K_S^0 K^+ K^-$  channels, combining the LL and DD categories. The  $D$ -mass region included in the selection of signal decays is illustrated with the green band. The plots in the  $B^\pm \rightarrow DK^\pm$  channels look almost identical.

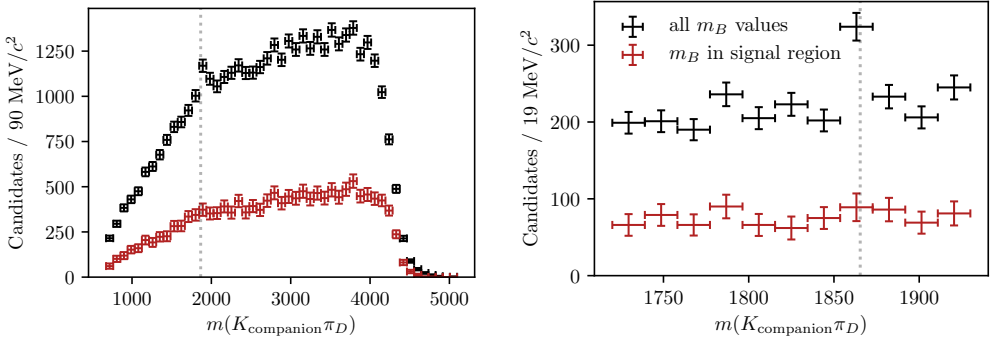


**Figure 5.23:** Invariant mass spectrum of the  $m^2(K^\pm \pi^\mp)$  combination in the  $B^\pm \rightarrow (K_S^0 \pi^+ \pi^-)K^\pm$  data sample for (black) all candidates and (red) candidates for which  $m_B \in m_B^{PDG} \pm 30 \text{ MeV}/c^2$ . The LL and DD categories are combined. The only difference between the left and right plots is the  $m(K\pi)$  mass range on the horizontal axis. The dotted line indicated the known  $D$  mass [31].

real companion is swapped with the  $D$ -decay product of the same charge. The signature of this background type is a peak at the  $D$  mass, when the invariant mass corresponding to the companion track and some subset of the  $D$ -decay tracks is formed. The presence of the background has been investigated by forming all such combinations, for all data categories, after the full selection has been applied. Only in a single channel is a peak visible: the  $B^\pm \rightarrow (K_S^0 \pi^+ \pi^-)K^\pm$  channel, where  $m(K^\pm \pi^\mp)$  has a peak, as shown in Fig. 5.23. Thus, a background is present from the favoured two-body  $D$  decay  $B^\pm \rightarrow (K^\pm \pi^\mp)_D K_S^0 \pi^\pm$ , where the  $K^\mp$  is reconstructed as the companion, and the  $K_S^0$  meson and both pions are assigned to the  $D$  decay. Is is not favourable to veto this background, because a requirement on the invariant mass of a track combination that includes the companion track would impact the Dalitz-plot acceptance differently in the  $DK^\pm$  and  $D\pi^\pm$  channels. Thus

it would break a fundamental underlying feature of the measurement: the identical selection efficiency profile between these modes. However, the yield excess in the  $m(K_{\text{companion}}^\pm \pi^\mp D)$  range around  $m_D$ , attributed to the background, corresponds to only about 0.5% of the signal yield. A background at this level does not lead to a limiting systematic uncertainty on the measurement, as described in Section 5.6.9.

## 5.4 Signal and background mass shapes

The measurement employs *extended maximum-likelihood fits* [153] to the  $m(Dh^\pm)$  distribution of signal candidates to determine the observables of interest. The analysis implements a two-step fit procedure: first the data samples are analysed without separating the candidates by  $B$  charge or Dalitz bin, in order to determine appropriate parametrisations of the  $m(Dh^\pm)$  distribution of the signal and relevant background components. The parameterisations are then kept fixed in a subsequent fit of the observables of interest, where the candidates are split by  $B$  charge and Dalitz bin. This section describes the first step, whereas the latter fit is the subject of Section 5.5.

In both steps, the candidates are split in 8 categories depending on whether the companion is categorised as a kaon or pion, whether the  $K_S^0$  meson is in the LL or DD category, and by whether the  $D$  meson is reconstructed in the  $K_S^0\pi^+\pi^-$  or  $K_S^0K^+K^-$  final state. In the remainder of this text, these categories are indexed with the letter  $c$ . For each category,  $c$ , the expected number of observed decays at a given  $B$  mass,  $F^c(m)$ , is given by the sum of a signal contribution and a number of background distributions

$$F^c(m|\theta) = N_s^c(\theta)f_s^c(m|\theta) + \sum_b N_b^c(\theta)f_b^c(m|\theta), \quad (5.4)$$

where  $\theta$  denotes a set of parameters that describe the mass shapes and expected yields, in which some parameters are shared between categories. The distributions  $f_{s/b}^c$  are normalised to integrate to unity, and the expected signal (background) yields are denoted  $N_s^c$  ( $N_b^c$ ). A total, normalised distribution can then be defined

$$f^c(m|\theta) = \frac{1}{N_{\text{tot}}^c(\theta)} F^c(m|\theta), \quad N_{\text{tot}}^c(\theta) = N_s^c(\theta) + \sum_b N_b^c(\theta). \quad (5.5)$$

Given a set of  $N_{\text{observed}}^c$  measured  $B$  masses,  $\{m_i^c\}$ , in a given category, the extended log-likelihood function is defined

$$\ln \mathcal{L}_c(\theta|\{m_i^c\}) \equiv \sum_i \ln f^c(m_i^c|\theta) + \ln \text{Poisson}(N_{\text{tot}}^c(\theta), N_{\text{observed}}^c) \quad (5.6)$$

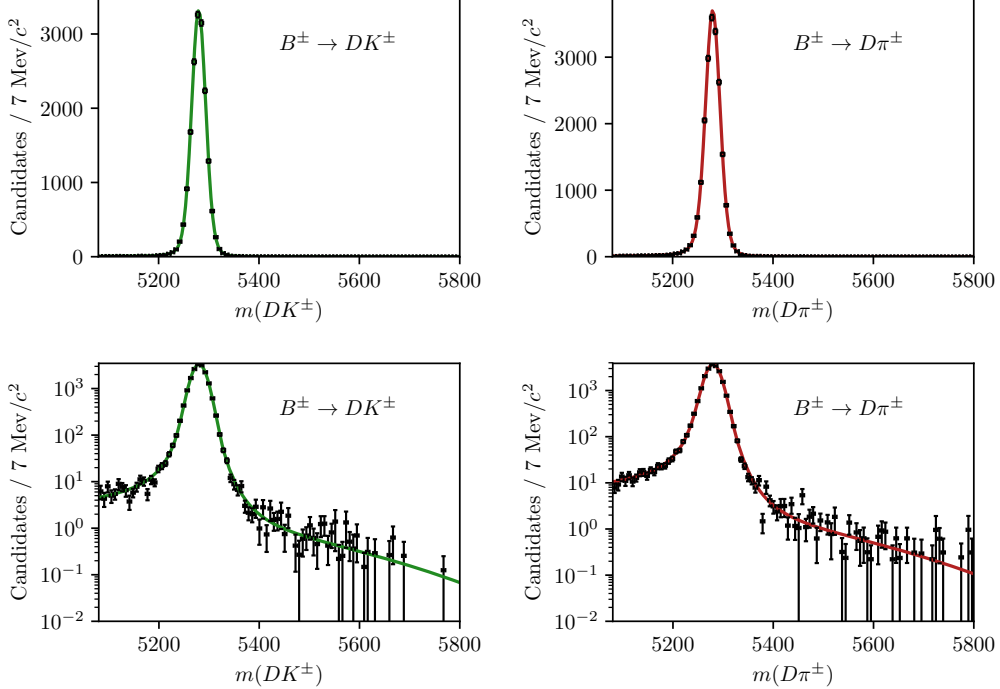


**Figure 5.24:** Fit projection of the signal shape to simulated  $B^\pm \rightarrow D(\rightarrow K_0^0\pi^+\pi^-)h^\pm$  samples reconstructed in the LL category. (Left) shows  $DK$  shapes, and (right) shows  $D\pi$  shapes. The shapes are shown with both linear and logarithmic  $y$ -axis scales.

In a simultaneous fit the total, negative log-likelihood is  $-\ln \mathcal{L} = -\sum_c \mathcal{L}_c$ , and this function can be minimised to find the maximum-likelihood estimates of the parameters in  $\theta$ , as well as their confidence regions and correlation coefficients. This is handled with the `RooFit` package [154].

Apart from signal decays, the fit includes components that describe combinatorial background, backgrounds from decays where a companion pion is misidentified as a kaon or vice versa, and partially reconstructed backgrounds. Each of these components are described in detail in the following, before the results of the first-stage fit are presented in Section 5.4.5.

#### 5.4.1 Signal decays

The signal component is modelled with a sum of a Gaussian density function,  $f_G(m|m_B, \sigma)$ , and a modified Gaussian distribution with the parameterisation

$$f_C(m|m_B, \sigma, \alpha_L, \alpha_R, \beta) \propto \begin{cases} \exp \left[ \frac{-\Delta m^2(1+\beta\Delta m^2)}{2\sigma^2 + \alpha_L \Delta m^2} \right], & \Delta m = m - m_B < 0 \\ \exp \left[ \frac{-\Delta m^2(1+\beta\Delta m^2)}{2\sigma^2 + \alpha_R \Delta m^2} \right], & \Delta m = m - m_B > 0, \end{cases} \quad (5.7)$$

which is Gaussian when  $\Delta m^2 \ll \sigma^2/\alpha_{L/R}$  or  $\Delta m^2 \gg \beta^{-1}$  (with widths of  $\sigma$  and  $\sqrt{\alpha_{L/R}/\beta}$  respectively), with an exponential-like transition that is able to

model the effect of the experimental resolution of LHCb very well. For the case  $\beta = 0$  the shape is denoted the *Cruijff* shape; however, in this case it tends to a uniform distribution for large  $\Delta m^2$  values, and cannot model the tails of the signal distribution. Thus, the full density function is

$$f_s(m|m_B, \sigma, \alpha_L, \alpha_R, \beta) = k_C f_C(m|m_B, \sigma, \alpha_L, \alpha_R, \beta) + (1 - k_C) f_G(m|m_B, \sigma). \quad (5.8)$$

The tail parameters  $(\alpha_{L/R}, \beta)$  and the constant  $k_C$  are determined in fits to simulated signal decays that have passed the full selection. The parameters are shared between the  $K_S^0 \pi^+ \pi^-$  and  $K_S^0 K^+ K^-$  channels, but otherwise independent in the fit categories. An example of a fit to simulated  $B^\pm \rightarrow D(\rightarrow K_S^0 \pi^+ \pi^-) h^\pm$  decays is given in Fig. 5.24. The resolution parameters  $\sigma$  are determined in the fit to actual data. Separate parameters are determined in the LL and DD categories, because the LL category has a better resolution on the  $K_S^0$  momentum, and therefore a narrow peak in reconstructed  $B$  mass. Likewise, separate resolution parameters are used for  $B^\pm \rightarrow D\pi^\pm$  and  $B^\pm \rightarrow DK^\pm$  decays, because the smaller  $Q$  value in the latter case leads to smaller momenta of the decay products, and a correspondingly better resolution.

The signal yields are determined independently in each  $B^\pm \rightarrow D\pi^\pm$  category. The yields in the  $B^\pm \rightarrow DK^\pm$  categories are then parameterised in terms of a single yield-ratio  $\mathcal{R}_{K/\pi}$ , and  $\epsilon^c$ , the corresponding selection efficiency for a given category

$$N_{DK^\pm}^c = \mathcal{R}_{K/\pi} \times N_{D\pi^\pm}^c \times \frac{\epsilon_{DK^\pm}^c}{\epsilon_{D\pi^\pm}^c}. \quad (5.9)$$

The selection efficiency is obtained in simulation, except for the PID efficiencies which are obtained in calibration data as described in Section 5.1.3. The parameter  $\mathcal{R}_{K/\pi}$  is shared between all categories, and corresponds to the branching ratio between  $B^\pm \rightarrow DK^\pm$  and  $B^\pm \rightarrow D\pi^\pm$  decays. Therefore, it can be compared to the known branching ratio [31], which serves as an important cross check of the determination of relative efficiencies.

#### 5.4.2 Cross-feed between $B^\pm \rightarrow Dh^\pm$ channels

There is a cross-feed between the  $B^\pm \rightarrow D\pi^\pm$  and  $B^\pm \rightarrow DK^\pm$  channels, where real  $B^\pm \rightarrow D\pi^\pm$  decays are reconstructed as  $B^\pm \rightarrow DK^\pm$  decays, or where  $B^\pm \rightarrow DK^\pm$  decays are reconstructed as  $B^\pm \rightarrow D\pi^\pm$  decays. Due to relative branching fractions the former contribution is by far the most important, but both are modelled.

The cross-feed shapes are obtained in a data-driven manner using the sPlot method [151], and fixed in the fit to data. Separate shapes are determined for each category, using the following steps:

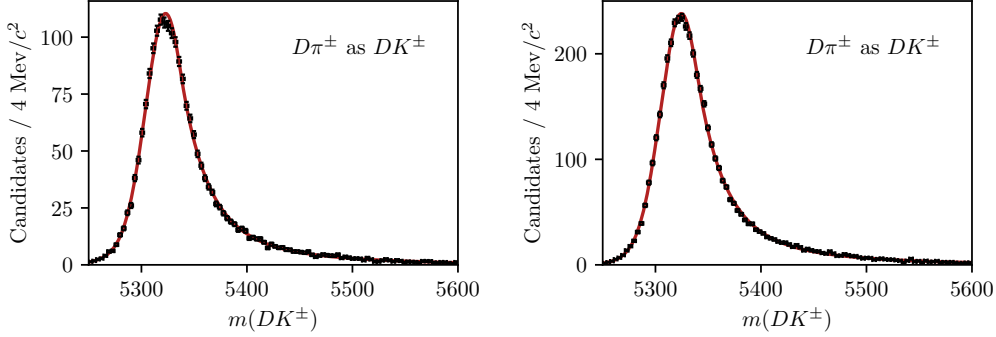


**Figure 5.25:** Fitted shape of the  $B^\pm$  invariant mass spectrum for  $B^\pm \rightarrow D\pi^\pm$  decays misidentified as  $B^\pm \rightarrow DK^\pm$  decays for (left) LL and (right) DD candidates in the  $D \rightarrow K_S^0 \pi^+ \pi^-$  mode.

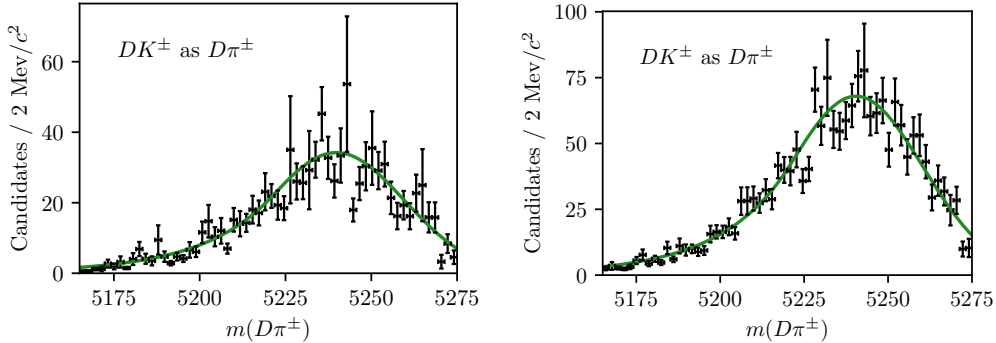


**Figure 5.26:** Fitted shape of the  $B^\pm$  invariant mass spectrum for  $B^\pm \rightarrow DK^\pm$  decays misidentified as  $B^\pm \rightarrow D\pi^\pm$  decays for (left) LL and (right) DD candidates in the  $D \rightarrow K_S^0 \pi^+ \pi^-$  mode.

- The procedure is based on the reasonably pure  $B^\pm \rightarrow D\pi^\pm$  sample obtained when the full selection is applied. A simple mass fit is performed to the invariant mass spectrum and the sPlot method [151] is used to obtain the sWeights,  $w_s$ , for the signal component. The mass fit uses the same components for signal, low mass shape, and combinatorial background as described in this section.
- A set of weights are defined, based on the candidate-by-candidate PID efficiencies obtained as described in Section 5.1.3:
  - The extracted PID efficiencies of the  $\text{PIDK} < 4$  cut  $\epsilon_{D\pi \rightarrow D\pi}(p, \eta, n_{\text{tracks}})$  are used to reverse-weight the  $B^\pm \rightarrow D\pi^\pm$  sample, in order to obtain the companion kinematic distributions before the  $\text{PIDK} < 4$  cut is applied.

- 2471 – The extracted PID efficiencies of the  $\text{PIDK} > 4$  cut  $\epsilon_{D\pi \rightarrow DK}(p, \eta, n_{\text{tracks}})$  are  
2472 used to obtain the companion kinematic distribution of the  $B^\pm \rightarrow D\pi^\pm$   
2473 candidates mis-identified as  $B^\pm \rightarrow DK^\pm$ .
- 2474 • The raw distribution of the invariant mass of  $B^\pm$  particles with a misidentified  
2475 companion,  $m_B^{\text{mis-ID}}$ , is produced by also doing the `DecayTreeFitter` kine-  
2476 matic refit while swapping the companion mass hypothesis of each  $B^\pm \rightarrow D\pi^\pm$   
2477 candidate to a kaon hypothesis.
- 2478 • Each candidate is reweighted by the overall weight  $w = w_s^{\text{cand.}} / \epsilon_{D\pi \rightarrow D\pi}^{\text{cand.}}$ .  
2479  $\epsilon_{D\pi \rightarrow DK}^{\text{cand.}}$ , and the reweighed  $m_B^{\text{mis-ID}}$  distribution is fitted to obtain the cross-  
2480 feed mass distribution function.

2481 The distributions are modelled with a sum of two Crystal Ball density functions,  
2482 each defined by the parameterisation [155]

$$f_{\text{CB}}(m, \mu, \sigma, \alpha, n) \propto \begin{cases} \exp \left[ -\frac{1}{2} \left( \frac{m-\mu}{\sigma} \right)^2 \right] & \text{if } (m-\mu)/\sigma > -\alpha \\ A \left( B - \frac{m-\mu}{\sigma} \right)^{-n} & \text{otherwise,} \end{cases} \quad (5.10)$$

2483 where  $\alpha > 0$ , and

$$A = \left( \frac{n}{\alpha} \right)^n \exp[-\alpha^2/2], \quad B = \frac{n}{\alpha} - \alpha. \quad (5.11)$$

2484 The obtained  $m_B^{\text{mis-ID}}$  spectrum and obtained mass shape is given in Fig. 5.25  
2485 for the  $D \rightarrow K_S^0 \pi^+ \pi^-$  category; the  $D \rightarrow K_S^0 K^+ K^-$  shapes are very similar. An  
2486 analogous procedure is used to obtain the mass distribution of  $B^\pm \rightarrow DK^\pm$  decays  
2487 reconstructed in the  $B^\pm \rightarrow D\pi^\pm$  category. In the first stage where sPlots are  
2488 extracted by a fit to the  $B^\pm \rightarrow DK^\pm$  mass spectrum, the cross-feed component  
2489 determined as described above is included. An example of one of the resulting  
2490 shapes is given in Fig. 5.26. The shape obtained in this manner performs better  
2491 than one obtained using simulated decays, because the precision of the momentum  
2492 determination is slightly overestimated in simulation.

2493 The yield of cross-feed from  $B^\pm \rightarrow D\pi^\pm$  decays in a given  $B^\pm \rightarrow DK^\pm$  category  
2494 is parameterised in terms of the yield of correctly identified  $B^\pm \rightarrow D\pi^\pm$  decays and  
2495 the mis-identification probability extracted from calibration samples as described  
2496 in Section 5.1.3. Denoting the rate at which a pion is reconstructed as a kaon  
2497 by  $\epsilon_{\pi \rightarrow K}^c$  in a given category,  $c$ , the yield is

$$N_{\pi \rightarrow K}^c = N_{D\pi^\pm}^c \frac{\epsilon_{\pi \rightarrow K}^c}{1 - \epsilon_{\pi \rightarrow K}^c}, \quad (5.12)$$

2498 with an analogous definition of the yield of the cross-feed component from  
2499  $B^\pm \rightarrow DK^\pm$  decays in the  $B^\pm \rightarrow D\pi^\pm$  spectrum.

### 2500 5.4.3 Partially reconstructed backgrounds

2501 A number of background candidates stem from partly reconstructed  $B$  decays of the  
 2502 type  $B \rightarrow DhX$ , where  $X$  denotes a photon or a pion that is not reconstructed. It  
 2503 is not possible to reject these decays in the selection, due to the similarity to signal  
 2504 decays. The missing momentum results in reconstructed  $B$  masses below the actual  
 2505  $B$  mass, and therefore the backgrounds are also denoted *lowmass* backgrounds.  
 2506 These mass distributions are modelled with analytic shapes, derived based on two  
 2507 principles. Firstly, the kinematic endpoints of the distributions are fully defined by  
 2508 the particle masses in the decay. Secondly, the angular distribution of the missing  
 2509 particle has a one-to-one relation to the missing momentum, and therefore to the  
 2510 reconstructed  $B$  mass. Depending on the spin-parity of the particles and resonances  
 2511 involved in the decay, two different mass distributions arise.

2512 In  $B$  decays where the missing particle is a scalar that is produced in the  
 2513 decay of a vector resonance (eg.  $B^\pm \rightarrow D^{*0}(\rightarrow D^0\pi^0)\pi^\pm$  decays where the  $\pi^0$  is  
 2514 not reconstructed), the  $m(D^0\pi^\pm)$  distribution has a double-peak structure. The  
 2515  $D^{*0}$  helicity angle  $\theta$  is defined as the angle between the  $\pi^0$  momentum vector in  
 2516 the  $D^{*0}$  rest frame and the  $D^{*0}$  boost vector in the  $B$  rest frame. The helicity  
 2517 of the  $D^{*0}$  meson means that the  $\pi^0$  will travel predominantly in the direction  
 2518 where  $\theta = 0$  or  $\theta = \pi$ . When  $\theta = 0$  the fraction of momentum carried by the  
 2519 missing  $\pi^0$  is lower, leading to a higher reconstructed  $m(D^0\pi^\pm)$ . When  $\theta = \pi$   
 2520 the converse occurs. The resulting  $B$  mass distribution is a parabola  $f_{\text{HORNS}}^0(m)$   
 2521 peaking near both kinematic endpoints  $a$  and  $b$

$$f_{\text{HORNS}}^0(m) = \begin{cases} (m - \frac{a+b}{2})^2, & \text{if } a < m < b \\ 0, & \text{otherwise.} \end{cases} \quad (5.13)$$

2522 Due to the double-peaking structure, and the fact that was developed by Paolo  
 2523 Gandini for the two-body ADS/GLW analyses [156], this shape is denoted a  
 2524 *HORNSdini* shape when convolved with a resolution function as described below.

2525 The second relevant decay situation is where the missing particle is a vector,  
 2526 again produced via the intermediate decay of a vector resonance (eg.  $B^\pm \rightarrow$   
 2527  $D^{*0}(\rightarrow D^0\gamma)\pi^\pm$  decays where the photon is not reconstructed). In this case, the  
 2528 spin-parity of the photon ( $1^-$ ) means that it will decay preferentially in the  $\theta = \frac{\pi}{2}$   
 2529 or  $\theta = \frac{3\pi}{2}$  directions, and so a double-peak structure is not seen. In this case  
 2530 the parabolic distribution  $f_{\text{HILL}}^0(m)$  with kinematic endpoints  $a, b$  has negative  
 2531 curvature and can be described by

$$f_{\text{HILL}}^0(m) = \begin{cases} -(m - a)(m - b), & \text{if } a < m < b \\ 0, & \text{otherwise.} \end{cases} \quad (5.14)$$

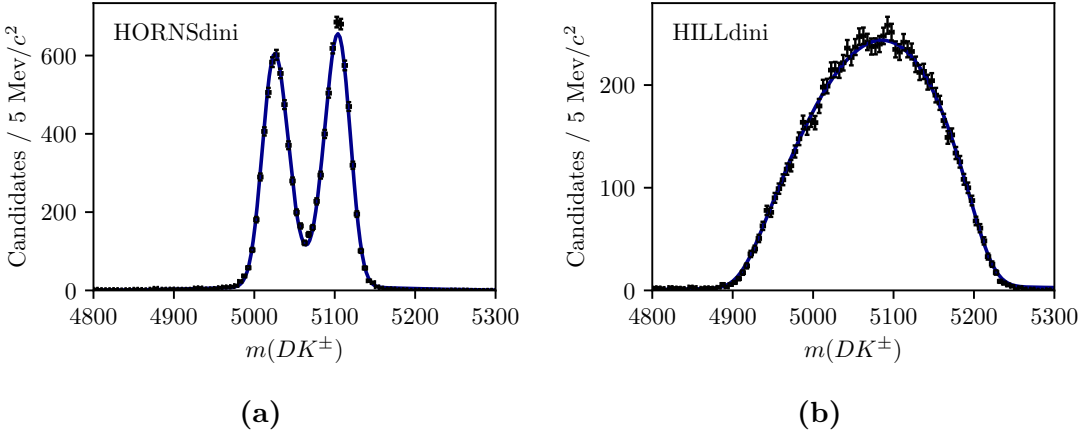


**Figure 5.27:** Examples of (a) the *HORNSdini* distribution fit to simulated  $B^\pm \rightarrow (D^{*0} \rightarrow D^0[\pi^0])K^\pm$  decays, and (b) the *HILLSdini* distribution fit to simulated  $B^\pm \rightarrow (D^{*0} \rightarrow D^0[\gamma])K^\pm$  decays. The fits in this figure are made to illustrate the features of each shape, but do not enter the actual fit to data.

This shape is denoted a *HILLdini* shape when convolved with a resolution function. A convolution is applied to take into the non-perfect resolution in the momentum determination. The resolution function is chosen to be a sum of two Gaussians. For a single Gaussian shape  $f_G(x|\mu, \sigma)$  with mean  $\mu$  and width  $\sigma$ , the double Gaussian is expressed as

$$f_{DG}(x) = f_G(x|\mu, \sigma) + k_G f_G(x|\mu, R_\sigma \sigma). \quad (5.15)$$

where  $\sigma$  is the width of the first Gaussian,  $k_G$  is the relative fractions between the two Gaussians, and  $R_\sigma$  is their relative widths. Further, selection effects can distort the horns shape such that one of the peaks is higher than the other. This is taken into account by introducing a linear polynomial with slope parameter  $\xi$ . As  $\xi \rightarrow 0$ , the left hand peak decreases in size relative to the right hand peak. The resulting *HORN<sub>dini</sub>* and *HILL<sub>dini</sub>* distributions are therefore

$$f_{\text{HORNS/HILL}}(m) = \int_a^b dx f_{\text{HORNS/HILL}}^0(x) f_{DG}(m|x, \sigma, k_G, R_\sigma) \left( \frac{1-\xi}{b-a}x + \frac{b\xi - a}{b-a} \right). \quad (5.16)$$

Examples of the shapes are given in Fig. 5.27. These shapes are used to fit all partially reconstructed backgrounds, as described in the following section.

## Determination of the partially reconstructed background distributions

In both the  $B^\pm \rightarrow DK^\pm$  and  $B^\pm \rightarrow D\pi^\pm$  categories, components are included to describe contributions from the partially reconstructed decays

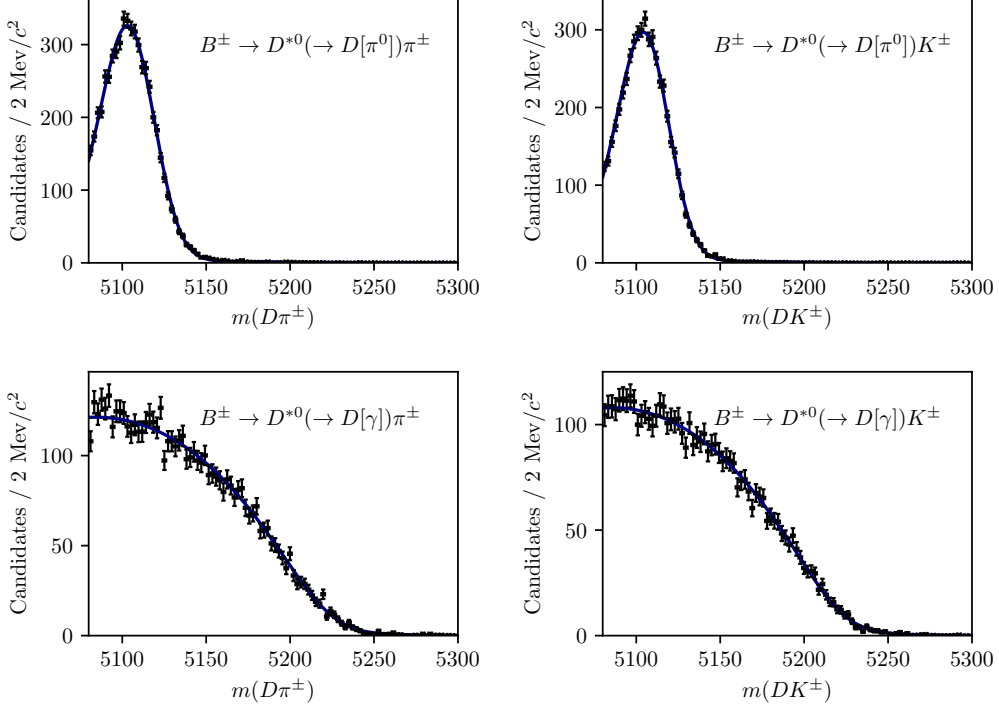


**Figure 5.28:** Fit projection of the fit to (top) simulated  $B^+ \rightarrow D^{*0}(\rightarrow D^0[\pi^0])h^\pm$  decays and (bottom) simulated  $B^+ \rightarrow D^{*0}(\rightarrow D^0[\gamma])h^\pm$  decays, all reconstructed in the DD category. Both the (left)  $DK$  and (right)  $D\pi$  shapes are shown.

- $B^\pm \rightarrow (D^{*0} \rightarrow D^0[\pi^0])h^\pm$ , described using a *HORNsdini* distribution,
- $B^\pm \rightarrow (D^{*0} \rightarrow D^0[\gamma])h^\pm$ , described using a *HILLdini* distribution
- $B^0 \rightarrow (D^{*\pm} \rightarrow D^0[\pi^\pm])h^\mp$ , described using a *HORNsdini* distribution,
- $B^{\pm(0)} \rightarrow D^0 h^\pm [\pi^{0(\mp)}]$ , described using a *HORNsdini* distribution,

where the particle in square brackets is not reconstructed. The mass distributions of all the  $B \rightarrow D^*h^\pm$  contributions are obtained from fits to samples of full LHCb simulation. Examples of these fits are shown in Fig. 5.28. All shape parameters are kept fixed in the fit to data, except for the parameter  $\sigma$  of the resolution function in Eq. (5.15) which is allowed to obtain the value preferred by data.

The mass distribution of  $B^\pm \rightarrow D^0 h^\pm [\pi^0]$  and  $B^0 \rightarrow D^0 h^\pm [\pi^\mp]$  decays reconstructed in the  $B^\pm \rightarrow D\pi^\pm$  categories is obtained from full LHCb simulation samples of  $B^\pm \rightarrow D^0\rho^\pm$  and  $B^0 \rightarrow D^0\rho^0$  decays. The shapes were compared to those predicted by an amplitude model for  $B^0 \rightarrow D^0\pi^\pm\pi^\mp$  decays developed by LHCb [157], but found to be very similar for the  $m(D\pi^\pm)$  range relevant to this analysis. The obtained shapes are shown in Fig. 5.29.

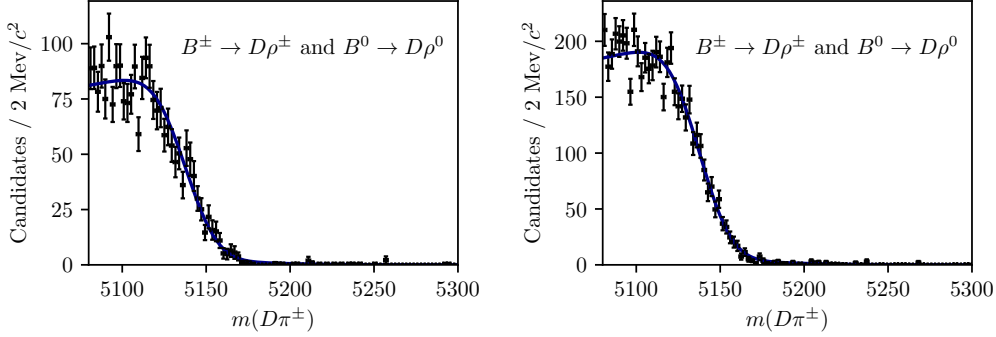


**Figure 5.29:** Projections of the fit to simulated  $B^\pm \rightarrow D\rho^\pm$  and  $B^0 \rightarrow D\rho^0$  samples reconstructed as  $B^\pm \rightarrow D\pi^\pm$  decays for the (left) LL and (right) DD categories.

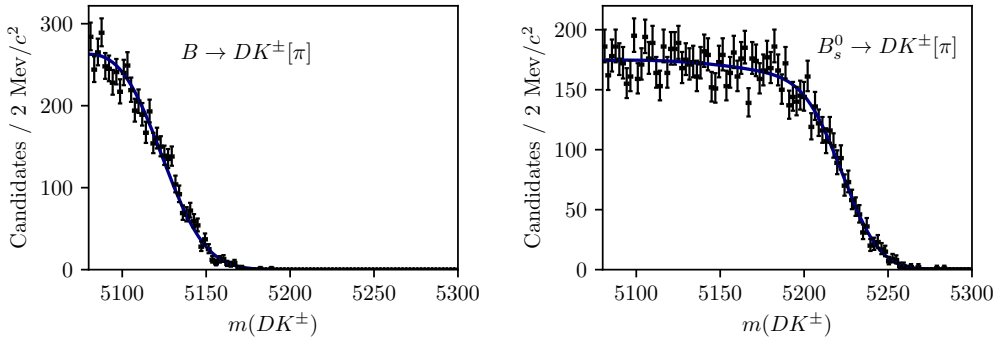


**Figure 5.30:** Fit projection for the fit used to obtain a shape for the partly reconstructed background from (left)  $B \rightarrow DK\pi$  decays and (right)  $B_s^0 \rightarrow DK^+\pi^-$  decays where a pion is not reconstructed.

2563     The mass distribution of  $B^\pm \rightarrow D^0 K^\pm[\pi^0]$  and  $B^0 \rightarrow D^0 K^+[\pi^-]$  decays recon-  
 2564     structed in the  $B^\pm \rightarrow DK^\pm$  categories, on the other hand, is obtained from a  
 2565     sample of signal decays, generated via a an amplitude model for  $B^0 \rightarrow D^0 K^+ \pi^-$   
 2566     decays developed by LHCb [158] and smeared to take the LHCb resolution into  
 2567     account. This follows an approach developed in the context of a GLW analysis  
 2568     based on partially reconstructed decays made within LHCb [159]. The obtained  
 2569     shape is shown in Fig. 5.30.

2570     The background yields of these backgrounds are parameterised in terms of  
 2571     one total yield parameter, accounting for all partially reconstructed  $B^\pm$  and  
 2572      $B^0$  decays, and a number of parameters that describe the relative rates of the  
 2573     different contributions. In the  $B^\pm \rightarrow D\pi^\pm$  channels, the relative rates of the  
 2574      $B^\pm \rightarrow (D^{*0} \rightarrow D^0[\pi^0])h^\pm$  and  $B^0 \rightarrow (D^{*\pm} \rightarrow D^0[\pi^\pm])h^\mp$  backgrounds are fixed  
 2575     from the known branching fractions, and relative selection efficiencies in simulation.  
 2576     These backgrounds have almost identical mass distributions and it is not possible to  
 2577     determine the ratio in the fit to data. The relative yield of  $B^\pm \rightarrow D^*(\rightarrow D^0[\gamma])\pi^\pm$

2578 compared to the  $B \rightarrow D^*(\rightarrow D^0[\pi])\pi^\pm$  is denoted  $f_{D^*\gamma}^{D\pi}$  and is floated in the fit to  
 2579 data, as is the relative yield of  $B \rightarrow D^0\pi^\pm[\pi]$  decays compared to the  $B \rightarrow D^*\pi$   
 2580 modes, denoted  $f_{D\pi\pi}^{D\pi}$ . In the  $B^\pm \rightarrow DK^\pm$  channels, all the relative background  
 2581 rates are fixed via known branching fractions and relative selection efficiencies; this  
 2582 is necessary to obtain a stable fit, due to the lower yields.

2583 In the  $B^\pm \rightarrow DK^\pm$  categories, an additional partially reconstructed background  
 2584 is considered from  $B_s^0 \rightarrow \bar{D}^0[\pi^+]K^-$  (and conjugate) decays. The mass shape is  
 2585 obtained from simulated decays, generated using an amplitude model published by  
 2586 LHCb [160] and smeared to account for the experimental resolution. The obtained  
 2587 shape is shown in Fig. 5.30. The yield of this background component is fixed relative  
 2588 to the signal yields in the corresponding  $B^\pm \rightarrow D\pi^\pm$  category, taking the relative  
 2589 efficiencies, branching ratios and hadronisation factors into account [31, 161].

2590 In the  $B^\pm \rightarrow DK^\pm$  channels there is a contribution from partially reconstructed  
 2591  $B \rightarrow D^*\pi^\pm X$  decays where the companion pion is misidentified as a kaon. The  
 2592 reverse contribution is negligible due to the relative branching fractions, and the  
 2593 fact that the  $K \rightarrow \pi$  misidentification shifts most of these background decays  
 2594 below the mass range of the fit. These are modelled using analytic, empirical  
 2595 mass distributions (essentially sums of a number of regular *HORN*/*HILLdini*  
 2596 distributions), with parameters that are determined in fits to simulated  $B \rightarrow D^*\pi^\pm$   
 2597 and  $B \rightarrow D\rho$  decays where the pion is reconstructed with the kaon mass hypothesis.  
 2598 The shapes are fixed in the fit to data.

2599

## 2600 Partially reconstructed backgrounds that are not modelled

2601 It was considered whether a background from  $\Lambda_b^0 \rightarrow D^0 p \pi^-$  decays where a pion is  
 2602 not reconstructed, and the proton is misidentified as the companion, can be expected  
 2603 to contribute significantly. This background has been investigated using full LHCb  
 2604 simulation samples for the  $D$  final state  $K_S^0\pi^+\pi^-$ . Taking into account the selection  
 2605 efficiencies, branching fractions, and hadronisation fraction of this background, the  
 2606 expected relative yield of the  $\Lambda_b^0$  background compared to signal of 0.03 % in the  
 2607  $B^\pm \rightarrow D\pi^\pm$  channel, which is completely negligible. In the  $B^\pm \rightarrow DK^\pm$  channel  
 2608 the yield relative to signal is about 1.2 %, for total of about 200 decays. However,  
 2609 most of these lie at  $B$  masses smaller than the signal peak, and their impact is  
 2610 small. Therefore it is not necessary to model the background in the nominal fit; a  
 2611 systematic uncertainty is assigned that accounts for the small potential impact.

2612 In the analogous case of  $\Lambda_b^0 \rightarrow D^0 p K^-$  decays, the missing energy of the non-  
 2613 reconstructed kaon results in a reconstructed  $B$  mass below the fit range.

2614 It has also been investigated whether a background from  $\Lambda_b^0 \rightarrow \Lambda_c^+ \pi^-$  or  
 2615  $\Lambda_b^0 \rightarrow \Lambda_c^+ K^-$  decays can be expected, where  $\Lambda_c^+ \rightarrow p K_S^0 \pi^+ \pi^-$ , a pion is missed  
 2616 and the proton is misidentified as a pion or kaon from the  $D$  decay. In practice,  
 2617 the background is sufficiently suppressed from the applied  $D$  mass requirement to  
 2618 have no significant impact, and is therefore not modelled. A systematic uncertainty  
 2619 is assigned that accounts for any potential impact on the measurement due  
 2620 to this choice.

#### 2621 5.4.4 Combinatorial background

2622 The combinatorial background is modelled with an exponentially falling density  
 2623 function, where both the yield and exponential slope are determined independently  
 2624 for each category. This shape is found to model the combinatorial well in all  
 2625 categories, most evident in the high- $m_B$  regions where this background dominates.

#### 2626 5.4.5 Fit results

2627 The fit range is chosen to be  $m_B \in [5080, 5800] \text{ MeV}/c^2$ . The low end of this  
 2628 interval includes the higher mass peak of the double-peak structure in the partially  
 2629 reconstructed background, which helps the fit constrain the relative contributions  
 2630 of backgrounds in the lowmass region. A number of additional backgrounds exist at  
 2631 even lower  $m_B$  values, thus extending the fit range to lower masses would necessitates  
 2632 an extended model, but not benefit the description of the signal region. The high  
 2633 end of the interval includes enough combinatorial background to allow the fit to  
 2634 determine the exponential slope parameter accurately.

2635 A large number of pseudoexperiments are carried out to verify that the fit  
 2636 procedure is self-consistent, in which toy data sets are generated according to  
 2637 the expected  $B$  mass distributions, and then fitted. None of the parameters  
 2638 obtained in the fit exhibit a mean bias different from zero. For most parameters  
 2639 the uncertainties are well estimated. This is the case for the signal yields, and  
 2640 the  $DK^\pm - D\pi^\pm$  yield ratio  $\mathcal{R}_{K/\pi}$ , as evidenced by the pull plots in Fig. 5.31. The  
 2641 fit underestimates the uncertainty by 10-20 % for some of the parameters related  
 2642 to the partly reconstructed backgrounds, as shown in Fig. 5.32, but this is taken  
 2643 into account when the uncertainties are propagated to the observables in the  
 2644 second-stage fit, as described in Section 5.6.3.

2645 The projections of the fit to data are shown in Figs. 5.33 and 5.34, for the  
 2646  $D \rightarrow K_S^0 \pi^+ \pi^-$  and  $D \rightarrow K_S^0 K^+ K^-$  data sets, respectively. The obtained yields for  
 2647 each fit component are given in Table 5.6. The total yield of  $B^\pm \rightarrow D\pi^\pm$  decays is

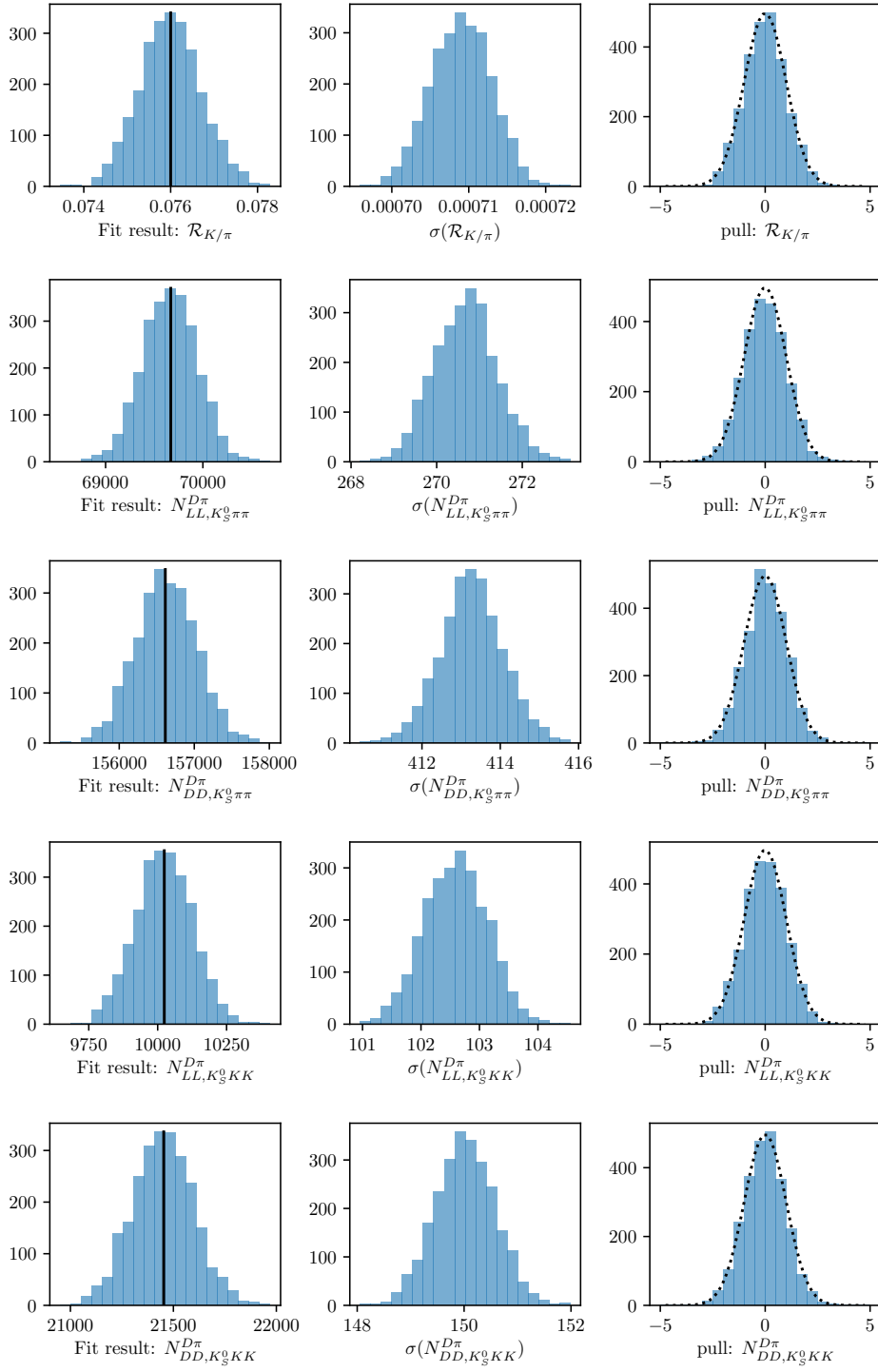


**Figure 5.31:** The (left) fitted value, (centre) estimated statistical uncertainty, and (right) pull plots for the signal yield parameters, as obtained in a number of pseudo experiments. The black line on the left shows the value used to generate the pseudo data sets; the dotted line on the right shows a Gaussian distribution with mean equal to zero and a standard deviation equal to unity.

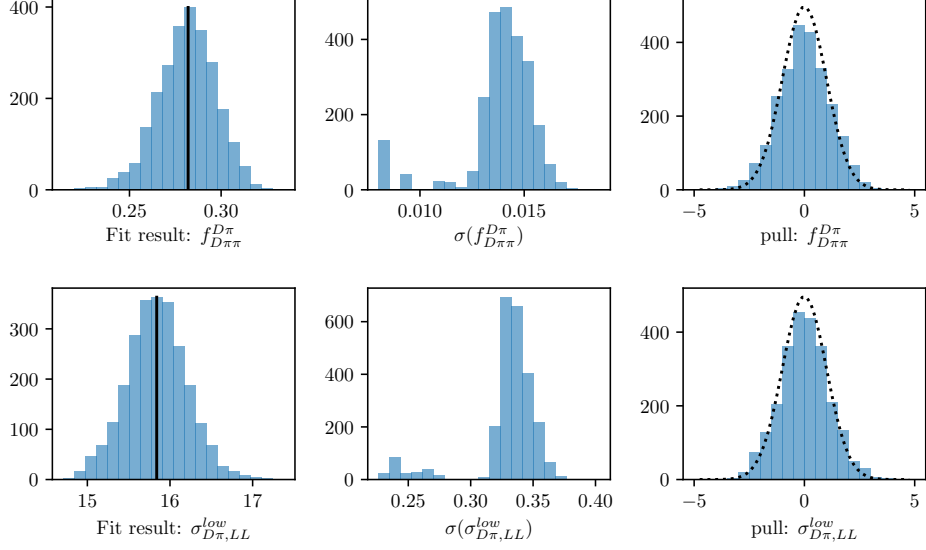


**Figure 5.32:** The (left) fitted value, (centre) estimated statistical uncertainty, and (right) pulls obtained in a number of pseudo experiments for two examples of parameters relating to the partially reconstructed backgrounds, where the uncertainties are slightly underestimated on average. The standard deviation of the pull distributions is approximately 1.15 in both cases.

approximately 230,000 across all channels. The obtained value of the yield ratio is  $\mathcal{R}_{K/\pi} = (7.7 \pm 0.1) \%$ , corresponding to a total  $B^\pm \rightarrow DK^\pm$  yield of 16,500, of which about 14,300 pass the PID requirement and are reconstructed in the  $B^\pm \rightarrow DK^\pm$  category. This value of  $\mathcal{R}$  is in excellent agreement with expectation from the known branching fractions [31], which predict  $\mathcal{R}_{K/\pi}^{\text{PDG}} = (7.8 \pm 0.3) \%$ .<sup>2</sup> The shape parameters determined in the fit to data are summarised in Table 5.7.

<sup>2</sup>While it would seem this measurement thus determines the yield ratio  $\mathcal{R}_{K/\pi}$  with a much better precision than the current world average uncertainty, that is because the result quoted here does not include any systematic uncertainties; it is only included to serve as a, successfully passed, cross check.

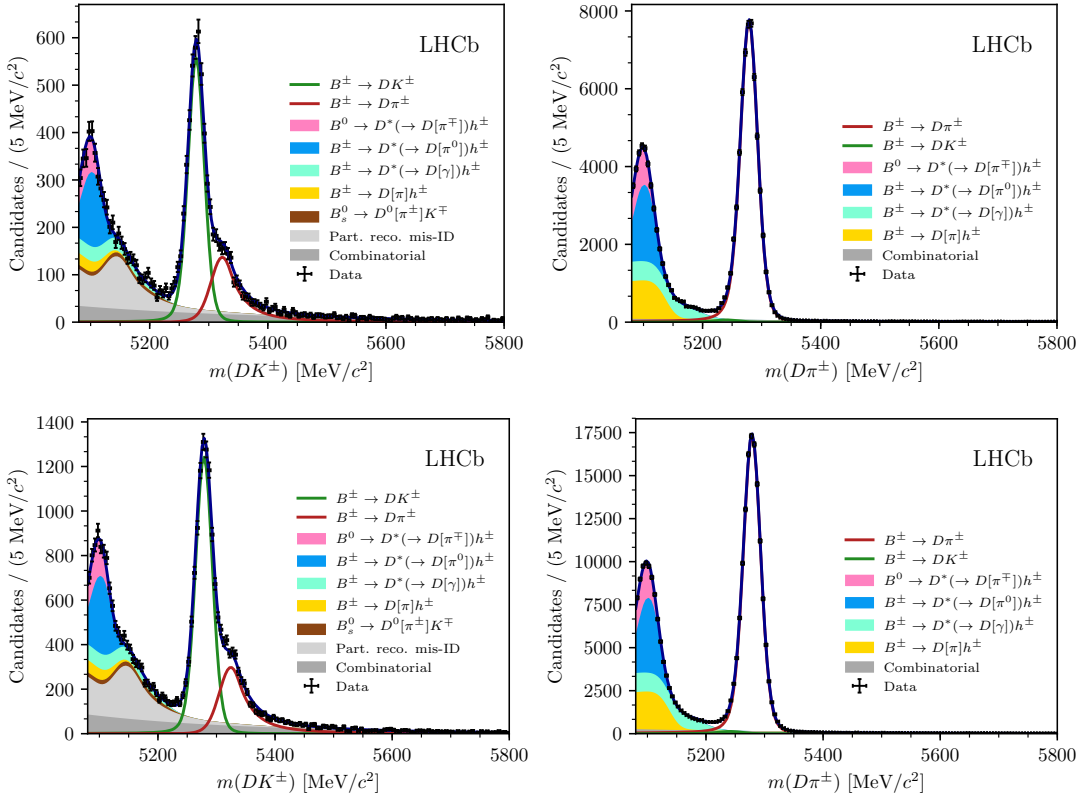


**Figure 5.33:** The invariant mass distribution for the (left)  $B^\pm \rightarrow DK^\pm$  channel and (right)  $B^\pm \rightarrow D\pi^\pm$  channel, where  $D \rightarrow K_S^0\pi^+\pi^-$  and the  $K_S^0$  is in the (top) LL and (bottom) the DD categories. The particle within square brackets in the legend denotes the particle that has not been reconstructed.

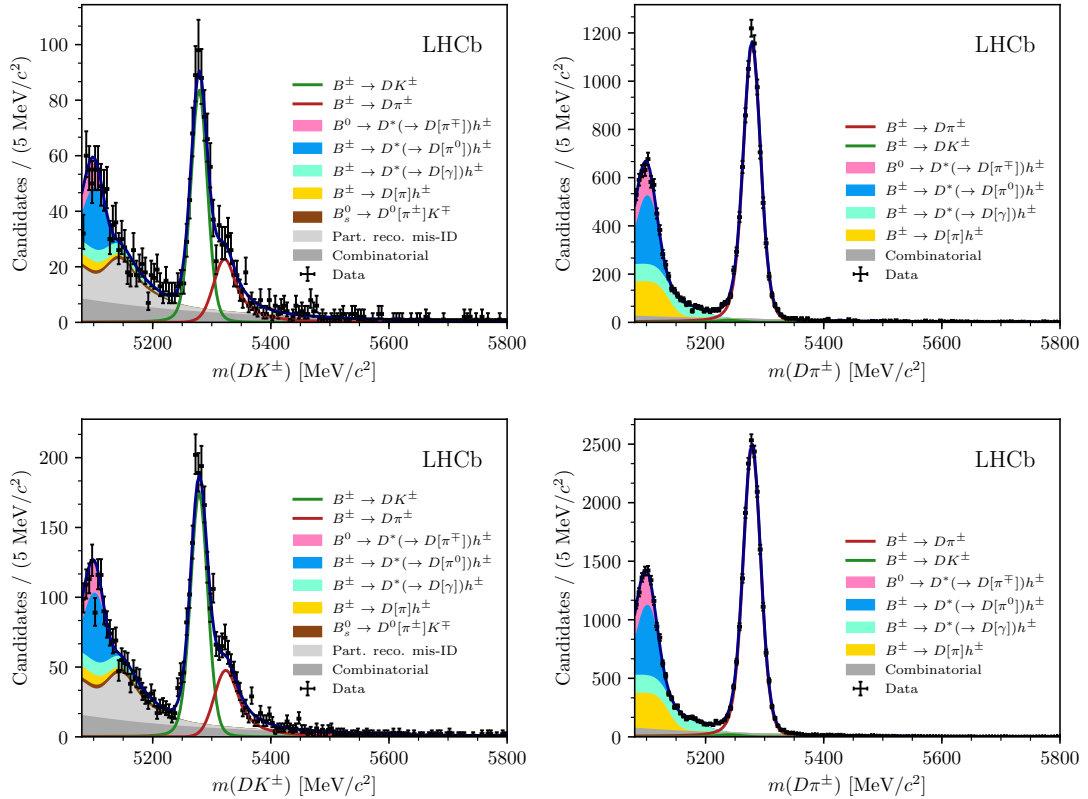


**Figure 5.34:** The invariant mass distribution for the (left)  $B^\pm \rightarrow DK^\pm$  channel and (right)  $B^\pm \rightarrow D\pi^\pm$  channel, where  $D \rightarrow K_S^0 K^+ K^-$  and the  $K_S^0$  is in the (top) LL and (bottom) the DD categories. The particle within square brackets in the legend denotes the particle that has not been reconstructed.

**Table 5.6:** Fitted total candidate yields. The quoted signal yields are for the number of candidates that survive the respective PID cut, whereas the  $DK^\pm$ - $D\pi^\pm$  ratio is corrected for PID and selection efficiencies so that it corresponds to the branching ratio.

Component	LL	DD
Signal		
$B^\pm \rightarrow D(\rightarrow K_S^0\pi^+\pi^-)\pi^\pm$	$61,573 \pm 254$	$139,080 \pm 389$
$B^\pm \rightarrow D(\rightarrow K_S^0K^+K^-)\pi^\pm$	$9,160 \pm 98$	$19,910 \pm 144$
$R_{K/\pi} = n(DK)/n(D\pi)$ (%)		$7.72 \pm 0.08$
Combinatorial background		
$B^\pm \rightarrow D(\rightarrow K_S^0\pi^+\pi^-)\pi^\pm$	$3,479 \pm 198$	$9,928 \pm 376$
$B^\pm \rightarrow D(\rightarrow K_S^0K^+K^-)\pi^\pm$	$1,103 \pm 94$	$2,545 \pm 155$
$B^\pm \rightarrow D(\rightarrow K_S^0\pi^+\pi^-)K^\pm$	$1,826 \pm 107$	$3,987 \pm 177$
$B^\pm \rightarrow D(\rightarrow K_S^0K^+K^-)K^\pm$	$380 \pm 39$	$655 \pm 58$
Partially reconstructed background		
$B^\pm \rightarrow D(\rightarrow K_S^0\pi^+\pi^-)\pi^\pm$	$43,004 \pm 242$	$95,452 \pm 403$
$B^\pm \rightarrow D(\rightarrow K_S^0K^+K^-)\pi^\pm$	$6,247 \pm 99$	$13,241 \pm 157$
$R_{K/\pi}^{low} = n_{low}(DK)/n_{low}(D\pi)$ (%)		$6.65 \pm 0.12$

**Table 5.7:** Fitted parameter values.

	LL	DD
$\sigma_{D\pi}$ (MeV/ $c^2$ )	$14.27 \pm 0.05$	$14.58 \pm 0.04$
$\sigma_{DK}$ (MeV/ $c^2$ )	$13.61 \pm 0.24$	$14.19 \pm 0.17$
$\mu$ (MeV/ $c^2$ )		$5278.60 \pm 0.04$
Combinatorial Slopes		
Decay mode	Slope ( $10 \times 10^{-3} GeV^{-1}c^2$ )	
$B^\pm \rightarrow D(\rightarrow K_S^0\pi^+\pi^-)\pi^\pm$	$-3.1 \pm 0.2$	$-4.0 \pm 0.1$
$B^\pm \rightarrow D(\rightarrow K_S^0K^+K^-)\pi^\pm$	$-4.1 \pm 0.4$	$-5.5 \pm 0.3$
$B^\pm \rightarrow D(\rightarrow K_S^0\pi^+\pi^-)K^\pm$	$-3.2 \pm 0.2$	$-3.9 \pm 0.2$
$B^\pm \rightarrow D(\rightarrow K_S^0K^+K^-)K^\pm$	$-4.2 \pm 0.4$	$-4.3 \pm 0.4$
Part. Reco.		
$\sigma_{D\pi}^{low}$ (MeV/ $c^2$ )	$13.73 \pm 0.33$	$13.78 \pm 0.28$
$f_{D\pi\pi}^{D\pi}$		$0.268 \pm 0.013$
$f_{D^*\gamma}^{D\pi}$		$0.317 \pm 0.005$

## 2654 5.5 Measurement of the CP-violation observables

2655 The section describes the second fit stage, in which the *CP*-violation observables  
 2656 of interest are determined. Compared to the first fit stage, the candidates are  
 2657 further split by  $B$  charge, and by the assigned Dalitz bin number, making for a  
 2658 total of 160 subcategories.<sup>3</sup> Another extended maximum-likelihood fit is carried  
 2659 out, in which shape parameters of all signal and background components are fixed  
 2660 to those determined in the first fit stage, and all floating parameters relate to  
 2661 the signal and background yields. The signal yields are expressed in terms of the  
 2662 observables of interest,  $(x_\pm^{DK}, y_\pm^{DK}, x_\xi^{D\pi}, y_\xi^{D\pi})$ , allowing the fit to determine their  
 2663 optimal values. The details of the fit setup are summarised in the following section,  
 2664 along with a number of studies that lead to the specific setup being chosen. The  
 2665 results are presented in Section 5.5.2, and a wide range of consistency checks  
 2666 are described in Section 5.5.3.

### 2667 5.5.1 Fit setup

2668 The basic principle of the measurement is that the signal yields in each bin  
 2669 (in a given category) are defined using the equations of Chapter 2, in order to  
 2670 allow for the determination of the *CP*-violation observables. In practice, a set  
 2671 of variables are defined

$$Y_{c,i}^- = F_{c,-i} + [(x_-^c)^2 + (y_-^c)^2]F_{c,-i} + 2\sqrt{F_{c,i}F_{c,-i}}(c_i^cx_-^c + s_i^cy_-^c), \quad (5.17)$$

$$Y_{c,i}^+ = F_{c,-i} + [(x_+^c)^2 + (y_+^c)^2]F_{c,-i} + 2\sqrt{F_{c,i}F_{c,-i}}(c_i^cx_+^c - s_i^cy_+^c), \quad (5.18)$$

2672 for each data category,  $c$ , in terms of which the bin yields that enter the like-  
 2673 lihood are given by

$$N_{c,i}^\pm = \frac{Y_{c,i}^\pm}{\sum_j Y_{c,j}^\pm} \times N_{c,\text{total}}^\pm. \quad (5.19)$$

2674 This parameterisation is essentially identical to the expressions in Section 2.4,  
 2675 slightly modified so that the phase-space-integrated yields of  $B^+$  and  $B^-$  decays  
 2676 in a given category are determined directly, in lieu of the normalisation constants  
 2677  $h^\pm$  of that section. As discussed briefly in Section 2.4, there are choices to be  
 2678 made in terms of how the  $x$  and  $y$  are parameterised in the  $B^\pm \rightarrow D\pi^\pm$  channel,  
 2679 and how the  $F_i$  parameters are determined. A series of feasibility studies were  
 2680 carried out to determine the optimal setup; these are presented in the following  
 2681 section, before the final fit setup is described in detail.

---

<sup>3</sup>In the thesis, the word *category* is used for the 8-way split of data by companion species,  $K_S^0$  track type, and  $D$ -decay mode, indexed with a  $c$ ; the word *bin* denotes the 16 (4) regions of the  $D \rightarrow K_S^0\pi^+\pi^-$  ( $D \rightarrow K_S^0K^+K^-$ ) Dalitz plots, indexed with an  $i$ ; the simultaneous grouping by *category*, *bin*, and  $B$  charge is denoted a *subcategory*, of which there are  $4 \times 2 \times (16 + 4) = 160$ .

2682 **Feasibility of alternative fit setups**

2683 The motivation for promoting the  $B^\pm \rightarrow D\pi^\pm$  channel to a signal channel is two-fold:  
 2684 one aim is to extract the information on  $\gamma$  from the  $B^\pm \rightarrow D\pi^\pm$  data, even the  
 2685 precision gain is limited, and another is to be able to the  $F_i$  parameters directly  
 2686 from the  $B^\pm \rightarrow Dh^\pm$  channels, to avoid the need for a control channel and a  
 2687 simulation-reliant efficiency correction. Two different sets of observables can be  
 2688 defined to describe the  $CP$ -violation effects in the  $B^\pm \rightarrow D\pi^\pm$  channel:

- 2689 • one option, defined the 8-parameters setup below, is to define a new set of four  
 2690 Cartesian for the  $B^\pm \rightarrow D\pi^\pm$  mode,  $(x_-^{D\pi}, y_-^{D\pi}, x_+^{D\pi}, y_+^{D\pi})$ , defined analogously  
 2691 to the  $B^\pm \rightarrow DK^\pm$  observables

$$x_\pm^{D\pi} = r_B^{D\pi} \cos(\delta_B^{D\pi} \pm \gamma), \quad y_\pm^{D\pi} = r_B^{D\pi} \sin(\delta_B^{D\pi} \pm \gamma), \quad (5.20)$$

- 2692 • another, proposed in Refs. [84, 85], is to introduce the parameter

$$\xi_{D\pi^\pm} = \left( \frac{r_B^{D\pi^\pm}}{r_B^{DK^\pm}} \right) \exp[i(\delta_B^{D\pi^\pm} - \delta_B^{DK^\pm})] \quad (5.21a)$$

2693 and then determine the observables

$$x_\xi^{D\pi} = \text{Re}[\xi_{D\pi^\pm}] \quad y_\xi^{D\pi} = \text{Im}[\xi_{D\pi^\pm}]. \quad (5.21b)$$

2694 This is denoted the 6-parameters setup below. In terms of  $x_\xi^{D\pi}$  and  $y_\xi^{D\pi}$ , the  
 2695 usual Cartesian  $x_\pm$  and  $y_\pm$  are given by

$$x_\pm^{D\pi} = x_\xi^{D\pi} x_\pm^{DK} - y_\xi^{D\pi} y_\pm^{DK}, \quad y_\pm^{D\pi} = x_\xi^{D\pi} y_\pm^{DK} + y_\xi^{D\pi} x_\pm^{DK}. \quad (5.22)$$

2696 The former parameterisation has the benefit that information on  $\gamma$  from the  
 2697  $B^\pm \rightarrow DK^\pm$  and  $B^\pm \rightarrow D\pi^\pm$  channels is encoded in separate sets of observables,  
 2698 whereas the latter parameterisation encodes information on  $CP$  violation from both  
 2699 channel in the  $(x_\pm^{DK}, y_\pm^{DK})$  parameters. In combinations of many measurements, it  
 2700 is a useful cross check to be able to compare constraints obtained from individual  
 2701 decay modes; a good example is the LHCb combination from 2016 [48] where both  
 2702  $B^\pm \rightarrow DK^\pm$  and  $B^\pm \rightarrow Dh^\pm$  combinations are made and compared in detail. This  
 2703 is only possible with the former parameterisation. On the other hand, the latter  
 2704 parameterisation avoids the introduction of two non-physical degrees of freedom,  
 2705 which, as seen below, leads to better statistical behaviour.

2706 In order to inform the choice of parameterisation, a series of pseudo experiments  
 2707 has been carried out to compare the obtainable precision on  $\gamma$  (these studies

were performed, and discussed within LHCb, prior to the publication of Ref. [85]; thus, the results presented here constitute independent work, even if there is some overlap in scope and conclusions with that reference). Many simulated data sets were generated, constituting of a number signal yields approximately equal to the expected yields in the full Run 1 and 2 LHCb data set: approximately 15,000  $B^\pm \rightarrow DK^\pm$  decays and 210,000  $B^\pm \rightarrow D\pi^\pm$  decays.<sup>4</sup> The signal decays were distributed between Dalitz bins according to  $(\gamma, r_B^{DK}, \delta_B^{DK}) = (75^\circ, 0.1, 130^\circ)$  in the  $B^\pm \rightarrow DK^\pm$  mode, which is to the world average values of direct  $\gamma$  measurements at the time. In the  $B^\pm \rightarrow D\pi^\pm$  mode, the behaviour is investigated for different sets of input values; of most importance is the case  $(r_B^{D\pi}, \delta_B^{D\pi}) = (0.005, 300^\circ)$ , because it corresponds to the solution in the LHCb combination [48] that is in agreement with the theoretical expectation  $r_B^{D\pi} \simeq 0.005$  [50]. The behaviour at larger  $r_B^{D\pi}$  values is also investigated. For each generated data set

1. the observables are measured in a fit to the data set, using both the 6-parameter and 8-parameter setups
2. the obtained observables are then fitted to obtain the underlying physics parameters  $(\gamma, r_B^{DK}, \delta_B^{DK}, r_B^{D\pi}, \delta_B^{D\pi})$  using a maximum-likelihood fit, essentially following the procedure outlined in Section 5.7.1.

In the 8-parameter setup it is possible to determine  $\gamma$  using the results in either the  $B^\pm \rightarrow DK^\pm$  or  $B^\pm \rightarrow D\pi^\pm$  channels separately, or consider the combined results; in the 6-parameter setup only the latter option is available. The studies are performed in two modes: with the  $F_i$  floating in the fit, emulating a realistic fit to data, as well as with the  $F_i$  fixed to the input values used in data generation. The latter studies emulate a setup where the  $F_i$  parameters are determined in an ultra-high statistics control channel, and perfect efficiency corrections are applied. In all cases, a single set of  $F_i$  parameters is shared between the  $B^\pm \rightarrow DK^\pm$  and  $B^\pm \rightarrow D\pi^\pm$  modes.

The 6-parameter setup shows significantly better statistical performance than the 8-parameter setup in the realistic case where the  $F_i$  parameters are determined in the fit and  $r_B^{D\pi} \sim 0.005$ .<sup>5</sup> The fits that employ the 6-parameter setup behave well in this case, whereas the additional degrees of freedom in the 8-parameter fit leads to essentially all parameters being 100% (anti-)correlated, and a significant number of fits not converging. For the fits that do converge, the uncertainties

---

<sup>4</sup>No backgrounds were included in these studies, and thus the quoted uncertainties on  $\gamma$  are better than what is obtainable in the final measurement; a similar study including realistic backgrounds is presented for the final setup below.

<sup>5</sup>For larger, non-physical values of  $r_B^{D\pi} > 0.03$  both fit setups behave well.

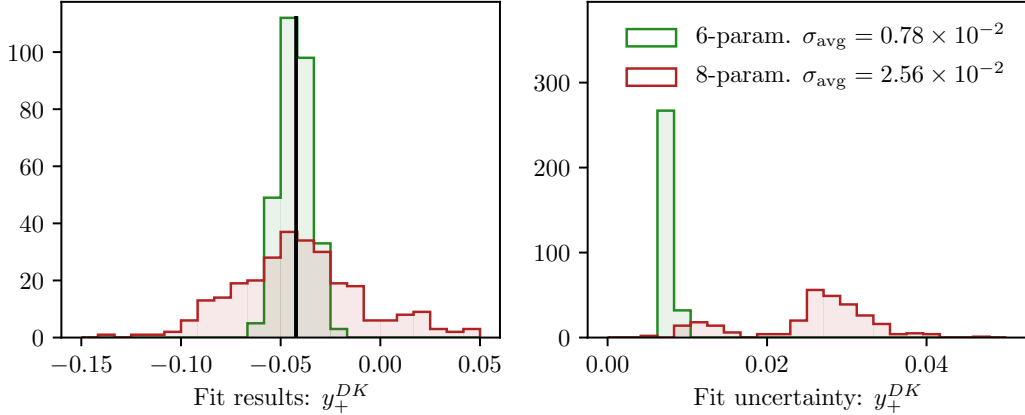


**Figure 5.35:** The distribution of (left) fit values and (right) statistical uncertainty estimate for  $y_+^{DK}$  in a series of pseudo experiments, for both the (green) 6-parameter and (red) 8-parameter setups.

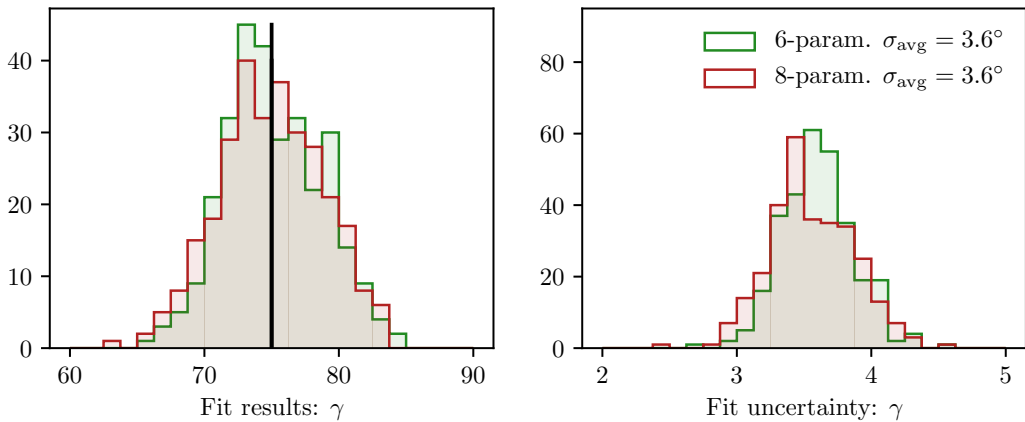


**Figure 5.36:** The distribution of (left) fit values and (right) statistical uncertainty estimate for  $\gamma$  in a series of pseudo experiments, for both the (green) 6-parameter and (red) 8-parameter setups.

on the observables are significantly larger due to the large correlations, as shown exemplified with the case of  $y_+^{DK}$  in Fig. 5.35. This essentially determines the choice of parameterisation: it is possible to reliably model  $CP$  violation in the  $B^\pm \rightarrow D\pi^\pm$  channel and simultaneously determine the  $F_i$  parameters by using the 6-parameter setup, but not by using the 8-parameter setup.

Interestingly, when the constraints on  $\gamma$  are compared, both setup lead to similar precision; in spite of the large uncertainties on the individual observables in the 8-parameter setups, the constraints on  $\gamma$  are tight. This is illustrated in Fig. 5.36. Nevertheless, it remains true that the 8-parameter setup is ruled out due the statistical behaviour in the determination of the observables.

Furthermore, both the 6- and 8-parameter setups lead to fits that behave well in the studies where the  $F_i$  parameters are kept fixed, and the resulting uncertainties on the Cartesian observables and  $\gamma$  are essentially identical. Thus, the 6-parameter setup does not inherently lead to a gain in precision over the 8-parameter setup; the strength of the parameterisation is that it allows for a reliable, simultaneous determination of the  $F_i$  parameters and the observables of interest. This conclusion differs somewhat from the one drawn in Ref. [85].

The fixed- $F_i$  studies allow for an assessment of the gain in precision on  $\gamma$  due to the inclusion of the  $B^\pm \rightarrow D\pi^\pm$  mode, by comparing the precision obtained in the simultaneous fits with that obtained when  $\gamma$  is constrained using only information from the  $B^\pm \rightarrow DK^\pm$  channel. In the realistic case where  $r_B^{D\pi} = 0.005$ , the gain in precision is about  $0.1^\circ$ . The reason for the small impact, in spite of the yield being approximately 14 times larger in the  $B^\pm \rightarrow D\pi^\pm$  channel than in the  $B^\pm \rightarrow DK^\pm$  channel, is that  $r_B$  is 20 times smaller, and the  $CP$  asymmetries are proportional to  $r_B$ . Thus, the main improvement to the analysis from including  $B^\pm \rightarrow D\pi^\pm$  as a signal channel comes from the ability to determine the  $F_i$  parameters without adding a large systematic uncertainty.<sup>6</sup>

Finally, it is worth considering whether any precision can be gained by including further information on the  $F_i$  parameters from a control channel, even if the fit is well behaved without external information. The potential yield in the  $\bar{B}^0 \rightarrow D^{*+}(\rightarrow D^0\pi^+)\mu^-\bar{\nu}_\mu X$  control channel is approximately three times larger than in the  $B^\pm \rightarrow D\pi^\pm$  channel, and it does therefore offer a better statistical handle on the  $F_i$  values (at the significant cost of having to worry about efficiency corrections). This question can be answered by comparing the obtained precision on  $\gamma$  in the fits where  $F_i$  parameters were floating, to the precision in the case where they were kept fixed. Such a comparison is shown for the 6-parameter setup in Fig. 5.37 for the realistic scenario where  $r_B^{D\pi} = 0.005$ . The difference in the average  $\sigma(\gamma)$  is *less than*  $0.05^\circ$ , which is of course completely negligible. Therefore, no gain in precision can be obtained by including the control channel in the analysis, and it is not considered further.

---

<sup>6</sup>If this comparison is made using the parameter set  $(r_B^{D\pi}, \delta_B^{D\pi}) = (0.03, 330^\circ)$ , which corresponds to the alternative, non-physical solution in the LHCb combination [48], the gain in precision from the  $B^\pm \rightarrow D\pi^\pm$  channel is  $1.3^\circ$  instead, resulting in a final uncertainty of about  $2.3^\circ$ . This fact made the statistical interpretation of the  $B^\pm \rightarrow Dh^\pm$  combination in Ref. [48] non-trivial.

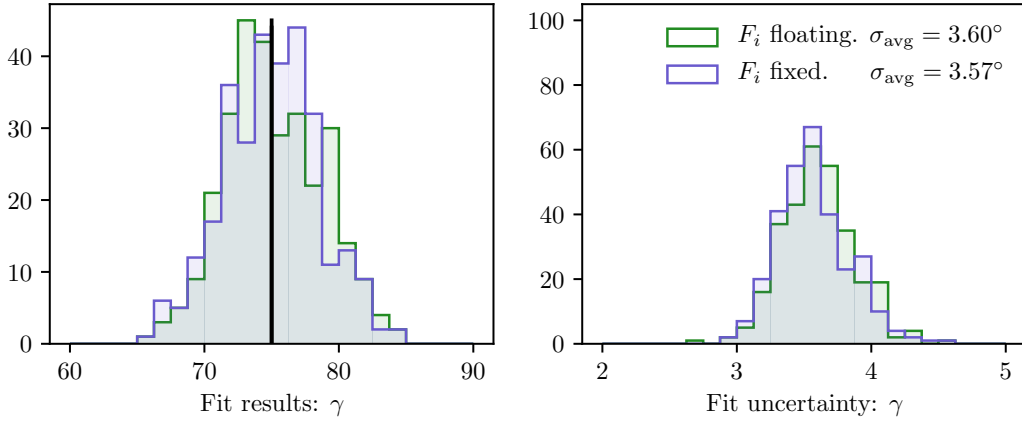


**Figure 5.37:** The distribution of (left) central values and (right) statistical uncertainty estimate for  $\gamma$  in a series of pseudo experiments that use the 6-parameter setup, where (green) the  $F_i$  parameters are determined in the fit and (blue) where they are kept fixed at their input values.

#### 2780 Final choice of observables and the determination of the $F_i$ parameters

2781 In the chosen setup, a single set of four parameters,  $(x_-^{DK}, y_-^{DK}, x_+^{DK}, y_+^{DK})$ , are  
 2782 shared between *all*  $B^\pm \rightarrow DK^\pm$  categories; they enter the expressions of Eq. (5.17)  
 2783 directly, and are thus determined in the fit. In the  $B^\pm \rightarrow D\pi^\pm$  categories, the  
 2784 four corresponding parameters,  $(x_-^{D\pi}, y_-^{D\pi}, x_+^{D\pi}, y_+^{D\pi})$ , are parameterised in terms  
 2785 of  $(x_\pm^{DK}, y_\pm^{DK})$  and the additional two observables  $(x_\xi^{D\pi}, y_\xi^{D\pi})$ . The  $F_i$  parameters  
 2786 are determined in the fit, being shared between the  $B^\pm \rightarrow DK^\pm$  and  $B^\pm \rightarrow D\pi^\pm$   
 2787 channels. However, separate parameter sets are determined for the LL and DD  
 2788 categories because the acceptance profile over the Dalitz plot differs between them.

2789 The  $F_i$  parameters are subject to the constraint that  $\sum_{i=-N}^N F_i^c = 1$ , for each  
 2790 category,  $c$ . Therefore, it is beneficial to introduce a reparameterisation in the  
 2791 likelihood function, where the  $F_i$  parameters are expressed in terms of a set of  
 2792 recursive fractions

$$\mathcal{R}_i = \begin{cases} F_i & , \quad i = -N \\ F_i / (\sum_{j \geq i} F_j) & , \quad -N < i < +N \end{cases} \quad (5.23)$$

2793 for which the constraint is much simpler, namely that each individual  $\mathcal{R}_i$  parameter  
 2794 lies in the interval  $[0, 1]$ . This parameterisation leads to well behaved fits, where  
 2795 the  $\mathcal{R}_i$  parameters do not suffer from significant correlations.

#### 2796 Strong-phase inputs

2797 The strong-phase parameters  $(c_i, s_i)$  are fixed in the fit to data. In the  $D \rightarrow$   
 2798  $K_S^0 \pi^+ \pi^-$  channels, the combined CLEO [74] and BESIII [76] measurement results

2799 are used, as reported in Ref. [76]. The  $D \rightarrow K_S^0 K^+ K^-$  categories also use combined  
 2800 CLEO [76] and BESIII results [77], which are reported in Ref. [77]. The experimental  
 2801 uncertainty on these measurements is propagated to the measured  $CP$ -violation  
 2802 observables as part of the systematic uncertainties in Section 5.6.1.

2803 **Treatment of backgrounds**

2804 The yield of combinatorial background decays is determined independently in each  
 2805 bin. A single, overall bin yield of partially reconstructed background from  $B^\pm$  and  
 2806  $B^0$  decays is determined in each of the 160 subcategories; the relative contribution  
 2807 from each individual background is fixed from the results of the first-stage fit,  
 2808 corrected for the different fit region (a systematic uncertainty is assigned due to this  
 2809 choice). In the  $B^\pm \rightarrow DK^\pm$  channels, the bin yields of the partially reconstructed  
 2810 background from  $B_s^0 \rightarrow \bar{D}^0[\pi^+]K^-$  decays are expressed via the  $F_i$ , exploiting that  
 2811 a positive companion particle is always produced along with a  $\bar{D}^0$  meson (and vice  
 2812 versa). The overall yield is fixed from the results of the first stage fit. Finally,  
 2813 the yield of the  $D\pi^\pm \leftrightarrow DK^\pm$  cross-feed components in each bin are determined  
 2814 via the obtained yield of correctly identified decays in the corresponding bin, and  
 2815 the known PID efficiencies. This is true for both fully and partially reconstructed  
 2816 decays, although only a  $D\pi^\pm \rightarrow DK^\pm$  component is included in the latter case.

2817 **The choice of fit range**

2818 The fit range is decreased to  $m_B \in [5150, 5800] \text{ MeV}/c^2$ . The information from  
 2819 candidates with lower reconstructed  $B$  masses was useful in determining the relative  
 2820 rates and free mass shape parameters of the partially reconstructed background  
 2821 components in the first-stage fit; however, with these fixed in the second-stage  
 2822 fit, this is no longer the case. Furthermore, the setup assumes that the shape of  
 2823 the partially reconstructed background is identical across the Dalitz bins. This  
 2824 assumption is not perfectly true, but the impact is minimal when the lower limit of  
 2825 the fit range is taken to be  $5150 \text{ MeV}/c^2$ , as described further in Section 5.6.3.

2826 **Self-consistency check**

2827 In order to establish the fit stability and investigate a potential bias, a series of  
 2828 pseudo experiments are run, in which data sets are generated using the model, and  
 2829 then fitted back. The total yields are taken from the first-stage fit. The signal  
 2830 yields are distributed between Dalitz bins using input physics parameters that  
 2831 approximately equal the values obtained in Section 5.5.2 from the results of the fit

**Table 5.8:** Mean biases and pulls for the observables of interest in the final, binned fit, obtained in a large number of pseudoexperiments.

Parameter	Mean bias ( $\times 10^{-2}$ )	Mean pull	Pull width
$x_-^{DK}$	$-0.018 \pm 0.022$	$-0.01 \pm 0.02$	$1.01 \pm 0.02$
$y_-^{DK}$	$-0.014 \pm 0.026$	$-0.00 \pm 0.02$	$0.99 \pm 0.02$
$x_+^{DK}$	$-0.018 \pm 0.022$	$-0.01 \pm 0.02$	$1.00 \pm 0.02$
$y_+^{DK}$	$-0.016 \pm 0.028$	$0.01 \pm 0.02$	$1.00 \pm 0.02$
$x_\xi^{D\pi}$	$0.029 \pm 0.052$	$0.06 \pm 0.02$	$1.00 \pm 0.02$
$y_\xi^{D\pi}$	$0.000 \pm 0.060$	$0.01 \pm 0.02$	$1.00 \pm 0.02$

to data. The  $F_i$  parameters are taken from a fit to data. The partly reconstructed background is distributed as " $D^0$ -like", ie. in the  $B^\pm$  channels  $N_i^\pm \propto F_{\mp i}$ , except for the  $B_s^0$  background, which is " $\bar{D}^0$ -like" ( $N_i^\pm \propto F_{\pm i}$ ). The combinatorial background includes real  $D$  mesons paired with a random companion, as well as fake  $D$  mesons that are themselves made up of random tracks. The former is distributed as 50/50  $D^0$ -like and  $\bar{D}^0$ -like in the toy generation, whereas the latter is assumed to be evenly distributed over the Dalitz plot (ie. the bin yield is proportional to the bin area).

A set of 2000 pseudo experiments has been run, out of which 98.8 % converged properly. The pull plots for the observables of interest are shown in Figs. 5.38 and 5.39; the mean biases and pulls are summarised in Table 5.8. No biases are statistically significant, and the uncertainties are seen to be well estimated.

### 5.5.2 Main results

The values and statistical uncertainties of observables obtained in the fit are

$$\begin{aligned} x_-^{DK} &= (-5.68 \pm 0.96) \times 10^{-2}, & y_-^{DK} &= (-6.55 \pm 1.14) \times 10^{-2}, \\ x_+^{DK} &= (-9.30 \pm 0.98) \times 10^{-2}, & y_+^{DK} &= (-1.25 \pm 1.23) \times 10^{-2}, \\ x_\xi^{D\pi} &= (-5.47 \pm 1.99) \times 10^{-2}, & y_\xi^{D\pi} &= (0.71 \pm 2.33) \times 10^{-2}. \end{aligned} \quad (5.24)$$

The statistical correlation matrix for the observables is given in Table 5.9. None of the correlations are larger than 15 % and the values of both uncertainties and correlation coefficients are similar to those obtained in the feasibility studies. The 2D log-likelihood profile for the observables is shown in Fig. 5.40, based on a full likelihood scan, where the fit is repeated with the observables fixed to a range of values around the optimal solution. It can be seen in the figure that the likelihood profile obtained in the scan is very well modelled by the Gaussian approximation, based on the Hessian matrix at maximum likelihood. Thus, the

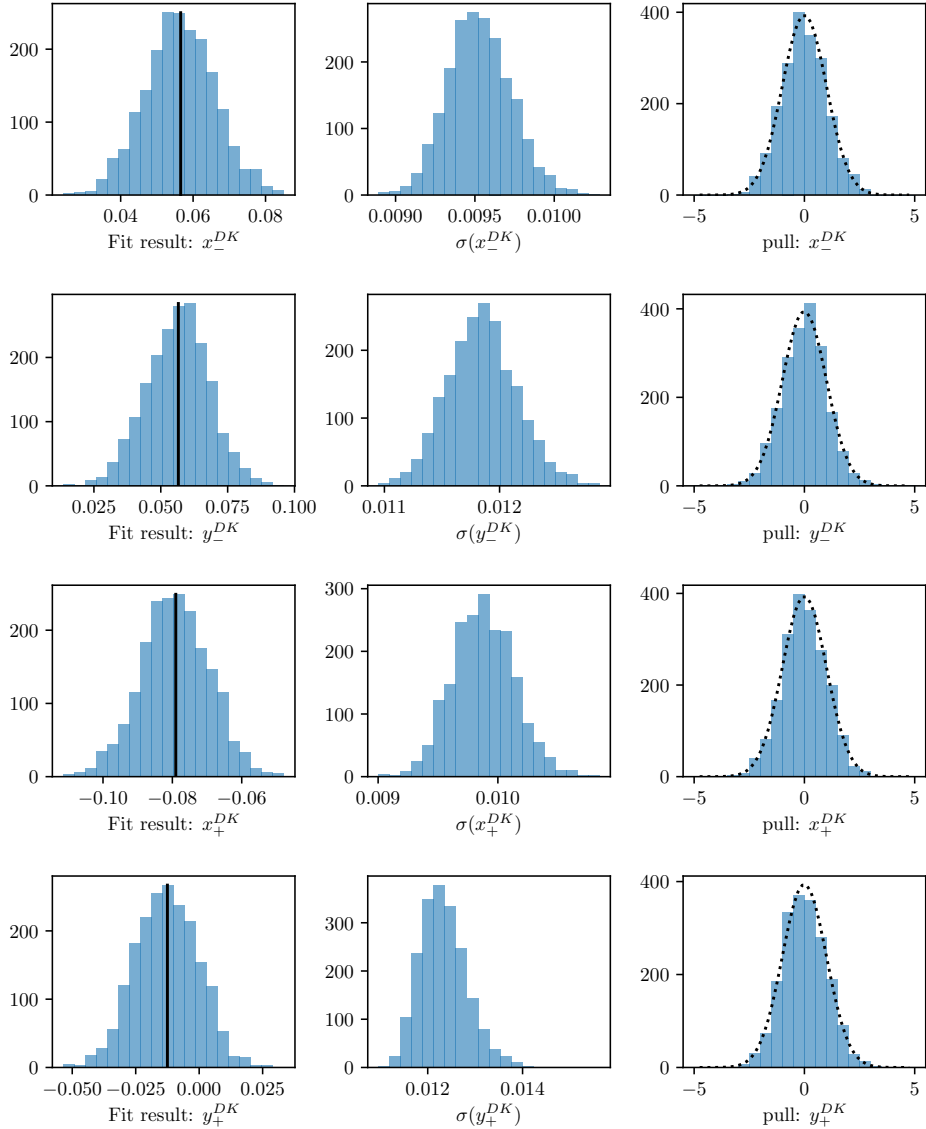


**Figure 5.38:** The (left) fitted value, (centre) estimated statistical uncertainty, and (right) pulls for the  $B^\pm \rightarrow DK^\pm$  observables, as obtained in a number of pseudo experiments. The black line on the left shows the value used to generate the pseudo data sets; the dotted line on the right shows a Gaussian distribution with mean equal to zero and a standard deviation equal to unity.

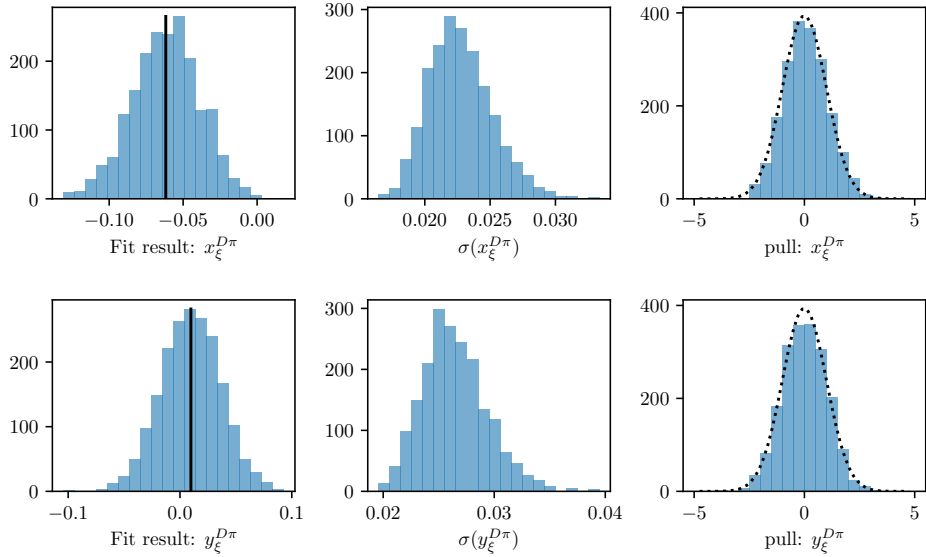


**Figure 5.39:** The (left) fitted value, (centre) estimated statistical uncertainty, and (right) pulls for the  $B^\pm \rightarrow D\pi^\pm$  observables, as obtained in a number of pseudo experiments. The black line on the left shows the value used to generate the pseudo data sets; the dotted line on the right shows a Gaussian distribution with mean equal to zero and a standard deviation equal to unity.

statistical uncertainties quoted in Eq. (5.24) are likely to be accurate. The signature of  $CP$  violation is that  $(x_+^{DK}, y_+^{DK}) \neq (x_-^{DK}, y_-^{DK})$ , very clearly the case for the measurement results. Finally, the figure illustrates how the opening angle between the two points defined by  $(x_+^{DK}, y_+^{DK})$  and  $(x_-^{DK}, y_-^{DK})$  is equal to  $2\gamma$ .

The full set of fit projections in all 160 subcategories is included in Appendix A. While the  $CP$  asymmetry of the phase-space integrated yield is small, this is not the case for all individual bin-pairs. This is shown in Fig. 5.41 where, as an example, the fit projections for the  $B^+ \rightarrow DK^+$  decays in bin +2 and the  $B^- \rightarrow DK^-$  decays in bin -2 of the  $D \rightarrow K_S^0 \pi^+ \pi^-$  Dalitz plot are compared. The presence of  $CP$  violation is clearly visible.

The obtained  $F_i$  parameter values are shown in Table 5.10. These parameters can be useful in other BPGGSZ measurements made within the LHCb collaboration: it is expected that the systematic uncertainty due to differences between the Dalitz-plot acceptance profile in  $B^\pm \rightarrow Dh^\pm$  decays and, say,  $B \rightarrow D^*K$  or  $B \rightarrow DK^*$  decays is smaller than the systematic arising from extracting the efficiency profile from simulated decays. Therefore, the obtain central values and uncertainties have been made public [1], including a set of systematic uncertainties discussed in Section 5.6.12.<sup>7</sup>

<sup>7</sup>In practice, it is the obtained  $\mathcal{R}_i$  values that are made public, related to the  $F_i$  parameters via Eq. (5.23).

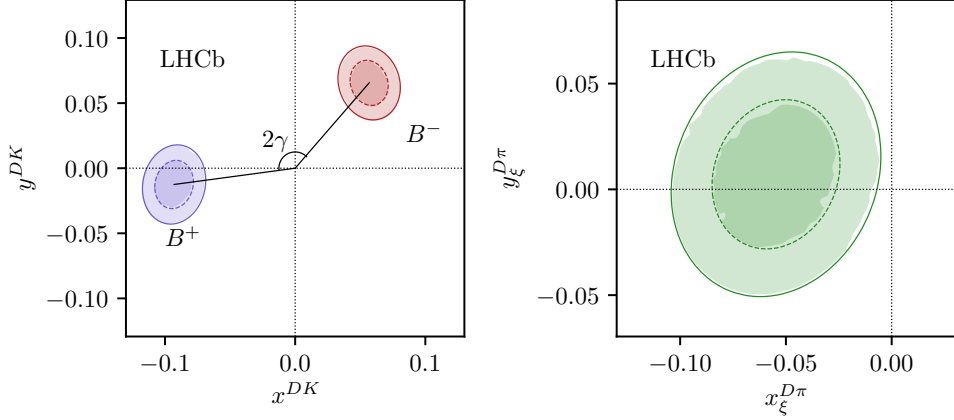


**Figure 5.40:** The 68 % and 95 % confidence regions for the fitted observables. The lines show the regions estimated from the covariance matrix returned by the default fit. The shaded areas are obtained in a likelihood scan, where the binned fit is run many times with all observables held at fixed values, scanning pairs of observables over the relevant ranges. The scan is made separately for the three pairs  $(x_{-}^{DK}, y_{-}^{DK})$ ,  $(x_{+}^{DK}, y_{+}^{DK})$ , and  $(x_{\xi}^{D\pi}, y_{\xi}^{D\pi})$ , holding the four other parameters fixed at their default-fit central values during a given scan. Then the minimum log-likelihood is related to a  $\chi^2$  via  $\mathcal{L}_{\min} = \frac{1}{2}\chi^2$  (discarding an irrelevant constant), and the confidence region limits placed at  $\chi^2 = 2.30$  and  $\chi^2 = 6.18$ , yielding the relevant percentiles for a  $\chi^2$  distribution with 2 degrees of freedom.

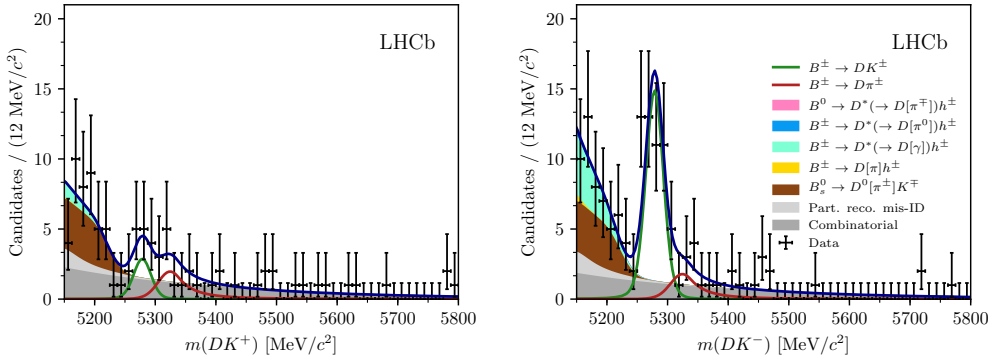


**Figure 5.41:** The invariant mass distribution for the (left)  $B^+ \rightarrow DK^+$  candidates in bin -2 and (right) the  $B^- \rightarrow DK^-$  candidates in bin +2, where  $D \rightarrow K_S^0\pi^+\pi^-$  and the  $K_S^0$  is reconstructed in the DD category.

### 2871 5.5.3 Cross checks

2872 A series of cross checks are performed to verify that the fit to data is behav-  
2873 ing as expected.

**Table 5.9:** Statistical uncertainties and correlation matrix for the fit to data.

Uncertainty ( $\times 10^{-2}$ )						
	$x_-^{DK^\pm}$	$y_-^{DK^\pm}$	$x_+^{DK^\pm}$	$y_+^{DK^\pm}$	$x_\xi^{D\pi^\pm}$	$y_\xi^{D\pi^\pm}$
$\sigma$	0.96	1.14	0.96	1.20	1.99	2.34

Correlations						
	$x_-^{DK^\pm}$	$y_-^{DK^\pm}$	$x_+^{DK^\pm}$	$y_+^{DK^\pm}$	$x_\xi^{D\pi^\pm}$	$y_\xi^{D\pi^\pm}$
$x_-^{DK^\pm}$	1.000	-0.125	-0.013	0.019	0.028	-0.165
$y_-^{DK^\pm}$		1.000	-0.011	-0.009	0.105	0.030
$x_+^{DK^\pm}$			1.000	0.088	-0.099	0.038
$y_+^{DK^\pm}$				1.000	-0.076	-0.141
$x_\xi^{D\pi^\pm}$					1.000	0.146
$y_\xi^{D\pi^\pm}$						1.000

2874 **Comparison to results of earlier analyses**

2875 It is confirmed that the results obtained in fits of the Run 1 or 2015+16 data  
 2876 sets in isolation are compatible with the results obtained in the original LHCb  
 2877 analyses of those data sets [3, 73]. In order to do so, the whole analysis procedure  
 2878 is carried out using only the relevant subset of data, and the strong-phase inputs  
 2879 from the CLEO collaboration are used in the fit. Two effects need to be taken  
 2880 into account when comparing the central values.

2881 Firstly, the overlap between the data samples is not 100 % due to changes in  
 2882 the candidate selection. The overlap between the new selection and the data set  
 2883 of the original analysis of Run 1 data is about 70 %, whereas is it about 90 % for  
 2884 the 2015+16 data set. In order to determine the expected difference between the  
 2885 observables fitted from data sets with significant overlap, a large number of toy data  
 2886 sets were generated in sets of two, where 70 (90) % of decays were shared between the  
 2887 data sets. Both data sets were fitted and the difference between the obtained central  
 2888 values for each observable tabulated; the standard deviation of these distributions  
 2889 are used to calculate the pulls between the old analysis results and the new fits to  
 2890 data. This check does not take into account that the semi-leptonic PID cuts were  
 2891 introduced to remove a potential peaking background, which may have had a small  
 2892 systematic effect on the earlier measurement results. Thus the expected differences  
 2893 are likely to be slightly underestimated and the check is conservative.

2894 Furthermore, the  $F_i$  parameters were determined in a semi-leptonic control  
 2895 channel in the earlier analyses. Therefore, the expected difference obtained above is

**Table 5.10:** The fitted  $F_i$  values including statistical uncertainties. The associated systematic uncertainties are negligible, as discussed in Section 5.6.12.

$F_i$ values: $D \rightarrow K_S^0 \pi^+ \pi^-$		
bin	LL	DD
-8	$0.024 \pm 0.001$	$0.024 \pm 0.000$
-7	$0.127 \pm 0.001$	$0.133 \pm 0.001$
-6	$0.062 \pm 0.001$	$0.056 \pm 0.001$
-5	$0.046 \pm 0.001$	$0.042 \pm 0.001$
-4	$0.095 \pm 0.001$	$0.095 \pm 0.001$
-3	$0.160 \pm 0.001$	$0.160 \pm 0.001$
-2	$0.153 \pm 0.001$	$0.153 \pm 0.001$
-1	$0.095 \pm 0.001$	$0.097 \pm 0.001$
1	$0.022 \pm 0.001$	$0.020 \pm 0.000$
2	$0.005 \pm 0.000$	$0.005 \pm 0.000$
3	$0.004 \pm 0.000$	$0.004 \pm 0.000$
4	$0.055 \pm 0.001$	$0.056 \pm 0.001$
5	$0.027 \pm 0.001$	$0.022 \pm 0.000$
6	$0.004 \pm 0.000$	$0.003 \pm 0.000$
7	$0.055 \pm 0.001$	$0.057 \pm 0.001$
8	$0.067 \pm 0.001$	$0.072 \pm 0.001$

$F_i$ values: $D \rightarrow K_S^0 K^+ K^-$		
bin	LL	DD
-2	$0.207 \pm 0.004$	$0.202 \pm 0.003$
-1	$0.222 \pm 0.004$	$0.230 \pm 0.003$
1	$0.290 \pm 0.005$	$0.296 \pm 0.003$
2	$0.281 \pm 0.005$	$0.271 \pm 0.003$

adjusted by adding the  $F_i$ -related systematic uncertainty of the original analysis in quadrature, when comparing the old results to those in new fits to the Run 1 and 15+16 data sets. No further corrections have been made to the expected differences, which effectively assumes all other systematic uncertainties to be 100 % correlated. Also for this reason can the check be considered conservative. As can be seen in Tables 5.11 and 5.12, neither the Run 1 and 2015+16 comparisons show unreasonable differences in central values.

### Directly fitting the signal yields

As a cross-check, the fit is run in an alternative mode, in which the signal yields of each bin are independent parameters. The obtained yields are compared to those

**Table 5.11:** Comparison between the results on the Run 1 analysis [73] and the central values obtained when fitting the Run 1 dataset with the selection and fit setup described in this note. The pull is calculated using the  $1\sigma$  expected difference, which takes the sample overlap and the systematic uncertainty on the  $F_i$  parameters in the previous analysis into account, but assumes all other systematic uncertainties to be perfectly correlated. The new fits are performed using the CLEO strong-phase inputs.

Observable	Run 1 result [73]	New Fit (central value $\times 10^{-2}$ )	Pull
$x_-^{DK}$	2.50	4.04	0.85
$y_-^{DK}$	7.50	9.14	1.02
$x_+^{DK}$	-7.70	-9.40	-0.91
$y_+^{DK}$	-2.20	0.80	1.77
<i>p</i> -value: 0.057			

**Table 5.12:** Comparison between the results on the 2015+16 analysis [3] and the central values obtained when fitting the 2015+16 dataset with the selection and fit setup described in this note. The pull is calculated using the  $1\sigma$  expected difference, which takes the sample overlap and the systematic uncertainty on the  $F_i$  parameters in the previous analysis into account, but assumes all other systematic uncertainties to be perfectly correlated. The new fits are performed using the CLEO strong-phase inputs.

Observable	15+16 result [3]	New Fit (central value $\times 10^{-2}$ )	Pull
$x_-^{DK}$	9.00	8.36	-0.50
$y_-^{DK}$	2.10	1.16	-0.62
$x_+^{DK}$	-7.70	-8.58	-0.56
$y_+^{DK}$	-1.00	-2.82	-1.39
<i>p</i> -value: 0.239			

predicted from the results of the default fit in Fig. 5.42. The yields are shown for each "effective bin", where effective bin  $i$  is defined as bin  $+i$  for  $B^+$  decays and bin  $-i$  for  $B^-$  decays; in the  $CP$  symmetric case, these bins are expected to have equal yields (modulo production and detection asymmetries). The agreement between the two fit set-ups is seen to be excellent. The normalised yield asymmetries, defined as

$$A^i \equiv \frac{N_{-i}^- - N_i^+}{N_{-i}^- + N_i^+} \quad (5.25)$$

are shown in Fig. 5.43 for all decay channels. Again, the agreement between the nominal fit and the alternative fit with independent yields is found to be excellent for both  $B^\pm \rightarrow Dh^\pm$  decays. It is also clear how, in the case of  $B^\pm \rightarrow DK^\pm$  decays, the asymmetry is significantly different from zero for a number of bin pairs. The reason

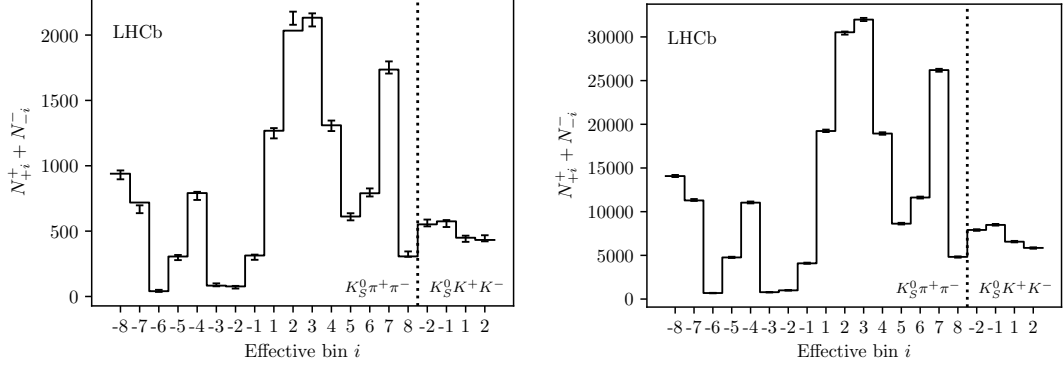


**Figure 5.42:** Comparison of (lines) the predicted yield given the determined  $CP$  observables and (error bars) the yield obtained in fits to data where each yield is an independent parameter. The yields are shown for (left)  $B^\pm \rightarrow DK^\pm$  decays and (right)  $B^\pm \rightarrow D\pi^\pm$  decays. The LL and DD categories have been combined, as has the  $B^+$  and  $B^-$  yields for each effective Dalitz bin, defined as bin  $+i$  for  $B^+$  decays and bin  $-i$  for  $B^-$  decays.

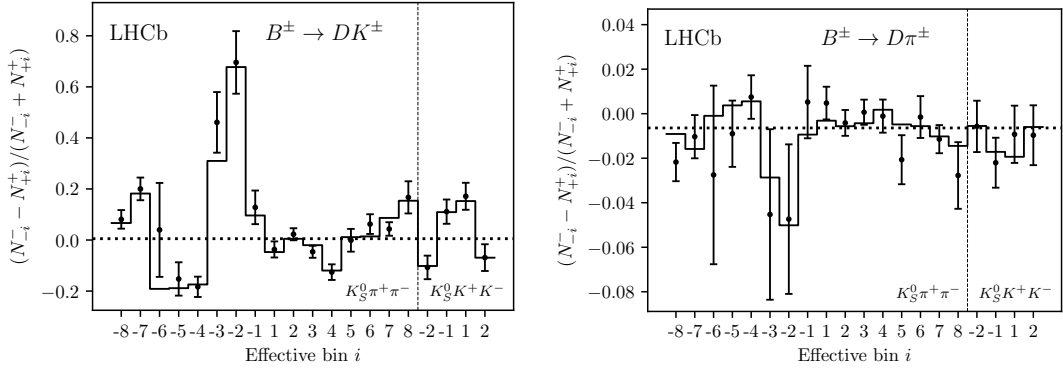


**Figure 5.43:** The bin-by-bin asymmetries  $(N_{-i}^- - N_{+i}^+)/N_{-i}^- + N_{+i}^+$  for each Dalitz-plot bin number for (left)  $B^\pm \rightarrow DK^\pm$  decays and (right)  $B^\pm \rightarrow D\pi^\pm$  decays. The prediction from the central values of the  $CP$ -violation observables is shown with a solid line and the asymmetries obtained in fits with independent bin yields are shown with the error bars. The predicted asymmetries in a fit that does not allow for  $CP$  violation are shown with a dotted line.

that the yield asymmetry is not zero in the fit that does not allow for  $CP$  violation,  
 is that the overall yield of  $B^+$  and  $B^-$  decays are allowed to differ in this fit; only the  
 phase-space distribution of the decays is enforced to be  $CP$ -symmetric. The observed  
 asymmetry is due to a combination of production and detection asymmetries,  
 $CP$ -violation and material interaction of the  $K_S^0$  meson, and  $CP$  violation in the  
 $B^\pm \rightarrow Dh^\pm$  decays, but no attempt is made to disentangle the effects.

2921 **Fitting subsets of the data separately**

2922 One cross check is carrying out, by determining the  $CP$  observables using a number  
2923 of independent sub samples of the data set separately. This is done for the  
2924 following following data splits

- 2925 • Fig. 5.44a shows the same plots, comparing the fits to the data set split by  
2926  $K_S^0$  track type.
- 2927 • Fig. 5.44b shows the same plots, comparing the fits to the data set split by  
2928 whether the  $D$  meson decays to the  $K_S^0\pi^+\pi^-$  or  $K_S^0K^+K^-$  final state.
- 2929 • Fig. 5.45a shows the two dimensional log likelihood contours for the observables  
2930 for fits to the Run 1, 2015+16, 2017 and 2018 datasets separately
- 2931 • Fig. 5.45b shows the same plots, comparing the fits to the data set split by  
2932 whether the candidate event was triggered by one of the signal particles at the  
2933 hardware level (TOS), or by another particle in the underlying event (TIS).
- 2934 • Fig. 5.45c shows the same plots, comparing the fits to the data set split the  
2935 magnet polarity during data taking.

2936 All figures show the Gaussian likelihood contours corresponding to the statistical  
2937 uncertainties. There is good agreement between the results in all cases, given  
2938 that in each cases the sub datasets are independent and therefore the statistical  
2939 errors are uncorrelated.

2940 **Constraints from a subset of bins**

2941 An alternative way to subdivide the data is to examine the constraints from a subset  
2942 of bins individually; this forms as a cross check because the observables favoured by  
2943 each sub set should be compatible, and also serves as a useful illustration of the  
2944 features of the BPGBGSZ method. Likelihood contours for  $(x_\pm^{DK}, y_\pm^{DK})$  are shown in  
2945 Fig. 5.46, obtained using the binned yields in the  $D \rightarrow K_S^0\pi^+\pi^-$  bins, determined  
2946 in the fits of individual bin yields described in Section 5.5.3. The bins are split by  
2947 whether they are ADS-like, GLW-like, or Odd-even according to the classification in  
2948 Section 2.3.5. It is clear that the likelihood regions show a reasonable overlap, and  
2949 also how it is the GLW bins that constrain the  $x_\pm$  parameter, while the Odd-even  
2950 and ADS-like bins provide the ability to constrain the  $y_\pm$  parameters.

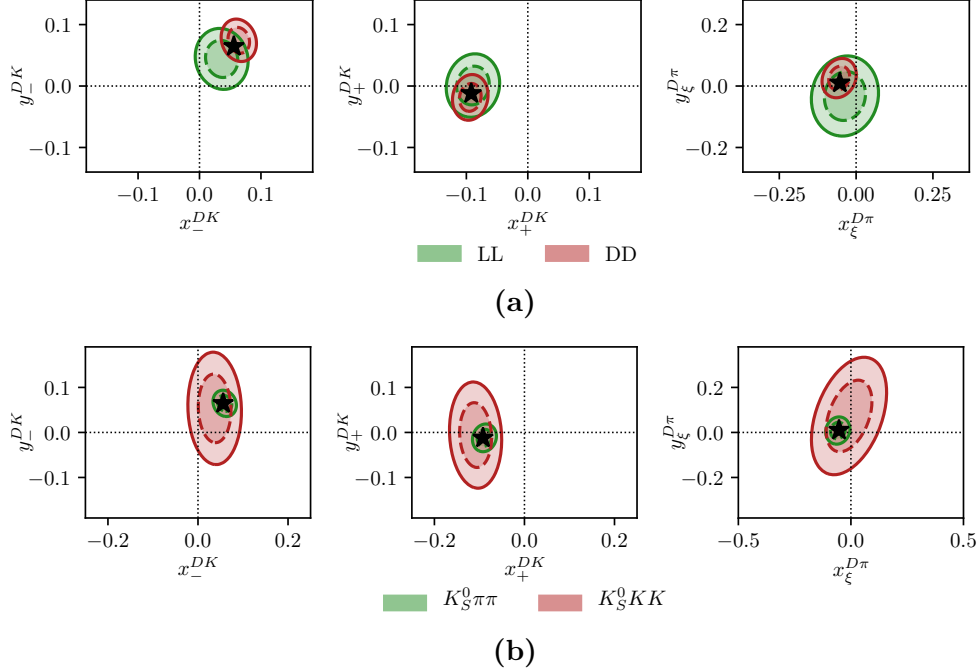


**Figure 5.44:** Comparison of the 68 % and 95 % confidence regions for (left)  $(x_{-}^{DK}, y_{-}^{DK})$ , (centre)  $(x_{+}^{DK}, y_{+}^{DK})$ , and (right)  $(x_{\xi}^{D\pi}, y_{\xi}^{D\pi})$  obtained from fits to sub sets of the data set. The uncertainties are statistical only. The central values of the default fit are shown with a black star. The dataset is split by (a) LL and DD  $K_S^0$  types and (b)  $D$  decay mode.

### 2951 Significantly reducing the $B^\pm \rightarrow D\pi^\pm$ to $B^\pm \rightarrow DK^\pm$ cross feed

2952 One of the dominant backgrounds in the signal region of the  $B^\pm \rightarrow DK^\pm$  channel  
 2953 is from partly reconstructed  $B \rightarrow D\pi X$  decays where the companion pion is  
 2954 misidentified as a kaon. The background mode is well described by the included  
 2955 shape component, and included in all relevant systematic studies. Nevertheless, an  
 2956 additional cross check is carried out to ensure that it is not having a significant effect  
 2957 on the fit: the analysis is repeated with PID requirement of  $\text{PID}_K > 12$  required  
 2958 to place a candidate in the  $B^\pm \rightarrow DK^\pm$  category, instead of  $\text{PID}_K > 4$ . With this  
 2959 requirement 99.7 % of  $B^\pm \rightarrow D\pi^\pm$  decays are correctly identified, making the cross-  
 2960 feed component in the  $B^\pm \rightarrow DK^\pm$  channels significantly smaller than in the default  
 2961 fit. This is clearly visible in Fig. 5.47, where the fit projections for the global fit of the  
 2962  $D \rightarrow K_S^0\pi^+\pi^-$  modes are shown. In return, the probability of correctly identifying a  
 2963 kaon companion drops to about 68–69 %, resulting in a smaller effective signal yield.

2964 The measurement results are compared in Table 5.13, where the differences  
 2965 in central value are seen to be reasonably small. It is not trivial to determine  
 2966 whether the difference is statistically significant or not: the same candidates are  
 2967 analysed in both cases, the difference being that a number of candidates that are

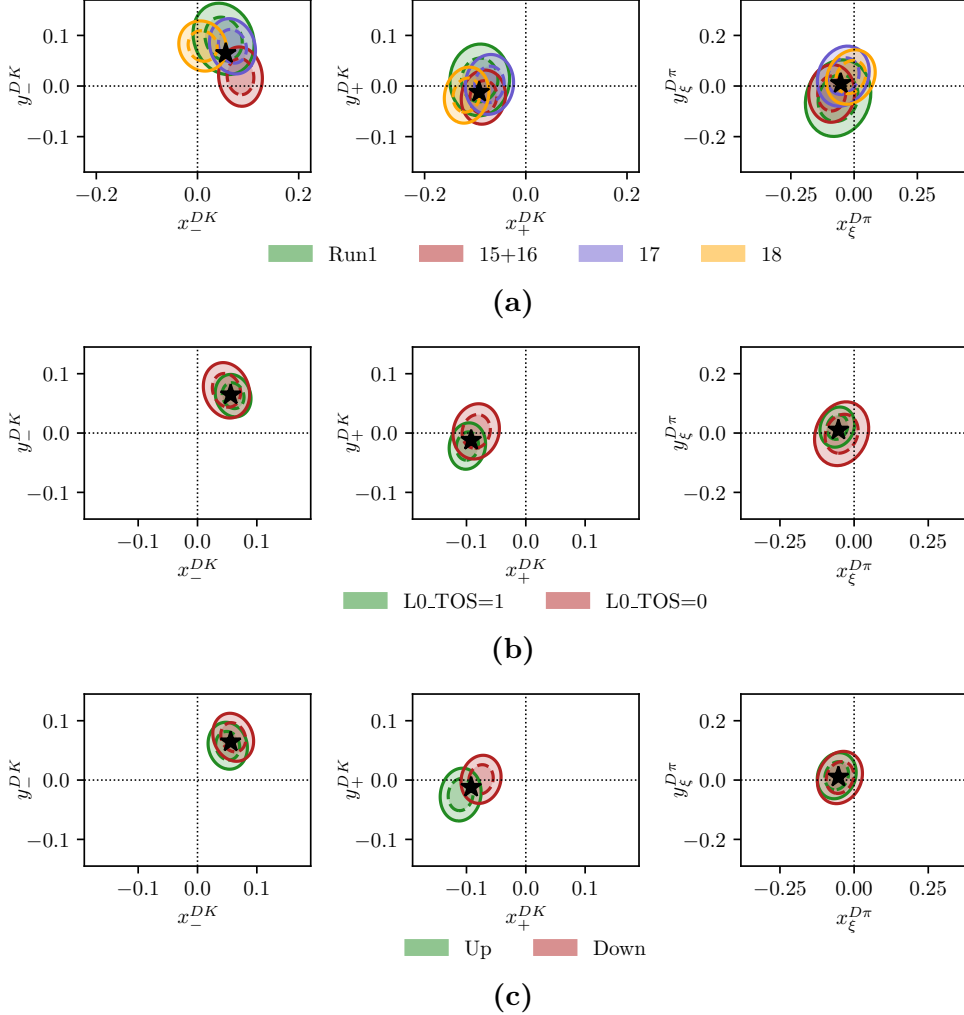


**Figure 5.45:** Comparison of the 68 % and 95 % confidence regions for (left)  $(x_-^{DK}, y_-^{DK})$ , (centre)  $(x_+^{DK}, y_+^{DK})$ , and (right)  $(x_\xi^{D\pi}, y_\xi^{D\pi})$  obtained from fits to sub sets of the data set. The uncertainties are statistical only. The central values of the default fit are shown with a black star. The dataset is split by (a) data taking year, (b) trigger category, and (c) magnet polarity.

placed in the  $B^\pm \rightarrow DK^\pm$  category in the nominal fit are placed in the  $B^\pm \rightarrow D\pi^\pm$  category in the alternative fit. The uncertainty will not be 100 % correlated because signal events that move from the  $DK$  to  $D\pi$  category are placed in a region with high background; however, this is somewhat compensated for by candidates that remain in the  $DK$  category gaining statistical power due to the increased purity. An estimate of the expected statistical fluctuation can be determined by taking the difference of the statistical uncertainties in quadrature. Using this estimate, the observed shifts are found to be consistent with statistical fluctuation, and thus there is no sign of the background from  $D\pi^\pm \rightarrow DK^\pm$  cross-feed causing issues.

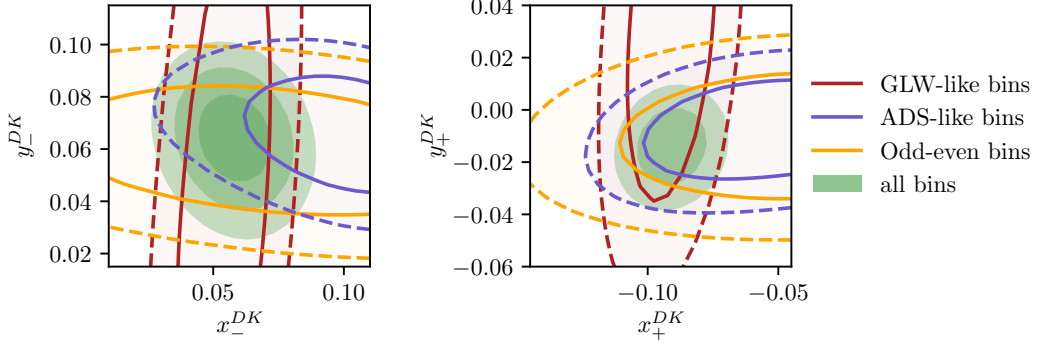


**Figure 5.46:** Constraints on the  $B^\pm \rightarrow DK^\pm$  observables from the signal yields of different subsets the  $D \rightarrow K_S^0 \pi^+ \pi^-$  Dalitz bins, using the bin categorisation developed in Section 2.3.5.

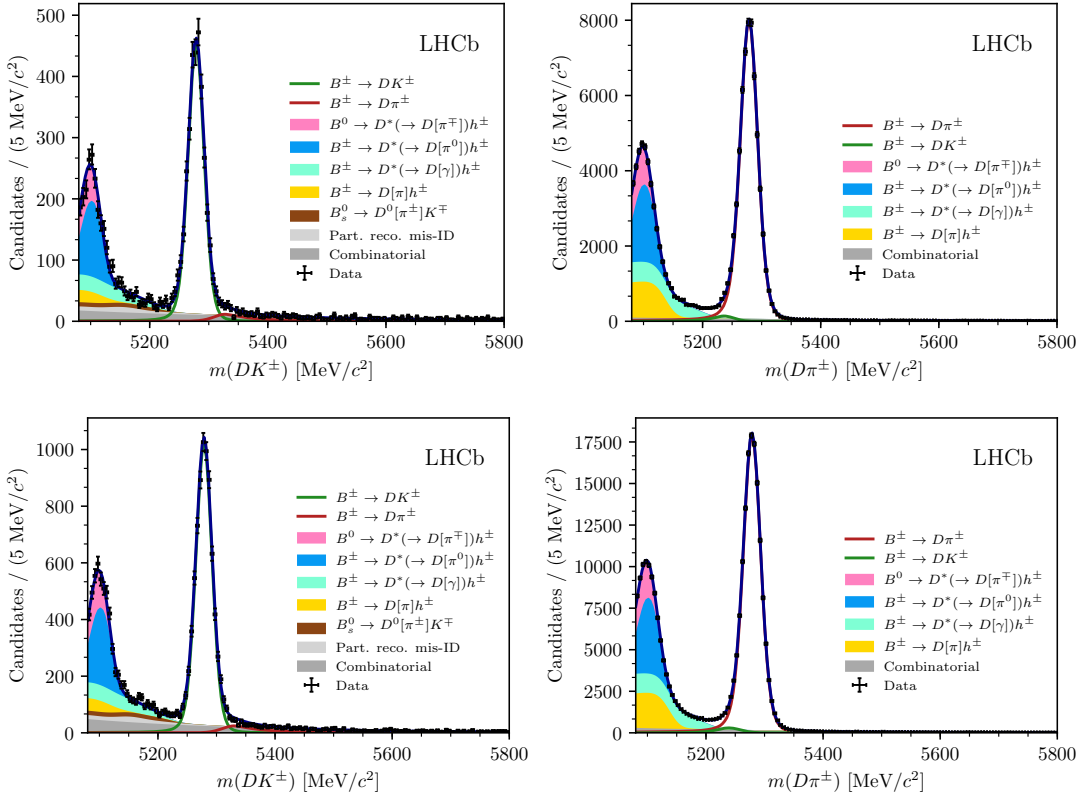


**Figure 5.47:** Fit projections for fits to the  $D \rightarrow K_S^0 \pi^+ \pi^-$  candidates with a companion PIDK requirement at 12 instead of 4 used to split into (left)  $B^\pm \rightarrow DK^\pm$  and (right)  $B^\pm \rightarrow D\pi^\pm$  candidates, for the (top) LL and (bottom) DD categories.

**Table 5.13:** Results of running the measurement with the default PIDK requirement at 4 used to separate  $B^\pm \rightarrow DK^\pm$  and  $B^\pm \rightarrow D\pi^\pm$  candidates, as well as with an alternative PIDK requirement at 12, resulting in much lower cross-feed from misidentified  $B^\pm \rightarrow D\pi^\pm$  decays. We also show the pulls, defined as  $\Delta x / \sqrt{|\sigma_{PIDK>12}^2 - \sigma_{PIDK>4}^2|}$  as described in the main text body. The comparison was made before the BESIII measurement of the  $D \rightarrow K_S^0 K^+ K^-$  strong-phase inputs became available; therefore the fits use the CLEO-only results [74] for this mode, which explains why the results quoted for  $PIDK > 4$  differ slightly from the nominal fit results.

Parameter	$PIDK > 4$	$PIDK > 12$	$\sigma = \sqrt{\sigma_{PIDK>12}^2 - \sigma_{PIDK>4}^2}$	Pull
$x_-^{DK}$	$5.59 \pm 0.96$	$5.82 \pm 1.01$	0.30	0.77
$y_-^{DK}$	$6.45 \pm 1.14$	$6.86 \pm 1.19$	0.36	1.13
$x_+^{DK}$	$-9.21 \pm 0.96$	$-8.94 \pm 1.01$	0.30	0.93
$y_+^{DK}$	$-1.21 \pm 1.20$	$-0.94 \pm 1.26$	0.37	0.71
$x_\xi^{D\pi}$	$-5.30 \pm 1.99$	$-5.13 \pm 2.02$	0.32	0.52
$y_\xi^{D\pi}$	$1.03 \pm 2.34$	$1.71 \pm 2.33$	0.28	2.40

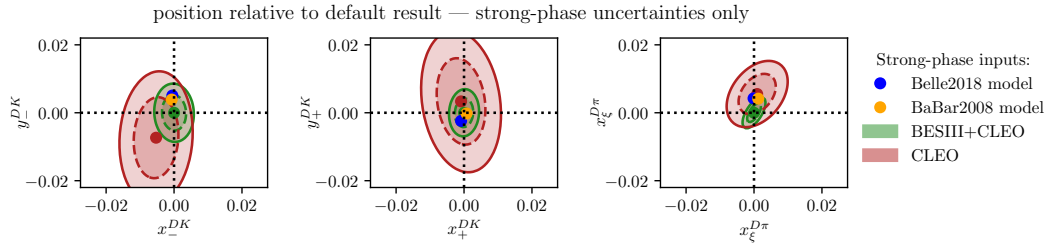


**Figure 5.48:** Fit results for (left)  $(x_-^{DK}, y_-^{DK})$ , (centre)  $(x_+^{DK}, y_+^{DK})$ , and (right)  $(x_\xi^{D\pi}, y_\xi^{D\pi})$  depending on strong-phase inputs, shown relative to the default fit results. The included results are based on (green) the BESIII-CLEO combination, which is the default, (red) the CLEO-only results, (blue dot) the 2018 Belle model [55] and (orange dot) the 2008 BaBar model [63]. For the measurements, only strong-phase related uncertainties are included in the plotted confidence regions.

## 2977 Compare results obtained with different strong-phase inputs

2978 It is interesting to compare the results obtained with different strong-phase inputs.  
 2979 This is done in Fig. 5.48, where the default fit results are compared to those  
 2980 obtained if the  $CP$  fit is done with the CLEO-only inputs [74], and with the model  
 2981 predictions from the 2018 Belle model [55] and the 2008 BaBar model [63]. For the  
 2982 measurements, only the strong-phase-related uncertainties are included in the plot,  
 2983 since the statistical uncertainties are correlated. All results are found to agree well.

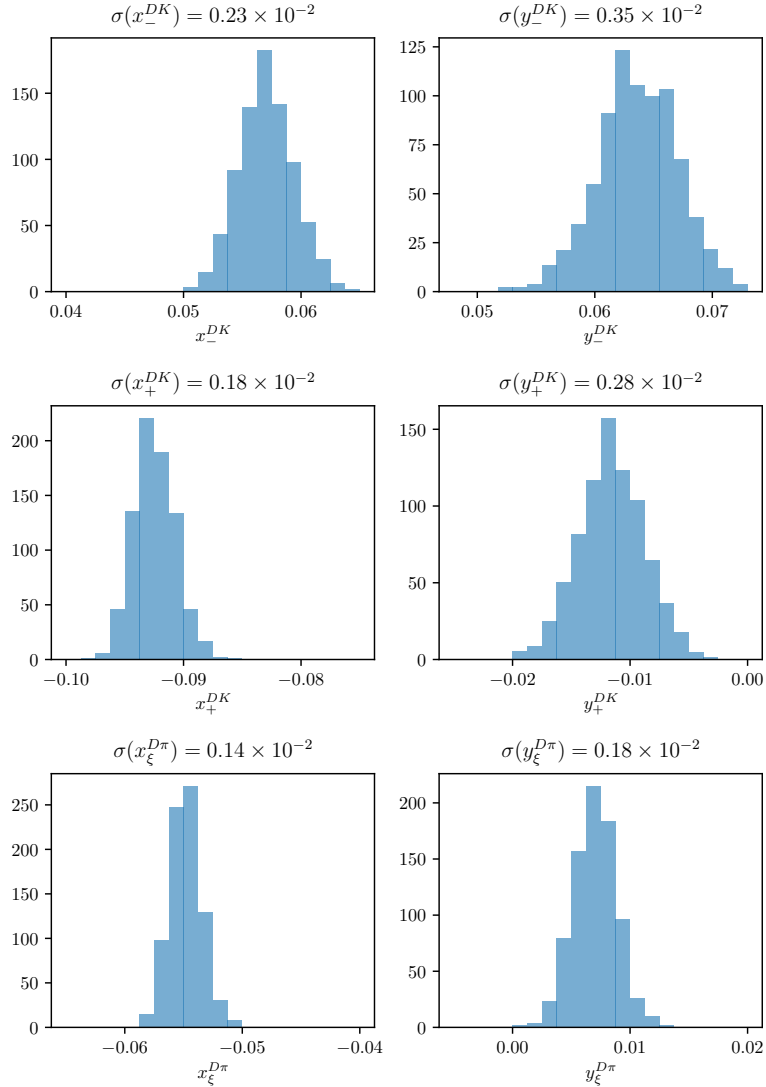


**Figure 5.49:** Spread of central values for the fitted observables when the input  $c_i$  and  $s_i$  from the BESIII+CLEO combination are varied according to their uncertainties and correlations.

## 2984 5.6 Systematic uncertainties

2985 The following sections cover the suite of systematic uncertainties on the measurement  
2986 that has been considered. All uncertainties are summarised in Section 5.6.12.

2987 **5.6.1 Strong phase uncertainties**

2988 The observables  $x_\pm^{DK}$ ,  $y_\pm^{DK}$ ,  $x_\xi^{D\pi}$  and  $y_\xi^{D\pi}$  are extracted using the central values  
2989 of  $c_i$  and  $s_i$  from the BESIII–CLEO combinations [74, 76, 77]. The measurement  
2990 uncertainty on these inputs is propagated to the observables by performing a large  
2991 set of fits to data that use alternative values of  $c_i$  and  $s_i$ . The new  $c_i$  and  $s_i$

**Table 5.14:** Systematic uncertainties and correlation matrix due to strong-phase inputs.

Uncertainty ( $\times 10^{-2}$ )						
	$x_-^{DK\pm}$	$y_-^{DK\pm}$	$x_+^{DK\pm}$	$y_+^{DK\pm}$	$x_\xi^{D\pi\pm}$	$y_\xi^{D\pi\pm}$
$\sigma$	0.23	0.35	0.18	0.28	0.14	0.18

Correlations						
	$x_-^{DK\pm}$	$y_-^{DK\pm}$	$x_+^{DK\pm}$	$y_+^{DK\pm}$	$x_\xi^{D\pi\pm}$	$y_\xi^{D\pi\pm}$
$x_-^{DK\pm}$	1.000	-0.047	-0.490	0.322	0.189	0.144
$y_-^{DK\pm}$		1.000	0.059	-0.237	-0.116	-0.117
$x_+^{DK\pm}$			1.000	0.061	0.004	-0.139
$y_+^{DK\pm}$				1.000	0.127	-0.199
$x_\xi^{D\pi\pm}$					1.000	0.638
$y_\xi^{D\pi\pm}$						1.000

values are obtained by smearing the central values by their measured statistical and systematic uncertainties while taking into account their correlations. The use of different  $c_i$  and  $s_i$  values changes the extracted  $x_\pm^{DK}$ ,  $y_\pm^{DK}$ ,  $x_\xi^{D\pi}$  and  $y_\xi^{D\pi}$  values. The standard deviation of the distributions of central values extracted from 1000 data fits are assigned as a systematic uncertainty. The distributions are shown in Fig. 5.49 and the assigned uncertainties are summarised in Table 5.14. The correlation matrix related to the strong-phase uncertainty can be obtained from the correlations observed between observables in the fits, and is also given in the table.

The set of  $(c_i, s_i)$  that was employed in this analysis will be used in a series of future BPFGGSZ measurements, both with additional  $B$  decay modes within the LHCb collaboration and by the Belle II collaboration. This introduces some correlation between the measurement results. In order to allow for an estimate of the degree of correlation by future analysts, the 1000 samples  $(c_i, s_i)$  values and the corresponding fit results for  $(x_\pm^{DK}, y_\pm^{DK}, x_\xi^{D\pi}, y_\xi^{D\pi})$  will be made public as supplementary material to Ref. [1].

### 5.6.2 Efficiency-profile-related systematic uncertainties

The non-trivial efficiency profile over the Dalitz plot,  $\eta(s_-, s_+)$ , can have a range of effects, considered in the sections below.

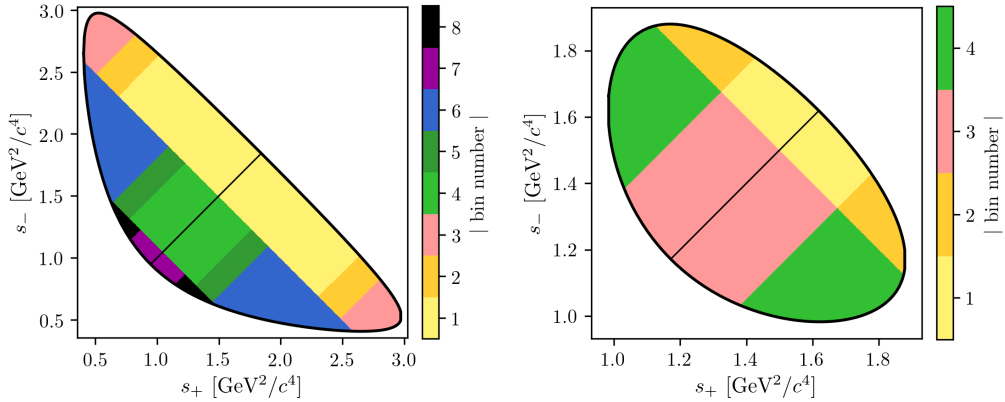


**Figure 5.50:** The rectangular binning schemes used to group candidates in (left) the  $D \rightarrow K_S^0 \pi^+ \pi^-$  and (right) the  $D \rightarrow K_S^0 K^+ K^-$  categories in a number of systematic uncertainty studies.

3010 **The assumption that  $\eta^{DK}(s_-, s_+) = \eta^{D\pi}(s_-, s_+)$**

3011 The assumption that the acceptance profile over the  $D$ -decay Dalitz plot is identical  
 3012 between  $B^\pm \rightarrow DK^\pm$  and  $B^\pm \rightarrow D\pi^\pm$  decays was examined in detail in Section 5.2.2.  
 3013 It was found that with signal yields similar to those in the data set, no statistically  
 3014 significant difference between the efficiency profiles  $\eta^{DK}(s_-, s_+)$  and  $\eta^{D\pi}(s_-, s_+)$   
 3015 was discernible, and no additional uncertainty due to this assumption is assigned.

3016 **The assumption that  $\eta(s_-, s_+) = \eta(s_+, s_-)$**

3017 The measurement is sensitive to effects that break the assumption  $\eta(s_-, s_+) =$   
 3018  $\eta(s_+, s_-)$ . Such a breakdown would mean that opposite points on the Dalitz plot  
 3019 have different efficiencies and can only arise through a charge detection asymmetry  
 3020 (e.g that it is more likely to detect a  $K^+$  in the detector rather than a  $K^-$ ).<sup>8</sup>

3021 The potential size of such an asymmetry can be studied in simulation  
 3022 where the  $D$  decay has a uniform distribution over the allowed phase space; in such  
 3023 simulated samples, it would manifest itself as an observation different fractional  
 3024 yields of  $B^-$  decays in bin  $i$  and  $B^+$  decays in bin  $-i$ . This effect has been looked for  
 3025 using the large samples of  $B^\pm \rightarrow D\pi^\pm$  decays that were generated for the analysis  
 3026 of 2015 and 2016 data. The study is performed using the rectangular binning  
 3027 schemes shown in Fig. 5.50, because this scheme is most sensitive to effects that vary  
 3028 smoothly over phase space. The comparison plots are shown in Fig. 5.51, where it  
 3029 can be seen that the  $p$  values for the hypothesis that there is no asymmetry all take  
 3030 on reasonable values. Hence no further systematic uncertainty is considered.

---

<sup>8</sup>Note that the measurement is insensitive to any asymmetry in the reconstruction of the companion track.

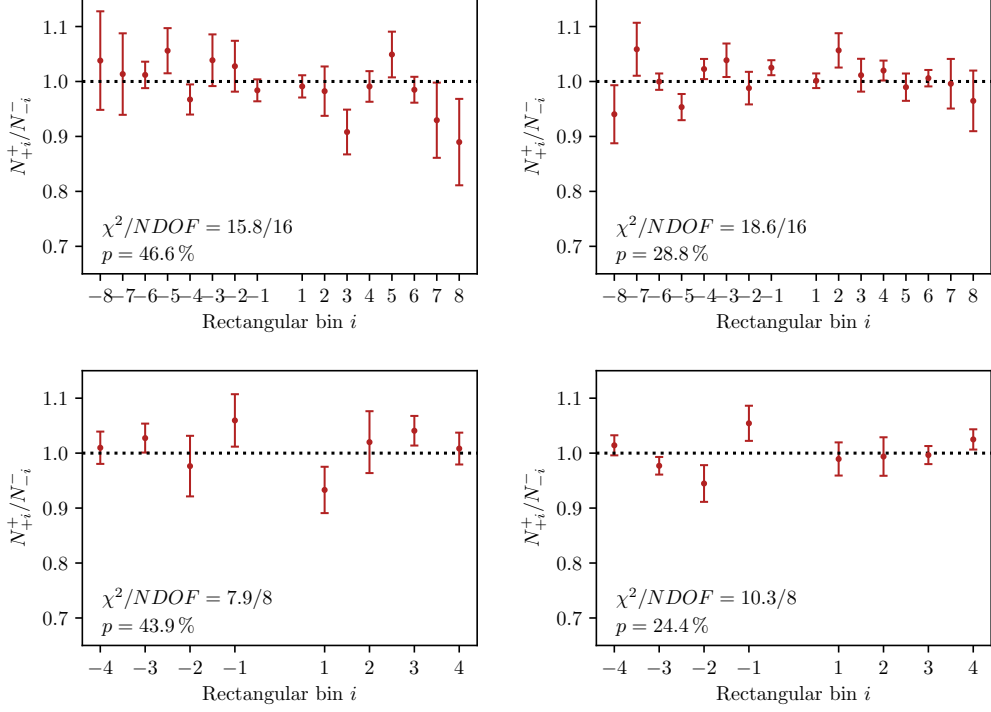


**Figure 5.51:** Comparison of the ratio of  $B^+$  decays reconstructed in bin  $+i$  to  $B^-$  decays reconstructed in bin  $-i$  for simulated  $B^\pm \rightarrow D\pi^\pm$  decays where (top)  $D \rightarrow K_S^0 \pi^+ \pi^-$  and (bottom)  $D \rightarrow K_S^0 K^+ K^-$ , also split into (left) the LL and (right) the DD categories, using the rectangular binning schemes in Fig. 5.50. Calculated  $p$  values for the hypothesis that the ratio is flat are also shown, all of them being at least 20 %.

### 3031 Effect of phase-space efficiency profile on $c_i$ and $s_i$

3032 As discussed in Section 2.4 there is a small bias, because the  $c_i$  and  $s_i$  values  
 3033 that are used correspond to the definition

$$c_i = \frac{\int_i ds^2 |A_S^D(s_{-+})| |A_S^D(s_{+-})| \cos[\Delta\delta_D(s_{-+})]}{\sqrt{\int_i ds^2 |A_S^D(s_{-+})|^2} \sqrt{\int_i ds^2 |A_S^D(s_{+-})|^2}}, \quad (\text{and equivalent for } s_i,) \quad (5.26)$$

3034 whereas the non-flat efficiency profile in LHCb,  $\eta(s_-, s_+) \equiv \eta(s_{-+})$ , means that the  
 3035 appropriate  $c_i'$  and  $s_i'$  entering the exact yield expressions are

$$c_i^{\text{eff}} = \frac{\int_i ds^2 \eta(s_{-+}) |A_S^D(s_{-+})| |A_S^D(s_{+-})| \cos[\Delta\delta_D(s_{-+})]}{\sqrt{\int_i ds^2 \eta(s_{-+}) |A_S^D(s_{-+})|^2} \sqrt{\int_i ds^2 \eta(s_{-+}) |A_S^D(s_{+-})|^2}}, \quad (\text{and equivalent for } s_i^{\text{eff}}.) \quad (5.27)$$

3036 The shifts  $\Delta c_i = c_i^{\text{eff}} - c_i$ ,  $\Delta s_i = s_i^{\text{eff}} - s_i$  can be estimated using the efficiency  
 3037 profile in simulation and the latest amplitude models: the 2018 Belle model [55]  
 3038 for  $D \rightarrow K_S^0 \pi^+ \pi^-$  and the 2010 BaBar model [64] for  $D \rightarrow K_S^0 K^+ K^-$ . The strong-  
 3039 phase parameters are first calculated assuming a uniform reconstruction efficiency

**Table 5.15:** The  $c_i$  and  $s_i$  values for  $D \rightarrow K_S^0 \pi^+ \pi^-$  decays calculated via the 2018 Belle model [55] in two cases: assuming a uniform reconstruction efficiency over phase space, denoted  $(c/s)_i^{\text{model}}$ , and including the LHCb efficiency profile as obtained in simulation, averaged for LL and DD, denoted  $(c/s)_i^{\text{eff}}$ . The change due to including the efficiency is also tabulated.

Bin	$c_i^{\text{model}}$	$c_i^{\text{eff}}$	$\Delta c_i$	$s_i^{\text{model}}$	$s_i^{\text{eff}}$	$\Delta s_i$
1	-0.027	-0.007	0.019	0.812	0.794	-0.018
2	0.837	0.859	0.022	0.164	0.152	-0.012
3	0.163	0.163	-0.000	0.872	0.880	0.008
4	-0.914	-0.915	-0.001	0.076	0.082	0.006
5	-0.149	-0.170	-0.021	-0.856	-0.854	0.002
6	0.373	0.362	-0.011	-0.782	-0.805	-0.023
7	0.863	0.862	-0.000	-0.203	-0.202	0.002
8	0.860	0.862	0.002	0.330	0.336	0.006

**Table 5.16:** The  $c_i$  and  $s_i$  values for  $D \rightarrow K_S^0 K^+ K^-$  decays calculated via the 2010 BaBar model [64] in two cases: assuming a uniform reconstruction efficiency over phase space, denoted  $(c/s)_i^{\text{model}}$ , and including the LHCb efficiency profile as obtained in simulation, averaged for LL and DD, denoted  $(c/s)_i^{\text{eff}}$ . The change due to including the efficiency is also tabulated.

Bin	$c_i^{\text{model}}$	$c_i^{\text{eff}}$	$\Delta c_i$	$s_i^{\text{model}}$	$s_i^{\text{eff}}$	$\Delta s_i$
1	0.738	0.735	-0.002	0.266	0.263	-0.003
2	-0.697	-0.744	-0.046	0.332	0.329	-0.003

3040 over phase space according to Eq. (5.26), obtaining a set of values  $\{c_i^{\text{model}}, s_i^{\text{model}}\}$ .  
 3041 Then, an alternative set is calculated,  $\{c_i^{\text{eff}}, s_i^{\text{eff}}\}$ , using the same model, and  
 3042 the reconstruction efficiency profile found in full LHCb simulation. The LHCb  
 3043 reconstruction efficiency at a given point in phase-space is taken to be proportional  
 3044 to the yield in simulation, as the simulated decays were generated with a uniform  
 3045 distribution over phase space. The efficiency is averaged over the LL and DD  
 3046 categories in the calculation, according to the relative signal yields in these categories.  
 3047 The results, as well as their differences, are tabulated in Tables 5.15 and 5.16.

3048 A systematic uncertainty due to employing the measured  $c_i$  and  $s_i$  directly  
 3049 in the fit is assigned by generating a large number of toy data sets where the  
 3050 signal yields are calculated using  $(c_i^{\text{eff}}, s_i^{\text{eff}})$ , and then fitting the data sets using  
 3051  $(c_i^{\text{model}}, s_i^{\text{model}})$ . The mean bias of each observable in these toys is assigned as the  
 3052 systematic uncertainty, and is determined to be  $0.1 \times 10^{-2}$  or less for all observables.  
 3053 The smallness of the effect is the reason no effort is made to correct the  $c_i$  and  
 3054  $s_i$  values in the nominal measurement.

3055 **5.6.3 Mass shapes**

3056 A number of uncertainties relate to the mass distributions that enter the fit model.  
 3057 Each is described in detail the sections below.

3058 **Determination of shape parameters**

3059 The statistical uncertainties on the shape parameters that are obtained in fits  
 3060 to simulated decays and in the first stage fit to data need to be propagated to  
 3061 the uncertainty on the obtained parameters. This is done via a bootstrapping  
 3062 procedure, repeating these steps many times:

- 3063     • Each of the data sets used to determine parameters of the signal, crossfeed,  
 3064       and lowmass shapes that are fixed in the first-stage fit to data of Section 5.4  
 3065       are re-sampled with replacement, drawing a number of events equal to the  
 3066       original data-set size. These are from simulation for signal and lowmass  
 3067       shapes, and real data for the crossfeed shapes. All of the shapes are fit again,  
 3068       on the re-sampled data sets.
- 3069     • The real dataset is re-sampled with replacement, drawing a number of events  
 3070       equal to the original data-set size. Then, the first-stage fit of Section 5.4 is  
 3071       repeated with the shapes obtained as described above, obtaining values for  
 3072       the remaining shape parameters.
- 3073     • Finally, the  $CP$  fit is repeated using the shape parameters determined in the  
 3074       preceding steps, but *without* re-sampling the dataset (to avoid a statistical  
 3075       spread in the obtained central values that is independent of the shape  
 3076       parameters).

3077 The uncertainty on each observable is taken to be the standard deviation of the  
 3078 set of central values obtained as described above. This procedure propagates the  
 3079 statistical uncertainty on the fixed parameters to the observables, in a way that  
 3080 takes correlations into account, and which does not rely on the uncertainty estimates  
 3081 in the preliminary fits being accurate. The uncertainties are less than  $0.1 \times 10^{-2}$   
 3082 for all  $DK^\pm$  observables and less than  $0.2 \times 10^{-2}$  for all  $D\pi^\pm$  observables.

3083 A potential bias arises due the use of the sPlot method when obtaining the  
 3084 mass distribution of decays where a  $\pi \leftrightarrow K$  misidentification has taken place.  
 3085 This is because the  $m_{\text{swap}}(Dh^\pm)$  mass that is calculated while assuming a swapped  
 3086 companion hypothesis and the nominal  $m_{\text{default}}(Dh^\pm)$  mass are correlated (it is  
 3087 always the case that  $m_{\text{swap}} > m_{\text{default}}$  for a  $\pi \rightarrow K$  misidentification ,for example).

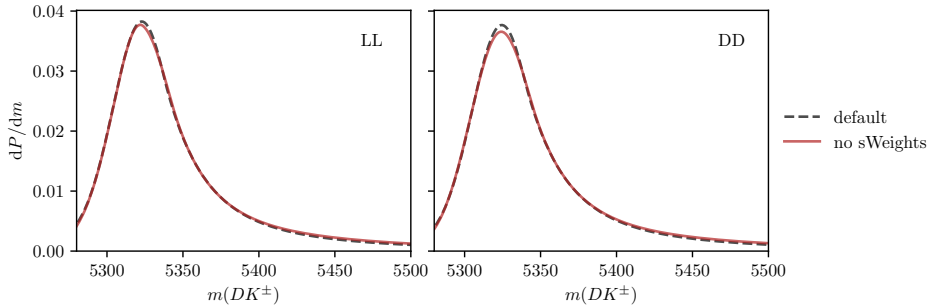


**Figure 5.52:** Comparison of the default and no-sWeights alternative shape for the  $D\pi \rightarrow DK$  cross-feed component in the (left) LL and (right) DD categories where  $D \rightarrow K_S^0 \pi^+ \pi^-$ . The binned fit obtains essentially the same central values for the  $CP$ -violation observables, independently of which shape is used.

Thus, the assumptions of the sPlot method are not satisfied [151]. The correlation coefficient in the signal region is about 20 % for simulated signal decays. In order to assess the potential impact, an alternative mass distribution for  $(B^\pm \rightarrow D\pi^\pm) \rightarrow (B^\pm \rightarrow DK^\pm)$  cross-feed is derived that does not rely on sWeights. Instead of fitting  $B^\pm \rightarrow D\pi^\pm$  sample in the whole fit range and assigning sWeights before recalculating the  $B$  mass under the kaon companion hypothesis, the shape is obtained using  $B^\pm \rightarrow D\pi^\pm$  candidates in the signal region. This is possible because the  $B^\pm \rightarrow D\pi^\pm$  sample is very pure. The shapes are compared in Fig. 5.52 and are seen to be almost identical. Thus the sWeights do successfully subtract the contribution of combinatorial and partially reconstructed backgrounds in the default setup. The impact on the obtained  $CP$ -violation observables of using one or the other shape in the fits is negligible, and no further systematic uncertainty is assigned due to this effect.

### Using the same mass shapes in all Dalitz bins

The mass shapes obtained the first-stage fit where all Dalitz bins are combined, are used in each individual bin of the subsequent binned fit. However, there could be some variation in the shape over the  $D$ -decay phase space, due to correlations between the phase-space coordinates and particle kinematics. The potential effect is investigated in pseudoexperiments, where toy data sets are generated with alternative signal, crossfeed, and combinatorial-background shapes that are allowed to differ between bins, and fitted with the default shapes. The partially reconstructed background is treated in a separate study, because further physics effects contribute to bin-by-bin variation, as described in the following section.

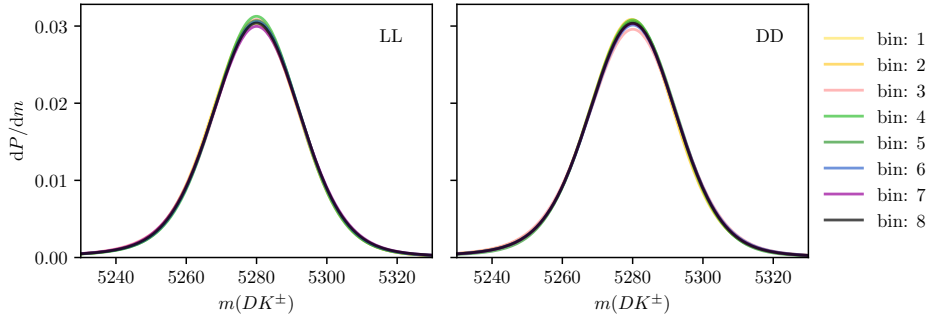


**Figure 5.53:** Signal shapes obtained in fits simulated  $B^\pm \rightarrow D\pi^\pm$  decays for individual Dalitz bins in the optimal binning scheme, for (left) LL and (right) DD candidates in the  $B^\pm \rightarrow D(\rightarrow K_S^0\pi^+\pi^-)\pi^\pm$  category.

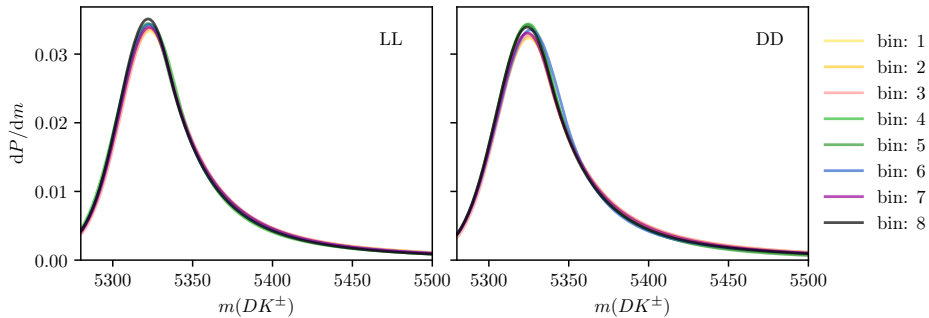


**Figure 5.54:** Mass shapes for  $D\pi \rightarrow DK$  cross feed obtained for individual Dalitz bins in the optimal binning scheme, for (left) LL and (right) DD candidates in the  $D \rightarrow K_S^0\pi^+\pi^-$  category.

The alternative signal and cross-feed mass shapes are fitted independently in each bin, following identical procedures to those outlined in Sections 5.4.1 and 5.4.2. Examples of the obtained shapes are compared in Figs. 5.53 and 5.54.

The shape of the combinatorial background can also vary over the  $D$  decay phase-space; for example, the relative amount of fake  $D$  candidates versus real  $D$  decays paired with a random companion certainly depends on the real  $D$  decay amplitude for a given phase-space region. The effect is investigated in the high  $B$ -mass sideband  $m_B \in [5600, 6500] \text{ MeV}/c^2$ , in which the  $m(Dh^\pm)$  distribution is fitted with a single exponential distribution, in bins of the Dalitz plot. The fits combine  $B^+$  and  $B^-$  candidates and merge bins  $+i$  and  $-i$ , and are carried out for both the *optimal* binning scheme of Fig. 2.7 (on page 24) and a *rectangular* binning scheme, shown in Fig. 5.50, which better captures continuous trends over the Dalitz plot. The study is done for  $D \rightarrow K_S^0\pi^+\pi^-$  only due to available statistics. The DD category of  $B^\pm \rightarrow D\pi^\pm$  decays has the largest statistics and shows the largest variation, and the fitted slopes for this channel are shown in Fig. 5.55. Two

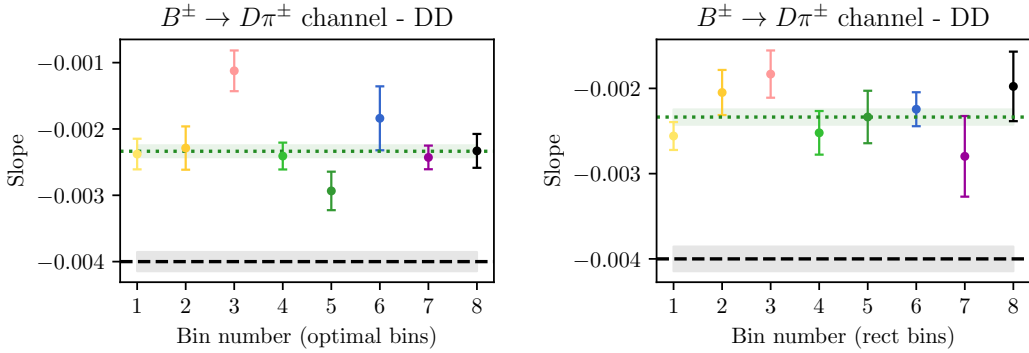


**Figure 5.55:** Plot of (dots) combinatorial slope in the high  $B$  mass background for each bin in the (left) the optimal binning scheme and (right) the rectangular binning scheme, for the DD  $B^\pm \rightarrow D(\rightarrow K_S^0 \pi^+ \pi^-) \pi^\pm$  category. The slope when all bins are combined (green, dashed line) is also shown, and compared with (black dashed line) the slope in the default fit region.

3126 effects are visible: 1) there is some variation in the slope as a function of the Dalitz  
 3127 bin, especially visible for the rectangular scheme, and 2) the exponential slope is  
 3128 larger in general in the high  $B$ -mass sideband. The latter effect does not pose a  
 3129 problem, since the employed exponential is found to provide an excellent fit in  
 3130 the default fit region. It does however need to be taken into account when when  
 3131 deriving alternative, bin-dependent combinatorial slopes relevant for the default  
 3132 fit region. In order to do so, the alternative slope for bin  $i$  is defined

$$\alpha_{\text{default-range}}^i = \frac{\alpha_{\text{high-}m_B}^i}{\alpha_{\text{high-}m_B}^{\text{all-}DP}} \times \alpha_{\text{default-range}}^{\text{all-}DP}, \quad (5.28)$$

3133 and used when generating the combinatorial-background component of the toy  
 3134 data sets for the study.

3135 The average bias obtained for each observable in the ensemble of pseudo-  
 3136 experiments is assigned as a systematic uncertainty, found to be about  $0.1 \times 10^{-2}$   
 3137 for each observable.

### 3138 Ignoring physics effects in the lowmass background

3139 In the  $CP$  fit, the same relative fractions of partly reconstructed  $B^\pm$  and  $B^0$   
 3140 backgrounds are used in each bin, as determined in the first-stage fit described  
 3141 in Section 5.4 (whereas the partly reconstructed  $B_s^0 \rightarrow \bar{D}^0[\pi^+]K^-$  background is  
 3142 treated separately). However the distribution over the Dalitz plot depends on  
 3143 whether the partly reconstructed decays occur via an intermediate  $D^0$  meson, a  $\bar{D}^0$   
 3144 meson, or and admixture of both. Consider a decay reconstructed as  $B^- \rightarrow DK^-$   
 3145 but which is actually a partially-reconstructed background. There are then four  
 3146 types of background that should be considered:

- Decays in which the  $D$ -meson in the true decay is a  $D^0$ -meson. An example of this is  $B^- \rightarrow D^{*0}(D^0\pi^0)\pi^-$  for which the  $\pi^0$  from the  $D^{*0}$  decay is missed and the  $\pi^-$  is misidentified as the companion  $K^-$ . These are denoted ' $D^0$ -like'.<sup>9</sup>
- Decays in which the  $D$ -meson in the true decay is a  $\bar{D}^0$ -meson. An example of this is  $B_s^0 \rightarrow \bar{D}^0\pi^+K^-$  for which the  $\pi^+$  is missed and the  $K^-$  is reconstructed as the companion  $K^-$ . These are denoted ' $\bar{D}^0$ -like'.
- Decays in which the  $D$  meson in the true decay can be either flavour, and both  $D$  flavours contribute to the decay amplitude. An example of this is  $B^- \rightarrow D^*K^-$  for which the total decay amplitude into a  $D$  final state has contributions from both  $D^{*0}$  (decaying to  $D^0$ ) and  $\bar{D}^{*0}$  (decaying to  $\bar{D}^0$ ). The relative amplitude magnitude and phase between the two possible  $B$  decays are denoted  $r_B^{D^*}$  and  $\delta_B^{D^*}$  respectively. These are denoted ' $r_B$ -like'.
- Decays that can be reconstructed as both  $D^0$ - and  $\bar{D}^0$ -like but where there is no quantum-mechanical interference. An example is  $\bar{B}^0 \rightarrow D^0\pi^+\pi^-$  decays where either the  $\pi^+$  or  $\pi^-$  can be reconstructed as the companion particle.<sup>10</sup> These are denoted 50/50  $D^0$ -like and  $\bar{D}^0$ -like.

For  $B^+ \rightarrow DK^+$  decays everything is CP conjugated. The Dalitz-plot distribution for each of these cases is:

- $D^0$  decays (' $D^0$ -like')

$$\begin{aligned} N_{\pm i}(B^-) &\propto F_{\pm i} \\ N_{\pm i}(B^+) &\propto F_{\mp i} \end{aligned} \tag{5.29}$$

- $\bar{D}^0$  decays (' $\bar{D}^0$ -like'):

$$\begin{aligned} N_{\pm i}(B^-) &\propto F_{\mp i} \\ N_{\pm i}(B^+) &\propto F_{\pm i} \end{aligned} \tag{5.30}$$

- Decays with a quantum-mechanical admixture of  $D^0$  and  $\bar{D}^0$  (' $r_B$ -like'):

$$\begin{aligned} N_{\pm i}(B^-) &\propto F_{\pm i} + (r_B^*)^2 F_{\mp i} + 2\sqrt{F_{+i}F_{-i}}[x_{-}^*c_{\pm i} + y_{-}^*s_{\pm i}] \\ N_{\pm i}(B^+) &\propto F_{\mp i} + (r_B^*)^2 F_{\pm i} + 2\sqrt{F_{+i}F_{-i}}[x_{+}^*c_{\pm i} - y_{+}^*s_{\pm i}] \end{aligned} \tag{5.31}$$

where  $(x_{\pm}^*, y_{\pm}^*)$  are defined analogously to the standard  $B^\pm \rightarrow DK^\pm$  case.

---

<sup>9</sup>The naming convention is defined in terms of the  $D$  present in candidates reconstructed as  $B^-$  decays. For the charge conjugate case this decay would of course happen via a  $\bar{D}^0$ , but is still denoted ' $D^0$ -like'.

<sup>10</sup>This mode is likely to show a small amount of CP violation, similar to  $B^\pm \rightarrow D\pi^\pm$  decays. However, it is a very good approximation that a true  $D^0$  will be reconstructed with a positive or negative companion with equal probability.

- 3169 • 50/50  $D^0$ -like and  $\bar{D}^0$ -like:

$$\begin{aligned} N_{\pm i}(B^-) &\propto F_{\pm i} + F_{\mp i} \\ N_{\pm i}(B^+) &\propto F_{\pm i} + F_{\mp i} \end{aligned} \quad (5.32)$$

3170 The use of a single background shape across all bins may therefore introduce biases  
 3171 because such a shape has no sensitivity to the bin-to-bin variations that will arise  
 3172 if an admixture of these backgrounds is present.

3173 In the  $D\pi$  channel, the dominant backgrounds are all  $D^0$ -like ( $\bar{B}^0 \rightarrow D^{*-}\pi^0$ ,  
 3174  $B^- \rightarrow D^0\rho^-$ ,  $B^- \rightarrow D^{*0}\pi^-$ ). There is a small contribution from  $\bar{B}^0 \rightarrow D^0\rho(\rightarrow$   
 3175  $\pi^+\pi^-)$  decays where either the  $\pi^+$  or  $\pi^-$  from the  $\rho^0$  decay can be assigned as the  
 3176 companion, and thus this background is 50/50  $D^0$ -like and  $\bar{D}^0$ -like. The background  
 3177 only corresponds to about 0.5 % of the total partially reconstructed background and  
 3178 thus the impact is small. Nevertheless it is considered in the study described below.

3179 In the  $DK$  channel all categories of background appear. In the mass region of  
 3180 the  $CP$  fit approximately 75.5% of backgrounds are  $D^0$ -like ( $\bar{B}^0 \rightarrow D^{*-}K^-$ , mis-  
 3181 identified  $B^- \rightarrow D^{*0}\pi^-$ , and mis-identified  $B^- \rightarrow D^0\rho^-$ ), 7.5 % are  $\bar{D}^0$ -like ( $B_s^0 \rightarrow$   
 3182  $\bar{D}^0\pi^+K^-$ ), 1 % is 50/50  $D^0$ - $\bar{D}^0$ -like (mis-identified  $B^0 \rightarrow D\rho^0$ ; assuming negligible  
 3183  $CP$  violation), and 16% are  $r_B$ -like ( $B^- \rightarrow D^*K^-$ ,  $B^0 \rightarrow DK^{*0}$ , and  $B^- \rightarrow DK^{*-}$ ).

3184 In order to estimate the bias due to ignoring this effect, a large number of toy  
 3185 data sets are generated using the default low mass shapes and total yields from  
 3186 the first-stage fit in Section 5.4, but distributing each of them individually over  
 3187 the Dalitz-bins according to Eqs. (5.29)-(5.31). When calculating the distribution  
 3188 of  $B^+ \rightarrow D^{*0}K^+$  decays over the Dalitz plot, the values [49]

$$r_B^{D^*} = 0.191 \quad \delta_B^{D^*} = 331.6^\circ \quad (5.33)$$

3189 are used. When calculating the distribution of  $B^+ \rightarrow D^0K^{*+}$  decays over the  
 3190 Dalitz plot the values [49]

$$r_B^{K^*} = 0.092 \quad \delta_B^{K^*} = 40^\circ. \quad (5.34)$$

3191 are used. The toy data sets are then fit with the default set up, and the observed  
 3192 mean bias assigned as the corresponding uncertainty. The corresponding uncer-  
 3193 tainties were found to be about  $0.1 \times 10^{-2}$  for all uncertainties. The variation in  
 3194 the shapes is rather small in the mass range included in the fit, which explains  
 3195 the small impact.

3196 If the  $B_s^0$  background is *not* treated separately in the default fit, but instead  
 3197 included in a single lowmass background shape along with the  $B^0$  and  $B^\pm$  contribu-  
 3198 tions, the systematic uncertainty is an order of magnitude larger when evaluated  
 3199 as described above, and would be a dominating systematic. This motivates the  
 3200 separate treatment of the  $B_s^0$  background.

### 3201 5.6.4 $CP$ violation and material interaction of the $K_S^0$

3202 A systematic uncertainty due to  $CP$ -violation effects and material interaction of  
 3203 the  $K_S^0$  is assigned using the results obtained in Section 4.3.7. In that section, the  
 3204 expected bias on each of the observables in a combined  $B^\pm \rightarrow Dh^\pm$  measurement  
 3205 was evaluated for the detector geometry and particle kinematics of the LHCb  
 3206 experiment. The calculation was made for  $(r_B^{DK^\pm/D\pi^\pm}, \delta_B^{DK^\pm/D\pi^\pm})$  values close to  
 3207 the world averages, and a number of  $\gamma$  values; the results were summarised in Fig. 4.8.  
 3208 The systematic uncertainty is taken to be the largest absolute bias observed for each  
 3209 parameter in the study. The largest uncertainty (on  $y_\xi^{D\pi}$  where it is  $0.46 \times 10^{-2}$ ) is  
 3210 still an order of magnitude smaller than the statistical uncertainty.

### 3211 5.6.5 Impact of $D$ mixing

3212 The effect of  $D$ -mixing is not accounted for in the measurement, which leads to  
 3213 a small bias. Earlier studies have shown this to lead to a sub-degree bias on  
 3214 measurements of  $\gamma$  in  $B^\pm \rightarrow DK^\pm$  decays, in the case where the  $F_i$  parameters  
 3215 are determined experimentally under the same experimental conditions as the  $\gamma$   
 3216 measurement [162]. A number of pseudoexperiments are carried out to verify that  
 3217 this is also the case for the combined  $DK^\pm-D\pi^\pm$  setup employed in the thesis.  
 3218 They are performed following the same procedure described in Section 5.6.4 for  
 3219 the case of neutral-kaon  $CP$  violation. The yields are calculated while taking  $D$   
 3220 mixing into account, using the mixing parameter values  $x = (0.39^{+0.11}_{-0.12})\%$  and  
 3221  $y = (0.65^{+0.06}_{-0.07})\%$  [31], and then fitted back assuming no  $D$  mixing. The biases are  
 3222 found to be small, as expected, all of them smaller than  $0.05 \times 10^{-2}$ . The largest  
 3223 relative biases are on the  $B^\pm \rightarrow D\pi^\pm$  parameters, but even for those the relative  
 3224 effect is less than 2 %. In agreement with Ref. [162], it is found that the biases  
 3225 increase with an order of magnitude if the  $F_i$  parameters are fixed to the expected  
 3226 values with no  $D$ -mixing, instead of being determined as part of the fit.

### 3227 5.6.6 PID efficiencies

3228 The uncertainty related to PID efficiencies is assessed by repeating the full two-stage  
 3229 fit procedure a number of times, each time varying the PID efficiencies within  
 3230 the uncertainties. The used uncertainty includes both a statistical and systematic  
 3231 component, as described in detail in Section 5.1.3. The standard deviations of  
 3232 the central values obtained for each observable are assigned as the systematic  
 3233 uncertainty. The uncertainties come out below  $0.1 \times 10^{-2}$  for all observables.

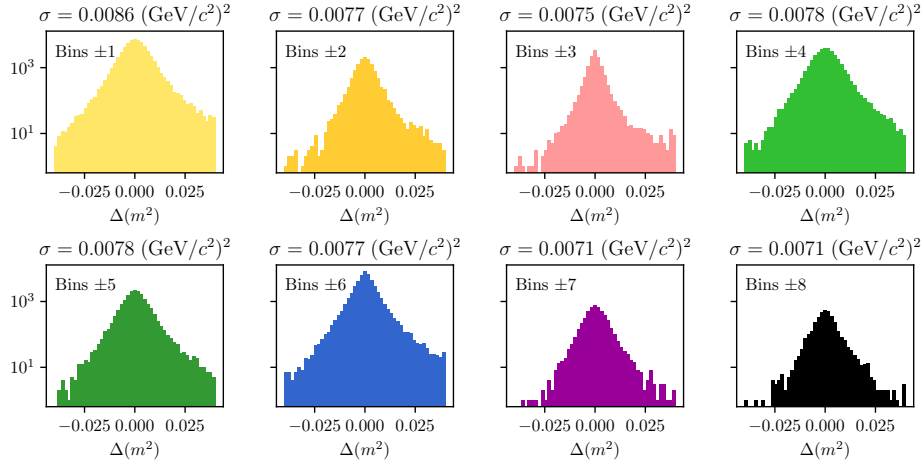


**Figure 5.56:** Distribution of the biases  $\Delta(m^2) = m_{true}^2 - m_{reconstructed}^2$  in simulation for  $m^2(K_S^0\pi^\pm)$  in bins of the rectangular binning scheme of Fig. 5.50.

### 5.6.7 Dalitz-coordinate resolution

There is a small systematic uncertainty related to Dalitz-plot-bin migration, where the non-perfect resolution on the momentum measurement means that a candidate is assigned to a different bin than it truly belongs to. This leads to non-negligible net migration between bins that share a border in a region of phase space where the amplitude varies rapidly. However, since the  $F_i$  are measured in the data set, all leading order effects of migration are inherently taken into account. The measurement is only sensitive to differences in migration between the  $DK^\pm$  and  $D\pi^\pm$  channels and the effect is small.

The systematic uncertainty due to this effect is assigned using pseudoexperiments. The study is made for the  $D \rightarrow K_S^0\pi^+\pi^-$  mode only, which is sufficient since it completely dominates the overall sensitivity.

1. Signal  $B^\pm \rightarrow DK^\pm$  and  $B^\pm \rightarrow D\pi^\pm$  decays are generated continuously over phase space, according to the expected distribution obtained with the latest amplitude model from the Belle collaboration [55], assuming values of  $\gamma$  and  $(r_B^{DK^\pm/D\pi^\pm}, \delta_B^{DK^\pm/D\pi^\pm})$  close to the current world averages.
2. The Dalitz coordinates of each candidate are then smeared using the experiment resolution obtained in simulation. This is described further below.
3. Finally, the generated candidates are binned and fit using the default setup.

The resolution is obtained via simulation, by comparing the reconstructed phase-space coordinates with those calculated from the true momenta in samples of

3255 simulated  $D \rightarrow K_S^0 \pi^+ \pi^-$  decays. As can be seen in Fig. 5.56, the resolution is found  
3256 to vary over phase space and the distribution of shifts has significant exponential  
3257 tails. In order to take both effects into account, the smearing is done by shifting each  
3258 generated decay with a realised coordinate shift in full simulation, for a simulated  
3259 decay that took place at approximately the same place in the Dalitz plot. The  
3260 shift is multiplied with 120 % to take into account that the resolution is generally  
3261 better in simulation than data. If the shift results in Dalitz coordinates outside the  
3262 kinematically allowed region, a different shift is applied randomly instead.

3263 The average bias seen in the pseudoexperiments is assigned as the systematic  
3264 uncertainty. The uncertainties come out at about  $(0.1 - 0.2) \times 10^{-2}$  for all parameters.  
3265 It is found that the bias is towards a smaller value of  $r_B^{DK}$  for all four  $DK^\pm$   
3266 parameters ; this is to be expected, as bin migration washes out the asymmetries  
3267 in different areas of the Dalitz plot.

### 3268 5.6.8 The fixed yield fractions

3269 A number of relative yields are fixed from efficiencies in simulation and branching  
3270 fractions. In the  $DK^\pm$  modes, this is the case for all the relative yields of the  
3271 partially reconstructed backgrounds, including partially reconstructed  $B \rightarrow D\pi[X]$   
3272 decays where the pion is misidentified as a kaon, and the yield of the  $B_s^0 \rightarrow DK\pi$   
3273 background relative to the  $B \rightarrow D\pi$  yield. In the  $B^\pm \rightarrow D\pi^\pm$  channel, the only fixed  
3274 yield ratio is that of the partially reconstructed  $B^\pm \rightarrow D^{*0}(\rightarrow D\pi^0)\pi^\pm$  and  $B^0 \rightarrow$   
3275  $D^{*\mp}(\rightarrow D\pi^\mp)\pi^\pm$  modes. The uncertainty on the observables due to uncertainties  
3276 on these fixed fractions is assessed by repeating the two-stage fit procedure many  
3277 times, each time shifting the yield ratios randomly within their uncertainties. The  
3278 uncertainty on each observable is taken to be the standard deviation of the set of  
3279 central values obtained in these fits. These are all smaller than  $0.1 \times 10^{-2}$ .

### 3280 5.6.9 Systematic uncertainty due to backgrounds that are 3281 not modelled in fit

3282 There are a number of backgrounds that are expected to be present at a small  
3283 level, but which are not modelled in the fits to data because their impact on the fit  
3284 results is minimal. Instead, a systematic uncertainty is assigned. Each contribution  
3285 is described in the following sections and the related systematic uncertainties  
3286 are summarised in Table 5.17.

**Table 5.17:** Summary of systematic uncertainties due to backgrounds that are potentially present with a small yield, but not included in the mass fit.

All uncertainties are quoted with implicit: $\times 10^{-2}$						
Mode	$\sigma(x_-^{DK^\pm})$	$\sigma(y_-^{DK^\pm})$	$\sigma(x_+^{DK^\pm})$	$\sigma(y_+^{DK^\pm})$	$\sigma(x_\xi^{D\pi^\pm})$	$\sigma(y_\xi^{D\pi^\pm})$
$\Lambda_b^0$ backgrounds	0.04	0.05	0.04	0.06	0.08	0.13
$B \rightarrow D\mu\nu X$	0.04	0.07	0.04	0.05	0.10	0.11
$B^\pm \rightarrow D(\rightarrow K_S^0\pi\mu\nu)h^\pm$	0.00	0.03	0.02	0.02	0.00	0.00
Swapped tracks	0.10	0.13	0.12	0.08	0.00	0.01
Total	0.11	0.16	0.13	0.12	0.08	0.13

### Background from $\Lambda_b$ decays

This section considers the possible impact of the two potential backgrounds from  $\Lambda_b^0$  decays described in Section 5.4.3:  $\Lambda_b^0 \rightarrow D^0 p\pi^-$  decays where the pion is not included in the candidate reconstruction and the proton assigned as the companion, and  $\Lambda_b^0 \rightarrow \Lambda_c^+(\rightarrow pK_S^0\pi^+\pi^-)\pi^-$  decays where a pion in the  $\Lambda_c^+$  decay is not reconstructed and the proton reconstructed as one of the  $D$  decay products. The impact of not including these in the default fit is assessed by generating toy data sets where the backgrounds are included in the generation step, which are then fitted back with default model. The former background is distributed over the Dalitz plot as  $\bar{D}^0$ -like, cf. the terminology of Section 5.6.3, since a positive companion is produced along with a  $D^0$  meson (assuming no  $CP$  violation). The latter is also distributed as  $\bar{D}^0$ -like in the study; the exact distribution is unknown, but a  $\bar{D}^0$ -like background is likely to have the largest effect and thus this is a conservative choice. The total yields are taken relative to the signal yields, using the yield ratios discussed in Section 5.4.3. The  $m(Dh^\pm)$  distributions are obtained using simulated samples, produced with `RapidSim`. The mean biases come out to be less than  $0.1 \times 10^{-2}$  for each  $CP$ -violation observable, which is assigned as a systematic uncertainty.

### Semi-leptonic backgrounds

The impact of remnant  $B \rightarrow D\mu\nu_\mu$  decays after requiring `isMuon=0` on the companion is assessed in pseudo experiments. Data sets are generated where the background is added in the generation step at a rate corresponding to the expectation after the veto, which are then fit with the default model. The background yield relative to signal and the mass shape are obtained from a sample of fully simulated decays for conditions corresponding to the run conditions in 2012. The obtained bias in the toys is assigned as the systematic uncertainties: it is below  $0.1 \times 10^{-2}$  for all parameters.

3313     The systematic uncertainty relating to the presence of  $D^0 \rightarrow K_S^0 \pi^- \mu^+ \nu_\mu$  is  
 3314   estimated by repeating the bias studies of Section 5.3.3, but scaling the background  
 3315   yields to 10% to take into account the lepton veto on the  $D$  decay products. All  
 3316   biases are less than  $0.05 \times 10^{-2}$  in this case.

3317   **Swapped tracks**

3318   There is a peaking background present from  $B^\pm \rightarrow D(\rightarrow K^\mp \pi^\pm) K_S^0 \pi^\pm$  decays where  
 3319   the kaon is reconstructed as the companion and the  $K_S^0$  is assigned to the  $D$  decay.  
 3320   The yield of this background is determined to be 0.5% of the signal yield in the  
 3321    $B^\pm \rightarrow DK^\pm$  channel in Section 5.3.5. The potential impact from the presence  
 3322   of the background is estimated by

- 3323     1. Calculating the expected  $B^\pm \rightarrow D\pi^\pm$  and  $B^\pm \rightarrow DK^\pm$  signal yields in each  
 3324       bin for physics parameters similar to the world average values.
  - 3325     2. Then calculating the background bin yields in each  $B^\pm \rightarrow DK^\pm$  bin, using  
 3326       a total yield equal to 0.5% of the signal yield, and the bin distribution  
 3327       from simulated samples of  $B^\pm \rightarrow D(\rightarrow K^\mp \pi^\pm) K_S^0 \pi^\pm$  decays, produced via  
 3328       **RapidSim**. The study is carried out for multiple simulated samples, including  
 3329       decays where the  $K_S^0 \pi$  pair in the  $B$  decay originate in different  $K^*$  resonances  
 3330       (generated with EvtGen and the proper resonance-spin models), as well as  $B$   
 3331       decays that are evenly distributed over the allowed phase space.
  - 3332     3. For each sample, the signal and background yields are added, and the  
 3333       new  $B^\pm \rightarrow D\pi^\pm$  and  $B^\pm \rightarrow DK^\pm$  yields are fit with the default signal-yield  
 3334       expressions (including a fit of the  $F_i$  parameters).
- 3335   For each parameter, the most significant bias seen across the different **RapidSim**  
 3336   samples is taken as the related systematic uncertainty. The uncertainty is below  
 3337    $0.15 \times 10^{-2}$  for all parameters.

3338   **5.6.10 Bias correction**

3339   In the default sensitivity study, the bias was found to be compatible with zero.  
 3340   However, the size of a potential bias can vary depending on the input parame-  
 3341   ters. The size of the bias has been investigated with alternate input values of  
 3342    $(\gamma, r_B^{DK^\pm}, \delta_B^{DK^\pm}, r_B^{D\pi^\pm}, \delta_B^{D\pi^\pm})$ , obtaining the results in Table 5.18. A systematic  
 3343   uncertainty due to a potential, small bias is calculated as the difference between  
 3344   the maximum and minimum bias for a given parameter. The uncertainty assigned  
 3345   in this way is very small in general, and less than  $0.1 \times 10^{-2}$  for all parameters.

**Table 5.18:** Biases observed with alternative input parameters and the systematic uncertainty assigned for the bias correction. All numbers are quoted with an implicit  $\times 10^{-2}$ .

Input ( $\gamma, r_B^{DK^\pm}, \delta_B^{DK^\pm}, r_B^{D\pi^\pm}, \delta_B^{D\pi^\pm}$ )	$x_-^{DK^\pm}$	$y_-^{DK^\pm}$	$x_+^{DK^\pm}$	$y_+^{DK^\pm}$	$x_\xi^{D\pi^\pm}$	$y_\xi^{D\pi^\pm}$
(72, 0.080, 117, 0.005, 288)	-0.02	-0.01	-0.02	-0.02	0.03	0.00
(75, 0.100, 130, 0.005, 300)	-0.03	-0.04	-0.00	0.02	0.01	-0.03
(82, 0.112, 144, 0.005, 330)	0.00	-0.01	0.00	0.03	-0.03	0.02
(71, 0.099, 129, 0.005, 300)	-0.02	-0.04	-0.00	-0.00	0.05	-0.00
Syst. uncertainty	0.04	0.03	0.02	0.04	0.09	0.05

### 3346 5.6.11 Charmless backgrounds

3347 As discussed in Section 5.3.1, a small number of charmless background decays  
 3348 survive the  $D$  flight distance cut. In this section the systematic uncertainty related  
 3349 to those is assessed, in a series of pseudoexperiments. Toy datasets are generated,  
 3350 where a charmless background component is included, using the yields and shapes  
 3351 obtained in the studies of Section 5.3.1. The Dalitz-bin distribution is obtained  
 3352 by repeating the fits of that section for each bin individually. These datasets are  
 3353 subsequently fitted back using the default model, which does not include a charmless  
 3354 component. No statistically significant bias is observed.

3355 The study described above does not allow for charge-asymmetries in the charmless  
 3356 backgrounds, in terms of overall yields and phase-space distributions. These  
 3357 asymmetries are likely to be present, due to large local  $CP$ -violation in regions of  
 3358 phase space in  $B^\pm$  decays to hadrons [163,164]. The yields in the data-driven studies  
 3359 of Section 5.3.1 are not large enough to assess asymmetries, let alone asymmetric  
 3360 bin distributions with any degree of statistical precision. Instead, an extreme-case  
 3361 scenario is investigated, where *all* the charmless background is added to either the  $B^+$   
 3362 or  $B^-$  data sample in generation. In both cases, no statistically significant biases are  
 3363 observed, and it is concluded that the impact of charmless background is negligible.

### 3364 5.6.12 Summary of systematic uncertainties

3365 The complete set of included systematic uncertainties are summarised in Table 5.19.  
 3366 It can be seen that the measurement is statistically limited. The correlation matrix  
 3367 pertaining to the LHCb related systematics is given in Table 5.20. For studies  
 3368 where the systematic uncertainty is obtained by repeating fits to data multiple times  
 3369 while varying some input, the correlation matrix is obtained from the correlations  
 3370 of the central values. For studies that are based on generating a large number of

**Table 5.19:** Overview of all sources of uncertainty on the measurement.

Source	All uncertainties are quoted with implicit: $\times 10^{-2}$					
	$\sigma(x_-^{DK\pm})$	$\sigma(y_-^{DK\pm})$	$\sigma(x_+^{DK\pm})$	$\sigma(y_+^{DK\pm})$	$\sigma(x_\xi^{D\pi\pm})$	$\sigma(y_\xi^{D\pi\pm})$
Statistical	0.96	1.14	0.96	1.20	1.99	2.34
Strong-phase inputs	0.23	0.35	0.18	0.28	0.14	0.18
Efficiency correction of ( $c_i, s_i$ )	0.11	0.05	0.05	0.10	0.08	0.09
Mass-shape parameters	0.05	0.08	0.03	0.08	0.16	0.17
Mass-shape bin dependence	0.05	0.07	0.04	0.08	0.07	0.09
Lowmass physics effects	0.04	0.10	0.15	0.05	0.10	0.09
$CP$ violation of $K_S^0$	0.03	0.04	0.08	0.08	0.09	0.46
$D$ mixing	0.04	0.01	0.00	0.02	0.02	0.01
PID efficiencies	0.03	0.03	0.01	0.05	0.02	0.02
Fixed yield ratios	0.05	0.06	0.03	0.06	0.02	0.02
Dalitz-bin migration	0.04	0.08	0.08	0.11	0.18	0.10
Bias correction	0.04	0.03	0.02	0.04	0.09	0.05
Small backgrounds	0.11	0.16	0.13	0.12	0.08	0.13
Total LHCb systematic	0.20	0.25	0.24	0.26	0.32	0.54
Total systematic	0.31	0.43	0.30	0.38	0.35	0.57

**Table 5.20:** Total LHCb-related systematic uncertainties and their correlation matrix.

Uncertainty ( $\times 10^{-2}$ )						
	$x_-^{DK\pm}$	$y_-^{DK\pm}$	$x_+^{DK\pm}$	$y_+^{DK\pm}$	$x_\xi^{D\pi\pm}$	$y_\xi^{D\pi\pm}$
$\sigma$	0.20	0.25	0.24	0.26	0.32	0.54

Correlations						
	$x_-^{DK\pm}$	$y_-^{DK\pm}$	$x_+^{DK\pm}$	$y_+^{DK\pm}$	$x_\xi^{D\pi\pm}$	$y_\xi^{D\pi\pm}$
$x_-^{DK\pm}$	1.000	0.864	0.734	0.897	0.349	0.318
$y_-^{DK\pm}$		1.000	0.874	0.903	0.408	0.362
$x_+^{DK\pm}$			1.000	0.771	0.563	0.447
$y_+^{DK\pm}$				1.000	0.507	0.451
$x_\xi^{D\pi\pm}$					1.000	0.484
$y_\xi^{D\pi\pm}$						1.000

<sup>3371</sup> toy data sets and determining the average bias, the correlation of a systematic  
<sup>3372</sup> on two observables is taken to be +100 % if the biases are in the same direction,  
<sup>3373</sup> and -100 % if they are in opposite directions. The total systematic correlation  
<sup>3374</sup> matrix, including both LHCb-related systematics and that of the strong-phase  
<sup>3375</sup> inputs, is given in Table 5.21.

<sup>3376</sup> The studies described in this section also allow for an estimate of the systematic  
<sup>3377</sup> uncertainties on the  $\mathcal{R}_i$  parameters of Eq. (5.23) or, equivalently the  $F_i$  parameters,  
<sup>3378</sup> in a completely analogous manner to how the uncertainty on the  $CP$ -violation  
<sup>3379</sup> observables was assigned. In all cases, however, the systematic uncertainty in found

**Table 5.21:** Total systematic uncertainties and their correlation matrix, including contributions due to strong-phase inputs as well as LHCb-related uncertainties.

Uncertainty ( $\times 10^{-2}$ )						
	$x_-^{DK\pm}$	$y_-^{DK\pm}$	$x_+^{DK\pm}$	$y_+^{DK\pm}$	$x_\xi^{D\pi\pm}$	$y_\xi^{D\pi\pm}$
$\sigma$	0.31	0.43	0.30	0.38	0.35	0.57

Correlations						
	$x_-^{DK\pm}$	$y_-^{DK\pm}$	$x_+^{DK\pm}$	$y_+^{DK\pm}$	$x_\xi^{D\pi\pm}$	$y_\xi^{D\pi\pm}$
$x_-^{DK\pm}$	1.000	0.301	0.156	0.576	0.265	0.231
$y_-^{DK\pm}$		1.000	0.437	0.218	0.183	0.170
$x_+^{DK\pm}$			1.000	0.445	0.414	0.310
$y_+^{DK\pm}$				1.000	0.353	0.243
$x_\xi^{D\pi\pm}$					1.000	0.502
$y_\xi^{D\pi\pm}$						1.000

<sup>3380</sup> to be much smaller than the statistical uncertainties that were given in Table 5.10.  
<sup>3381</sup> The central values, statistical, and systematic uncertainties of the  $\mathcal{R}_i$  parameters  
<sup>3382</sup> have been made public in Ref. [1] because they can be employed in future LHCb  
<sup>3383</sup> measurements, as discussed in Section 5.5.2.

## 5.7 Obtained constraints on $\gamma$

<sup>3384</sup> The measured values of  $(x_\pm^{DK}, y_\pm^{DK}, x_\xi^{D\pi}, y_\xi^{D\pi})$  can be used to put constraints on the  
<sup>3385</sup> possible values of the CKM angle  $\gamma$  and the hadronic nuisance parameters  $r_B^{DK\pm}$ ,  
<sup>3386</sup>  $\delta_B^{DK\pm}$ ,  $r_B^{D\pi\pm}$ , and  $\delta_B^{D\pi\pm}$ . This is handled using the `gammacombo` package, which is also  
<sup>3387</sup> used to combine all measurements of  $\gamma$  made by the LHCb collaboration [48, 165].  
<sup>3388</sup>

### 5.7.1 Statistical approach

<sup>3389</sup> The optimal central values determined in a maximum likelihood fit. The set of  
<sup>3390</sup> all observables for which a measurement has been made is denoted  $A$ , and the set  
<sup>3391</sup> of underlying physics parameters is denoted  $\theta$ . The physics parameters of course  
<sup>3392</sup> determine the probability density function of measurement results of  $A$ ,  $f(A|\theta)$ .  
<sup>3393</sup> Given a specific set of measurement results,  $A_{\text{obs}}$ , a likelihood function is defined  
<sup>3394</sup>

$$\mathcal{L}(\theta|A_{\text{obs}}) = f(A_{\text{obs}}|\theta) \quad (5.35)$$

3395 and the estimate of  $\theta$  is the set of parameters that maximize the likelihood

$$\hat{\theta} = \arg \max_{\theta} \mathcal{L}(\theta | A_{\text{obs}}). \quad (5.36)$$

3396 In practice, a  $\chi^2$  function is defined

$$\chi^2(\theta | A_{\text{obs}}) = -2 \ln \mathcal{L}(\theta | A_{\text{obs}}) \quad (5.37)$$

3397 and minimized instead. In the specific case where the likelihood profile is Gaussian,  
3398 it can be described by the simple expression

$$\chi^2(\theta | A_{\text{obs}}) = (A_{\text{obs}} - A(\theta))^T \Sigma_{A_{\text{obs}}}^{-1} (A_{\text{obs}} - A(\theta)) + c, \quad (5.38)$$

3399 where  $\Sigma_{A_{\text{obs}}}$  is the *measured* covariance matrix for the observables (used as an  
3400 estimate of the true, underlying covariance matrix),  $A(\theta)$  denotes the value of the  
3401 observables expressed in terms of the underlying physics parameters, and  $c$  is a  
3402 constant that is independent of  $\theta$ . In the specific case considered here

$$\begin{aligned} A &= (x_-^{DK}, y_-^{DK}, x_+^{DK}, y_+^{DK}, x_\xi^{D\pi}, y_\xi^{D\pi}) \\ \theta &= (\gamma, r_B^{DK\pm}, \delta_B^{DK\pm}, r_B^{D\pi\pm}, \delta_B^{D\pi\pm}). \end{aligned} \quad (5.39)$$

3403 The likelihood scan presented in Section 5.5.2 proved that the Gaussian expression  
3404 in Eq. (5.38) provides an excellent description of the likelihood profile of the  
3405 measurement, when  $\Sigma_{A_{\text{obs}}}$  is taken to be the covariance matrix obtained in that  
3406 section. Thus, the  $\chi^2$  function defined in Eq. (5.38) is minimised to determine  
3407 the best estimate of  $\gamma$ .

3408 Two different methods are employed to construct confidence regions for the  
3409 observables of interest, known within the `gammacombo` framework as the PROB and  
3410 PLUGIN methods. Both methods aim to construct confidence regions for some  
3411 subset,  $\phi$ , of the full parameter set  $\theta$ . The remaining parameters, dubbed nuisance  
3412 parameters below, are denoted  $\eta = \theta \setminus \phi$ . In practice,  $\phi$  most often denotes a single  
3413 parameter, and of special interest is of course the case where  $\phi = \gamma$ . Both methods  
3414 aim to solve the problem that due to the number of parameters in  $\theta$  (five in the case  
3415 considered here, but up to 40 in the latest LHCb combination [49]), it is not feasible  
3416 to derive the confidence regions from a full-fledged Neumann construction [166].  
3417 Under assumptions discussed below, the methods achieve reasonable coverage  
3418 nonetheless, ie. had the measurement been repeated many times, the confidence  
3419 region is expected to cover the true parameter(s) with a probability at least at large  
3420 as the quoted confidence level (CL), independently of the true parameter value.  
3421 The presentation follows the `gammacombo` manual [165].

The PROB method is a simple profile-likelihood method. The minimum value of the  $\chi^2$  function is denoted  $\chi_{\min}^2 \equiv \chi^2(\hat{\theta}|A_{\text{obs}})$ . To evaluate the CL for a specific value (set of values) of  $\phi_0$ , the  $\chi^2$  function is again minimised, this time under the constraint that  $\phi = \phi_0$ , resulting in a new minimum  $\hat{\theta}' = (\phi_0, \hat{\eta}')$ . In the approximation that all likelihoods are exactly Gaussian, the variable

$$\Delta\chi^2(\phi_0|A_{\text{obs}}) = \chi^2(\hat{\theta}'|A_{\text{obs}}) - \chi_{\min}^2 \quad (5.40)$$

follows a  $\chi^2$  distribution with  $n$  degrees of freedom, where  $n$  is the number of parameters in  $\phi$  [31]. This can be used to evaluate CL at that point as

$$CL(\phi_0|A_{\text{obs}}) = F_n(\Delta\chi^2(\phi_0|A_{\text{obs}})) \quad (5.41)$$

where  $F_n$  is the cumulative distribution function of a  $\chi^2$  distribution with  $n$  degrees of freedom. The method takes its colloquial name from the fact that this function is named **Prob** in the **ROOT** package. Confidence regions can be defined by scanning the values of  $\phi_0$  over a region of interest. These confidence regions assume that the estimates  $\hat{\theta}$  follow a Gaussian distribution centred on the true values, which is the case for maximum likelihood estimates in asymptotically large samples [167]; in other cases they may not have good coverage properties. Given the Gaussian shape obtained in the likelihood scan of Section 5.5.2 the confidence regions are likely to be well behaved in the case considered here.

However, for the purpose of comparing to the combination of several LHCb measurements in Section 5.5.3 below, the PLUGIN method is necessary. The method is described in Ref. [168], based on the hybrid resampling method presented in Ref. [169]. It foregoes the assumption that  $\Delta\chi^2$  follows a  $\chi^2$  distribution, and instead estimates the distribution in a bootstrapping scheme. The procedure is as follows: the values of  $\hat{\theta}$ ,  $\hat{\theta}'$ , and  $\Delta\chi^2(\phi_0|A_{\text{obs}})$  are determined as described above; then the following steps are carried out a number,  $N_{\text{toys}}$ , of times

- 3445 1. Generate a "toy" result,  $A_{\text{toy}}^i$ , following the distribution  $f(A|\hat{\theta}')$
- 3446 2. Determine  $\Delta\chi^2(\phi_0|A_{\text{toy}}^i)$  by minimising the  $\chi^2$  function for the results  $A_{\text{toy}}^i$   
3447 twice, once where all parameters in  $\theta$  are free, and once where  $\phi = \phi_0$  is  
3448 enforced

3449 Then the CL is defined by

$$CL(\phi_0) = 1 - \frac{N(\Delta\chi^2(\phi_0|A_{\text{obs}}) < \Delta\chi^2(\phi_0|A_{\text{toy}}^i))}{N_{\text{toys}}} \quad (5.42)$$

3450 While the coverage properties are not proven, evidence is presented in terms of  
3451 asymptotic results and simulation studies in Refs. [168,169]. The coverage properties  
3452 have also been investigated in relation to LHCb combinations, and the intervals  
3453 were found to perform well in most cases [48].

<sup>3454</sup> **5.7.2 Interpretation results**

<sup>3455</sup> The central values and confidence regions obtained for the physics parameters are

$$\begin{aligned}\gamma &= (68.7^{+5.2}_{-5.1})^\circ, \\ r_B^{DK^\pm} &= 0.0904^{+0.0077}_{-0.0075}, \\ \delta_B^{DK^\pm} &= (118.3^{+5.5}_{-5.6})^\circ, \\ r_B^{D\pi^\pm} &= 0.0050^{+0.0017}_{-0.0017}, \\ \delta_B^{D\pi^\pm} &= (291^{+24}_{-26})^\circ,\end{aligned}\tag{5.43}$$

<sup>3456</sup> where the quoted uncertainties are obtained via the PLUGIN method. The one-  
<sup>3457</sup> dimensional CL plots are shown in Fig. 5.57. It is also clear that the PROB and  
<sup>3458</sup> PLUGIN confidence regions agree well; this is expected given the Gaussian likelihood.  
<sup>3459</sup> A series of two-dimensional confidence regions are shown in Fig. 5.58, where it  
<sup>3460</sup> can be seen that the observables define a single solution for  $\gamma$  as expected. It  
<sup>3461</sup> is worth noticing that the uncertainty of this measurement alone is on par with  
<sup>3462</sup> the current world average, due to the increased data sample, and the significant  
<sup>3463</sup> reduction of systematic uncertainties due to the new measurement strategy and  
<sup>3464</sup> updated inputs from BESIII.

<sup>3465</sup> The contribution to the uncertainty on  $\gamma$  from each of the statistical, strong-  
<sup>3466</sup> phase-related, and LHCb-related uncertainties in isolation can be estimated by  
<sup>3467</sup> repeating the interpretation while only including subsets of the uncertainties on  
<sup>3468</sup> the input parameters. Such studies have been performed using the PROB method.  
<sup>3469</sup> Running with statistical uncertainties only yields an uncertainty on  $\gamma$  of  $5.05^\circ$ .  
<sup>3470</sup> Including only the statistical and LHCb-related systematic uncertainties yields an  
<sup>3471</sup> uncertainty on  $\gamma$  of  $5.08^\circ$ , suggesting that the LHCb-related systematics contribute  
<sup>3472</sup> an uncertainty of  $0.6^\circ$ . This is a reduction compared to earlier analyses, where  
<sup>3473</sup> the contribution was about  $2^\circ$ . A significant contribution to the improvement is  
<sup>3474</sup> the efficiency-related systematic that has been avoided by promoting  $B^\pm \rightarrow D\pi^\pm$   
<sup>3475</sup> to a signal channel. Including only the statistical and the strong-phase-related  
<sup>3476</sup> uncertainties leads to an uncertainty on  $\gamma$  of  $5.09^\circ$ , showing the strong-phase-related  
<sup>3477</sup> uncertainty to be  $0.6^\circ$ , somewhat lower than the expectation of  $1.2^\circ$  presented in  
<sup>3478</sup> Ref. [76]. This is partly because the uncertainty estimate of that paper does not  
<sup>3479</sup> take into account the use of the  $D \rightarrow K_S^0 K^+ K^-$  channel, and partly because the  
<sup>3480</sup> uncertainty estimate depends on the specific central values.

<sup>3481</sup> The obtained statistical uncertainty on  $\gamma$  is in excellent agreement with the  
<sup>3482</sup> expectation from pseudoexperiments. The interpretation procedure outlined above  
<sup>3483</sup> has been performed for each of the pseudoexperiments performed to establish the

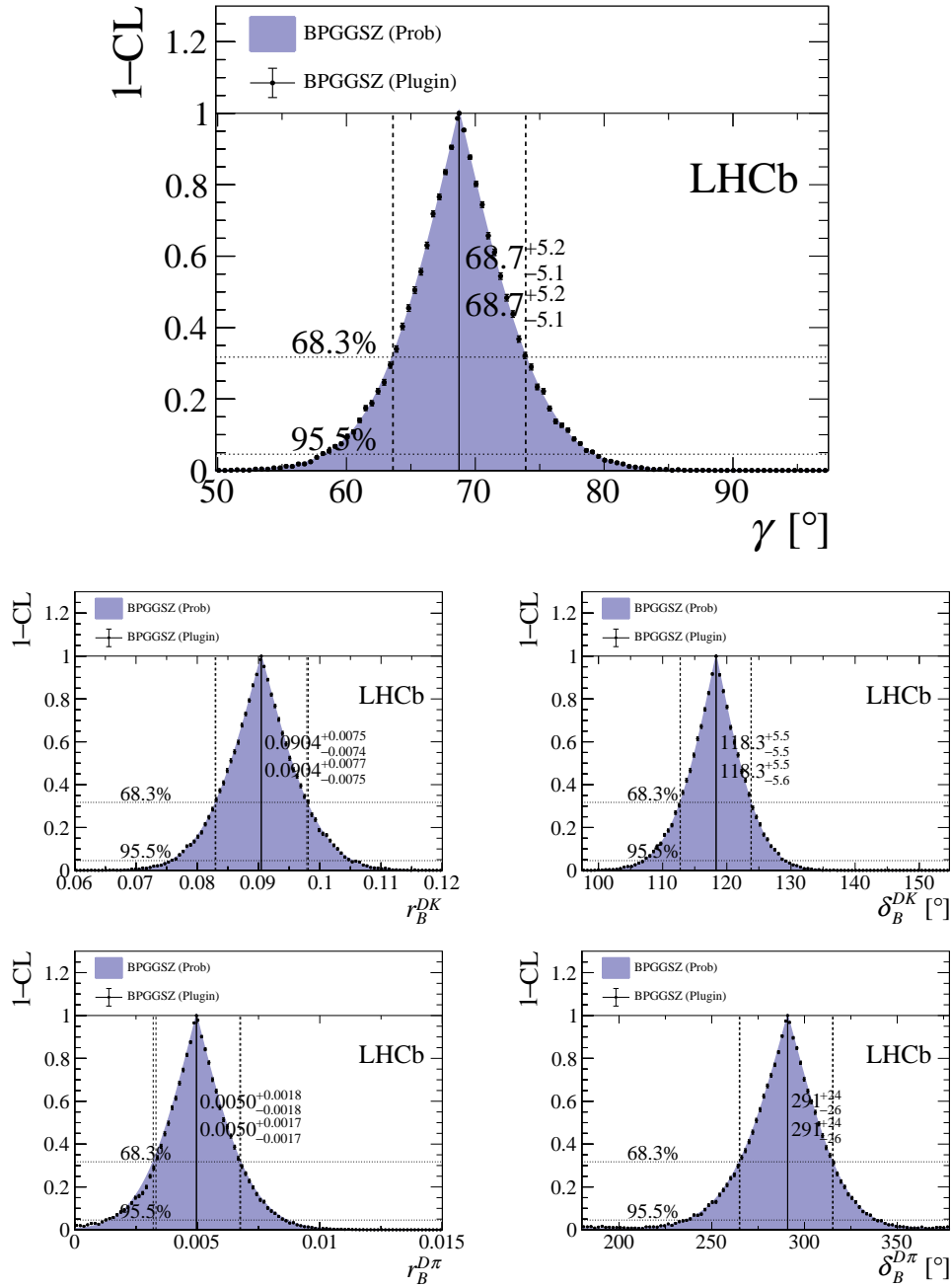


**Figure 5.57:** Confidence levels for the physics parameters of interest. The solutions are written on the plots, where the top number is given with PROB uncertainties and the bottom number with PLUGIN uncertainties.

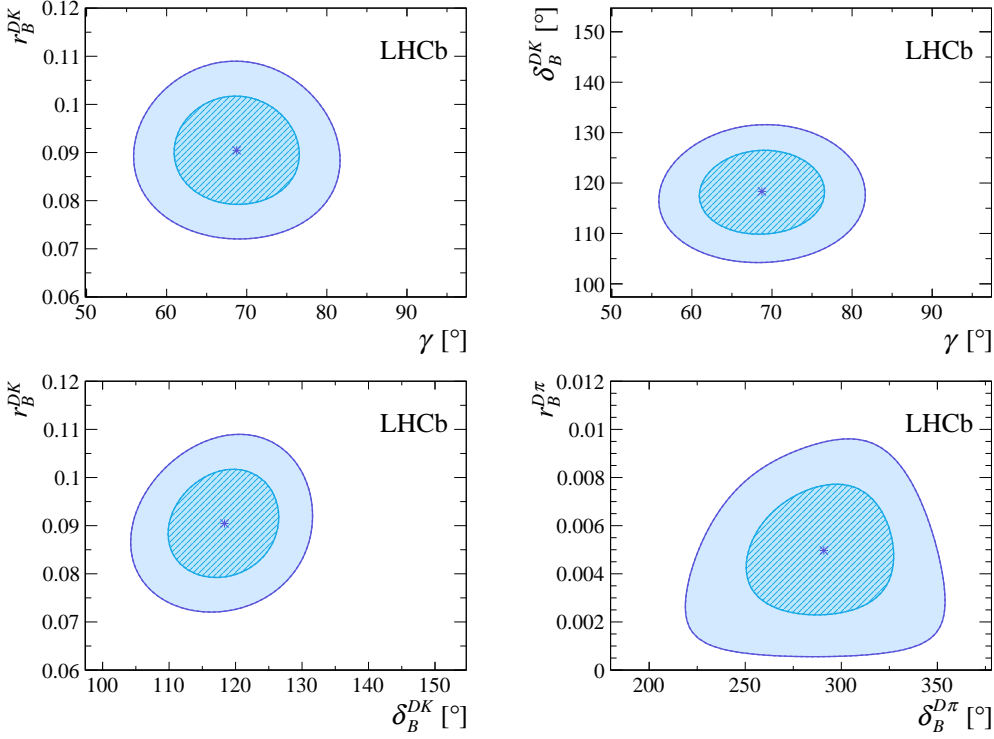


**Figure 5.58:** The 68 % and 95 % confidence regions for combinations of the physics parameters of interest, as obtained from the results of this measurement. The regions are calculated via the PROB method of gammacombo.

3484 feasibility of the  $CP$  fit in Section 5.5.1 (including only statistical uncertainties on the  
 3485 observables) and the central 90 % interval of the obtained uncertainties is  $[4.4^\circ, 6.0^\circ]$ .  
 3486 Furthermore, interpretation of  $\gamma$  is found to be unbiased, and the uncertainties on  $\gamma$   
 3487 show the expected coverage properties. Similar studies have been carried out where  
 3488 no background decays are included in the generated toy data sets. In this case, the  
 3489 precision on  $\gamma$  is improved by about 30 %. These pseudo experiments do suggest  
 3490 small biases on  $r_B^{DK}$  and  $r_B^{D\pi}$  in the interpretation step, of 10 % and 25 % of the  
 3491 statistical uncertainty, respectively. In absolute terms, this corresponds to positive  
 3492 biases of  $\Delta r_B^{DK} = +0.0008$  (ie. 1 % of the central value) and  $\Delta r_B^{D\pi} = +0.0004$  (about  
 3493 8 % of the central value). These biases have been observed before [48], and have  
 3494 been determined to arise due to the constraint that  $r_B > 0$ . The results quoted in  
 3495 Eq. (6.5) have *not* been corrected for the bias and should be interpreted accordingly.  
 3496 The results from this thesis that will be used in combinations of  $\gamma$  measurements by  
 3497 LHCb (and others) is the measured observables,  $(x_\pm^{DK}, y_\pm^{DK}, x_\xi^{D\pi}, y_\xi^{D\pi})$ , and these  
 3498 were shown to be determined without a bias in Section 5.5.

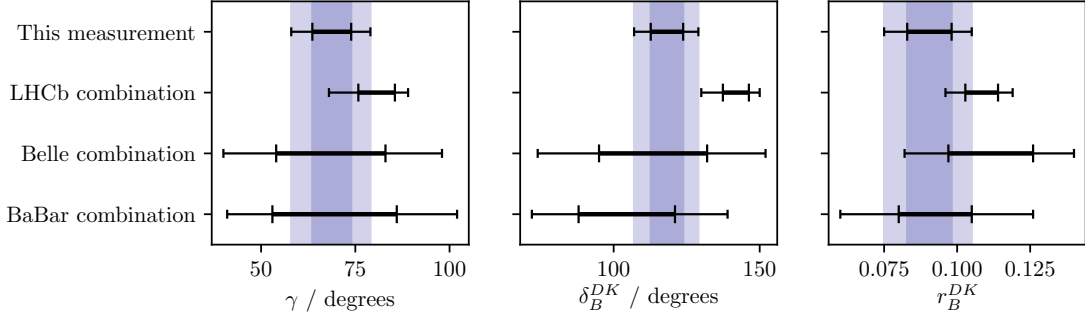


**Figure 5.59:** Comparison of the  $1\sigma$  and  $2\sigma$  confidence intervals obtained results for  $\gamma$  and the physics parameters relating to  $B^\pm \rightarrow DK^\pm$  decays, with those from the combinations of  $\gamma$  measurements by the Belle [46] and BaBar [47] collaborations, and the 2018 combination of LHCb results [49] where the BPGBGSZ measurements have been excluded.

### 3499 5.7.3 Compatibility with other measurements

3500 It is worth comparing the obtained constraints on the physics parameters with the  
 3501 information available from other measurements, made at the  $B$  factories and by  
 3502 the LHCb collaboration using other decay channels. This comparison is made for  $\gamma$   
 3503 and the hadronic parameters in the  $B^\pm \rightarrow DK^\pm$  decay in Fig. 5.59, comparing to  
 3504 the results of the combinations of  $\gamma$  measurements by the Belle [46] and BaBar [47]  
 3505 collaborations presented in 2013, and the 2018 combination of LHCb results [49]. For  
 3506 this purpose, the LHCb combination is re-performed, removing the input from earlier  
 3507 BPGBGSZ measurements that use  $B^\pm \rightarrow DK^\pm$  decays, because they were made  
 3508 using data that is re-analysed in the present thesis; thus they need to be excluded  
 3509 to make the results that are compared independent. The combination employs the  
 3510 same statistical method outlined above, with the exception that the likelihood now  
 3511 depends on observables measured in a number of different analyses. The included  
 3512 measurements are summarised in Table 5.22. It can be seen in Fig. 5.59 that the  
 3513 results obtained in this thesis agree well with the Belle and BaBar results, but are in  
 3514 some tension with the 2018 LHCb combination, especially for the  $\delta_B^{DK}$  parameter.

3515 The level of compatibility can be quantified by calculating the three-dimensional  
 3516  $\chi^2$  of the BPGBGSZ results and those of the LHCb combination (without the earlier  
 3517 BPGBGSZ measurements), with respect to the best fit values of  $(\gamma, r_B^{DK\pm}, \delta_B^{DK\pm})$   
 3518 when all measurements are combined. The two-dimensional confidence regions  
 3519 obtained in these three cases are compared in Fig. 5.60, where some tension in  $r_B^{DK\pm}$   
 3520 and  $\delta_B^{DK\pm}$  is visible again. The calculation is based on the PLUGIN uncertainties; for  
 3521 the LHCb combination these uncertainty estimates are slightly larger than the ones  
 3522 obtained via the PROB method. One obtains  $\chi^2 = \chi_{GGSZ}^2 + \chi_{LHCb}^2 = 0.7 + 9.1 = 9.8$ ,

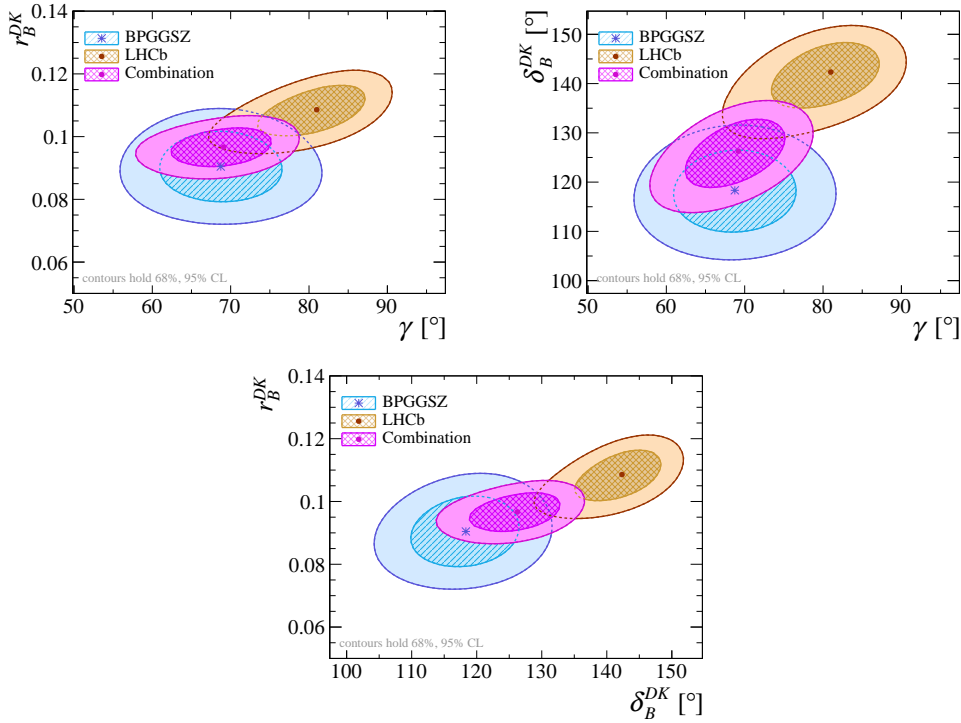


**Figure 5.60:** The 68 % and 95 % confidence regions for  $(\gamma, r_B^{DK\pm})$ ,  $(\gamma, \delta_B^{DK\pm})$ , and  $(\delta_B^{DK\pm}, r_B^{DK\pm})$  for this measurement, the 2018 LHCb combination [49] where the BPGGSZ results have been excluded, and the combination thereof, calculated via the PROB method of `gammacombo`.

which for 3 degrees of freedom correspond to a  $p$ -value of 2 %, or a  $2.3\sigma$  deviation. However, this tension is expected to be reduced when other measurements in the LHCb combination are updated to include results based on the full Run 1 and 2 data set. The most important update is that of the two-body ADS/GLW measurement in  $B^\pm \rightarrow DK^\pm$  decays because that measurement, and the BPGGSZ measurement presented in this thesis, have the largest impact in the combination.<sup>11</sup> The impact of the BPGGSZ measurement on the LHCb average can also be gauged by these studies: the 2018 LHCb combination [49] determines that  $\gamma = (81.0^{+4.5}_{-5.2})^\circ$  when the earlier BPGGSZ measurements are excluded; with the inclusion of the results presented here the favoured solution changes to  $\gamma = (69.1^{+4.1}_{-4.6})^\circ$ . The new central value is in excellent agreement with the expected value given other CKM measurements,  $\gamma = (65.66^{+0.90}_{-2.65})^\circ$ , and the uncertainties are reduced a fair amount.

The latest LHCb combination in which  $B^\pm \rightarrow D\pi^\pm$  parameters were determined is from 2016 [48]. Two solutions existed for  $(r_B^{D\pi\pm}, \delta_B^{D\pi\pm})$  which made the interpretation problematic. As can be seen in Fig. 5.61, the measurement presented in

<sup>11</sup>The ADS/GLW results based on the full Run 1 and 2 data set are not public at the time of writing, and can therefore not be included in the present discussion.

**Table 5.22:** List of the LHCb measurements used in the combination that the results obtained in the present thesis is compared to. These correspond to the 2018 LHCb combination [49], except that the earlier BPGGSZ results made with  $B^\pm \rightarrow DK^\pm$  decays have not been included in the comparison. In the method column, TD stands for "time-dependent", the ADS/GLW/BPGGSZ acronyms were defined in Chapter 2, and references are provided for the remaining methods.

$B$ decay	$D$ decay	Method	Ref.	Data set
$B^+ \rightarrow DK^+$	$D \rightarrow h^+h^-$	GLW	[159]	2011-16
$B^+ \rightarrow DK^+$	$D \rightarrow h^+h^-$	ADS	[156]	2011-12
$B^+ \rightarrow DK^+$	$D \rightarrow h^+\pi^-\pi^+\pi^-$	GLW/ADS	[156]	2011-12
$B^+ \rightarrow DK^+$	$D \rightarrow h^+h^-\pi^0$	GLW/ADS	[170]	2011-12
$B^+ \rightarrow DK^+$	$D \rightarrow K_S^0 K^+\pi^-$	GLS [171]	[172]	2011-12
$B^+ \rightarrow D^*K^+$	$D \rightarrow h^+h^-$	GLW	[159]	2011-16
$B^+ \rightarrow DK^{*+}$	$D \rightarrow h^+h^-$	GLW/ADS	[173]	2011-16
$B^+ \rightarrow DK^{*+}$	$D \rightarrow h^+\pi^-\pi^+\pi^-$	GLW/ADS	[173]	2011-16
$B^+ \rightarrow DK^+\pi^+\pi^-$	$D \rightarrow h^+h^-$	GLW/ADS	[174]	2011-12
$B^0 \rightarrow DK^{*0}$	$D \rightarrow K^+\pi^-$	ADS	[175]	2011-12
$B^0 \rightarrow DK^+\pi^-$	$D \rightarrow h^+h^-$	GLW-Dalitz [176]	[158]	2011-12
$B^0 \rightarrow DK^{*0}$	$D \rightarrow K_S^0 \pi^+\pi^-$	BPGGSZ	[68]	2011-12
$B_s^0 \rightarrow D_s^\mp K^\pm$	$D_s^\mp \rightarrow h^+h^-\pi^\pm$	TD	[177]	2011-12
$B^0 \rightarrow D^\mp \pi^\pm$	$D^\mp \rightarrow K^+\pi^-\pi^\pm$	TD	[178]	2011-12
Measurements included in Ref. [49] but not in the present comparison				
$B^+ \rightarrow DK^+$	$D \rightarrow K_S^0 h^+h^-$	BPGGSZ	[73]	2011-12
$B^+ \rightarrow DK^+$	$D \rightarrow K_S^0 h^+h^-$	BPGGSZ	[3]	2015-16

<sup>3538</sup> this thesis picks out one of these solutions, with which it is in excellent agreement.

<sup>3539</sup> This solution agrees with the theoretically expected value of  $r_B^{D\pi^\pm} \sim 0.005$  [50].

<sup>3540</sup> Thus, the inclusion of the results presented here are expected to lead to a much less

<sup>3541</sup> problematic inclusion of the  $B^\pm \rightarrow D\pi^\pm$  channel in future LHCb combinations.

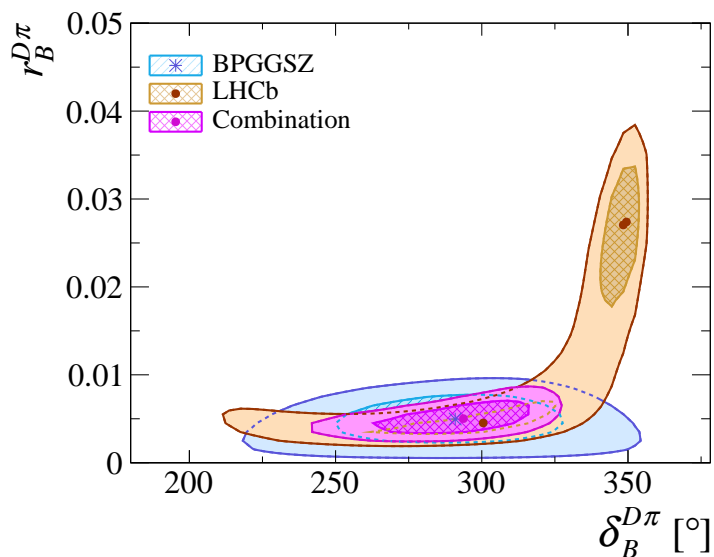


**Figure 5.61:** The 68 % and 95 % confidence regions for  $(\delta_B^{D\pi^\pm}, r_B^{D\pi^\pm})$  obtained from the results of this measurement, in the 2016 LHCb combination [48], and the combination thereof, calculated via the PROB method of `gammacombo`.

# 6

3542

3543

## Summary and outlook

3544 The main result of the thesis is a measurement of the CKM angle  $\gamma$  using  $B^\pm \rightarrow DK^\pm$   
3545 and  $B^\pm \rightarrow D\pi^\pm$  decays, where the  $D$  meson decays to one of the final states  
3546  $K_S^0\pi^+\pi^-$  and  $K_S^0K^+K^-$ . Approximately 17,500  $B^\pm \rightarrow DK^\pm$  decays<sup>1</sup> and 230,000  
3547  $B^\pm \rightarrow D\pi^\pm$  decays are analysed, obtained from the  $pp$  collision data set collected  
3548 by the LHCb experiment during Run 1 and 2 of the LHC. The total data set  
3549 corresponds to an integrated luminosity of about  $9\text{ fb}^{-1}$  collected at centre-of-  
3550 mass energies of  $\sqrt{s} = 7, 8,$  and  $13\text{ TeV}$ . The measurement relies on the phase-  
3551 space distribution of signal decays, analysed using a model-independent method  
3552 based on strong-phase measurements by the CLEO and BESIII collaborations;  
3553 an approach known as the model-independent BPFGGSZ method. The measured  
3554  $CP$ -violation observables are defined

$$x_\pm^{DK} = r_B^{DK} \cos(\delta_B^{DK} \pm \gamma), \quad y_\pm^{DK} = r_B^{DK} \sin(\delta_B^{DK} \pm \gamma), \quad (6.1)$$

3555 and measured to be

$$\begin{aligned} x_-^{DK} &= (-5.7 \pm 1.0 \pm 0.2 \pm 0.2) \times 10^{-2}, \\ y_-^{DK} &= (-6.6 \pm 1.1 \pm 0.3 \pm 0.4) \times 10^{-2}, \\ x_+^{DK} &= (-9.3 \pm 1.0 \pm 0.2 \pm 0.2) \times 10^{-2}, \\ y_+^{DK} &= (-1.3 \pm 1.3 \pm 0.3 \pm 0.3) \times 10^{-2}, \end{aligned} \quad (6.2)$$

3556 where the first uncertainty is statistical, the second arises due to systematic effects in  
3557 the measurement, and the third is the propagated uncertainty on the strong-phase

---

<sup>1</sup>This number includes the approximately 13.5 % of  $B^\pm \rightarrow DK^\pm$  that are reconstructed as  $B^\pm \rightarrow D\pi^\pm$  decays in the analysis.

3558 inputs from the CLEO and BESIII measurements. In addition, two nuisance  
3559 parameters relating to  $B^\pm \rightarrow D\pi^\pm$  decays are measured. These are defined

$$x_\xi^{D\pi} = (r_B^{DK}/r_B^{D\pi}) \cos(\delta_B^{DK} - \delta_B^{D\pi}), \quad y_\xi^{D\pi} = (r_B^{DK}/r_B^{D\pi}) \sin(\delta_B^{DK} - \delta_B^{D\pi}), \quad (6.3)$$

3560 and measured to be

$$\begin{aligned} x_\xi^{D\pi} &= (-5.5 \pm 2.0 \pm 0.3 \pm 0.1) \times 10^{-2}, \\ y_\xi^{D\pi} &= (-0.7 \pm 2.3 \pm 0.5 \pm 0.2) \times 10^{-2}, \end{aligned} \quad (6.4)$$

3561 Due to the measurement approach, the information on  $\gamma$  obtained from  $B^\pm \rightarrow D\pi^\pm$   
3562 decays is encoded in the  $(x_\pm^{DK}, y_\pm^{DK})$  parameters. The measured observables have  
3563 been interpreted in terms of the underlying physics parameters, yielding the results

$$\begin{aligned} \gamma &= (68.7_{-5.1}^{+5.2})^\circ, \\ r_B^{DK\pm} &= 0.0904_{-0.0075}^{+0.0077}, \\ \delta_B^{DK\pm} &= (118.3_{-5.6}^{+5.5})^\circ, \\ r_B^{D\pi\pm} &= 0.0050_{-0.0017}^{+0.0017}, \\ \delta_B^{D\pi\pm} &= (291_{-26}^{+24})^\circ, \end{aligned} \quad (6.5)$$

3564 This is the most precise stand-alone measurement of  $\gamma$  to date, and surpasses  
3565 the precision of all earlier measurements of  $\gamma$  combined. The measured value  
3566 agrees with the expectation from global fits of all CKM parameters. For example,  
3567 the CKMFitter group obtain  $\gamma = (65.66_{-2.65}^{+0.90})^\circ$  [36] in a global fit that excludes  
3568 direct  $\gamma$  measurements, and the obtained values and uncertainties in other world  
3569 averages are similar [27, 39].

3570 It was the first BPGGSZ measurement by the LHCb collaboration to include  
3571  $B^\pm \rightarrow D\pi^\pm$  decays as a signal channel, and a series of feasibility studies that  
3572 informed the analysis strategy have also been presented. While the impact on  
3573 the  $\gamma$  precision from  $B^\pm \rightarrow D\pi^\pm$  decays is limited, the new strategy significantly  
3574 simplified the treatment of the non-uniform phase-space acceptance in LHCb, and  
3575 lead to a significant reduction of the systematic measurement uncertainty. This will  
3576 become especially important in future measurements, where the precision will no  
3577 longer be limited by the statistical uncertainty to the degree that it is now.

3578 The thesis also presented a careful analysis of the impact of neutral kaon  $CP$   
3579 violation and material interaction on  $\gamma$  measurements based on the BPGGSZ  
3580 method. This was a crucial step towards the promotion of the  $B^\pm \rightarrow D\pi^\pm$   
3581 channel to a signal channel: existing literature estimated the potential bias to be  
3582  $\mathcal{O}(1^\circ)$  in  $B^\pm \rightarrow DK^\pm$  decays *and to scale with*  $1/r_B$ . This suggested potentially

3583 large biases for a  $B^\pm \rightarrow D\pi^\pm$  analysis, since  $r_B^{D\pi} \simeq 0.005$  is twenty times smaller  
3584 than  $r_B^{DK} \simeq 0.1$ . However, the thesis argues that the actual impact is an order of  
3585 magnitude smaller, as long as the  $CP$ -violation observables are determined based  
3586 on the phase-space distribution of signal decays. This is confirmed in a number  
3587 of simple, numerical studies that take the detector geometries of the LHCb and  
3588 Belle II detectors into account; these studies are also used to assign a (reasonably  
3589 small) systematic uncertainty on the measurement results discussed above.

## 3590 6.1 A look towards the future

3591 Precise measurements of  $\gamma$  play an important role in the physics programmes of  
3592 both the LHCb and Belle II experiments, and the next 10–15 years will see huge  
3593 improvements in the obtainable precision. Given the results of Chapter 5, it is  
3594 clear that LHCb is well on course to reach, ever surpass, the expected goal of  
3595 determining  $\gamma$  with a precision of  $4^\circ$  using Run 1 and 2 data [179], when more  
3596 analyses are performed with the full data set. In the longer run, LHCb is expecting  
3597 to reach a precision of  $1.5^\circ$  in the combination of  $\gamma$  measurements by the end of  
3598 Run 3 of the LHC, and on improving that to  $\sim 0.35^\circ$  in the planned Upgrade  
3599 Phase II during the 2030’ies [40], with the BPGGSZ mode continuing to be an  
3600 important contributor to the obtainable precision. The mode plays an even more  
3601 significant role in the Belle II physics programme, being denoted the *golden mode*  
3602 in the physics programme [133], due to a much higher  $K_S^0$  reconstruction efficiency  
3603 in the experiment. When the planned data set corresponding to an integrated  
3604 luminosity of  $50 \text{ ab}^{-1}$  has been collected, the uncertainty on  $\gamma$  from the combination  
3605 of all Belle II results is expected to be about  $1.6^\circ$  [133]; this is expected to happen  
3606 in 2031 given the current schedule [180].

3607 The main reason for the impressive expected improvement in precision is that  
3608 current  $\gamma$  measurements are dominated by statistical uncertainties in all the major  
3609 signal modes. This is expected to remain true for the BPGGSZ modes throughout  
3610 the period described above. The current dominating systematic uncertainty on  $\gamma$  is  
3611 due to the uncertainty on the measured strong-phase inputs, currently contributing  
3612 an uncertainty of about  $\sim 1^\circ$ ; a number that represents a significant improvement  
3613 compared to earlier analyses, due to the recently published measurements by  
3614 the BESIII collaboration [76, 77]. These measurements are based on a data set  
3615 corresponding to an integrated luminosity of  $2.9 \text{ fb}^{-1}$ . The BESIII collaboration  
3616 is planning to take data corresponding to an additional  $17 \text{ fb}^{-1}$  under the same  
3617 running conditions during 2021–22 [181]; therefore, which will allow for significantly

improved measurements. Therefore, is not expected that the strong-phase inputs will be a limiting systematic uncertainty in model-independent BPGBSZ measurements for the current generation of experiments.

It used to be the case that the dominating systematic uncertainty in LHCb measurements of  $\gamma$  with the BPGBSZ method was due to the non-trivial phase-space acceptance profile [3], contributing most of the  $\sim 2^\circ$  systematic uncertainty on  $\gamma$  related to experimental effects. This would have been the largest systematic uncertainty in the measurement presented in the thesis, and would potentially become the dominating uncertainty during the first upgrade phase of LHCb. However, as described in detail in the thesis, the uncertainty can be avoided altogether in a simultaneous analysis of  $B^\pm \rightarrow DK^\pm$  and  $B^\pm \rightarrow D\pi^\pm$  decays, allowing for maximal use of the large data sets to be collected by the LHCb experiment in the future.

With the results of this thesis, the world averages of  $\gamma$  measurements will move closer to the value preferred by global fits and the Standard Model passes yet another test. As such, the question remains open as to whether the CKM picture will hold up to the increasingly stringent scrutiny of the next decades, or if signs of new physics will start to appear.

## Appendices

# A

3637

3638

## Projections of the main fit to data

3639 This appendix includes projections of the main fit to data described in Section 5.5.2,  
3640 for each of the 160 subcategories in the fit. The projections for LL candidates where  
3641  $D \rightarrow K_S^0\pi^+\pi^-$  are shown in Figs. A.1 and A.2; the equivalent projections for DD  
3642 candidates are shown in Figs. A.3 and A.4; finally the projections for candidates  
3643 where  $D \rightarrow K_S^0K^+K^-$  are shown in Figs. A.5 and A.6.

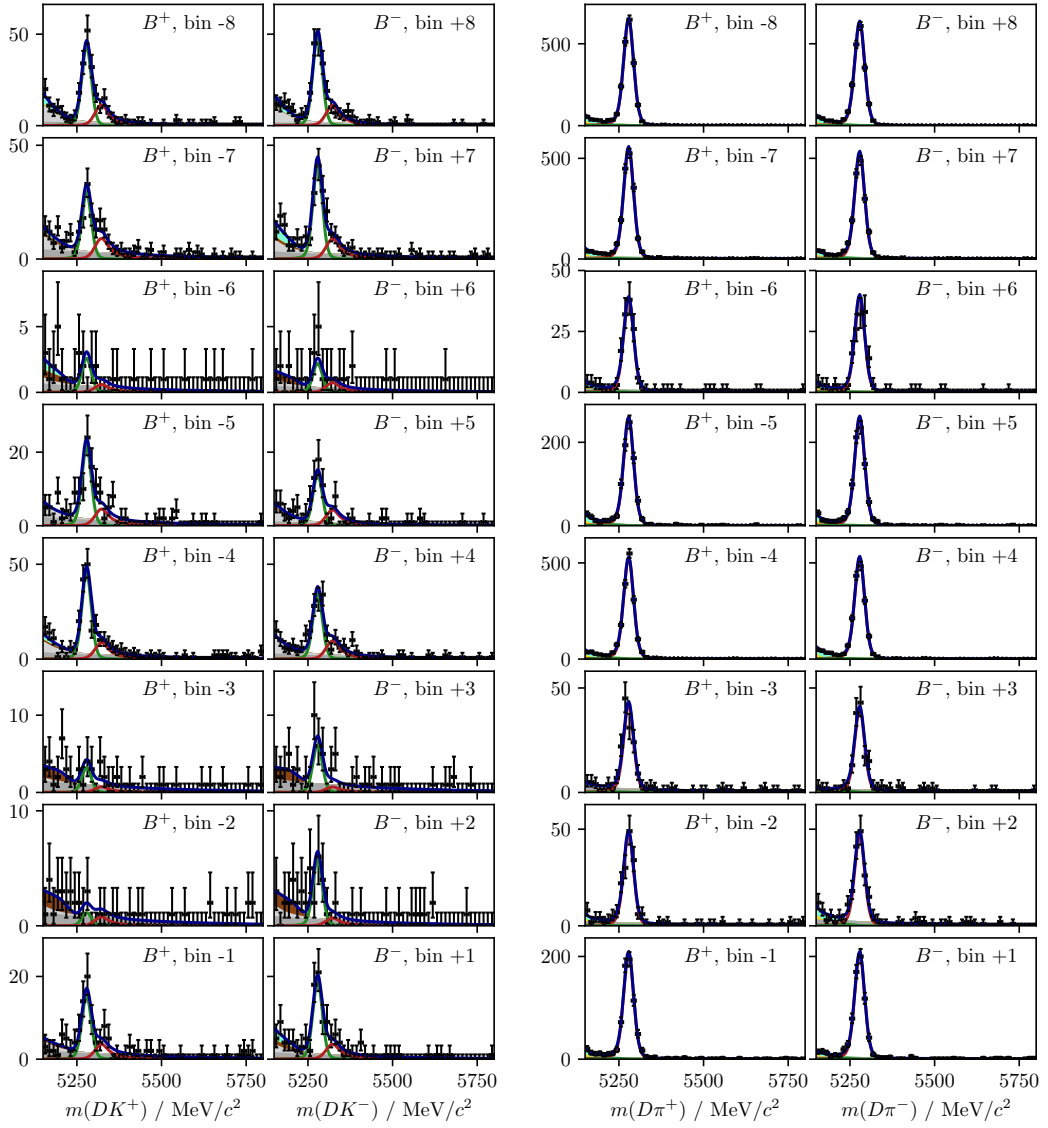


**Figure A.1:** Projections of the main fit to data described in Section 5.5. The two columns on the left show  $B^\pm \rightarrow DK^\pm$  candidates, split by charge, while the two columns on the right show  $B^\pm \rightarrow D\pi^\pm$  candidates. These projections are for the  $D \rightarrow K_S^0 \pi^+ \pi^-$  mode where the  $K_S^0$  meson is in the LL category.

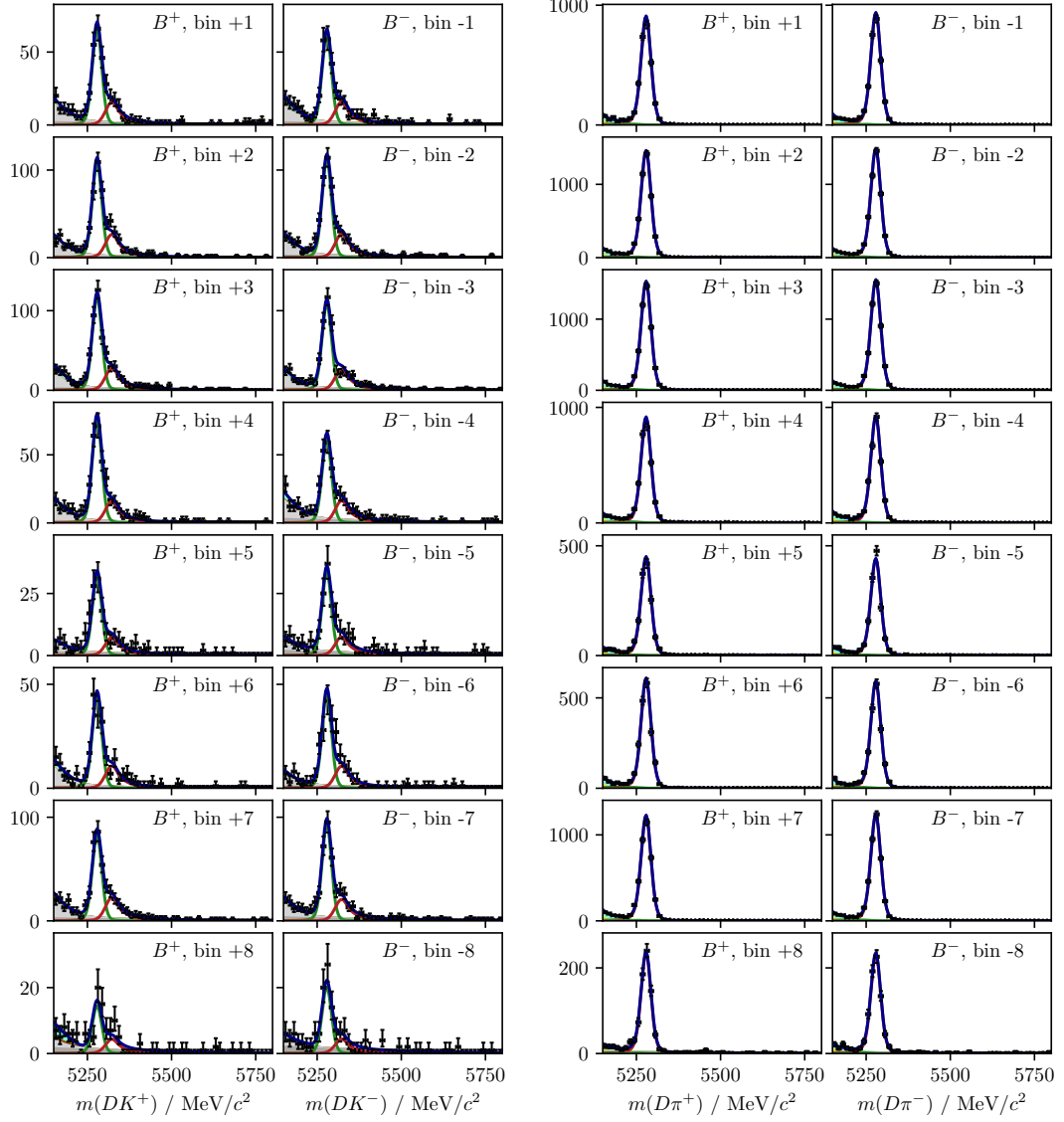


**Figure A.2:** Projections of the main fit to data described in Section 5.5. The two columns on the left show  $B^\pm \rightarrow DK^\pm$  candidates, split by charge, while the two columns on the right show  $B^\pm \rightarrow D\pi^\pm$  candidates. These projections are for the  $D \rightarrow K_S^0 \pi^+ \pi^-$  mode where the  $K_S^0$  meson is in the LL category.

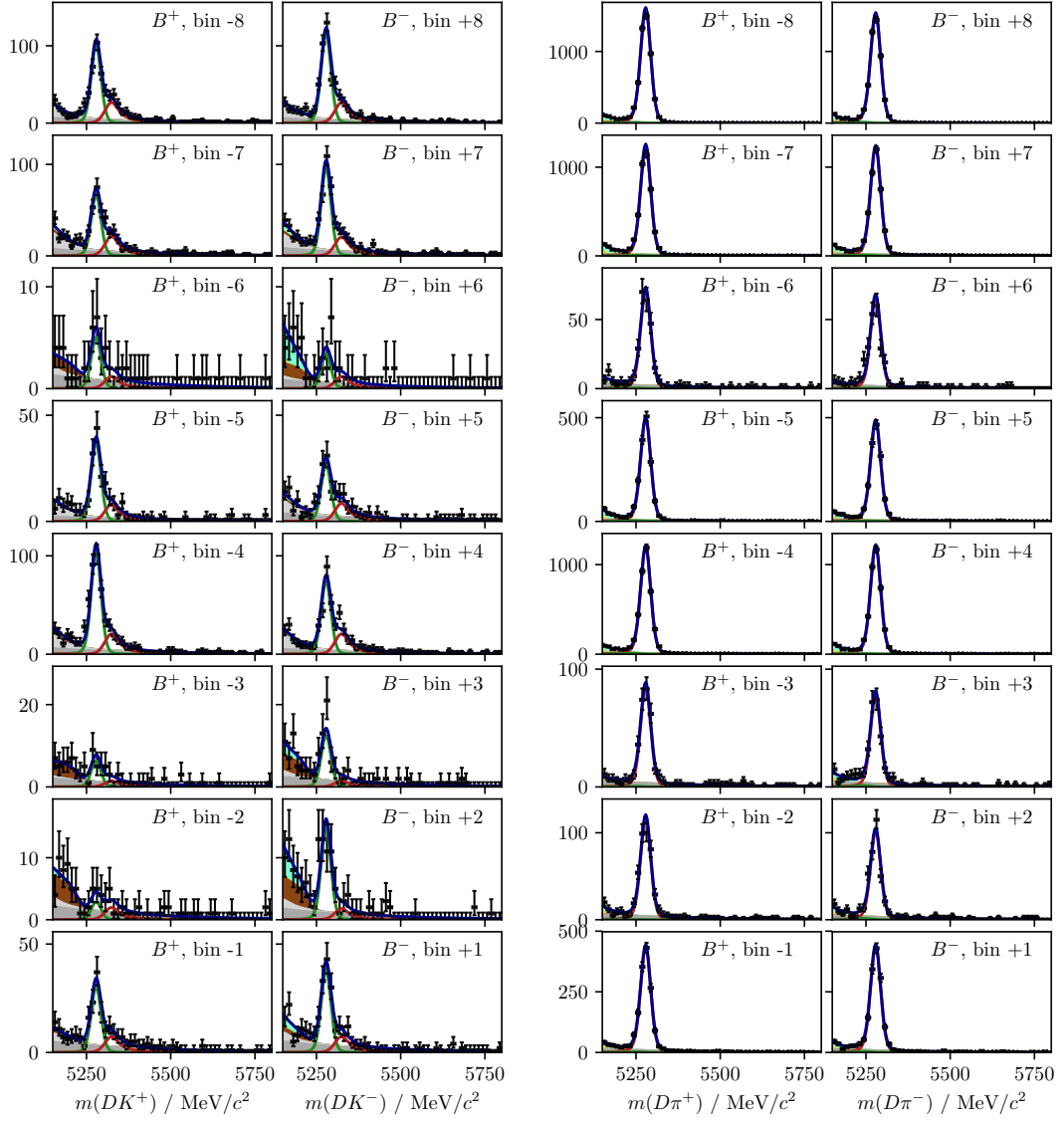


**Figure A.3:** Projections of the main fit to data described in Section 5.5. The two columns on the left show  $B^\pm \rightarrow DK^\pm$  candidates, split by charge, while the two columns on the right show  $B^\pm \rightarrow D\pi^\pm$  candidates. These projections are for the  $D \rightarrow K_S^0\pi^+\pi^-$  mode where the  $K_S^0$  meson is in the DD category.

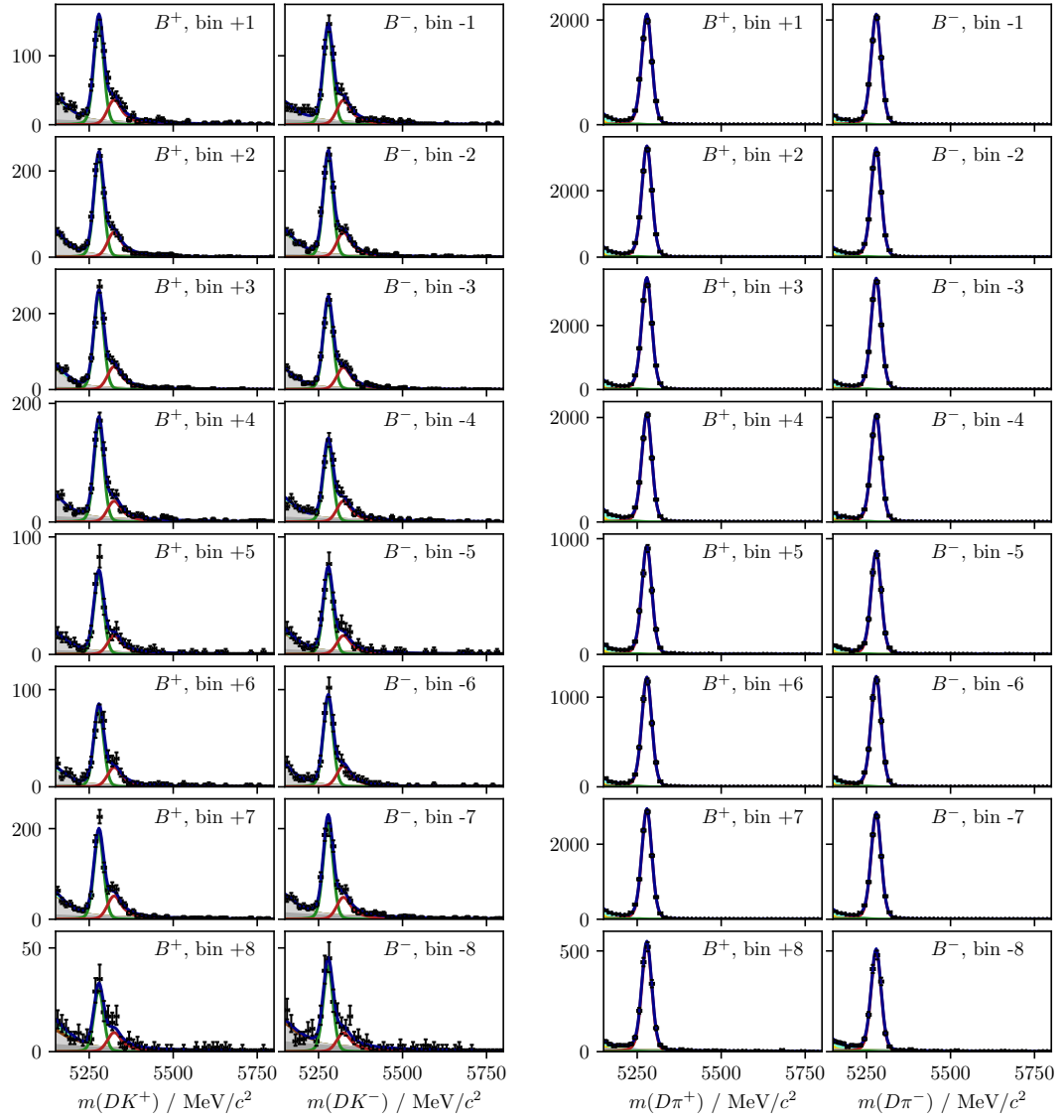


**Figure A.4:** Projections of the main fit to data described in Section 5.5. The two columns on the left show  $B^\pm \rightarrow DK^\pm$  candidates, split by charge, while the two columns on the right show  $B^\pm \rightarrow D\pi^\pm$  candidates. These projections are for the  $D \rightarrow K_S^0\pi^+\pi^-$  mode where the  $K_S^0$  meson is in the DD category.

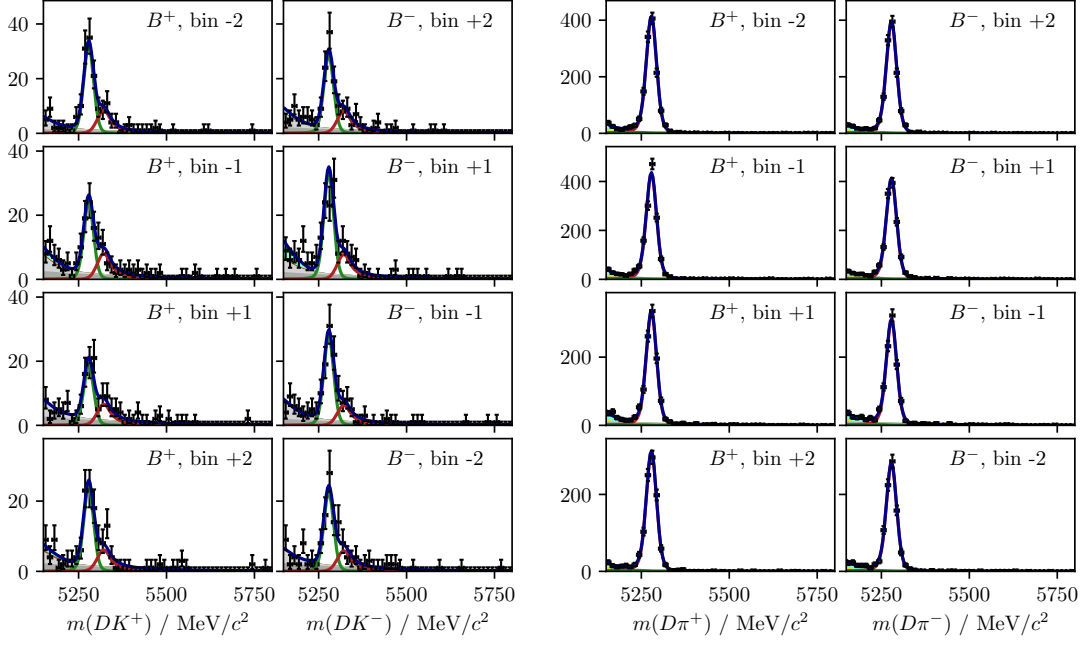


**Figure A.5:** Projections of the main fit to data described in Section 5.5. The two columns on the left show  $B^\pm \rightarrow DK^\pm$  candidates, split by charge, while the two columns on the right show  $B^\pm \rightarrow D\pi^\pm$  candidates. These projections are for the  $D \rightarrow K_S^0 K^+ K^-$  mode where the  $K_S^0$  meson is in the LL category.

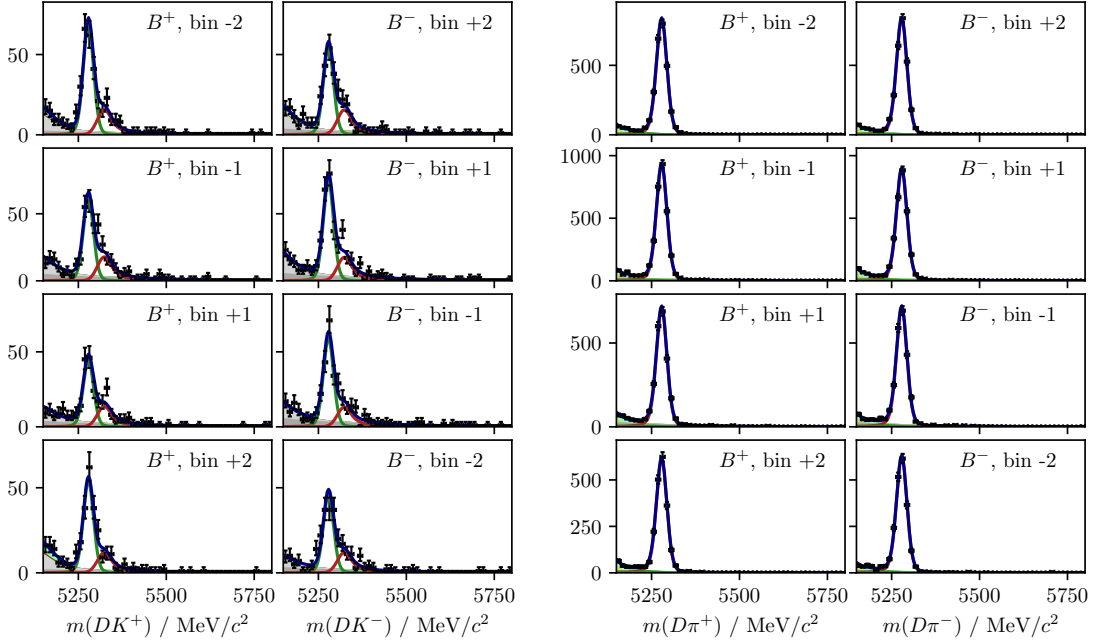


**Figure A.6:** Projections of the main fit to data described in Section 5.5. The two columns on the left show  $B^\pm \rightarrow DK^\pm$  candidates, split by charge, while the two columns on the right show  $B^\pm \rightarrow D\pi^\pm$  candidates. These projections are for the  $D \rightarrow K_S^0 K^+ K^-$  mode where the  $K_S^0$  meson is in the DD category.

# B

3644

3645

Contribution for the LHCb collaboration

## Bibliography

- [1] LHCb collaboration, R. Aaij *et al.*, *Measurement of the CKM angle  $\gamma$  in  $B^\pm \rightarrow DK^\pm$  and  $B^\pm \rightarrow D\pi^\pm$  decays with  $K_S^0 h^\pm h^\mp$* , Submitted to JHEP (2020).
- [2] M. Bjørn and S. Malde, *CP violation and material interaction of neutral kaons in measurements of the CKM angle  $\gamma$  using  $B^\pm \rightarrow DK^\pm$  decays where  $D \rightarrow K_S^0 \pi^+ \pi^-$* , JHEP **19** (2019) 106, [arXiv:1904.01129](https://arxiv.org/abs/1904.01129).
- [3] LHCb collaboration, R. Aaij *et al.*, *Measurement of the CKM angle  $\gamma$  using  $B^\pm \rightarrow DK^\pm$  with  $D \rightarrow K_S^0 \pi^+ \pi^-$ ,  $K_S^0 K^+ K^-$  decays*, JHEP **08** (2018) 176, Erratum ibid. **10** (2018) 107, [arXiv:1806.01202](https://arxiv.org/abs/1806.01202).
- [4] E. Noether, *Invariante Variationsprobleme*, Nachrichten von der Gesellschaft der Wissenschaften zu Göttingen, Mathematisch-Physikalische Klasse **1918** (1918) 235.
- [5] J. F. Donoghue, E. Golowich, and B. R. Holstein, *Dynamics of the Standard Model*, Cambridge University Press, Cambridge, 2014.
- [6] A. D. Sakarov, *Violation of CP Invariance, C Asymmetry, and Baryon Asymmetry of the Universe*, JETP Letters **5** (1966) 24.
- [7] G. Luders, *On the Equivalence of Invariance under Time Reversal and under Particle-Antiparticle Conjugation for Relativistic Field Theories*, Kong. Dan. Vid. Sel. Mat. Fys. Medd. **28N5** (1954) 1.
- [8] C. S. Wu *et al.*, *Experimental Test of Parity Conservation in Beta Decay*, Phys. Rev. **105** (1957) 1413.
- [9] T. D. Lee and C. N. Yang, *Question of Parity Conservation in Weak Interactions*, Phys. Rev. **104** (1956) 254.
- [10] J. H. Christenson, J. W. Cronin, V. L. Fitch, and R. Turlay, *Evidence for the  $2\pi$  Decay of the  $K_2^0$  Meson*, Phys. Rev. Lett. **13** (1964) 138.

- 3672 [11] BaBar collaboration, B. Aubert *et al.*, *Observation of CP Violation in the  $B^0$*   
 3673 *Meson System*, Phys. Rev. Lett. **87** (2001) 091801, [arXiv:hep-ex/0107013](#).
- 3674 [12] Belle collaboration, K. Abe *et al.*, *Observation of large CP violation*  
 3675 *in the neutral B meson system*, Phys. Rev. Lett. **87** (2001) 091802,  
 3676 [arXiv:hep-ex/0107061](#).
- 3677 [13] Belle collaboration, K. Abe *et al.*, *Study of  $B^\pm \rightarrow D_{CP}K^\pm$  and  $B^\pm \rightarrow D_{CP}^*K^\pm$*   
 3678 *decays*, Phys. Rev. **D73** (2006) 051106, [arXiv:hep-ex/0601032](#).
- 3679 [14] Belle collaboration, Y. Horii *et al.*, *Evidence for the Suppressed Decay  $B^- \rightarrow$*   
 3680  *$DK^-$ ,  $D \rightarrow K^+\pi^-$* , Phys. Rev. Lett. **106** (2011) 231803, [arXiv:1103.5951](#).
- 3681 [15] BaBar collaboration, P. del Amo Sanchez *et al.*, *Measurement of CP*  
 3682 *observables in  $B^\pm \rightarrow D_{CP}K^\pm$ ) decays and constraints on the CKM angle*  
 3683 *gamma*, Phys. Rev. **D82** (2010) 072004, [arXiv:1007.0504](#).
- 3684 [16] BaBar collaboration, P. del Amo Sanchez *et al.*, *Search for  $b \rightarrow u$  transitions*  
 3685 *in  $B^- \rightarrow DK^-$  and  $D^*K^-$  decays*, Phys. Rev. **D82** (2010) 072006,  
 3686 [arXiv:1006.4241](#).
- 3687 [17] CDF collaboration, T. Aaltonen *et al.*, *Measurements of branching fraction*  
 3688 *ratios and CP asymmetries in  $B^\pm \rightarrow D_{CP}K^\pm$  decays in hadron collisions*,  
 3689 Phys. Rev. **D81** (2010) 031105, [arXiv:0911.0425](#).
- 3690 [18] CDF collaboration, T. Aaltonen *et al.*, *Measurements of branching fraction*  
 3691 *ratios and CP-asymmetries in suppressed  $B^- \rightarrow D(\rightarrow K^+\pi^-)K^-$  and  $B^- \rightarrow$*   
 3692  *$D(\rightarrow K^+\pi^-)\pi^-$  decays*, Phys. Rev. **D84** (2011) 091504, [arXiv:1108.5765](#).
- 3693 [19] LHCb collaboration, R. Aaij *et al.*, *Observation of CP violation in  $B^\pm \rightarrow$*   
 3694  *$DK^\pm$  decays*, Phys. Lett. **B712** (2012) 203, Erratum *ibid.* **B713** (2012) 351,  
 3695 [arXiv:1203.3662](#).
- 3696 [20] LHCb collaboration, R. Aaij *et al.*, *First observation of CP violation in the*  
 3697 *decays of  $B_s^0$  mesons*, Phys. Rev. Lett. **110** (2013) 221601, [arXiv:1304.6173](#).
- 3698 [21] LHCb collaboration, R. Aaij *et al.*, *Observation of CP violation in charm*  
 3699 *decays*, Phys. Rev. Lett. **122** (2019) 211803, [arXiv:1903.08726](#).
- 3700 [22] T2K collaboration, K. Abe *et al.*, *Constraint on the matter–antimatter*  
 3701 *symmetry-violating phase in neutrino oscillations*, Nature **580** (2020) 339,  
 3702 [arXiv:1910.03887](#).

- 3703 [23] L. K. Gibbons *et al.*, *Measurement of the CP-violation parameter  $\text{Re}(\varepsilon'/\varepsilon)$* ,  
 3704 Phys. Rev. Lett. **70** (1993) 1203.
- 3705 [24] G. D. Barr *et al.*, *A new measurement of direct CP violation in the neutral*  
 3706 *kaon system*, Phys. Lett. **B317** (1993) 233.
- 3707 [25] NA48 collaboration, J. R. Batley *et al.*, *A precision measurement of direct*  
 3708 *CP violation in the decay of neutral kaons into two pions*, Phys. Lett. **B544**  
 3709 (2002) 97, [arXiv:hep-ex/0208009](https://arxiv.org/abs/hep-ex/0208009).
- 3710 [26] KTeV collaboration, A. Alavi-Harati *et al.*, *Measurements of direct CP*  
 3711 *violation, CPT symmetry, and other parameters in the neutral kaon system*,  
 3712 Phys. Rev. **D67** (2003) 012005, [arXiv:hep-ex/0208007](https://arxiv.org/abs/hep-ex/0208007).
- 3713 [27] HFLAV group, Y. S. Amhis *et al.*, *Averages of b-hadron, c-hadron, and  $\tau$ -*  
 3714 *lepton properties as of 2018*, [arXiv:1909.12524](https://arxiv.org/abs/1909.12524), updated results and plots  
 3715 available at <https://hflav.web.cern.ch/>.
- 3716 [28] M. Kobayashi and T. Maskawa, *CP-Violation in the Renormalizable Theory*  
 3717 *of Weak Interaction*, Prog. Theor. Phys. **49** (1973) 652.
- 3718 [29] N. Cabibbo, *Unitary Symmetry and Leptonic Decays*, Physical Review Letters  
 3719 **10** (1963) 531.
- 3720 [30] L.-L. Chau and W.-Y. Keung, *Comments on the Parametrization of the*  
 3721 *Kobayashi-Maskawa Matrix*, Phys. Rev. Lett. **53** (1984) 1802.
- 3722 [31] Particle Data Group, P. A. Zyla *et al.*, *Review of particle physics*, Prog. Theor.  
 3723 Exp. Phys. **2020** (2020) 083C01.
- 3724 [32] L. Wolfenstein, *Parametrization of the Kobayashi-Maskawa Matrix*, Phys. Rev.  
 3725 Lett. **51** (1983) 1945.
- 3726 [33] Y. H. Ahn, H.-Y. Cheng, and S. Oh, *Wolfenstein parametrization at higher*  
 3727 *order: Seeming discrepancies and their resolution*, Phys. Lett. **B703** (2011)  
 3728 571, [arXiv:1106.0935](https://arxiv.org/abs/1106.0935).
- 3729 [34] A. J. Buras, M. E. Lautenbacher, and G. Ostermaier, *Waiting for the Top*  
 3730 *Quark Mass,  $K^+ \rightarrow \pi^+ \nu \bar{\nu}$ ,  $B_s^0 - \bar{B}_s^0$  Mixing, and CP asymmetries in B decays*,  
 3731 Phys. Rev. **D50** (1994) 3433, [arXiv:hep-ph/9403384](https://arxiv.org/abs/hep-ph/9403384).
- 3732 [35] J. Charles *et al.*, *CP violation and the CKM matrix: Assessing the impact of the*  
 3733 *asymmetric B factories*, Eur. Phys. J. **C41** (2005) 1, [arXiv:hep-ph/0406184](https://arxiv.org/abs/hep-ph/0406184).

- [36] CKMfitter group, J. Charles *et al.*, *Current status of the Standard Model CKM fit and constraints on  $\Delta F = 2$  new physics*, Phys. Rev. **D91** (2015) 073007, arXiv:1501.05013, updated results and plots available at <http://ckmfitter.in2p3.fr/>.
- [37] J. Brod and J. Zupan, *The ultimate theoretical error on  $\gamma$  from  $B \rightarrow DK$  decays*, JHEP **2014** (2014) 51, arXiv:1308.5663.
- [38] M. Blanke and A. J. Buras, *Emerging  $\Delta M_d$ -anomaly from tree-level determinations of  $|V_{cb}|$  and the angle  $\gamma$* , Eur. Phys. J. **C79** (2019) 159, arXiv:1812.06963.
- [39] UTfit collaboration, M. Bona *et al.*, *The unitarity triangle fit in the standard model and hadronic parameters from lattice QCD: A reappraisal after the measurements of  $\Delta m_s$  and  $BR(B \rightarrow \tau\nu_\tau)$* , JHEP **10** (2006) 081, arXiv:hep-ph/0606167, updated results and plots available at <http://www.utfit.org/>.
- [40] LHCb collaboration, I. Bediaga *et al.*, *Physics case for an LHCb Upgrade II - Opportunities in flavour physics, and beyond, in the HL-LHC era*, arXiv:1808.08865.
- [41] Y. Grossman and M. Savastio, *Effects of  $K^0 - \bar{K}^0$  mixing on determining  $\gamma$  from  $B^\pm \rightarrow DK^\pm$* , JHEP **2014** (2014) 8, arXiv:1311.3575.
- [42] M. Gronau and D. Wyler, *On determining a weak phase from charged  $B$  decay asymmetries*, Phys. Lett. **B265** (1991) 172.
- [43] M. Gronau and D. London, *How to determine all the angles of the unitarity triangle from  $B_d^0 \rightarrow DK_S^0$  and  $B_s^0 \rightarrow D\phi$* , Phys. Lett. **B253** (1991) 483.
- [44] D. Atwood, I. Dunietz, and A. Soni, *Enhanced CP Violation with  $B \rightarrow KD^0(\bar{D}^0)$  Modes and Extraction of the Cabibbo-Kobayashi-Maskawa Angle  $\gamma$* , Phys. Rev. Lett. **78** (1997) 3257, arXiv:hep-ph/9612433.
- [45] D. Atwood, I. Dunietz, and A. Soni, *Improved methods for observing CP violation in  $B^\pm \rightarrow KD$  and measuring the CKM phase  $\gamma$* , Phys. Rev. **D63** (2001) 036005, arXiv:hep-ph/0008090.
- [46] Belle collaboration, K. Trabelsi, *Study of direct CP in charmed  $B$  decays and measurement of the CKM angle gamma at Belle*, arXiv:1301.2033.

- 3765 [47] BaBar collaboration, D. Derkach, *Combination of gamma measurements from*  
 3766 *BaBar*, arXiv:1301.3283.
- 3767 [48] LHCb collaboration, R. Aaij *et al.*, *Measurement of the CKM angle  $\gamma$  from a*  
 3768 *combination of LHCb results*, JHEP **12** (2016) 087, arXiv:1611.03076.
- 3769 [49] LHCb collaboration, M. W. Kenzie and M. P. Whitehead, *Update of the LHCb*  
 3770 *combination of the CKM angle  $\gamma$* , LHCb-CONF-2018-002, 2018.
- 3771 [50] M. Kenzie, M. Martinelli, and N. Tuning, *Estimating  $r_B^{D\pi}$  as an input to*  
 3772 *the determination of the CKM angle  $\gamma$* , Phys. Rev. **D94** (2016) 054021,  
 3773 arXiv:1606.09129.
- 3774 [51] T. Evans, J. Libby, S. Malde, and G. Wilkinson, *Improved sensitivity to the*  
 3775 *CKM phase  $\gamma$  through binning phase space in  $B^- \rightarrow DK^-$ ,  $D \rightarrow K^+\pi^-\pi^-\pi^+$*   
 3776 *decays*, Phys. Lett. **B802** (2020) 135188, arXiv:1909.10196.
- 3777 [52] P. K. Resmi, J. Libby, S. Malde, and G. Wilkinson, *Quantum-correlated mea-*  
 3778 *surements of  $D \rightarrow K_S^0\pi^+\pi^-\pi^0$  decays and consequences for the determination*  
 3779 *of the CKM angle  $\gamma$* , JHEP **01** (2018) 082, arXiv:1710.10086.
- 3780 [53] S. Harnew *et al.*, *Model-independent determination of the strong phase*  
 3781 *difference between  $D_0$  and  $\bar{D}_0 \rightarrow \pi^+\pi^-\pi^+\pi^-$  amplitudes*, JHEP **2018** (2018)  
 3782 144, arXiv:1709.03467.
- 3783 [54] R. H. Dalitz, *CXII. On the analysis of  $\tau$ -meson data and the nature of the*  
 3784  *$\tau$ -meson*, The London, Edinburgh, and Dublin Philosophical Magazine and  
 3785 Journal of Science **44** (1953) 1068.
- 3786 [55] BaBar and Belle collaborations, I. Adachi *et al.*, *Measurement of  $\cos 2\beta$  in*  
 3787  *$B^0 \rightarrow D^{(*)}h^0$  with  $D \rightarrow K_S^0\pi^+\pi^-$  decays by a combined time-dependent*  
 3788 *Dalitz plot analysis of BaBar and Belle data*, Phys. Rev. **D98** (2018) 112012,  
 3789 arXiv:1804.06153.
- 3790 [56] S. U. Chung *et al.*, *Partial wave analysis in K-matrix formalism*, Annalen der  
 3791 Physik **507** (1995) 404.
- 3792 [57] D. Aston *et al.*, *A study of  $K^-\pi^+$  scattering in the reaction  $K^-p \rightarrow \pi^+n$  at*  
 3793 *11 GeV/c*, Nucl. Phys. **B296** (1988) 493.
- 3794 [58] A. Bondar, *Proceedings of BINP special analysis meeting on Dalitz analysis,*  
 3795 *24-26 Sep. 2002, unpublished*.

- 3796 [59] Belle collaboration, A. Poluektov *et al.*, *Measurement of  $\phi_3$  with Dalitz*  
 3797 *plot analysis of  $B^\pm \rightarrow D^{(*)}K^\pm$  decay*, Phys. Rev. **D70** (2004) 072003,  
 3798 [arXiv:hep-ex/0406067](https://arxiv.org/abs/hep-ex/0406067).
- 3799 [60] A. Giri, Y. Grossman, A. Soffer, and J. Zupan, *Determining  $\gamma$  using*  
 3800  *$B^\pm \rightarrow DK^\pm$  with multibody  $D$  decays*, Phys. Rev. **D68** (2003) ,  
 3801 [arXiv:hep-ph/0303187](https://arxiv.org/abs/hep-ph/0303187).
- 3802 [61] A. Ceccucci *et al.*, *{Origins of the method to determine the CKM angle*  
 3803  *$\$\\gamma\$$  using  $B\{\\hat{\\pm}\\} \\rightarrow D K\{\\hat{\\pm}\\}$ ,  $D \\rightarrow K_{-}\\{\\rm S\\}\\hat{\\pi}\\hat{\\pm}\\}$*   
 3804 *decays}*, arXiv:2006.12404 [hep-ex, physics:hep-ph, physics:physics] (2020)  
 3805 [arXiv:2006.12404](https://arxiv.org/abs/2006.12404).
- 3806 [62] BaBar collaboration, B. Aubert *et al.*, *Measurement of the Cabibbo-Kobayashi-*  
 3807 *Maskawa angle  $\gamma$  in  $B^\mp \rightarrow D^{(*)}K^\mp$  decays with a Dalitz analysis of  $D \rightarrow$*   
 3808  *$K_S^0\pi^-\pi^+$* , Phys. Rev. Lett. **95** (2005) 121802, [arXiv:hep-ex/0504039](https://arxiv.org/abs/hep-ex/0504039).
- 3809 [63] BaBar collaboration, B. Aubert *et al.*, *Improved measurement of the CKM*  
 3810 *angle  $\gamma$  in  $B^\mp \rightarrow D^{(*)}K^{(*)\mp}$  decays with a Dalitz plot analysis of  $D$  decays to*  
 3811  *$K_S^0\pi^+\pi^-$  and  $K_S^0K^+K^-$* , Phys. Rev. **D78** (2008) 034023, [arXiv:0804.2089](https://arxiv.org/abs/0804.2089).
- 3812 [64] BaBar collaboration, P. del Amo Sanchez *et al.*, *Evidence for direct CP*  
 3813 *violation in the measurement of the Cabibbo-Kobayashi-Maskawa angle*  
 3814  *$\gamma$  with  $B^\mp \rightarrow D^{(*)}K^{(*)\mp}$  decays*, Phys. Rev. Lett. **105** (2010) 121801,  
 3815 [arXiv:1005.1096](https://arxiv.org/abs/1005.1096).
- 3816 [65] Belle collaboration, A. Poluektov *et al.*, *Measurement of  $\phi_3$  with Dalitz*  
 3817 *plot analysis of  $B^+ \rightarrow D^{(*)}K^{(*)+}$  decay*, Phys. Rev. **D73** (2006) 112009,  
 3818 [arXiv:hep-ex/0604054](https://arxiv.org/abs/hep-ex/0604054).
- 3819 [66] Belle collaboration, A. Poluektov *et al.*, *Evidence for direct CP violation in*  
 3820 *the decay  $B^\pm \rightarrow D^{(*)}K^\pm$ ,  $D \rightarrow K_S^0\pi^+\pi^-$  and measurement of the CKM phase*  
 3821  *$\phi_3$* , Phys. Rev. **D81** (2010) 112002, [arXiv:1003.3360](https://arxiv.org/abs/1003.3360).
- 3822 [67] LHCb collaboration, R. Aaij *et al.*, *Measurement of CP violation and*  
 3823 *constraints on the CKM angle  $\gamma$  in  $B^\pm \rightarrow DK^\pm$  with  $D \rightarrow K_S^0\pi^+\pi^-$  decays*,  
 3824 *Nucl. Phys. **B888** (2014) 169*, [arXiv:1407.6211](https://arxiv.org/abs/1407.6211).
- 3825 [68] LHCb collaboration, R. Aaij *et al.*, *Measurement of the CKM angle  $\gamma$*   
 3826 *using  $B^0 \rightarrow DK^{*0}$  with  $D \rightarrow K_S^0\pi^+\pi^-$  decays*, JHEP **08** (2016) 137,  
 3827 [arXiv:1605.01082](https://arxiv.org/abs/1605.01082).

- 3828 [69] A. Bondar and A. Poluektov, *Feasibility study of model-independent approach*  
 3829      to  $\phi_3$  measurement using Dalitz plot analysis, Eur. Phys. J. **C47** (2006) 347,  
 3830      arXiv:hep-ph/0510246.
- 3831 [70] A. Bondar and A. Poluektov, *The use of quantum-correlated  $D_0$  decays for*  
 3832       $\phi_3$  measurement, Eur. Phys. J. **C55** (2008) 51, arXiv:0801.0840.
- 3833 [71] Belle collaboration, H. Aihara *et al.*, *First measurement of  $\phi_3$  with a model-*  
 3834      *independent Dalitz plot analysis of  $B^\pm \rightarrow DK^\pm$ ,  $D \rightarrow K_S^0\pi^+\pi^-$  decay*, Phys.  
 3835      Rev. **D85** (2012) 112014, arXiv:1204.6561.
- 3836 [72] LHCb collaboration, R. Aaij *et al.*, *A model-independent Dalitz plot analysis*  
 3837      *of  $B^\pm \rightarrow DK^\pm$  with  $D \rightarrow K_S^0h^+h^-$  ( $h = \pi, K$ ) decays and constraints on the*  
 3838      *CKM angle  $\gamma$* , Phys. Lett. **B718** (2012) 43, arXiv:1209.5869.
- 3839 [73] LHCb collaboration, R. Aaij *et al.*, *Measurement of the CKM angle  $\gamma$  using*  
 3840       *$B^\pm \rightarrow DK^\pm$  with  $D \rightarrow K_S^0\pi^+\pi^-$ ,  $K_S^0K^+K^-$  decays*, JHEP **10** (2014) 097,  
 3841      arXiv:1408.2748.
- 3842 [74] CLEO collaboration, J. Libby *et al.*, *Model-independent determination of the*  
 3843      *strong-phase difference between  $D^0$  and  $\bar{D}^0 \rightarrow K_{S,L}^0h^+h^-$  ( $h = \pi, K$ ) and its*  
 3844      *impact on the measurement of the CKM angle  $\gamma/\phi_3$* , Phys. Rev. **D82** (2010)  
 3845      112006, arXiv:1010.2817.
- 3846 [75] A. Poluektov, *Unbinned model-independent measurements with coherent*  
 3847      *admixtures of multibody neutral D meson decays*, Eur. Phys. J. **C78** (2018)  
 3848      121, arXiv:1712.08326.
- 3849 [76] BESIII collaboration, M. Ablikim *et al.*, *Model-independent determination of*  
 3850      *the relative strong-phase difference between  $D^0$  and  $\bar{D}^0 \rightarrow K_{S,L}^0\pi^+\pi^-$  and its*  
 3851      *impact on the measurement of the CKM angle  $\gamma/\phi_3$* , arXiv:2003.00091.
- 3852 [77] BESIII collaboration, M. Ablikim *et al.*, *Improved model-independent deter-*  
 3853      *mination of the strong-phase difference between  $D^0$  and  $\bar{D}^0 \rightarrow K_{S,L}^0K^+K^-$*   
 3854      *decays*, arXiv:2007.07959.
- 3855 [78] LHCb collaboration, R. Aaij *et al.*, *Near-threshold  $D\bar{D}$  spectroscopy and obser-*  
 3856      *vation of a new charmonium state*, JHEP **07** (2019) 035, arXiv:1903.12240.
- 3857 [79] C. Thomas and G. Wilkinson, *Model-independent  $D^0 - \bar{D}^0$  mixing and CP*  
 3858      *violation studies with  $D^0 \rightarrow K_S^0\pi^+\pi^-$  and  $D^0 \rightarrow K_S^0K^+K^-$* , JHEP **2012** (2012)  
 3859      185, arXiv:1209.0172.

- [80] LHCb collaboration, R. Aaij *et al.*, *Model-independent measurement of the CKM angle  $\gamma$  using  $B^0 \rightarrow DK^{*0}$  decays with  $D \rightarrow K_S^0\pi^+\pi^-$  and  $K_S^0K^+K^-$* , JHEP **06** (2016) 131, arXiv:1604.01525.
- [81] M. Nayak *et al.*, *First determination of the CP content of  $D \rightarrow \pi^+\pi^-\pi^0$  and  $D \rightarrow K^+K^-\pi^0$* , Phys. Lett. **B740** (2015) 1, arXiv:1410.3964.
- [82] S. Malde *et al.*, *First determination of the CP content of  $D \rightarrow \pi^+\pi^-\pi^+\pi^-$  and updated determination of the CP contents of  $D \rightarrow \pi^+\pi^-\pi^0$  and  $D \rightarrow K^+K^-\pi^0$* , Phys. Lett. **B747** (2015) 9, arXiv:1504.05878.
- [83] M. Gronau, *Improving bounds on  $\gamma$  in  $B^\pm \rightarrow DK^\pm$  and  $B^{\pm,0} \rightarrow DX_s^{\pm,0}$* , Phys. Lett. **B557** (2003) 198, arXiv:hep-ph/0211282.
- [84] J. Garra Ticó, *A strategy for a simultaneous measurement of CP violation parameters related to the CKM angle  $\gamma$  in multiple B meson decay channels*, arXiv:1804.05597.
- [85] J. G. Ticó *et al.*, *A study of the sensitivity to CKM angle  $\gamma$  under simultaneous determination from multiple B meson decay modes*, arXiv:1909.00600.
- [86] C. De Melis, *The CERN accelerator complex. Complexe des accélérateurs du CERN*, <https://cds.cern.ch/record/2119882>, 2016.
- [87] ATLAS collaboration, *Luminosity determination in pp collisions at  $\sqrt{s} = 13$  TeV using the ATLAS detector at the LHC*, ATLAS-CONF-2019-021, 2019.
- [88] LHCb collaboration, A. A. Alves *et al.*, *The LHCb Detector at the LHC*, J. Inst. **3** (2008) S08005.
- [89] LHCb collaboration, *LHCb reoptimized detector design and performance: Technical Design Report*, LHCb-TDR-9, 2003.
- [90] LHCb collaboration, C. Elsässer,  $\bar{b}b$  production angle plots, [https://lhcb.web.cern.ch/lhcb/speakersbureau/html/bb\\_ProductionAngles.html](https://lhcb.web.cern.ch/lhcb/speakersbureau/html/bb_ProductionAngles.html).
- [91] LHCb collaboration, P. R. Barbosa-Marinho *et al.*, *LHCb VELO (VErtex LOcator) - Technical Design Report*, LHCb-TDR-5, 2001.
- [92] LHCb VELO group, R. Aaij *et al.*, *Performance of the LHCb Vertex Locator*, J. Inst. **9** (2014) P09007, arXiv:1405.7808.

- 3889 [93] LHCb Outer Tracker group, R. Arink *et al.*, *Performance of the LHCb Outer*
- 3890 *Tracker*, J. Inst. **9** (2014) P01002, arXiv:1311.3893.
- 3891 [94] LHCb collaboration, R. Aaij *et al.*, *LHCb detector performance*, Int. J. Mod.
- 3892 Phys **A30** (2015) 1530022, arXiv:1412.6352.
- 3893 [95] LHCb collaboration, S. Amato *et al.*, *LHCb RICH: Technical Design Report*,
- 3894 LHCb-TDR-3, 2000.
- 3895 [96] LHCb RICH collaboration, M. Adinolfi *et al.*, *Performance of the LHCb RICH*
- 3896 *detector at the LHC*, Eur. Phys. J. **C73** (2013) 2431, arXiv:1211.6759.
- 3897 [97] LHCb RICH collaboration, A. Papanestis *et al.*, *Performance of the LHCb*
- 3898 *RICH detectors during the LHC Run II*, Nucl. Instrum. Meth **A876** (2017)
- 3899 221, arXiv:1703.08152.
- 3900 [98] LHCb collaboration, S. Amato *et al.*, *LHCb calorimeters: Technical Design*
- 3901 *Report*, LHCb-TDR-2, 2000.
- 3902 [99] LHCb ECAL group, I. Machikhiliyan, *The LHCb electromagnetic calorimeter*,
- 3903 J. Phys. : Conf. Ser. **160** (2009) 012047.
- 3904 [100] LHCb collaboration, R. Aaij *et al.*, *Search for lepton-universality vi-*
- 3905 *olation in  $B^+ \rightarrow K^+ \ell^+ \ell^-$  decays*, Phys. Rev. Lett. **122** (2019) 191801,
- 3906 arXiv:1903.09252.
- 3907 [101] LHCb collaboration, R. Aaij *et al.*, *Measurement of CP-averaged observ-*
- 3908 *ables in the  $B^0 \rightarrow K^{*0} \mu^+ \mu^-$  decay*, Phys. Rev. Lett. **125** (2020) 011802,
- 3909 arXiv:2003.04831.
- 3910 [102] LHCb collaboration, R. Aaij *et al.*, *Measurement of the  $B_s^0 \rightarrow \mu^+ \mu^-$  branching*
- 3911 *fraction and effective lifetime and search for  $B^0 \rightarrow \mu^+ \mu^-$  decays*, Phys. Rev.
- 3912 Lett. **118** (2017) 191801, arXiv:1703.05747.
- 3913 [103] LHCb collaboration, *LHCb muon system: second addendum to the Technical*
- 3914 *Design Report*, LHCb-TDR-4-add-2, 2005.
- 3915 [104] D. Hutchcroft, *VELO Pattern Recognition*, LHCb-2007-013, 2007.
- 3916 [105] M. Needham and J. Van Tilburg, *Performance of the track matching*, LHCb-
- 3917 2007-020, 2007.
- 3918 [106] M. Needham, *Performance of the Track Matching*, LHCb-2007-129, 2007.

- 3919 [107] O. Callot, *Downstream Pattern Recognition*, LHCb-2007-026, 2007.
- 3920 [108] R. Frühwirth, *Application of Kalman filtering to track and vertex fitting*, Nucl.  
3921 Instrum. Meth **A262** (1987) 444.
- 3922 [109] J. Van Tilburg, *Track simulation and reconstruction in LHCb*, CERN-  
3923 THESIS-2005-040, 2005.
- 3924 [110] M. De Cian *et al.*, *Measurement of the track finding efficiency*, LHCb-PUB-  
3925 2011-025, 2012.
- 3926 [111] LHCb collaboration, *PID performance plots*,  
3927 <https://twiki.cern.ch/twiki/bin/view/LHCb/PIDConferencePlots>.
- 3928 [112] R. W. Forty and O. Schneider, *RICH pattern recognition*, LHCb-98-040, 1998.
- 3929 [113] J. R. T. De Mello-Neto and M. Gandelman, *Muon ID performance with the  
3930 reoptimized LHCb detector*, LHCb-2003-089, 2003.
- 3931 [114] M. Gandelman and E. Polycarpo, *The Performance of the LHCb Muon  
3932 Identification Procedure*, LHCb-2007-145, 2008.
- 3933 [115] H. Terrier and I. Belyaev, *Particle identification with LHCb calorimeters*,  
3934 LHCb-2003-092, 2003.
- 3935 [116] LHCb collaboration, R. Aaij *et al.*, *Design and performance of the LHCb  
3936 trigger and full real-time reconstruction in Run 2 of the LHC*, J. Inst. **14**  
3937 (2019) P04013, [arXiv:1812.10790](https://arxiv.org/abs/1812.10790).
- 3938 [117] LHCb collaboration, R. Aaij *et al.*, *The LHCb trigger and its performance in  
3939 2011*, J. Inst. **8** (2013) P04022, [arXiv:1211.3055](https://arxiv.org/abs/1211.3055).
- 3940 [118] V. V. Gligorov and M. Williams, *Efficient, reliable and fast high-level  
3941 triggering using a bonsai boosted decision tree*, J. Inst. **8** (2013) P02013,  
3942 [arXiv:1210.6861](https://arxiv.org/abs/1210.6861).
- 3943 [119] I. Bird, *Computing for the Large Hadron Collider*, Annual Review of Nuclear  
3944 and Particle Science **61** (2011) 99.
- 3945 [120] T. Sjöstrand, S. Mrenna, and P. Skands, *A brief introduction to PYTHIA 8.1*,  
3946 Comput. Phys. Commun. **178** (2008) 852, [arXiv:0710.3820](https://arxiv.org/abs/0710.3820); T. Sjöstrand,  
3947 S. Mrenna, and P. Skands, *PYTHIA 6.4 physics and manual*, JHEP **05** (2006)  
3948 026, [arXiv:hep-ph/0603175](https://arxiv.org/abs/hep-ph/0603175).

- 3949 [121] I. Belyaev *et al.*, *Handling of the generation of primary events in Gauss, the*  
3950 *LHCb simulation framework*, J. Phys. Conf. Ser. **331** (2011) 032047.
- 3951 [122] D. J. Lange, *The EvtGen particle decay simulation package*, Nucl. Instrum.  
3952 Meth. **A462** (2001) 152.
- 3953 [123] P. Golonka and Z. Was, *PHOTOS Monte Carlo: A precision tool for*  
3954 *QED corrections in Z and W decays*, Eur. Phys. J. **C45** (2006) 97,  
3955 arXiv:hep-ph/0506026.
- 3956 [124] Geant4 collaboration, J. Allison *et al.*, *Geant4 developments and applications*,  
3957 IEEE Trans. Nucl. Sci. **53** (2006) 270.
- 3958 [125] M. Clemencic *et al.*, *The LHCb simulation application, Gauss: Design,*  
3959 *evolution and experience*, J. Phys. Conf. Ser. **331** (2011) 032023.
- 3960 [126] D. Müller, M. Clemencic, G. Corti, and M. Gersabeck, *ReDecay: A novel*  
3961 *approach to speed up the simulation at LHCb*, Eur. Phys. J. **C78** (2018) 1009,  
3962 arXiv:1810.10362.
- 3963 [127] G. A. Cowan, D. C. Craik, and M. D. Needham, *RapidSim: An application*  
3964 *for the fast simulation of heavy-quark hadron decays*, Comput. Phys. Commun.  
3965 **214** (2017) 239, arXiv:1612.07489.
- 3966 [128] LHCb collaboration, *LHCb performance numbers*,  
3967 <https://lhcb.web.cern.ch/speakersbureau/html/PerformanceNumbers.html>.
- 3968 [129] LHCb collaboration, R. Aaij *et al.*, *Measurement of the  $B^\pm$  production*  
3969 *cross-section in pp collisions at  $\sqrt{s} = 7$  and 13 TeV*, JHEP **12** (2017) 026,  
3970 arXiv:1710.04921.
- 3971 [130] A. Pais and O. Piccioni, *Note on the decay and absorption of the  $\theta^0$* , Phys.  
3972 Rev. **100** (1955) 1487.
- 3973 [131] M. L. Good, *Relation between Scattering and Absorption in the Pais-Piccioni*  
3974 *Phenomenon*, Phys. Rev. **106** (1957) 591.
- 3975 [132] W. Fetscher *et al.*, *Regeneration of arbitrary coherent neutral kaon states: A*  
3976 *new method for measuring the  $K^0 - \bar{K}^0$  forward scattering amplitudeforward*  
3977 *scattering amplitude*, Z. Phys **C72** (1996) 543.
- 3978 [133] Belle II collaboration, E. Kou *et al.*, *The Belle II Physics Book*, Prog. Theor.  
3979 Exp. Phys **2019** (2019) 123C01, arXiv:1808.10567.

- [3980] [134] I. I. Bigi and H. Yamamoto, *Interference between Cabibbo allowed and doubly*  
 [3981] *forbidden transitions in  $D \rightarrow K_{S,L} + \pi$ 's decays*, Phys. Lett. **B349** (1995) 363,  
 [3982] arXiv:hep-ph/9502238.
- [3983] [135] CLEO collaboration, Q. He *et al.*, *Comparison of  $D \rightarrow K_S^0\pi$  and  $D \rightarrow K_L^0\pi$*   
 [3984] *decay rates*, Phys. Rev. Lett. **100** (2008) 091801, arXiv:0711.1463.
- [3985] [136] Y. Grossman and Y. Nir, *CP violation in  $\tau^\pm \rightarrow \pi^\pm K_S\nu$  and  $D^\pm \rightarrow \pi^\pm K_S$ : the*  
 [3986] *importance of  $K_S - K_L$  interference*, JHEP **2012** (2012) 2, arXiv:1110.3790.
- [3987] [137] Y. Ohnishi *et al.*, *Accelerator design at SuperKEKB*, Prog. Theor. Exp. Phys  
 [3988] **2013** (2013) .
- [3989] [138] J. Gassner, M. Needham, and O. Steinkamp, *Layout and Expected Performance*  
 [3990] *of the LHCb TT Station*, LHCb-2003-140, 2004.
- [3991] [139] Belle collaboration, A. B. Kaliyar *et al.*, *Measurements of branching fraction*  
 [3992] *and direct CP asymmetry in  $B^\pm \rightarrow K_S^0 K_S^0 K^\pm$  and a search for  $B^\pm \rightarrow$*   
 [3993]  *$K_S^0 K_S^0 \pi^\pm$* , Phys. Rev. **D99** (2019) 031102, arXiv:1812.10221.
- [3994] [140] N. Hiroshi, *Search for new physics by a time-dependent CP violation analysis*  
 [3995] *of the decay  $B \rightarrow K_S^0$  eta gamma using the Belle detector*, PhD thesis, Tohoku  
 [3996] University, Senday, 2015.
- [3997] [141] A. Gsponer *et al.*, *Precise Coherent  $K_S^0$  Regeneration Amplitudes for C, Al,*  
 [3998] *Cu, Sn, and Pb Nuclei from 20 to 140 GeV/c and Their Interpretation*, Phys.  
 [3999] Rev. Lett. **22** (1979) 13.
- [4000] [142] R. A. Briere and B. Weinstein, *Determining the Phase of a Strong Scattering*  
 [4001] *Amplitude from Its Momentum Dependence to Better Than 1°: The Example*  
 [4002] *of Kaon Regeneration*, Phys. Rev. Lett. **75** (1995) 402, arXiv:1006.1938.
- [4003] [143] B. R. Ko, E. Won, B. Golob, and P. Pakhlov, *Effect of nuclear interactions*  
 [4004] *of neutral kaons on CP asymmetry measurements*, Phys. Rev. **D84** (2011)  
 [4005] 111501, arXiv:1006.1938.
- [4006] [144] LHCb collaboration, *LHCb VELO Upgrade Technical Design Report*, LHCB-  
 [4007] TDR-013, 2013.
- [4008] [145] LHCb collaboration, *LHCb PID Upgrade Technical Design Report*, LHCB-  
 [4009] TDR-014, 2013.

- 4010 [146] P. K. Resmi, J. Libby, S. Malde, and G. Wilkinson, *Quantum-correlated mea-*  
 4011 *surements of  $D \rightarrow K_S^0 \pi^+ \pi^- \pi^0$  decays and consequences for the determination*  
 4012 *of the CKM angle  $\gamma$* , JHEP **01** (2018) 082, [arXiv:1710.10086](https://arxiv.org/abs/1710.10086).
- 4013 [147] W. D. Hulsbergen, *Decay chain fitting with a Kalman filter*, Nucl. Instrum.  
 4014 Meth. **A552** (2005) 566, [arXiv:physics/0503191](https://arxiv.org/abs/physics/0503191).
- 4015 [148] L. Breiman, J. H. Friedman, R. A. Olshen, and C. J. Stone, *Classification and*  
 4016 *regression trees*, Wadsworth international group, Belmont, California, USA,  
 4017 1984.
- 4018 [149] H. Voss, A. Hoecker, J. Stelzer, and F. Tegenfeldt, *TMVA - Toolkit for*  
 4019 *Multivariate Data Analysis with ROOT*, PoS **ACAT** (2007) 040; A. Hoecker  
 4020 *et al.*, *TMVA 4 — Toolkit for Multivariate Data Analysis with ROOT. Users*  
 4021 *Guide.*, [arXiv:physics/0703039](https://arxiv.org/abs/physics/0703039).
- 4022 [150] L. Anderlini *et al.*, *The PIDCalib package*, LHCb-PUB-2016-021, 2016.
- 4023 [151] M. Pivk and F. R. Le Diberder, *sPlot: A statistical tool to unfold data distri-*  
 4024 *butions*, Nucl. Instrum. Meth. **A555** (2005) 356, [arXiv:physics/0402083](https://arxiv.org/abs/physics/0402083).
- 4025 [152] A. N. Kolmogorov, *Sulla Determinazione Empirica di Una Legge di*  
 4026 *Distribuzione*, Giornale dell’Istitutio Italiano degli Attuari **4** (1933) 83;  
 4027 N. Smirnov, *Table for Estimating the Goodness of Fit of Empirical Dis-*  
 4028 *tributions*, Annals of Mathematical Statistics **19** (1948) 279.
- 4029 [153] R. Barlow, *Extended maximum likelihood*, Nucl. Instrum. Meth. **A297** (1990)  
 4030 496.
- 4031 [154] W. Verkerke and D. P. Kirkby, *The RooFit toolkit for data modeling*, eConf  
 4032 **C0303241** (2003).
- 4033 [155] T. Skwarnicki, *A study of the radiative cascade transitions between the Upsilon-*  
 4034 *prime and Upsilon resonances*, PhD thesis, Institute of Nuclear Physics,  
 4035 Krakow, 1986, DESY-F31-86-02.
- 4036 [156] LHCb collaboration, R. Aaij *et al.*, *Measurement of CP observables in  $B^\pm \rightarrow$*   
 4037  *$DK^\pm$  and  $B^\pm \rightarrow D\pi^\pm$  with two- and four-body D decays*, Phys. Lett. **B760**  
 4038 (2016) 117, [arXiv:1603.08993](https://arxiv.org/abs/1603.08993).
- 4039 [157] LHCb collaboration, R. Aaij *et al.*, *Dalitz plot analysis of  $B^0 \rightarrow \bar{D}^0 \pi^+ \pi^-$*   
 4040 *decays*, Phys. Rev. **D92** (2015) 032002, [arXiv:1505.01710](https://arxiv.org/abs/1505.01710).

- 4041 [158] LHCb collaboration, R. Aaij *et al.*, *Constraints on the unitarity triangle angle*  
 4042  *$\gamma$  from Dalitz plot analysis of  $B^0 \rightarrow DK^+\pi^-$  decays*, Phys. Rev. **D93** (2016)  
 4043 112018, Erratum ibid. **D94** (2016) 079902, [arXiv:1602.03455](https://arxiv.org/abs/1602.03455).
- 4044 [159] LHCb collaboration, R. Aaij *et al.*, *Measurement of CP observables in*  
 4045  *$B^\pm \rightarrow D^{(*)}K^\pm$  and  $B^\pm \rightarrow D^{(*)}\pi^\pm$  decays*, Phys. Lett. **B777** (2017) 16,  
 4046 [arXiv:1708.06370](https://arxiv.org/abs/1708.06370).
- 4047 [160] LHCb collaboration, R. Aaij *et al.*, *Dalitz plot analysis of  $B_s^0 \rightarrow \bar{D}^0 K^- \pi^+$*   
 4048 *decays*, Phys. Rev. **D90** (2014) 072003, [arXiv:1407.7712](https://arxiv.org/abs/1407.7712).
- 4049 [161] LHCb collaboration, R. Aaij *et al.*, *Measurement of b-hadron fractions*  
 4050 *in 13 TeV pp collisions*, LHCb-PAPER-2018-050 CERN-EP-2019-016, in  
 4051 preparation.
- 4052 [162] A. Bondar, A. Poluektov, and V. Vorobiev, *Charm mixing in a model-*  
 4053 *independent analysis of correlated  $D^0\bar{D}^0$  decays*, Phys. Rev. **D82** (2010)  
 4054 034033, [arXiv:1004.2350](https://arxiv.org/abs/1004.2350).
- 4055 [163] LHCb collaboration, R. Aaij *et al.*, *Measurement of CP violation in the three-*  
 4056 *body phase space of charmless  $B^\pm$  decays*, Phys. Rev. **D90** (2014) 112004,  
 4057 [arXiv:1408.5373](https://arxiv.org/abs/1408.5373).
- 4058 [164] LHCb collaboration, R. Aaij *et al.*, *TBD*, LHCb-PAPER-2019-018, in  
 4059 preparation.
- 4060 [165] M. Kenzie *et al.*, *Gammacombo user manual*, Can be obtained along with  
 4061 the code at: <https://gammacombo.github.io>.
- 4062 [166] J. Neumann, *Outline of a Theory of Statistical Estimation Based on the*  
 4063 *Classical Theory of Probability*, Phil. Trans. Royal Soc. London **A236** (1937).
- 4064 [167] E. L. Lehmann, *Elements of Large-Sample Theory*, Springer, 1998.
- 4065 [168] B. Sen, M. Walker, and M. Woodroffe, *On the Unified Method with Nuisance*  
 4066 *Parameters*, Statistica Sinica **19** (2009) 301.
- 4067 [169] C.-S. Chuang and T. L. Lai, *Resampling Methods for Confidence Intervals in*  
 4068 *Group Sequential Trials*, Biometrika **85** (1998) 317; C.-S. Chuang and T. L.  
 4069 Lai, *Hybrid Resampling Methods for Confidence Intervals*, Statistica Sinica  
 4070 **10** (2000) 1.

- [170] LHCb collaboration, R. Aaij *et al.*, *A study of CP violation in  $B^\mp \rightarrow Dh^\mp$  ( $h = K, \pi$ ) with the modes  $D \rightarrow K^\mp\pi^\pm\pi^0$ ,  $D \rightarrow \pi^+\pi^-\pi^0$  and  $D \rightarrow K^+K^-\pi^0$* , Phys. Rev. **D91** (2015) 112014, arXiv:1504.05442.
- [171] Y. Grossman, Z. Ligeti, and A. Soffer, *Measuring  $\gamma$  in  $B^\pm \rightarrow K^\pm(KK^*)_D$  decays*, Phys. Rev. **D67** (2003) 071301, arXiv:hep-ph/0210433.
- [172] LHCb collaboration, R. Aaij *et al.*, *A study of CP violation in  $B^\pm \rightarrow DK^\pm$  and  $B^\pm \rightarrow D\pi^\pm$  decays with  $D \rightarrow K_S^0 K^\pm \pi^\mp$  final states*, Phys. Lett. **B733** (2014) 36, arXiv:1402.2982.
- [173] LHCb collaboration, R. Aaij *et al.*, *Measurement of CP observables in  $B^\pm \rightarrow DK^{*\pm}$  decays using two- and four-body D-meson final states*, JHEP **11** (2017) 156, Erratum ibid. **05** (2018) 067, arXiv:1709.05855.
- [174] LHCb collaboration, R. Aaij *et al.*, *Study of  $B^- \rightarrow DK^-\pi^+\pi^-$  and  $B^- \rightarrow D\pi^-\pi^+\pi^-$  decays and determination of the CKM angle  $\gamma$* , Phys. Rev. **D92** (2015) 112005, arXiv:1505.07044.
- [175] LHCb collaboration, R. Aaij *et al.*, *Measurement of CP violation parameters in  $B^0 \rightarrow DK^{*0}$  decays*, Phys. Rev. **D90** (2014) 112002, arXiv:1407.8136.
- [176] T. Gershon, *On the measurement of the unitarity triangle angle  $\gamma$  from  $B^0 \rightarrow DK^{*0}$  decays*, Phys. Rev. **D79** (2009) 051301, arXiv:0810.2706; T. Gershon and M. Williams, *Prospects for the measurement of the unitarity triangle angle  $\gamma$  from  $B^0 \rightarrow DK^+\pi^-$  decays*, Phys. Rev. **D80** (2009) 092002, arXiv:0909.1495.
- [177] LHCb collaboration, R. Aaij *et al.*, *Measurement of CP asymmetry in  $B_s^0 \rightarrow D_s^\mp K^\pm$  decays*, JHEP **03** (2018) 059, arXiv:1712.07428.
- [178] LHCb collaboration, R. Aaij *et al.*, *Measurement of CP violation in  $B^0 \rightarrow D^\pm\pi^\mp$  decays*, JHEP **06** (2018) 084, arXiv:1805.03448.
- [179] LHCb collaboration, *Framework TDR for the LHCb Upgrade: Technical Design Report*, LHCB-TDR-012, 2012.
- [180] D. Kim, *CKM and CPV: Experimental Overview*, In talk presented 5 August, 2020, at the ICHEP conference.
- [181] C. Lin, *Hadronic Charm Meson Decays at BESIII*, In talk presented 28 July, 2020, at the ICHEP conference.